

*Journal of*  
***Mechanics of***  
***Materials and Structures***

*Volume 1, N° 8*

*October 2006*



mathematical sciences publishers

# JOURNAL OF MECHANICS OF MATERIALS AND STRUCTURES

<http://www.jomms.org>

EDITOR-IN-CHIEF Charles R. Steele

ASSOCIATE EDITOR Marie-Louise Steele  
Division of Mechanics and Computation  
Stanford University  
Stanford, CA 94305  
USA

SENIOR CONSULTING EDITOR Georg Herrmann  
Ortstrasse 7  
CH-7270 Davos Platz  
Switzerland

## BOARD OF EDITORS

D. BIGONI University of Trento, Italy  
H. D. BUI École Polytechnique, France  
J. P. CARTER University of Sydney, Australia  
R. M. CHRISTENSEN Stanford University, U.S.A.  
G. M. L. GLADWELL University of Waterloo, Canada  
D. H. HODGES Georgia Institute of Technology, U.S.A.  
J. HUTCHINSON Harvard University, U.S.A.  
C. HWU National Cheng Kung University, R.O. China  
IWONA JASIUK University of Illinois at Urbana-Champaign  
B. L. KARIHALOO University of Wales, U.K.  
Y. Y. KIM Seoul National University, Republic of Korea  
Z. MROZ Academy of Science, Poland  
D. PAMPLONA Universidade Católica do Rio de Janeiro, Brazil  
M. B. RUBIN Technion, Haifa, Israel  
Y. SHINDO Tohoku University, Japan  
A. N. SHUPIKOV Ukrainian Academy of Sciences, Ukraine  
T. TARNAI University Budapest, Hungary  
F. Y. M. WAN University of California, Irvine, U.S.A.  
P. WRIGGERS Universität Hannover, Germany  
W. YANG Tsinghua University, P.R. China  
F. ZIEGLER Technische Universität Wien, Austria

## PRODUCTION

PAULO NEY DE SOUZA Production Manager  
SILVIO LEVY Senior Production Editor  
NICHOLAS JACKSON Production Editor

---


See inside back cover or <http://www.jomms.org> for submission guidelines.

Regular subscription rate: \$500 a year.

Subscriptions, requests for back issues, and changes of address should be sent to Mathematical Sciences Publishers, 798 Evans Hall, Department of Mathematics, University of California, Berkeley, CA 94720-3840.

---

©Copyright 2007. Journal of Mechanics of Materials and Structures. All rights reserved.

 mathematical sciences publishers

## EFFECT OF TIP PROFILE ON CUTTING PROCESSABILITY OF A TRAPEZOIDAL CUTTING BLADE INDENTED TO AN ALUMINUM SHEET

SEKSAN CHAJIT, SHIGERU NAGASAWA, YASUSHI  
FUKUZAWA, MITSUHIRO MURAYAMA AND ISAMU KATAYAMA

This paper is an investigation of detaching phenomena of a trapezoidal cutting blade on a wedged surface of a thin work sheet. To study critical conditions for cutting off an aluminum sheet, the wedged profile of the work sheet was experimentally studied by varying the tip thickness of the trapezoidal cutting blade, which simulated a crushed bevel blade. To analyze the detached condition and separation force of the wedged sheet, an elastoplastic finite element program was used to analyze wedge indentation to the work sheet. The following results were obtained: (i) the deformation of the wedged sheet can be classified in four patterns; (ii) the critical condition for cutting off the work sheet depends on the ratio of tip thickness by sheet thickness  $w/t$ ; (iii) the separation of the work sheet occurred statistically for  $w/t = 0.13 \sim 0.28$ ; and (iv) the separation line force can be used to explain the necking mode and the detached condition.

### 1. Introduction

A cutting method in which a center bevel blade cuts into sheet material on a counter plate is widely used in the packaging or printing industry, for example, diecutting of paperboard, labels, laminated resin sheets, ductile metal film, and other similar materials [Inaba 1998; Hesse and Tenzer 1963; Tanaka and Akamatsu 2001]. However, many problems that affect product quality are caused by the variation of blade tip such as crushing or abrasion of the wedge profile during the cutting process. These problems occur because in a flatbed type cutting machine, the cutting blade moves reciprocally and contacts with the counter plate without any stopper. [Grebe and Hofer 1973] experimentally studied the relationship between the blade abrasion and its cutting force variance for both paperboards and corrugated boards. [Nagasawa et al. 2001; Nagasawa et al. 2004] investigated experimentally and numerically how the tip profile of a normal blade was crushed during cutting of a white-coated paperboard. It was shown that the cutting blade tip became trapezoidal (as a crushed form) when the cutting blade tip contacted with the counter plate. [Nagasawa et al. 2002] also reported on the effects on tip shape when string-like dust occurs, and on the relationship between breaking characteristics of paperboard and cutting force responses. These results indicated to us that study of the processability of the trapezoidal cutting blade would be of interest.

Several theoretical works [Grunzweig et al. 1954; Hill 1953] on wedge indentation into an isotropic plastic body are useful to understand the influence of friction, apex angle of the bevel blade, thickness of the work piece, and yield stress of the work piece on the indentation force. However, these traditional models were not sufficient to explain the profile effect of the crushed tip on the die cutting process. [Murayama et al. 2003; 2004] have reported on the load response of wedge indentation into a thin

*Keywords:* shear cutting, detaching, elastoplastic FEM, separation force, wedge indentation, upsetting.

aluminum sheet, by using a trapezoidal cutting blade having a flat region on the tip to simulate crushing. In that study, Murayama et al. found the second necking mode through FEM simulation and experimental cutting of an aluminum sheet, where the ratio of tip thickness  $w$  of the blade and the thickness  $t$  of the work sheet was  $w/t = 0.013 \sim 0.23$ . That result contributed to an explanation of how burrs of an aluminum sheet occur beneath the blade tip. The mechanism that generates the aluminum burrs seems to be similar to the one which generates string-like chips on white-coated paperboard. The occurrence of necking on the bottom surface of the worksheet depended on  $w/t$ .

When  $w/t$  becomes relatively large ( $w/t \gg 0.1$ ), the sliding surface of the wedge blade is prone to detach from the deformed work sheet, and the blade tip generally pushed the work sheet in an upsetting mode. However, the critical condition for wedge separation from the work sheet was not analyzed sufficiently for  $w/t > 0.3$ . However, thinner sheets, that is, those less than  $15 \mu\text{m}$  thickness with respect to the tip thickness of  $5 \mu\text{m}$ , are often required in pattern diecutting of resin sheets or thin metal sheets. In addition, the detaching condition on the sliding surface of the trapezoidal bevel blade, and the separation force of the wedged sheet were not covered.

In this paper, therefore, we analyzed the trapezoidal blade indentation into an aluminum sheet both numerically and experimentally for the range of  $0.036 < w/t < 0.64$ . To investigate the variance of cutting processability of the blade indented on the work sheet and the critical condition for cutting off the work sheet, we focused on the final separation stage of the worksheet in the pushing shear process. In addition, the detaching phenomenon between the blade surface and the deformed work sheet has also been discussed with respect to the separation line force. It seems that the critical condition and the detaching mechanism would be useful for designing a new blade profile or modifying the crushed blade tip.

This paper is laid out as follows: [Section 2](#) describes the experimental method and the simulation conditions. [Section 2.1](#) includes details of the experimental method and the material properties of specimen, and [Section 2.2](#) includes details about the finite element modeling and its conditions. A simulation model and several parameters with respect to the detaching phenomena are also introduced. [Section 3](#) presents results and discussion regarding wedge indentation to the work sheet. [Section 3.1](#) covers the relationship between the resistance of blade indentation and  $w/t$ . [Section 3.2](#) presents corresponding results for the deformation shape and the separation probability of the aluminum work sheet through varying  $w/t$ . [Section 3.3](#) and [Section 3.4](#) cover the detaching phenomena on the sliding surface of the wedge blade, and the effect of friction coefficients, respectively. [Section 3.5](#) gives the stress distribution around the blade tip on the final stage of indentation. [Section 3.6](#) presents critical conditions and work-sheet deformation patterns that were derived both from detaching phenomena on the wedge surface, and from the load response. [Section 3.7](#) covers numerical results regarding the separation line force of the wedged worksheet. Finally, in [Section 4](#), we draw conclusions.

## Nomenclature

$B$	Width of specimen, mm
$D$	Lower crosshead displacement, mm
$E$	Young's modulus, GPa
$F$	The plastic coefficient, MPa

$F_v$	Force applied in vertical to the cutter blade, kN
$K_v$	Equivalent spring constant of the apparatus, kN/m/mm
$L$	Length of specimen in the rolling direction, mm
$V$	Lower crosshead velocity, mm/min
$a_c$	Contact length, mm
$a_d$	Detached length, mm
$d$	Indentation depth, $d = (D - Fv/K_a)$ , mm
$d_{co}$	Upper-bound position depth of the detaching phenomena in the complete open position
$d_{so}$	Lower-bound position depth of the detaching phenomena in an open start position.
$k$	Shearing yield stress ( $\approx \sigma_{0.2}/\sqrt{3}$ )
$n$	Work-hardening exponent
$p$	Probability of separation, %
$p_m$	Normal pressure on the wedge surface of the cutting blade
$t$	Thickness of work sheet, mm
$w$	Tip thickness of cutting blade, $\mu\text{m}$
$f$	Cutting line force, $f = Fv/B$ , kN/m
$f_1$	First inflection of cutting line force
$f'_1$	First inflection of cutting line force for $w/t > 0.23$
$f_s$	Lateral component of the applied line force, called as the separation line force, kN/m
$\alpha$	Bevel apex angle, degrees
$\sigma_{0.2}$	Proof stress of the work sheet, MPa
$\sigma_B$	Ultimate tensile strength of the work sheet, MPa
$\tau_{\max}$	Maximum shear stress, MPa
$\sigma_{p\max}$	Maximum principal stress, MPa
$\mu_C$	Friction coefficient between the cutter blade and the work sheet
$\mu_P$	Friction coefficient between the work sheet and the counter plate

### Subscripts

$B$	denotes breaking
$c$	denotes contact condition
$d$	denotes detached condition
max	denotes maximum
$n$	denotes necking
$s$	denotes separation line force
$u$	denotes the local minimum point after breaking

## 2. Experimental and simulation methods

Since the cutting mechanism of the pushing shear process is assumed to be primarily characterized by the ratio of tip thickness to the sheet thickness  $w/t$ , the cutting line force  $f$  kN/m, which is applied

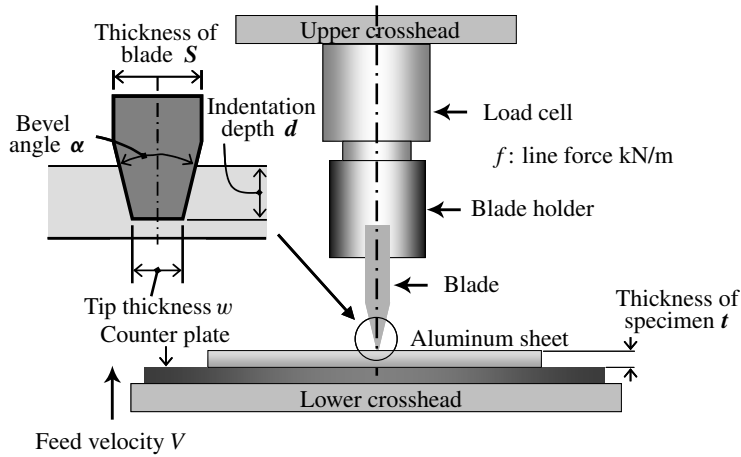


**Figure 1.** Schematic of experimental apparatus.

vertically to the cutting blade, and the contact condition on the blade surface or on the counter plate were investigated by varying the ratio of the indentation depth and the sheet thickness  $d/t$  with respect to  $w/t$ .

**2.1. Experimental method and specimen.** For the indentation experiment, we used a commercially available aluminum sheet (JIS-A1050P) of 0.39 mm thickness. Specimens were rectangle sheets with length in the rolling direction  $L = 50$  mm and width  $B = 20$  mm. Tensile properties of the sheet materials for both the longitudinal and transverse direction are shown in Table 1. The work hardening characteristic, that is, the stress-strain relation of the material, was approximated by the power law expression  $\sigma = F\varepsilon^n$ , where  $F$  is the plastic coefficient,  $\varepsilon$  is the equivalent plastic strain and  $n$  is the work-hardening exponent. In this study, we mainly considered the rolling direction of the material's behavior. The trapezoidal bevel blades had a length of 40 mm, thickness  $S = 0.9$  mm, bevel apex angle  $\alpha = 42$  degree, and tip hardness of 600 HV. The tips of the blades we used were filed using emery papers to tip thicknesses  $w = 14, 31, 54, 71, 92, 129, 166, 200$  and  $250 \mu\text{m}$ . Non-filed cutters had an average thickness of  $w = 5 \mu\text{m}$ .

Properties	RD	CD
Young's modulus $E$ [GPa]	76	76
Proof stress $\sigma_{0.2}$ [MPa]	115	140
Ultimate tensile strength $\sigma_B$ [MPa]	125	150
Plastic coefficient $F$ [MPa]	160	224
Work-hardening exponent $n$	0.07	0.08

**Table 1.** Mechanical properties of aluminum sheet (A1050P). RD is the rolling direction; CD the cross direction.

Figure 1 shows a schematic of the experimental apparatus. Measurements were carried out five times for each thickness  $w$ . The position of the cutter blade was vertical to the surface of the aluminum sheet, while the cross-angle between the rolling direction of the aluminum sheet and the longitudinal direction of the cutting blade was 90 degrees. On the experimental apparatus (universal testing equipment) the upper crosshead had a trapezoidal bevel center blade mounted on a load cell with maximum load of 5 kN.

Each specimen of the aluminum sheet was placed onto the counter plate fixed on the lower crosshead. The lower crosshead moved upward with a velocity  $V = 0.05$  mm/min. The indentation depth of the cutting blade into the specimen was estimated using the relation  $d = (D - F_v/K_v)$ , where  $K_v$  kN/m/mm is an equivalent spring constant of the apparatus,  $D$  mm is the lower crosshead displacement, and  $F_v$  kN/m is the line force applied in vertical to the cutting blade.

To ensure nonlubricated contact between the specimen and the counter plate, the tool surface was washed with alcohol before indenting. A previous experiment [Murayama et al. 2004] revealed that with the horizontal method based on JIS-P8147 the average friction coefficient  $\mu_C$  between the cutting blade and the specimen was 0.20 (max .0.28 ~ min .0.18), and the average friction coefficient  $\mu_P$  between the specimen and the counter plate was 0.25 (max .0.28 ~ min .0.20).

**2.2. Simulation method.** A commercial finite element program, MSC.MARC [MSC 2003], using an updated Lagrange procedure and large strain was used to simulate the trapezoidal cutting blade indentation on an aluminum sheet. Figure 2a shows a schematic illustration of the simulation model, in which the aluminum sheet was considered as a deformable body and modeled as the right-hand half symmetry of a rectangle of 4.0 mm in length. The cutting blade and the counter plate were modeled as rigid contact bodies. The finite element meshes of the deformed body consisted of 17,000 four-node quadrilateral elements with minimum side length of  $5 \mu\text{m}$ . The element type was considered to be plain-strain quadrilateral with four-point Gaussian integration. The coulomb friction model was assumed for each contact surface, since no sticking slip was observed clearly during the simulation of blade indentation into the aluminum sheet. The deformable body was assumed to be an isotropic, elastoplastic material obeying the isotropic hardening power law  $\sigma = F\varepsilon^n$ . The value of  $F = 160$  MPa and  $n = 0.07$  were chosen as described in previous section. Because of locally large deformation during the pushing process, a globally automatic re-meshing criterion with overlay meshing method was used. Elements were assumed to have no crack and no fracture during the cutting process. For the tip profile of the trapezoidal cutting blade and the friction coefficients, we chose parameters as shown in Table 2. Corner radii were assumed to be

Tip thickness: $w = 0, 10, 30, 50, 70, 90, 120, 150, 180, 200, 250 \mu\text{m}$
Sheet thickness: $t = 0.4$ mm.
Bevel apex angle: $\alpha = 42^\circ$
Friction coefficient of trapezoidal blade: $\mu_c = 0, 0.1, 0.2, 0.4$
Friction coefficient of counter plate: $\mu_p = 0, 0.1, 0.2, 0.4$

**Table 2.** Simulation parameters for blade indentation.

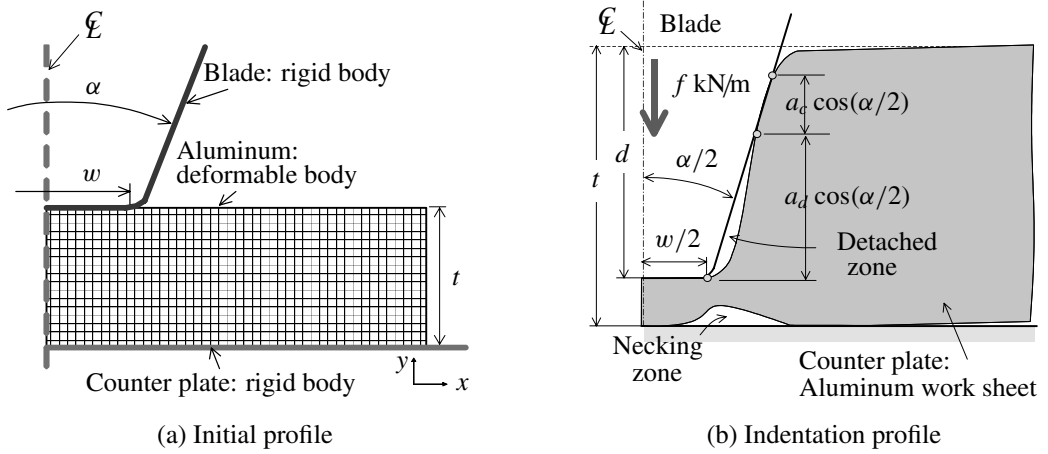


**Figure 2.** Simulation model with respect to detaching phenomena on the wedge surface.

$5 \mu\text{m}$  on both sides. From the experimental result of friction coefficients  $\mu_C, \mu_P$ , dispersion was roughly 0.1. therefore, the friction coefficients  $\mu_C, \mu_P$  were initially assumed to be 0.2.

Figure 2b schematically illustrates a deformed sheet with respect to the occurrence of a detached surface. When the blade was indented on the work sheet, a detached length  $a_d$  and a contact length  $a_c$  on the sliding surface of the blade were evaluated as shown in Figure 2. Where,  $a_d$  is defined as the projection length on the blade surface which is detached from the work sheet, while  $a_c$  is defined as the projection length on the blade surface which contacts with the worksheet.

### 3. Results and discussion

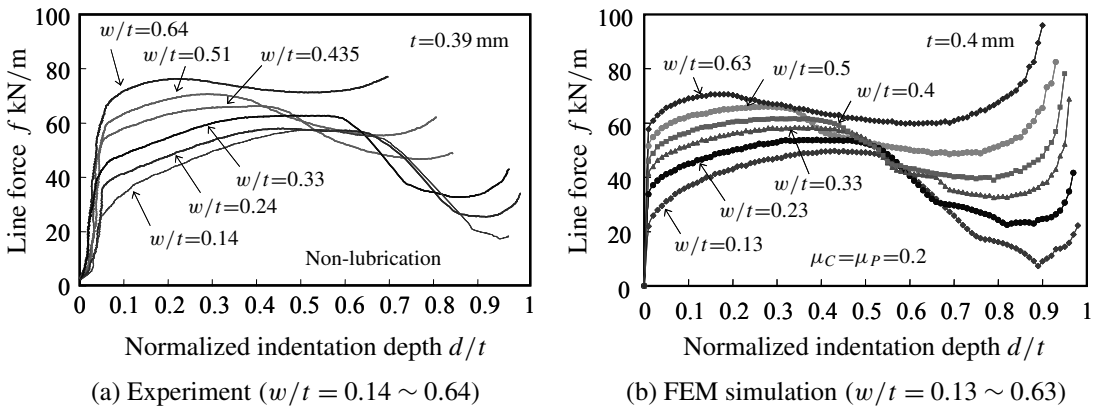


**Figure 3.** Relationship between line force and normalized indentation depth.



**3.1. Relationship between resistance of blade indentation and tip thickness.** Figure 3a–b shows the experimental and FEM simulation of the relationship between the line force  $f$  and the normalized indentation depth  $d/t$  for  $w/t = 0.14, 0.24, 0.33, 0.43, 0.51$  and  $0.64$ . The tendency of the load response in the FEM simulation was very similar to that of the experiment result. Figure 4a illustrates a force response model that includes cutting characteristics of Figure 3, where  $f_n$  is an inflection point of  $f$  and  $f_u$  is a local minimum point of  $f$ , as defined in [Murayama et al. 2004]. The maximum load point is denoted by  $(f_{\max}, d_{\max}/t)$ , where  $f_{\max}$  is the line force, and  $d_{\max}$  is the corresponding indentation depths of the blade.

Figure 5a shows the dependency of  $f_{\max}$ ,  $f_n$  and  $f_u$  on normalized tip thickness  $w/t$  in the experiment, while Figure 5b shows the dependency of  $f_{\max}$ ,  $f_n$  and  $f_u$  on normalized tip thickness  $w/t$  in the FEM simulation for  $\mu_P = \mu_C = 0.2$ .

Since  $f_{\max}$  was roughly linear to the variance of  $w/t$ , approximations of  $f_{\max}$  by the least squares method were derived as follows:

$$f_{\max} = 36.4(w/t) + 52.8 \text{ kN/m (experiment)} \quad (1)$$

$$f_{\max} = 43.4(w/t) + 44.3 \text{ kN/m (FEM)}. \quad (2)$$

The linear correlation coefficient  $R$  of (1) and (2) was 0.98 and 0.999, respectively. We supposed that the difference between (1) and (2) is mainly due to the assumption of the coulomb friction model. It is known that  $f_{\max}$  decreases [Murayama et al. 2004] as  $\mu_C$  decreases. Comparing the experimental  $f_n$  with Prandtl's theory  $f_n = 2k(1 + \pi/2)w$  [Hill 1983], where the shearing yield stress  $k$  was assumed to be  $\sigma_{0.2}/\sqrt{3}$ ,  $f_n$  can be estimated as a flat punch indentation (Prandtl's solution) for  $w/t < 0.23$ , but not for  $w/t > 0.23$ , due to the Hill's critical thickness.

When the blade indentation increased, after passing through the maximum load point, the aluminum sheet separated into two pieces; otherwise the aluminum sheet only showed a locally minimum line force without any separation. In particular, for  $d/t > d_{\max}/t$  for  $w/t \geq 0.13$ , the reduction stage of  $f$  had an

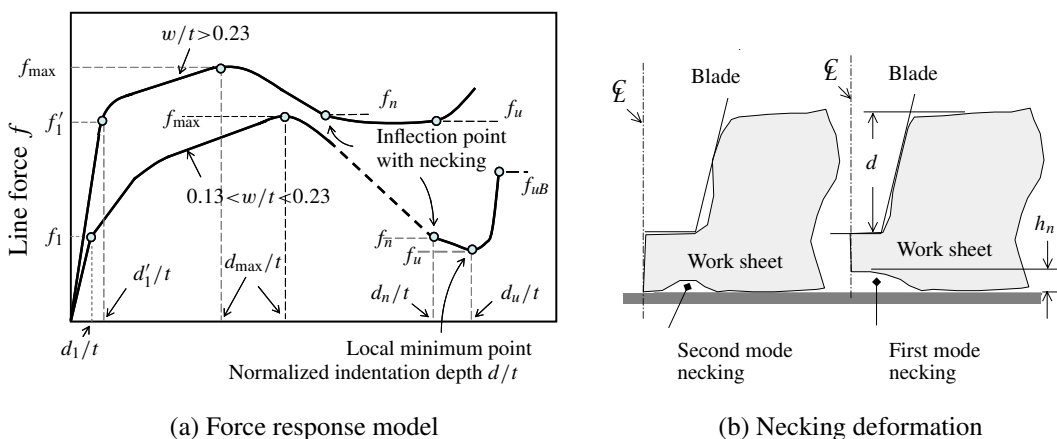


**Figure 4.** Force response model for the indentation process; schematic of necking deformation.

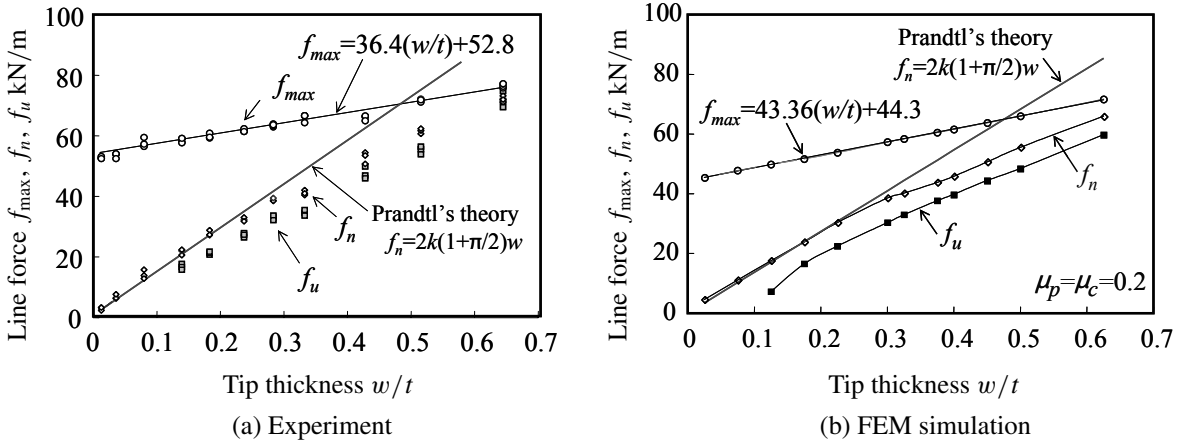


**Figure 5.** Relationship between line forces and tip thickness.

inflection point  $(d_n/t, f_n)$  and a local minimum point  $(d_u/t, f_u)$  as shown in Figure 4a. For  $w/t < 0.23$ , [Murayama et al. 2004] defined the height of necking  $h_n$  and necking deformation as shown in Figure 4b. The inflection point  $(d_n/t, f_n)$  corresponds to the maximum height of necking ( $h_n = h_{nmax}$ ).

Figure 6 shows the first inflection line force  $f_1$  and  $f'_1$ . The first inflection point was tentatively classified as  $f_1$  and  $f'_1$  from the disappearance condition of the second inflection point, depending on the critical thickness  $w/t = 0.23$ . Since  $f_n$  was almost equal to  $f_1$  from both the experiment and the FEM simulation, and considering that they could be estimated by the Prandtl's theory for a flat punch

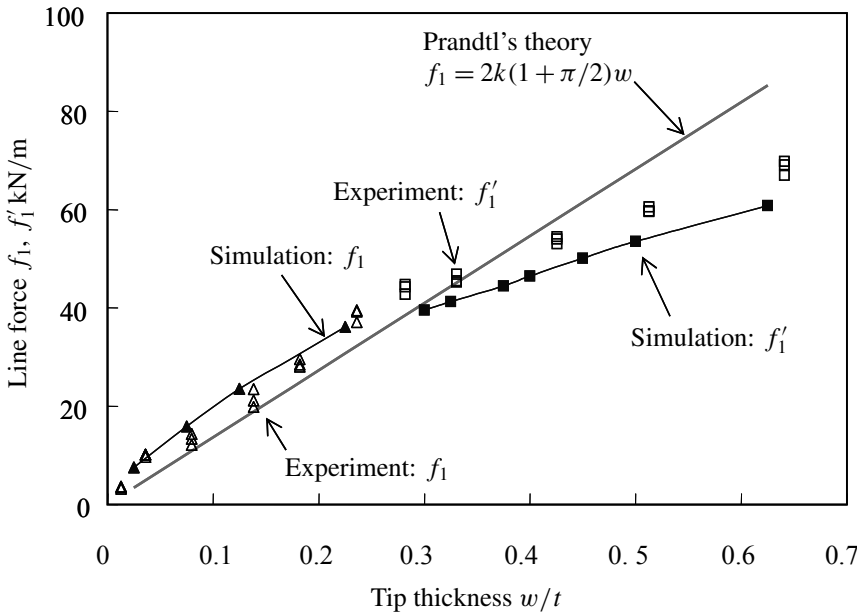


**Figure 6.** Variation of line force at first inflection point with respect to tip thickness.

indentation into a semi-infinite body [Hill 1983], we assumed that the wedge effect decreased and the upsetting effect increased at the inflection point  $(d_n/t, f_n)$ . In other words, the detaching phenomenon on the wedge surface of the blade seemed to occur at that time.

When  $f$  was equal to  $f_u$ , the bottom of the first necking zone contacted with the counter plate completely. When  $w/t < 0.13$ ,  $f$  decreased for  $d/t$  without the local minimum point  $(d_u/t, f_u)$ . The local minimum point of  $f_u$  corresponded to  $h_n = 0$ , the occurrence of the second necking zone, and also the upsetting on the burr. When  $w/t > 0.28$ , the second necking did not occur, but the first necking mode altered directly into the upsetting mode. Also, the local minimum point  $(d_u/t, f_u)$  corresponded to detaching the wedge surface from the worksheet and upsetting with the blade tip. The correlation between  $(d_n/t, f_n)$  and  $(d_u/t, f_u)$  was confirmed experimentally using the following approximations for  $0.51 > w/t > 0.13$ :

$$f_u = (0.36(w/t) + 0.75)f_n \quad (3)$$

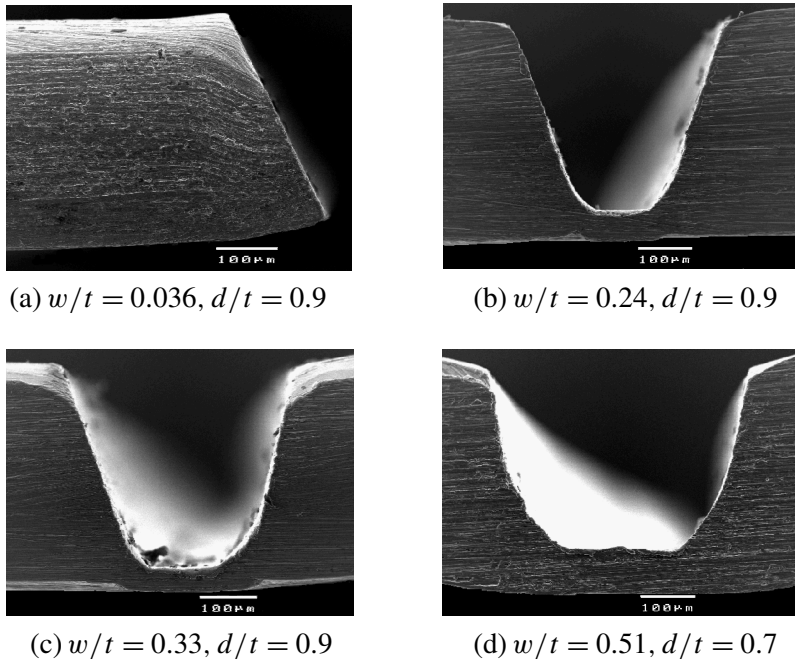
$$d_u = (0.46(w/t) + 0.99)d_n. \quad (4)$$

The linear correlation coefficient  $R$  for relations (3) and (4) were 0.815 and 0.926, respectively. When  $w/t > 0.5$ , the line force response does not include a sharply breaking down flow process. This tendency may be due to detaching of the wedge surface of the blade.

So far, detachment of the wedge surface under upsetting, the local minimum load point, and the inflection load point with the second necking on the second half stage ( $d > d_{\max}$ ) are important for estimating wedging separation of the aluminum worksheet. However, in past studies, the position of any inflection points on the second half stage and a transformation mechanism from the second necking to upsetting were not discussed with respect to the detaching condition. Therefore, in the following sections, we shall discuss the deformation mode and the detaching condition.

**3.2. Effect of deformations of a wedged sheet and tip thickness on the final stage.** The contact condition between the sliding surface of the trapezoidal cutting blade and the deformed aluminum work sheet on the second half stage ( $d/t > d_{\max}/t$ ) is analyzed here by observing both experimental photographs of the wedged aluminum sheet, and deformation in the FEM simulation. Figure 7 shows SEM micrographs of the wedged profile of the aluminum work sheet near the local minimum load point for  $w = 14, 92, 129$  and  $200 \mu\text{m}$ ,  $t = 0.39 \text{ mm}$ , and  $\alpha = 42$  degrees. By examining the bottom surface of specimens for  $w/t = 0.013 \sim 0.079$ , we observe that the first necking mode occurred near the blade tip, and the aluminum sheet successfully separated into two pieces without any burr.

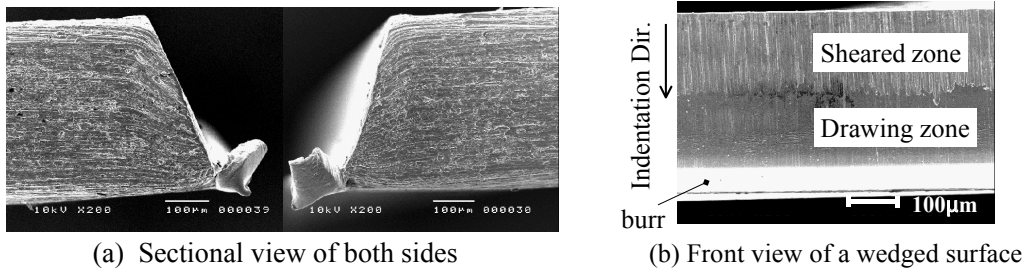
In the experiment, where  $0.28 > w/t > 0.13$ , second necking mode was observed after occurrence of the first necking mode. A burr occurred near the local minimum load point without final bursting of the worksheet in the region between the blade tip and the counter plate Figure 7b. However, for  $w/t = 0.13 \sim 0.28$ , by increasing the line force to the breaking line force  $f_{uB}$ , the burr was likely to be broken, or the aluminum worksheet frequently separated into two pieces.  $f_{uB}$  was roughly equal to  $f_n$  at  $w/t = 0.14$ , whereas it was nearly  $f_{\max}$  at  $w/t = 0.24$ . Throughout the experiment, we confirmed that the aluminum worksheet was not completely separated for  $w/t > 0.28$  when the indentation depth exceeded the local minimum load point. Under these conditions, only the upsetting deformation of the worksheet occurred beneath the blade tip, even when applying a line force  $f$  larger than  $f_{\max}$ .



**Figure 7.** Wedged profile of aluminum worksheet (experiment).

Figure 8 shows an example of a wedged worksheet burst at  $f_{uB} = 42$  kN/m on  $w/t = 0.18$ . Here, there was a round-shaped surface on both sides Figure 8b. There were two kinds of surfaces: the sheared zone and the drawing zone. The sheared zone is flat and seems to be formed by copying the profile of the blade edge. The drawing zone is round-shaped and seems to be formed by the extrusion effect of the blade tip pressure. Since this extrusion effect causes material flow in the outward lateral direction, we consider that the detached zone occurs beneath the wedge surface. We observed similar surfaces for  $w/t > 0.24$  (Figure 7b–d). Therefore, the surface of the wedge corner is considered to be detached from the deformed worksheet. On the other hand, when  $w/t = 0.036$ , the wedged surface of the worksheet appeared to be in contact with the blade edge. For  $w/t = 0.33$  and  $d/t = 0.75$ , the second necking mode was not observed. Only the upsetting deformation was generated beneath the tip blade. When  $w/t = 0.51, d/t = 0.7$ , the wedge surface of the blade is completely detached from the work sheet and the upsetting flow occurred beneath the blade tip without any necking of the bottom surface.

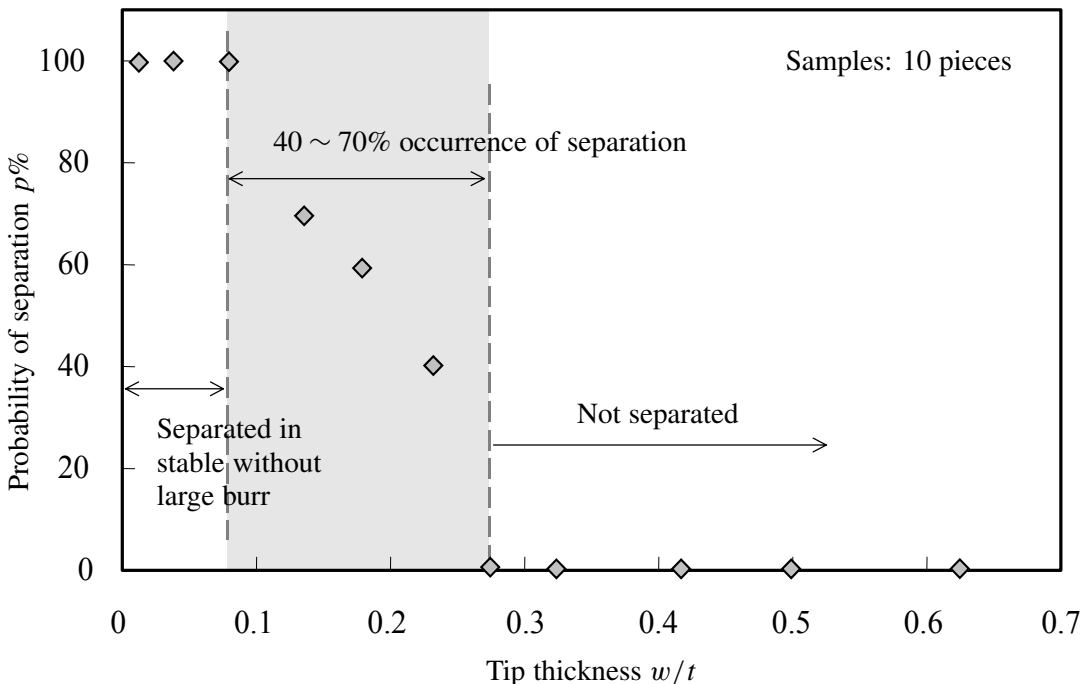
Figure 9 shows the probability of the occurrence of separation of the wedged aluminum sheet. Experiments were carried out on 10 specimens for each tip thickness  $w$  of the blade. The indentation of the blade was stopped at the breaking line force  $f_{uB}$ , which exceeded the local minimum load point  $(d_u/t, f_u)$ , but was less than the maximum line force  $f_{max}$ . The experimental probability  $p$  of separation was 100% for  $w/t < 0.079$ , but an intermediate value ( $0 < p < 100\%$ ) for  $0.14 < w/t < 0.23$ . When the worksheet was separated as  $0 < p < 100\%$  for  $0.14 < w/t < 0.23$ , the separated edge of the worksheet had a burr, as shown in Figure 8a.



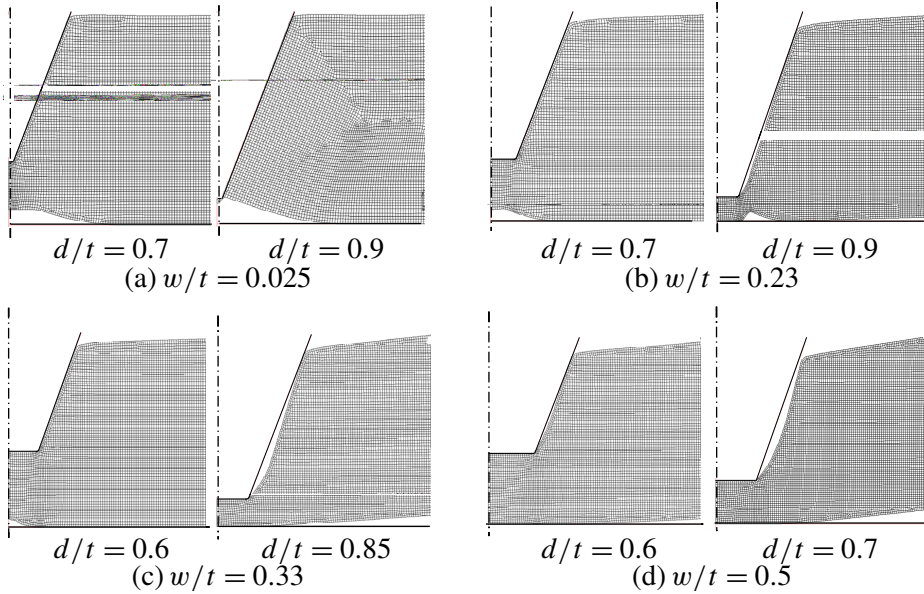
**Figure 8.** Wedged profile of aluminum worksheet ( $w/t = 0.18$ ,  $f_{uB} = 42$  kN/m in experiment).

Figure 10 shows a section profile of the wedged worksheet in the FEM simulation for  $w = 10, 90, 130$  and  $200 \mu\text{m}$ . Comparing Figure 10 with Figure 7, the simulated deformation of the worksheet shows good agreement with experimental observation.

By referring to this figure, we can confirm the following four main points. First, for  $w/t = 0.025$ , only the first necking mode was observed for  $d/t = 0.7, 0.9$ . Second, for  $w/t = 0.23$ , the first necking mode at  $d/t = 0.7$  altered to the second necking mode at  $d/t = 0.9$ . Third, when  $w/t = 0.33$ , the first necking mode at  $d/t = 0.6$  altered to the upsetting mode without the second necking at  $d/t = 0.85$ . Fourth, when  $w/t = 0.5$ , only the upsetting deformation was generated beneath the blade tip for  $d/t = 0.6, 0.7$ .



**Figure 9.** Probability of separation (experiment).



**Figure 10.** Wedged profile of worksheet on simulation.

In addition, the deformed surface of the worksheet was completely detached from the wedge surface of the blade near the inflection point  $(d_n/t, f_n)$  for  $w/t = 0.33$  and  $w/t = 0.5$ . Where  $w/t = 0.33$  and  $w/t = 0.5$ , upsetting flow of the worksheet was generated beneath the blade tip without any separation in the final stage. Therefore, we confirmed that both the detached condition on the sliding surface and the probability of separation of the blade depend on  $w/t$ .

**3.3. Effect of detached/contact length and indentation depth on an edge of cutting blade.** As mentioned in the previous section, the occurrence of a detached zone relates to the possibility of wedge separation. We investigate here the effect of detached length  $a_d$  and contact length  $a_c$  on the wedge surface as defined in Figure 2b. The detached length  $a_d$  and the contact length  $a_c$  were considered to be the projected length of the free surface on which  $p_m = 0$ , and the pressurized surface on which  $p_m \neq 0$ , respectively.  $p_m$  is defined as the normal pressure on the wedge surface of the cutting blade. The complete-open condition is that which occurs when the wedge surface is completely detached from the work material. After reaching the complete open condition, the detached length  $a_d$  is redefined as the projected length from the blade's edge to the end of the wear zone of the work sheet.

Figure 11 shows the normalized detached length  $a_d/(t/\cos(\alpha/2))$ , which was numerically calculated, and the normalized contact length  $a_c/(t/\cos(\alpha/2))$  obtained by varying  $d/t$  with respect to  $w/t = 0.13$ . The closed square symbols show normalized contact length  $a_c/(t/\cos(\alpha/2))$ , while the open round symbols show normalized detached length  $a_d/(t/\cos(\alpha/2))$ . In Figures 11–12, the symbol  $a$  denotes the total contact and detached length ( $a_c + a_d$ ), contact length  $a_c$ , or detached length  $a_d$ . The solid line represents the normalized total projection of contact and detached length  $(a_c + a_d)\cos(\alpha/2)/t$ , while the dashed line is the ideal indentation depth ( $d/t$ ). The normalized total projection length  $(a_c + a_d)\cos(\alpha/2)/t$ , which excludes the wear curve on sliding surface, is slightly smaller than that of the ideal indentation

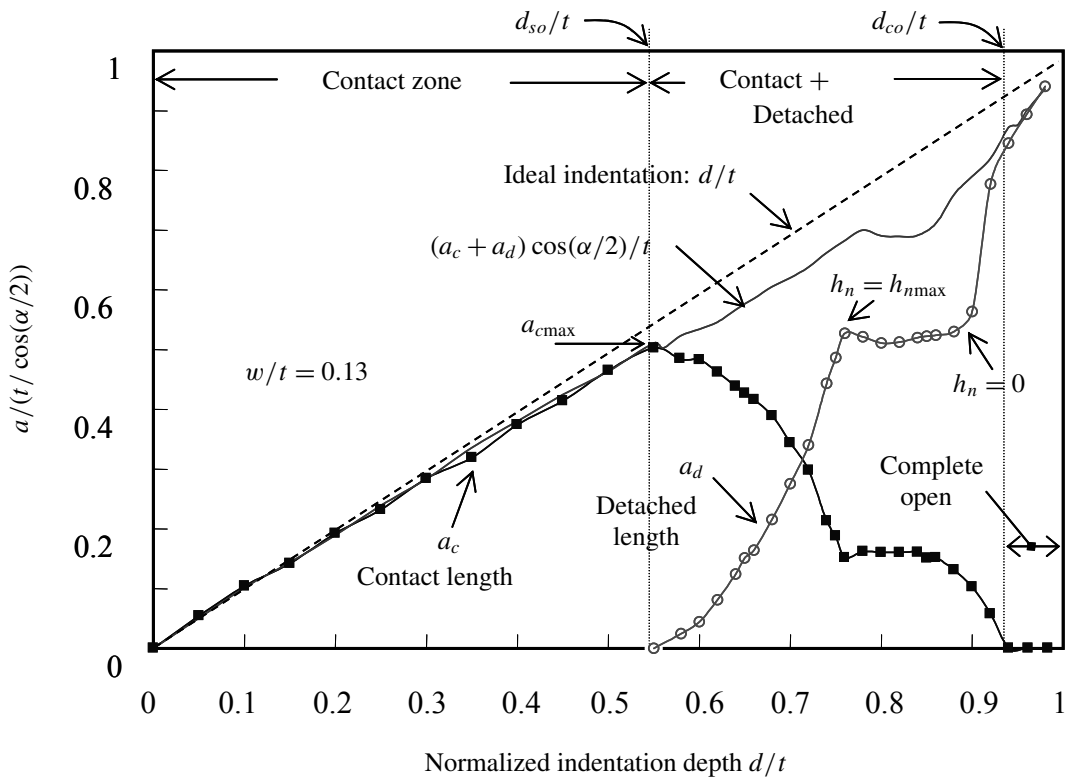


**Figure 11.** Relationship between detached/contact length and normalized indentation depth  $d/t$ .

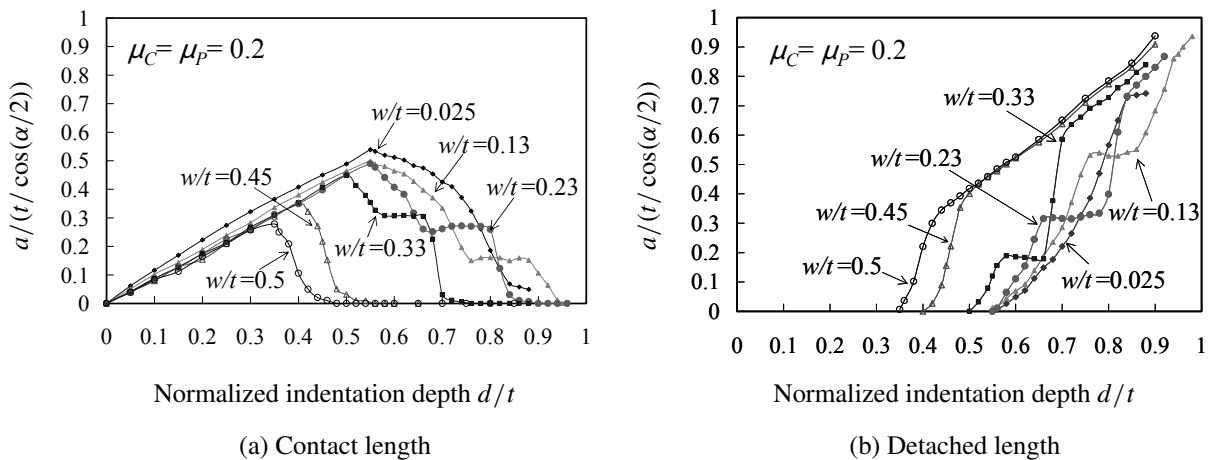


**Figure 12.** Effect of tip thickness  $w/t$  on the occurrence of contact length and detached length on simulation.

depth. We defined the first half stage  $d/t = 0 \sim 0.55$ , as the contact zone, since only the contact part was observed on the wedge surface. When  $a_c$  reaches the maximum peak value  $a_{c\max}$ , the detached length  $a_d$  began to appear at  $d/t = d_{so}/t$  and increased with increasing indentation depth. We define the contact + detached zone as that which  $a_c$  then decreases to zero. From these relations, we found that the position of  $a_{c\max}$  is nearly equal to the starting position of the detached zone. In addition, the maximum height of the first necking  $h_{n\max}$  was observed at  $d/t = 0.76$ , and with respect to  $w/t = 0.13$ , the bottom of the necking zone started to contact with the counter plate at  $d/t = 0.88$  ( $h_n = 0$  at this point). As the height  $h_n$  of the first necking mode decreased, the values of  $a_d$  and  $a_c$  were almost constant. When  $a_c$  reaches zero at  $d/t = d_{co}/t$ , the wedge is completely detached from the deformed worksheet. Thus far, we denote the critical depth  $d_{so}$  as the lower-bound position of the detaching phenomenon, and the critical depth  $d_{co}$  as the upper-bound position of the detaching phenomenon.

Assuming  $n = 0.08$  and  $F = 224$  MPa (Table 1), we considered the transverse direction model in the FEM simulation. Comparing the FEM simulation in the transverse direction of the material worksheet with that in the longitudinal direction, we confirmed that the detaching phenomena characterized by  $a_d$ ,  $a_c$  was almost the same with respect to  $w/t$  and  $d/t$ , except for the magnitude of the cutting line force.

Figures 12a and b show the effect of  $w/t$  on variation of the contact length and detached length. When  $w/t < 0.1$ , the wedge surface is contacted with a specific sliding surface area of the deformed aluminum sheet. However, we did not observe an inflection point of  $a_c$  for  $w/t > 0.4$ . This is because the upsetting flow only occurred beneath of the blade tip without the second necking mode.

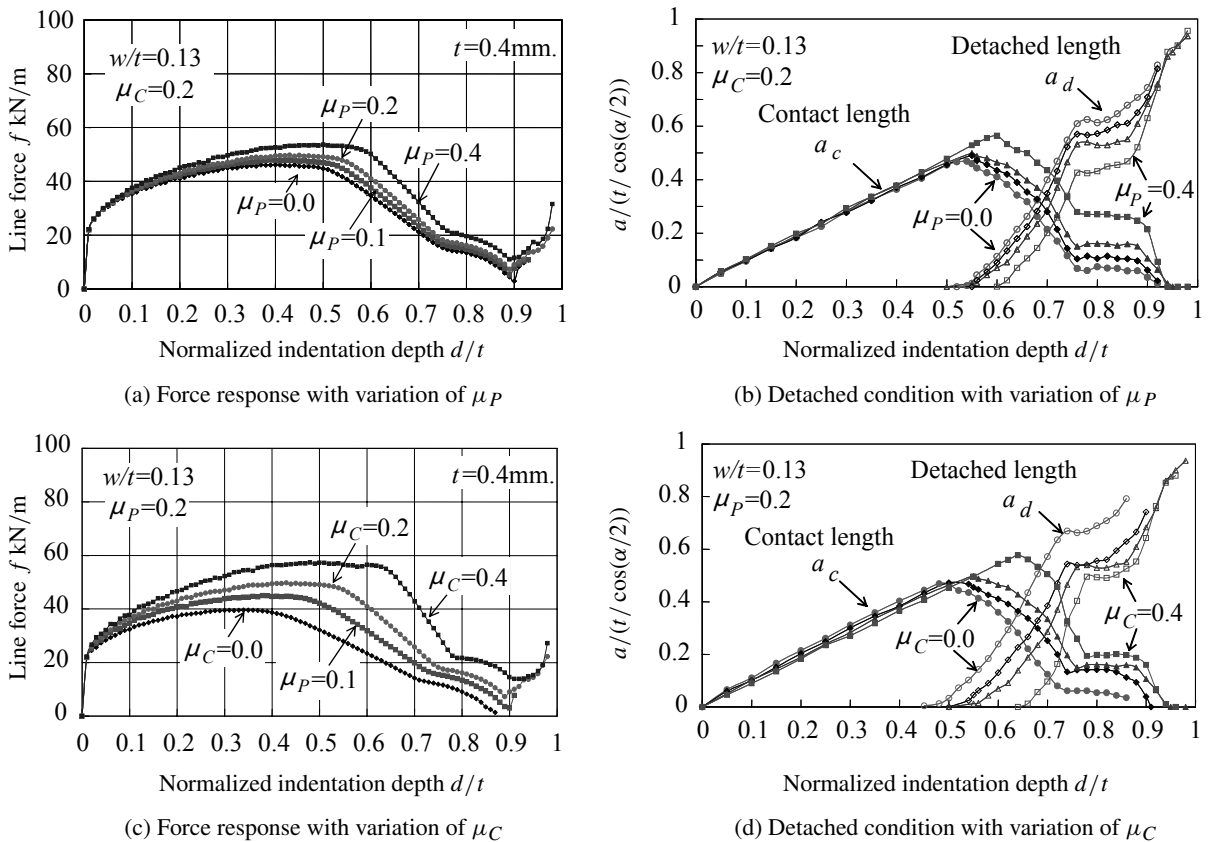
**3.4. Effect of friction coefficients on cutting load response and detached condition.** The effect of line force  $f$ , indentation depth  $d/t$ , and the corresponding contact/detached length  $a_c$ ,  $a_d$  on the wedge surface are analyzed here by varying the friction coefficients  $\mu_P$ ,  $\mu_C$  for  $w/t = 0.13$ . Figure 13a shows the relationship between  $f$  and  $d/t$  for friction coefficients  $\mu_P = 0.0, 0.1, 0.2$ , and  $0.4$ , with  $\mu_C = 0.2$ . Figure 13b shows the relationship between  $a_c$ ,  $a_d$ , and  $d/t$ . Similarly, Figure 13c shows the relationship between  $f$  and  $d/t$  for  $\mu_P = 0.0, 0.1, 0.2$ , and  $0.4$ , with  $\mu_P = 0.2$ , while Figure 13d shows the relationship between  $a_c$ ,  $a_d$  and  $d/t$ .

From these figures, we observe that  $f_{\max}$  and  $a_{c\max}$  depend on the variation of  $\mu_C$ ,  $\mu_P$ , as shown in the approximations

$$\begin{aligned}
 f_{\max} &= 18.6\mu_P + 46.1 && \text{for } \mu_C = 0.2 \\
 a_{c\max} &= 0.234\mu_P + 0.464 && \text{for } \mu_C = 0.2 \\
 f_{\max} &= 43.8\mu_C + 40.3 && \text{for } \mu_P = 0.2 \\
 a_{c\max} &= 0.282\mu_C + 0.455 && \text{for } \mu_P = 0.2.
 \end{aligned} \tag{5}$$

The linear correlation coefficients of (5) were larger than 0.99. The inflection position ( $h_n = h_{n\max}$ ) and the lower/upper-bound position  $d_{so}$ ,  $d_{co}$  almost did not depend on  $\mu_P$ , while the  $d_{so}$ ,  $d_{co}$  depended on  $\mu_C$ . The responses of  $a_c$  and  $a_d$  with  $d/t$  also depended on  $\mu_C$ ,  $\mu_P$ , except for the complete open condition. Therefore, we can confirm that the variation of  $\mu_C$ ,  $\mu_P$  affects the line force and also the detached condition. Furthermore, the effect of variance of  $\mu_C$  was relatively large.

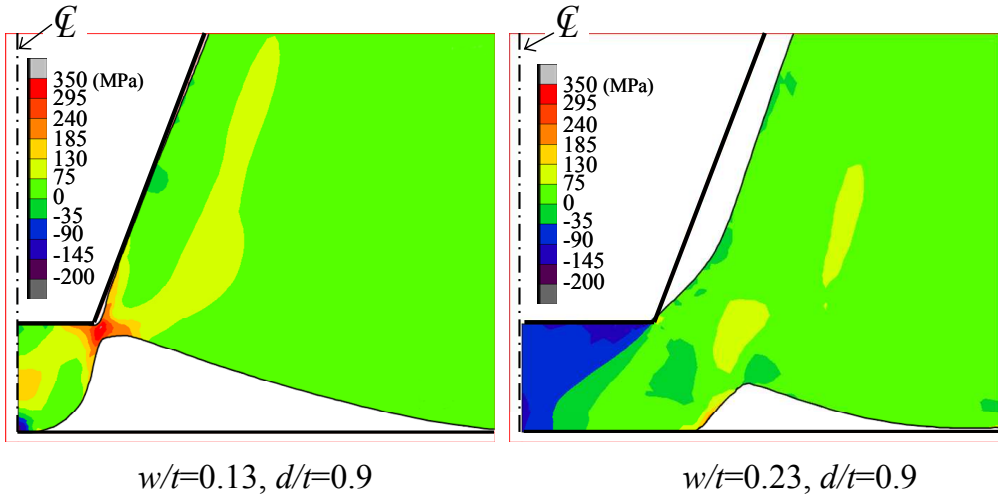




**Figure 13.** Effect of friction coefficient for load response and detached condition on simulation.

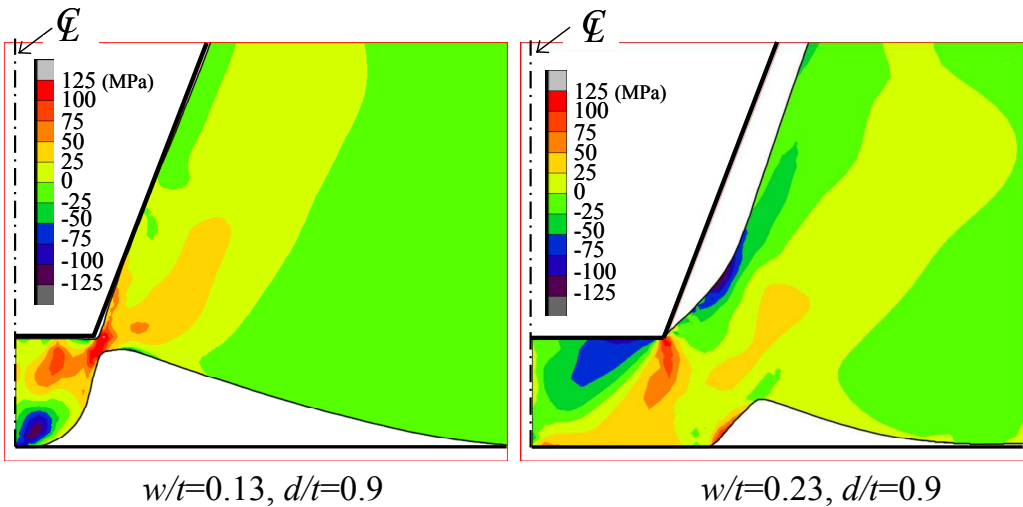
**3.5. Stress distribution in the necked zone on the final stage.** As mentioned in section 3.2, the probability of the occurrence of separation had the intermediate experimental value ( $0 < p < 100\%$ ) for  $0.14 < w/t < 0.23$ . In this section, we discuss the stress distribution around the blade tip. Figure 14 shows contour bands of maximum principal stress  $\sigma_{pmax}$  beneath the blade tip at  $d/t = 0.9$ , while Figure 15 shows those of maximum shear stress  $\tau_{max}$  at  $d/t = 0.9$  by the FEM simulation. Figure 16 illustrates selected vectors of principal stresses chosen near the necked zone. When  $w/t = 0.13$ , the maximum stress as the principal component was roughly  $\sigma_{pmax} = 320$  MPa (tensile) in the second necking zone, where the minimum dimension was roughly 17% of the chip height. For  $w/t = 0.23$ , the minimum dimension of the necked zone was roughly 102% of the chip height. The absolute value of  $\sigma_{pmax}$  was relatively small (less than 100 MPa) in the necked zone but increased remarkably as a compressive component beneath blade tip.

Figure 17 shows the distribution of  $\sigma_{pmax}$  along the specified nodes path  $X' - X$ , at  $d/t = 0.9$ . Here, the arc distance  $a_L$  was measured as the distance from the corner of the blade tip to the necked surface for  $w/t = 0.13, 0.18$ , and  $0.23$ , while the  $a_L$  was considered from the corner of the blade tip to the bottom surface of the work sheet for  $w/t = 0.3$  and  $0.5$ . When  $w/t = 0.13$ , the maximum value of  $\sigma_{pmax}$



**Figure 14.** Calculated contour bands of maximum principal stress in wedged worksheet at  $d/t = 0.9$ .

was roughly 320 MPa and the  $\tau_{\max}$  was larger than  $\sigma_{0.2}/\sqrt{3}$  in the necked zone. Applying the maximum tensile strength of the aluminum sheet to  $\sigma_B$ ,  $\sigma_{p\max} \approx 2\sigma_B$ , the worksheet would actually be separated. When  $w/t$  increased,  $\sigma_{p\max}$  was intensively compressive near the corner of the blade tip, and its absolute value was less than 50 MPa for  $w/t > 0.3$ . Therefore, it seemed that the aluminum worksheet could not be separated for  $w/t > 0.23$ . This result was in good agreement with experimental results.



**Figure 15.** Calculated contour bands of maximum shear stress in wedged worksheet at  $d/t = 0.9$ .

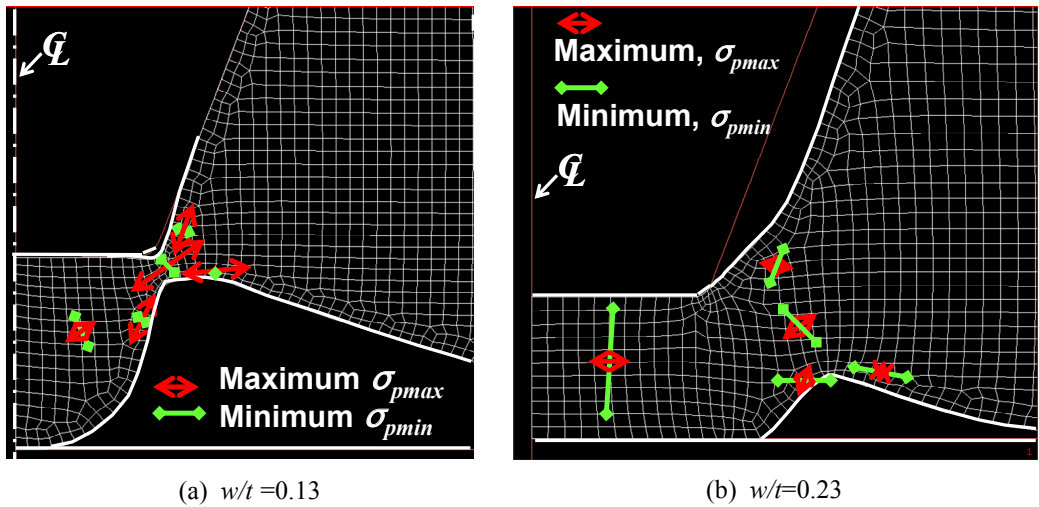


Figure 16. Calculated vectors of principal stresses at  $d/t = 0.9$ .

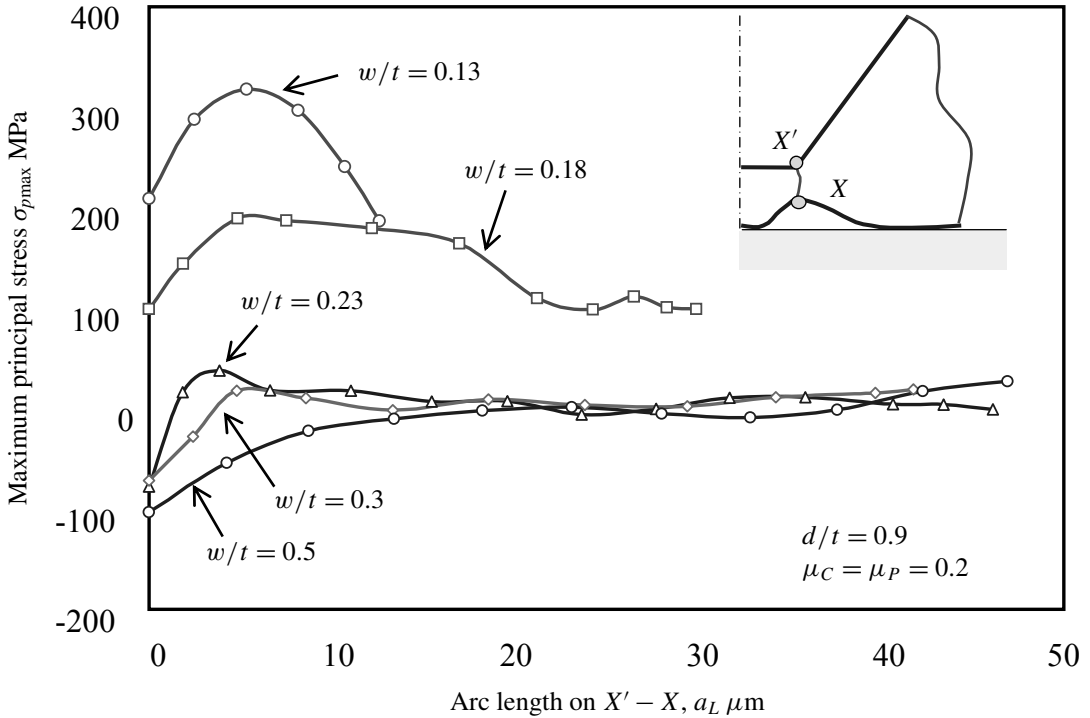
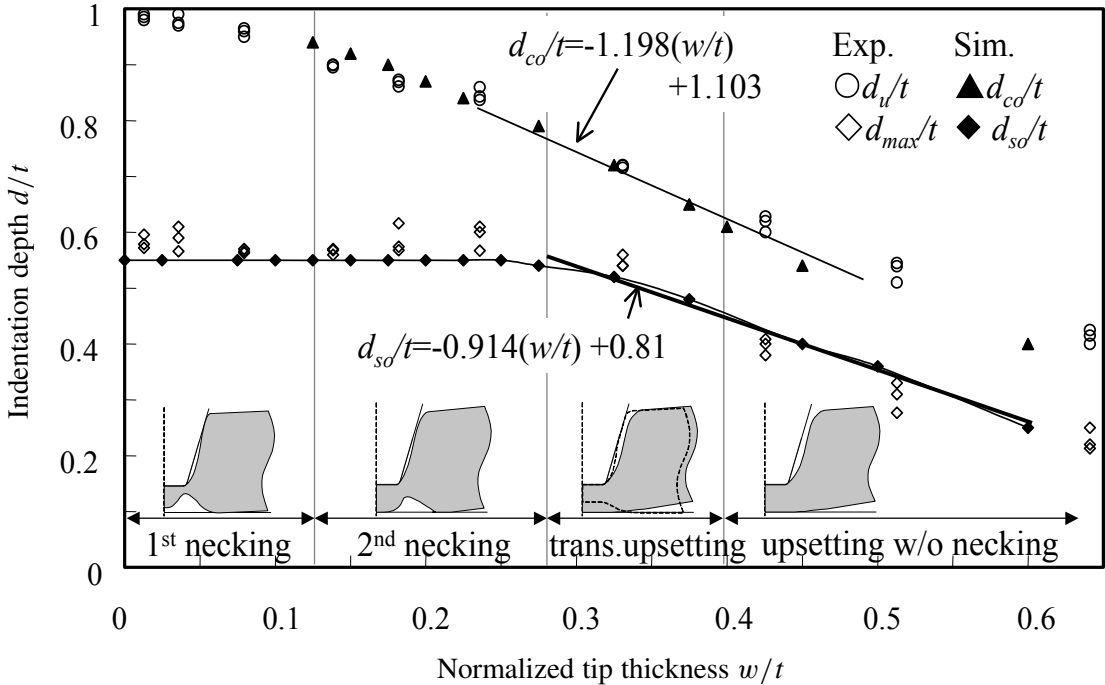


Figure 17. Distribution of maximum principal stress in  $X' - X$  at  $d/t = 0.9$  by varying  $w/t$ .



**Figure 18.** Relationship between indentation depth  $d_{so}$ ,  $d_{co}$  at critical detaching condition and tip thickness.

**3.6. Relationship between critical indentation depth of the detached condition and tip thickness.** Figure 18 shows the lower bound detaching position  $d_{so}/t$ , and the upper bound detaching position  $d_{co}/t$  derived from the detached length of the wedged surface by FEM simulation. Schematics of the deformed workpiece are also illustrated, showing four deformation modes: first necking, second necking, the transition state and the upsetting mode. The open squares and circles show experimental results  $d_{max}/t$  and  $d_u/t$  obtained by varying  $w/t$ , while the closed squares and triangles show the numerically derived  $d_{so}/t$  and  $d_{co}/t$ , respectively. Comparing these values, we confirm that the position of the maximum load point  $d_{max}/t$  corresponds to the initial detached position of  $d_{so}/t$ , while the position of the local minimum load point  $d_u/t$  is related to the complete-detached position  $d_{co}/t$ . Therefore, the position of the maximum line force  $f_{max}$  and the position of the local minimum line force  $f_u$  are useful for estimating the detached position  $d_{so}/t$  and  $d_{co}/t$ , respectively.

For  $w/t = 0 \sim 0.28$ ,  $d_{so}/t$  was nearly constant at 0.55. When  $w/t > 0.28$ ,  $d_{so}/t$  began to decrease linearly as

$$d_{so}/t = -0.914(w/t) + 0.81 \text{ for } w/t > 0.28 \quad (6)$$

When  $w/t > 0.13$ ,  $d_{co}/t$  decreases with  $w/t$  as

$$d_{co}/t = -1.198(w/t) + 1.103 \quad \text{for } w/t > 0.13. \quad (7)$$

Only if  $w/t < 0.13$  does the wedge surface always contact some part of the deformed aluminum sheet.

From the above discussion of Figure 18, we classified the pushing shear condition of the aluminum worksheet into the following four features derived from both the detached length on the wedge surface and from the load response:

- 1) When  $0 < w/t < 0.13$ , the first necking mode was observed and the wedge surface was in contact in some area of the aluminum sheet. In this stage, the work material is completely separated without any burrs.
- 2) When  $0.13 < w/t < 0.28$ , the second necking mode of the bottom surface occurred in the second half stage ( $d/t > d_{\max}/t$ ), while the first necking mode was generated in the first half stage ( $d/t < d_{\max}/t$ ). Lower-bound detaching on the wedge surface and upper-bound detaching on the wedge surface are observed under this condition. The blade is statistically able to separate the worksheet with a burr.
- 3) When  $0.28 < w/t < 0.4$ , upsetting deformation is generated after occurrence of the transient first necking mode. The wedge surface is always detached from work material in the final stage.
- 4) When  $w/t > 0.4$ , the plain upsetting mode without any necking always occurred beneath the tip blade. Specifically, the apex angle of the wedge is not effective to cut off the worksheet.

**3.7. Relationship between separation line force and indentation depth in the simulation.** Figure 19 describes the numerically calculated relationship between a separation line force  $f_s$  and the normalized indentation depth  $d/t$  obtained by varying the tip thickness  $w/t$ .  $f_s$  is a lateral component of the applied line force to the worksheet. It was obtained using a line integral of the normal stress  $\sigma_{xx}$  (the horizontal component) on the center line, from the bottom surface of the work material to the blade tip surface. Figure 19 shows three peaks, or inflection points ( $f_{s\max}$ ,  $d_{s\max}/t$ ), ( $f_{sn}$ ,  $d_{sn}/t$ ), and ( $f_{su}$ ,  $d_{su}/t$ ). When  $f_s = f_{s\max}$ ,  $d/t$  was almost constant (approximately 0.55 for  $w/t < 0.25$ ), while it decreased for  $w/t > 0.25$ . The position  $d_{s\max}/t$  corresponded to the lower-bound detaching position of depth  $d_{so}/t$ . When  $h_n = h_{n\max}$ ,  $f_s$  became the local minimum  $f_{sn}$ , and when  $h_n = 0$ ,  $f_s$  became the second peak position  $f_{su}$  which corresponds to the upper-bound detaching position.

However, the two peaks or inflection points  $f_{sn}$ ,  $f_{su}$  were not observed for  $w/t > 0.4$ , which corresponded to the dissipation of the first necking mode. The position depth of  $d_{sn}/t$  and  $d_{su}/t$  correspond to the position  $h_n = h_{n\max}$  and the position  $h_n = 0$ , respectively. In Figure 19, the cross point of the  $x$ -axis of the  $f_s$  curve corresponds to the complete open position. For  $w/t < 0.13$ ,  $f_s$  does not intersect with the  $x$ -axis at the final stage of indentation. That is, the separation force is always positive at the final stage.

#### 4. Conclusions

Indentation of the trapezoidal cutting blade to an aluminum sheet was carried out experimentally and numerically to investigate the separation mechanism and its critical processability. The trapezoidal blade simulates the crushed wedge of a 42 degree center bevel blade. The detaching condition of the wedge

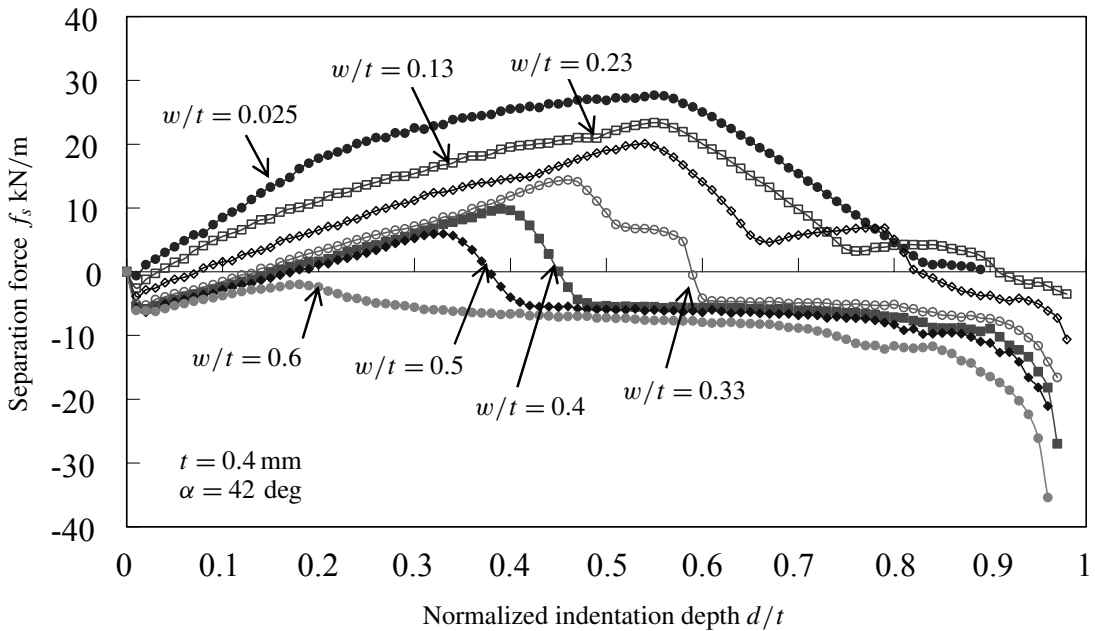


**Figure 19.** Relationship between separation line force  $f_s$  and  $d/t$  (simulation).

surface and the separation force were analyzed to explain the mechanism and the critical conditions which enable successful separation of a thin work sheet. Features of the deformation mechanism after occurrence of the detaching phenomenon were revealed as follows:

- 1) The wedged profile of the worksheet under the pushing shear can be classified into four patterns in terms of normalized tip thickness  $w/t$ . The first pattern is under sharp and fine conditions. When  $w/t < 0.13$ , the worksheet is successfully cut off without burrs or string-like chips. The second pattern is in the transition state of cutting. When  $0.13 < w/t < 0.28$ , a burr is generated and separation of the wedged sheet is statistically successful, although the probability of separation depends on  $w/t$ . The third pattern, where  $(0.28 < w/t < 0.4)$  and the fourth pattern, where  $(w/t > 0.4)$ , occur under unsuccessful cutting conditions. Due to the upsetting flow beneath the blade tip, the wedge surface detaches from the deformed work sheet. The third pattern includes the transient first necking mode in the first half stage of indentation, while the fourth is always in upsetting mode.
- 2) The maximum load point ( $f_{\max}$ ,  $d_{\max}/t$ ) and the local minimum (or inflection) load point ( $f_u$ ,  $d_u/t$ ) are characterized by the initial detaching and the complete-open condition. The detachment on the wedge surface of the blade occurs in the transition state from the lower bound point, also called the initial detaching point, through the upper-bound point, or complete open state.
- 3) It is useful to observe the separation line force to explain necking of the wedged zone and detachment on the wedge surface of the blade.
- 4) Maximum contact length occurs near the initially detached position of indentation depth.

- 5) In the second necking mode, for the duration of the decrease in height of the necking root, the contact length  $a_c$  and the detached length  $a_d$  remain almost constant. The separation line force also remains approximately constant.

## References

- [Grebe and Hofer 1973] W. Grebe and H. Hofer, "Praktische Hinweise zur Schonung der Messer in Bandstahl Werkzeugen", *Papier-verarbeitung und Druck* **9** (1973), 292–300.
- [Grunzweig et al. 1954] J. Grunzweig, I. Longman, and N. Petch, "Calculations and measurements on wedge-indentation", *J. Mech. Phys. Solids* **2:2** (1954), 81–86.
- [Hesse and Tenzer 1963] F. Hesse and H. J. Tenzer, "Grundlagen der Papier-verarbeitung", pp. 58–60 in *VEB Verlag fur Buch und Bibliotheks-wesen*, Leipzig, 1963.
- [Hill 1953] R. Hill, "On the mechanics of cutting metal strips with knife-edged tools", *J. Mech. Phys. Solids* **1:4** (1953), 265–270.
- [Hill 1983] R. Hill, *The mathematical theory of plasticity*, Clarendon Press, Oxford, 1983.
- [Inaba 1998] Y. Inaba, "Flatbed diecutting and maintenance of diecutter", *Carton Box* **17:200** (Oct 1998), 17–20. In Japanese. Translated in Proceedings of Third Diecutting Symposium (Tokyo, 1998), pp. 15–19.
- [MSC 2003] MSC Software, *Marc: theory and user information*, Santa Ana, CA, 2003.
- [Murayama et al. 2003] M. Murayama, S. Nagasawa, Y. Fukuzawa, and I. Katayama, "Effect of sheet thickness and friction on load characteristic of crushed center bevel cutter indented to aluminum sheet", pp. 115–124 in *Computational methods in contact mechanics, VI*, edited by C. A. Brebbia, Trans. Wessex Inst. Eng. Sci. **38**, WIT Press, Ashurst, UK, 2003.
- [Murayama et al. 2004] M. Murayama, S. Nagasawa, Y. Fukuzawa, and I. Katayama, "Cutting mechanism and load characteristic of trapezoidal center bevel cutter indented on aluminum sheet", *JSME Int. J. C: Mech. Syst. Mach. Elem. Manuf.* **47:1** (2004), 21–28.
- [Nagasawa et al. 2001] S. Nagasawa, H. Sato, D. Yamaguchi, Y. Fukuzawa, I. Katayama, and A. Yoshizawa, "Effects of tip clearance and blade hardness on cutting resistance and tip shape in paperboard die cutting", *J. Japan Soc. Technol. Plasticity* **42:480** (Jan 2001), 38–42. In Japanese.
- [Nagasawa et al. 2002] S. Nagasawa, Y. Fukuzawa, T. Yamaguchi, M. Murayama, D. Yamaguchi, and I. Katayama, "Effects of blade tip shape on thread dross occurrence in paperboard die cutting", *J. Japan Soc. Technol. Plasticity* **43:498** (Jul 2002), 50–54. In Japanese.
- [Nagasawa et al. 2004] S. Nagasawa, H. Sekikawa, M. Murayama, Y. Fukuzawa, and I. Katayama, "Effect of initial tip profile on crushing of center bevelled cutter – numerical analysis of crushing of cutter tip indented on paperboard", *J. Japan Soc. Technol. Plasticity* **45:524** (2004), 747–751. In Japanese.
- [Tanaka and Akamatsu 2001] Y. Tanaka and H. Akamatsu, "Development of testing system for cutting characteristics of pressure-sensitive adhesive tape", *Nitto Denko Technical Report* **39** (2001), 62–65. In Japanese.

Received 12 Jan 2006.

SEKSAN CHAIJIT: [seksan@stn.nagaokaut.ac.jp](mailto:seksan@stn.nagaokaut.ac.jp)

Graduate School of Information Science and Control Engineering, Nagaoka University of Technology, Nagaoka, Niigata, 940-2188 Japan

SHIGERU NAGASAWA: [snaga@mech.nagaokaut.ac.jp](mailto:snaga@mech.nagaokaut.ac.jp)

Department of Mechanical Engineering, Nagaoka University of Technology, Nagaoka, Niigata, 940-2188 Japan

YASUSHI FUKUZAWA: [fukuzawa@vos.nagaokaut.ac.jp](mailto:fukuzawa@vos.nagaokaut.ac.jp)

Department of Mechanical Engineering, Nagaoka University of Technology, Nagaoka, Niigata, 940-2188 Japan

MITSUHIRO MURAYAMA: Faculty of Business Administration, Nagaoka University, Nagaoka, Niigata, 940-0828 Japan

ISAMU KATAYAMA: Katayama Steel Rule Die Co., Ltd., Tokyo, 162-0381 Japan

## A ONE-DIMENSIONAL VARIATIONAL FORMULATION FOR QUASIBRITTLE FRACTURE

CLAUDIA COMI, STEFANO MARIANI, MATTEO NEGRI AND UMBERTO PEREGO

Besides efficient techniques allowing for the finite-element modeling of propagating displacement discontinuities, the numerical simulation of fracture processes in quasibrittle materials requires the definition of criteria for crack initiation and propagation. Among several alternatives proposed in the literature, the possibility to characterize energetically the discontinuous solution has recently attracted special interest. In this work, the initiation and propagation of cohesive cracks in an inhomogeneous elastic bar, subject to an axial body force is considered. The incremental finite-step problem for the evolving discontinuity is formulated accounting for progressive damage in the cohesive interface. For assigned loading conditions, it is shown that the equilibrium of the system and the position where the crack actually forms can be obtained from the minimality conditions of an energy functional including the bulk elastic energy and the crack surface energy. The subsequent step-by-step propagation of the cohesive crack is also obtained from the minimality conditions of an energy functional defined for each step. The issue of the algorithmic selection of the energetically more convenient solution is briefly discussed.

### 1. Introduction

Computational finite element approaches to the simulation of crack inception and propagation in brittle and quasibrittle solids can be subdivided into the broad categories of smeared and discrete crack descriptions.

Smeared crack approaches, based on the simulation of damage growth in the bulk material, are particularly suited for the description of the initial phase of strain localization and consequent material degradation, but lack of physical foundation in the late stage of material separation and, in general, require a finer discretization to accurately resolve the localization band.

Conversely, discrete crack approaches, by their very nature, do not incorporate information on the initial stage of formation of microdamage in the bulk, but are particularly suited for the description of the propagation of displacement discontinuities in the material.

In the past, the simulation of a propagating discontinuity in a finite element mesh was one of the main problems involved with the discrete crack approach. Nowadays, computationally effective techniques are available, for example, adaptive remeshing [Askes and Sluys 2000; Rodríguez-Ferran and Huerta 2000; Pandolfi and Ortiz 2002], the strong discontinuity approach (SDA) [Simo et al. 1993; Oliver et al. 2002; Oliver et al. 2003], the extended finite element method (X-FEM) [Moës et al. 1999; Wells and Sluys

---

*Keywords:* cohesive crack, variational formulation, finite-step problem.

This work has been carried out within the context of MIUR-PRIN 2003 contract 2003082105\_003 on *Interfacial damage failure in structural systems: applications to civil engineering and emerging research fields.*



2001; Moës and Belytschko 2002; Mariani and Perego 2003], which, in conjunction with the adoption of cohesive crack models, have greatly improved the accuracy and efficiency of the simulation.

If attention is restricted to the case of a cohesive crack propagating in an elastic medium, one of the main issues still open in the finite element implementation is the definition of a criterion for initiation and propagation. In a portion of the mesh which is not yet crossed by a crack, the displacement discontinuity does not exist until it is introduced according to a pre-defined criterion which is either local (that is, based on some measure of the local stress or strain state) or global (for example, based on some measure of the energy or other averaged quantities).

In the case of propagation, another problem is the definition of the correct shape and length of the incremental discontinuity corresponding to the assigned load increment. This is usually solved in an iterative way by assigning a tentative length of propagation, solving the problem with the augmented crack extension, and then verifying a posteriori whether at the new tip the propagation condition is still satisfied.

Variational approaches, in which the shape of the crack increment is chosen so as to minimize an energy functional, have attracted considerable attention in recent times in view of their strong mechanical foundation. Both numerical [Bourdin et al. 2000; Negri 2003; Angelillo et al. 2003] and theoretical results [Francfort and Marigo 1998; Dal Maso and Toader 2002; Chambolle 2003] have been presented for perfectly brittle materials, employing a potential given by the sum of elastic and fracture energies. In this framework, the propagation history is obtained as a quasistatic evolution, defined by means of a minimizing sequence: the time interval is discretized with a finite increment  $\Delta t$  and the configuration at the end of each time step is given by a minimizer, with suitable irreversibility constraints. In this kind of model the main source of mathematical difficulties is related to the convergence of the fracture sets as  $\Delta t \rightarrow 0$ . In the case of brittle materials this technical problem has been solved in different ways in [Dal Maso and Toader 2002; Chambolle 2003] and in [Francfort and Larsen 2003]. For cohesive energies some results have been obtained in [Dal Maso and Zanini 2007], assuming a priori the path of propagation, while the general case is still an open problem. A numerical application has been presented in [Dumstorff and Meschke 2005], without addressing, however, the convergence issue. In the one-dimensional framework, these kinds of difficulties are not encountered and more general forms of the fracture energy can be considered (see for instance [Braidès et al. 1999; Del Piero and Truskinovsky 2001]). This is the setting adopted in the present work.

A linear elastic bar, constrained at both ends, subjected to a uniformly distributed axial load and to an imposed displacement at one end is considered. The material has a limit strength with a cohesive fracture energy depending on the position. The axial force transmitted through the cohesive crack decreases with the crack opening and the loading-unloading behavior of the interface is governed by a nondecreasing, damage-like internal variable. The solution of the associated incremental problem is shown to be a local minimizer of the potential energy. Following [Braidès et al. 1999], it is shown that a single crack is energetically more convenient than multiple cracks at the first crack initiation. This is also shown to be true for subsequent time steps, provided that the algorithmic criterion proposed for the selection of feasible solutions is adopted. The position of the first fracture and the amplitude of its jump are again determined by enforcing minimality. The resulting evolution is quasistatic and satisfies the loading-unloading conditions in Kuhn–Tucker form.

## 2. Problem definition

A bar of unit cross section, constrained at both ends and subject to a body force  $b(x)$  directed along its axis, is considered. The reference configuration of the bar is represented by the interval  $I = (0, L)$ . In order to account for fractures, the admissible configurations are assumed to belong to a space of (possibly) discontinuous displacement fields  $u$  satisfying the boundary conditions  $u(0) = 0$  and  $u(L) = \eta$ . The set of points where  $u$  is discontinuous, denoted by  $S_u$ , is not prescribed a priori and may contain the endpoints of the bar. Interpenetration is ruled out by the constraint  $[u] \geq 0$ ,  $[u]$  denoting the jump of  $u$ . A cohesive softening model is assumed for the opening crack. This means that the fracture energy, necessary to create the crack, is progressively released as the jump  $[u]$  grows, until the critical value  $[u]_{\text{crit}}$  is reached, beyond which no tractions can be transmitted across the discontinuity.

In the bulk, that is, at points belonging to  $I \setminus S_u$ , the current state of the bar is governed by the following equations for compatibility, equilibrium with nonzero body forces  $b(x)$ , and elastic (bulk) behavior, respectively,

$$\varepsilon = \frac{du}{dx}, \quad \frac{d\sigma}{dx} + b = 0, \quad \sigma = E\varepsilon,$$

where  $\varepsilon$  is the longitudinal strain,  $\sigma$  the axial stress and  $E$  the Young's modulus. On the other hand, for every crack point  $z \in S_u$  we have conditions for compatibility at the interface and equilibrium across the crack

$$[u](z) = u^+(z) - u^-(z) \geq 0, \quad \sigma^+(z) = \sigma^-(z).$$

The bar behaves elastically as long as the axial stress  $\sigma(x)$  is below a threshold  $\bar{p}(x)$ , which is assumed to vary along the bar. The cohesive crack model is assumed to obey a nonreversible damaging law (see [Figure 1](#)). The accumulated damage is taken into account by a nondecreasing kinematic internal variable  $\xi$ , depending on the material point  $x$ . The traction  $p$  which can be transmitted across the crack is governed by a softening function  $g(\xi)$ , with  $\frac{dg}{d\xi} \leq 0$ , and the maximum  $\bar{p}$  of  $p$  is such that  $\bar{p}(x) = a(x)g(0)$ , where  $a(x)$  accounts for the variation of the resistance along the bar.

The inelastic potential  $G(\xi)$  for  $\xi \geq 0$  is defined as

$$G(\xi) = \int_0^\xi g(\mu) d\mu.$$

In this way, the softening function  $g(\xi)$  is interpreted as the static internal variable conjugate to the damage  $\xi$  through the state equation

$$g(\xi) = \frac{dG(\xi)}{d\xi},$$

where, for  $\xi = 0$ ,  $\frac{dG(\xi)}{d\xi}$  should be intended as the right derivative of  $G(\xi)$ . The quantity  $G(\xi = [u]_{\text{crit}})$  is commonly referred to as fracture energy and is a material property.

For increasing opening displacement  $[u]$ , following the softening branch  $a(z)g(\xi)$  the traction decreases until the limit opening  $[u]_{\text{crit}}$  is reached. For displacement jumps  $[u] > [u]_{\text{crit}}$  no traction is transmitted across the crack ([Figure 1](#)). For decreasing opening displacement, a linear unloading path is followed, with slope  $a(z)g(\xi)/\xi$  depending on the current value of damage. Upon reloading, the same linear path is followed until the current traction threshold  $\bar{p}(z) = a(z)g(\xi)$  is reached, then the softening

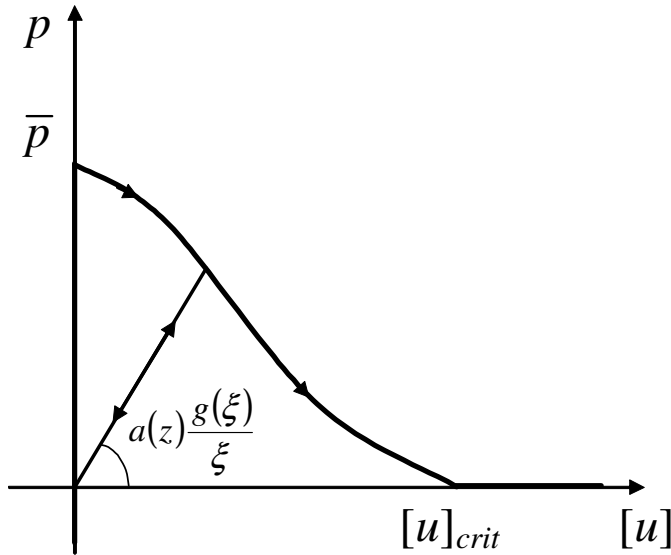


**Figure 1.** Traction-displacement discontinuity law for cohesive damaging crack.

branch is followed again. The traction-crack opening displacement relation is

$$\begin{aligned}
 p(z) &\in [0, \bar{p}(z)] && \text{for } \xi = 0, \\
 p(z) &= a(z) \frac{g(\xi)}{\xi} [u](z) && \text{for } \xi > 0,
 \end{aligned}$$

and the loading-unloading conditions are

$$p - a(z)g(\xi) \leq 0, \quad (p - a(z)g(\xi))\dot{\xi} = 0 \quad \text{for } \dot{\xi} \geq 0, \tag{1}$$

while the consistency condition  $p - a(x)g(\xi) \leq 0$  must be satisfied everywhere in the bulk.

These definitions imply that, for a crack at  $z \in S_u$ ,

$$\xi(t, z) = \max_{\tau \leq t} [u](\tau, z).$$

Note that the standard form of time-independent inelastic constitutive laws requires also the definition of an inelastic multiplier and of an evolution equation for the internal variable  $\xi$ . In the particularly simple damage law here adopted for the cohesive interface, the rate of the internal variable and the inelastic multiplier coincide. To simplify the notation, the rate of the internal variable has been directly introduced into the loading-unloading conditions (1) instead of the inelastic multiplier.

The “local” fracture energy, that is, the energy necessary to create the discontinuity in the point  $z$ , is defined as

$$G_f(z) = \lim_{[u] \rightarrow [u]_{crit}} a(z)G([u]) < \infty.$$

Note that cohesive models with  $[u]_{crit} \rightarrow \infty$  are also feasible as long as  $G_f(z)$  remains bounded.

Stable global response (that is, no snap-back) of the bar is assumed under the imposed end displacement  $\eta$ . It is easy to show that a snap-back response is ruled out if

$$L < -\frac{E}{a(z)\frac{dg}{d\xi}}, \quad \text{for } 0 \leq \xi \leq [u]_{\text{crit}}.$$

### 3. Finite-step problem

In view of the nonreversible nature of the crack evolution, the analysis of the bar response to an assigned history  $\eta(t)$ , with  $t \in [0, T]$ , of the imposed displacement, requires the definition of a step-by-step time marching procedure. The structural response  $u_{n+1}$  at time  $t_{n+1} = t_n + \Delta t$  satisfies in the bulk

$$\varepsilon_{n+1} = \frac{du_{n+1}}{dx}, \quad \sigma_{n+1} = E\varepsilon_{n+1}, \quad \frac{d\sigma_{n+1}}{dx} + b = 0, \quad (2)$$

and in the crack points

$$[u]_{n+1}(z) = u_{n+1}^+(z) - u_{n+1}^-(z) \geq 0, \quad \sigma_{n+1}^+(z) = \sigma_{n+1}^-(z) = p_{n+1}(z).$$

Knowing the configuration at time  $t_n$ , the following stepwise-reversible behavior is assumed for the cohesive cracks

$$\xi_{n+1} = \xi_n + \Delta\xi, \quad p_{n+1} = a(z)\frac{g(\xi_{n+1})}{\xi_{n+1}}[u]_{n+1}, \quad \text{for } \xi_{n+1} > 0, \quad (3)$$

$$p_{n+1} - a(z)g(\xi_{n+1}) \leq 0, \quad (p_{n+1} - a(z)g(\xi_{n+1}))\Delta\xi = 0, \quad \text{for } \Delta\xi \geq 0, \quad (4)$$

where the second equation in (3) is the traction-crack opening displacement relation, and the relations in (4) represent the loading-unloading conditions. Note that the above defined finite-step problem can be conceived as resulting from a backward-difference integration of the incremental problem, while the original (continuous) problem will be recovered for  $\Delta t \rightarrow 0$ .

It is therefore possible to define an energy  $\tilde{G}([u], \xi_n)$  associated to the reversible finite-step law

$$\tilde{G}([u], \xi_n) = \begin{cases} \frac{g(\xi_n)}{2\xi_n}[u]^2, & \text{for } [u] \leq \xi_n, \\ G([u]) - G(\xi_n) + \frac{\xi_n g(\xi_n)}{2}, & \text{for } [u] \geq \xi_n. \end{cases} \quad (5)$$

For  $\xi_n = 0$ , one has  $\tilde{G}([u], \xi_n) = G([u])$ . The adopted cohesive finite-step law with the associated energy is shown in Figure 2a at initiation and in Figure 2b in correspondence of a generic time-step.

For  $\eta = \eta_{n+1}$ , the following functional is defined for the current time-step

$$U^\eta(u, \xi_n) = \frac{1}{2} \int_I E \left( \frac{du}{dx} \right)^2 dx + \sum_{z \in \mathcal{S}_u} a(z) \tilde{G}([u](z), \xi_n(z)) - \int_I bu \, dx. \quad (6)$$

In the expression of the functional,  $\xi_n$  plays the role of an assigned parameter. At the end of each step, the internal variable is updated and the functional changes its expression. The updating procedure is schematically shown in Figure 3 where numbered dots denote the value of the functional at the end of the step, before updating, while dots with starred numbers denote the corresponding updated value.

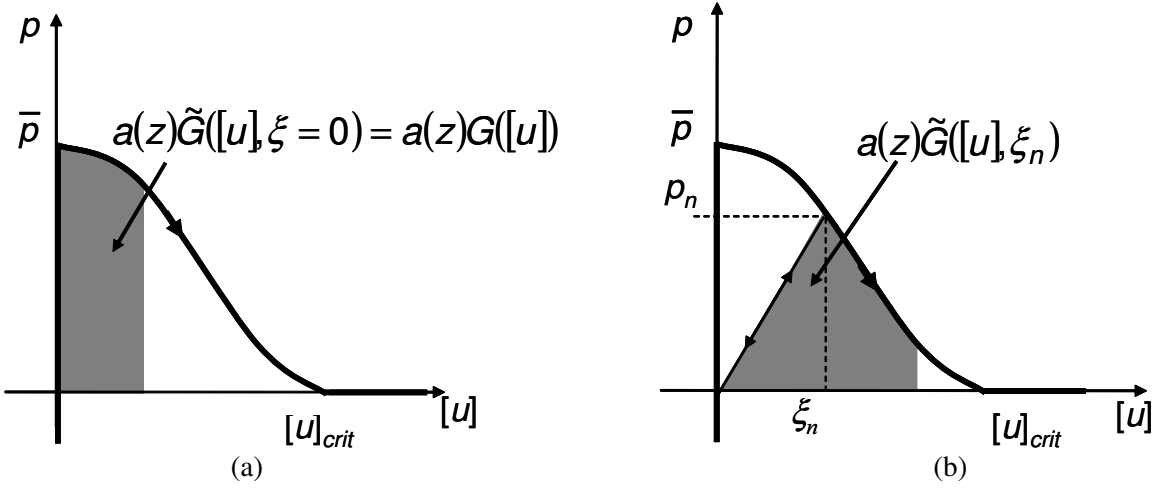


**Figure 2.** Finite-step cohesive law at initiation (a), at a time-step  $t_n$  (b).

Let  $u'$  denote the (distributional) derivative of  $u$ , that is,

$$u' = \frac{du}{dx}dx + \sum_{z \in S_u} [u](z)\delta_z, \tag{7}$$

where  $\delta_z$  denotes the Dirac delta concentrated in  $z$ . We assume that  $u'$  is a bounded measure, that is,

$$|u'| (I) = \int_I \left| \frac{du}{dx} \right| dx + \sum_{z \in S_u} |[u]| < \infty.$$

Following [Braides et al. 1999] let  $B(x)$  be a primitive of  $b(x)$  vanishing in zero. Integrating by parts the body force work, the functional can be rewritten as

$$U^\eta(u, \xi_n) = \frac{1}{2} \int_I E \left( \frac{du}{dx} \right)^2 dx + \sum_{z \in S_u} a(z)\tilde{G}([u](z), \xi_n(z)) + \int_{[0,L]} Bu' - B(L)\eta.$$

Taking into account the definition of the distributional derivative in Equation (7), one obtains

$$U^\eta(u, \xi_n) = \int_I \frac{du}{dx} \left( \frac{1}{2} E \frac{du}{dx} + B \right) dx + \sum_{z \in S_u} (a(z)\tilde{G}([u](z), \xi_n(z)) + B(z)[u](z)) - B(L)\eta. \tag{8}$$

**Remark 1.** Such functionals have been widely studied in the recent mathematical literature on free discontinuity problems (see, for instance, [Braides et al. 1999]). In this framework the potential energy would be defined in the space  $SBV(0, L)$  of special functions with bounded variation (for a definition of  $SBV$  spaces, see for example, [Ambrosio et al. 2000]), that is, for the displacements  $u$  whose distributional derivative is a bounded measure which can be written as in Equation (7). Existence of minimizers (local and global) in  $SBV$  will be discussed in the next section.

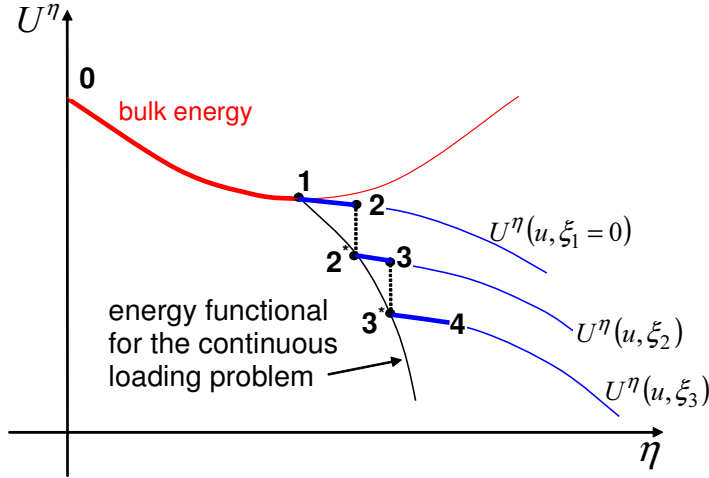


**Figure 3.** Updating procedure for energy functional. Numbers refer to end of step. Starred numbers refer to updated values of functional.

A displacement  $u_{n+1}$  at the end of the finite-step is considered a local minimizer of  $U^\eta$  defined in Equation (6) if  $U^\eta(v, \xi) \geq U^\eta(u, \xi)$  for every  $v \in SBV(0, L)$  such that

$$\int_I |v - u| dx \leq \alpha,$$

for some  $\alpha$  sufficiently small. In the following sections it will be shown that the discrete evolution defined by a sequence of local minimizers of Equation (6) satisfies the governing equations (2)-(4). To proceed in the discussion, it is convenient to consider separately the crack initiation problem ( $\xi_n = 0$ ) and the subsequent crack opening problem ( $\xi_n \neq 0$ ).

### 4. Crack initiation problem

The following crack initiation problem is considered. The bar is subject to an assigned body force  $b(x)$ , whose intensity is such that the tensile strength  $\bar{p}(x)$  is not exceeded in any point of the bar. Then a growing positive displacement  $\eta$  is imposed at  $x = L$  until the threshold value  $\bar{\eta}$  is reached for which, at a position  $\bar{z}$ , the stress  $\sigma$  reaches its limit value  $\bar{p}(\bar{z})$ . The value of  $\bar{\eta}$  depends on the strength of the bar and on the body force.

Following the path of reasoning proposed by Braides, Dal Maso and Garroni [Braides et al. 1999], first we prove that the minimizers (both local and global) have a single fracture. Assume that two cracks are activated at  $z_1$  and  $z_2$ , with jumps  $w_1$  and  $w_2$  respectively. Let  $w = w_1 + w_2$  and let  $a_i = a(z_i)$ ,  $B_i = B(z_i)$ . Let  $H([u])$  be the energy associated to the discontinuity in Equation (8), that is,

$$H([u]) = \sum_{z \in S_u} \{a(z) \tilde{G}([u](z), \xi_n(z)) + B(z)[u](z)\}.$$

Noting that at crack initiation ( $\xi_n = 0$ ) one has  $\tilde{G} \equiv G$  and considering  $z_1, z_2$  and  $w$  as fixed, we can write  $H$  and its second derivative as a function of  $w_1$  alone as

$$H(w_1) = a_1 G(w_1) + B_1 w_1 + a_2 G(w - w_1) + B_2 (w - w_1),$$

$$\frac{d^2 H(w_1)}{dw_1^2} = a_1 \frac{dg(w_1)}{dw_1} + a_2 \frac{dg(w - w_1)}{d(w - w_1)},$$

for  $0 \leq w_1 \leq w$ . As  $dg/dw_i \leq 0$  and  $a_i > 0$ , it follows that  $H$  is concave and thus its minimum, in the interval  $[0, w]$ , is in the endpoints. This means that either  $w_1 = w$  and  $w_2 = 0$  or  $w_1 = 0$  and  $w_2 = w$ . Hence in one of the points  $z_i$  there is no jump. Since the bulk energy does not depend on  $w$ , following the previous reasoning it is not hard to see that a minimizer can have only one fracture point. We will denote it by  $\bar{z}$ .

**Remark 2.** Note that by a similar argument it follows that the minimization problem in  $SBV$  is well posed even if the relaxed functional would be defined in the whole  $BV$  (see [Braidis et al. 1999] and the references therein).

Denoting for notation convenience  $U^{\eta \rightarrow \bar{\eta}^+} = \lim_{\eta \rightarrow \bar{\eta}^+} U^\eta$ , the following proposition holds.

**Proposition 3.** Starting from an elastic state with  $\xi_n = 0$ , for an assigned value  $\eta$  of the imposed displacement, the governing equations can be obtained from the stationarity conditions of  $U^\eta$ . The position  $\bar{z}$  of the activated crack can be obtained from the minimality of  $U^{\eta \rightarrow \bar{\eta}^+}(u, 0)$ .

*Proof.* Assume that  $u$  is a stationary point of  $U^\eta$  and consider the variations of the form  $u + \lambda v$ , where  $\lambda$  is a scalar variable and  $v : [0, L] \rightarrow \mathfrak{R}$  a suitable test function. As  $u + \lambda v$  must satisfy the boundary conditions, we assume that  $v(0) = v(L) = 0$ . Moreover,  $v$  may have a unit jump in  $S_v$ , which we denote by  $[v] = 1$ . Since interpenetration is not allowed, we must assume that  $[u] + \lambda[v] \geq 0$  for  $\lambda$  sufficiently small. The stationarity condition is given, in terms of the first variation of  $U^\eta$ , by the inequality

$$\begin{aligned} & \lim_{\lambda \rightarrow 0^+} \frac{1}{\lambda} \left( U^\eta(u + \lambda v, 0) - U^\eta(u, 0) \right) \\ &= \lim_{\lambda \rightarrow 0^+} \frac{1}{2\lambda} \int_I \left[ E \left( \frac{du}{dx} + \lambda \frac{dv}{dx} \right)^2 - E \left( \frac{du}{dx} \right)^2 \right] dx \\ & \quad + \lim_{\lambda \rightarrow 0^+} \frac{1}{\lambda} \sum_{z \in S_u \cup S_v} \left( a(z) G([u + \lambda v](z)) - a(z) G([u](z)) \right) - \int_I b v \, dx \\ &= \int_I \left( E \frac{du}{dx} \right) \frac{dv}{dx} \, dx + \lim_{\lambda \rightarrow 0^+} \frac{1}{\lambda} \sum_{z \in S_u \cup S_v} \left( a(z) G([u + \lambda v](z)) - a(z) G([u](z)) \right) - \int_I b v \, dx \geq 0. \end{aligned} \tag{9}$$

In general, the configuration  $u + \lambda v$  may have two jumps, at  $S_u = \{\bar{z}\}$  and  $S_v = \{z_v\}$ . If  $S_u = S_v$ , then  $S_{u+\lambda v} = S_u$ . In this case, the second term in Equation (9) can be written as

$$\lim_{\lambda \rightarrow 0^+} \frac{1}{\lambda} \left( a(\bar{z}) G([u + \lambda v](\bar{z})) - a(\bar{z}) G([u](\bar{z})) \right) = a(\bar{z}) g([u](\bar{z})) [v] \geq 0.$$

If  $S_u \neq S_v$ , then  $S_{u+\lambda v} = S_u \cup S_v$  and the previous condition becomes

$$\begin{aligned} & \lim_{\lambda \rightarrow 0^+} \frac{1}{\lambda} \left( a(\bar{z})G([u + \lambda v](\bar{z})) + a(z_v)G([u + \lambda v](z_v)) - a(\bar{z})G([u](\bar{z})) \right) \\ &= \lim_{\lambda \rightarrow 0^+} \frac{1}{\lambda} \left( a(\bar{z})G([u](\bar{z})) + a(z_v)G([\lambda v](z_v)) - a(\bar{z})G([u](\bar{z})) \right) = \lim_{\lambda \rightarrow 0^+} \frac{1}{\lambda} a(z_v)G([\lambda v](z_v)) \\ &= a(z_v)g(0)[v] \geq 0. \end{aligned}$$

Now we consider some particular variations  $v$  in order to obtain the governing equations.

- Assume first that  $S_u = \emptyset$  and that  $v(\bar{z}) = 0$ . Integrating by parts the first integral in Equation (9), the inequality becomes

$$\begin{aligned} E \frac{du}{dx} v \Big|_0^{\bar{z}} - \int_0^{\bar{z}} \left( E \frac{d^2u}{dx^2} + b \right) v \, dx + E \frac{du}{dx} v \Big|_{\bar{z}}^L - \int_{\bar{z}}^L \left( E \frac{d^2u}{dx^2} + b \right) v \, dx \\ = - \int_0^{\bar{z}} \left( E \frac{d^2u}{dx^2} + b \right) v \, dx - \int_{\bar{z}}^L \left( E \frac{d^2u}{dx^2} + b \right) v \, dx \geq 0, \end{aligned}$$

which gives  $(E \frac{d^2u}{dx^2} + b) = 0$ , a.e. in  $[0, L]$ . This is the condition of equilibrium in the bulk.

- Consider now a variation  $v$  such that  $v(\bar{z})^+ = v(\bar{z})^- \neq 0$ . Taking into account that  $(E \frac{d^2u}{dx^2} + b) = 0$ , Equation (9) then becomes

$$\left( E \frac{du}{dx} \right)^- v^- - \left( E \frac{du}{dx} \right)^+ v^+ \geq 0,$$

which gives easily  $\sigma^+(\bar{z}) = \sigma^-(\bar{z})$ . This is the condition of equilibrium across the crack.

- Now we can choose a variation  $v$  having a unit discontinuity at  $z_v \in [0, L]$ . According to this definition  $[v](z_v) = 1$  and  $\int_0^L \frac{dv}{dx} dx = -[v](z_v) = -1$ . Let us consider first the case  $\bar{z} \neq z_v$ . Making reference to the expression in Equation (8) of the energy, the stationarity condition can be written as

$$\int_I \left( E \frac{du}{dx} + B \right) \frac{dv}{dx} dx + B(z_v)[v] + a(z_v)g(0)[v] \geq 0. \tag{10}$$

Note that, in view of the bulk equilibrium  $(E \frac{d^2u}{dx^2} + b = 0)$ , the stress  $\sigma^\eta = E \frac{du}{dx} + B$ , which depends on the imposed boundary displacement  $\eta$ , is constant along  $x$ . Therefore, one can write

$$-\sigma^\eta + B(z_v) + a(z_v)g(0) \geq 0. \tag{11}$$

Taking into account that  $\sigma^\eta - B(z) = \sigma(z)$  is the stress in the bar due to the dead load and the imposed boundary displacement and that  $a(z_v)g(0) = \bar{p}(z_v)$ , one has

$$\sigma - \bar{p} \leq 0 \quad \text{for } z_v \neq \bar{z}. \tag{12}$$

When  $S_u = S_v$ , that is, for  $z_v = \bar{z}$ , since  $[u] > 0$  a perturbed configuration of the form  $u - \lambda v$  can be considered (as for  $\lambda$  small enough  $[u - \lambda v](\bar{z}) \geq 0$ ). Computing again the limit for  $\lambda \rightarrow 0^+$ , and



combining with Equation (10), the stationarity requires that

$$\int_I \left( E \frac{du}{dx} + B \right) \frac{dv}{dx} dx + B(\bar{z})[v] + a(\bar{z})g([u](\bar{z}))[v] = 0. \tag{13}$$

Since  $\xi_n \equiv 0$  at crack initiation,  $\Delta\xi(\bar{z}) = [u](\bar{z})$  at the end of the step and the traction  $p$  in the crack follows the softening branch. Therefore, equation Equation (13) becomes

$$\sigma - p = 0 \quad \text{for } z_v = \bar{z}.$$

It is now easy to see that the governing equations (2)–(4) are all satisfied. □

Finally, we remark that the position  $\bar{z}$  of the crack may depend on the amplitude of the time-step of the incremental solution, as it will be further discussed in Section 6. The correct position is recovered for  $\Delta t \rightarrow 0$  or equivalently for  $\eta \rightarrow \bar{\eta}^+$ , where  $\bar{\eta}$  is the critical value of the imposed displacement for which  $p(\bar{z}) = \bar{p}(\bar{z})$ . For  $\eta = \bar{\eta}$ , the crack will activate at a position  $\bar{z}$  where the stress  $\sigma(z) = \sigma^{\bar{\eta}} - B(z)$  reaches for the first time the critical value  $\sigma(\bar{z}) = \bar{p}(\bar{z})$ , which implies that  $B(\bar{z}) + \bar{p}(\bar{z}) = \sigma^{\bar{\eta}}$ . At all other points, one has  $\sigma(z) = \sigma^{\bar{\eta}} - B(z) \leq \bar{p}(z)$ , which implies that  $B(z) + \bar{p}(z) \geq \sigma^{\bar{\eta}}$ . One can conclude that the position  $\bar{z}$  of the crack is a minimizer of the function  $B(z) + \bar{p}(z)$ . If now one considers the case  $\eta \rightarrow \bar{\eta}^+$ , since  $[u] \rightarrow 0$  in correspondence of the crack initiation,  $G([u])$  behaves like  $g(0)[u]$ . Thus the energy given by Equation (8) can be written as

$$U^{\eta \rightarrow \bar{\eta}^+}(u, 0) = \int_I \frac{du}{dx} \left( \frac{1}{2} E \frac{du}{dx} + B \right) dx + (\bar{p}(z) + B(z))[u].$$

As the elastic energy does not depend on the position of cracks, it is clear that a minimizer of  $U^{\eta \rightarrow \bar{\eta}^+}(u, 0)$  will concentrate the jump  $[u]$  in a point where  $(\bar{p}(z) + B(z))$  reaches its minimum.

### 5. Crack opening problem

The same problem defined in Section 4 is considered at time  $t_n$  for an imposed displacement  $\eta > \bar{\eta}$ . However, this time the crack remains fixed in the position  $\bar{z}$  of the first activation for  $\eta = \bar{\eta}$ , since healing is not permitted by the assumed model, and the opening of a new crack is not energetically convenient, in the sense that will be specified in Section 6. A load step is considered where the imposed displacement is incremented by a quantity  $\Delta\eta$ . The functional defined in Equation (6) is considered for  $\xi_n > 0$ . The following proposition holds.

**Proposition 4.** For fixed crack position  $\bar{z}$ , consider an evolutionary problem, discretized in time steps with finite increment  $\Delta t$ . The displacement  $u_{n+1}$  at time  $t_{n+1} = t_n + \Delta t$  solution of the finite-step problem presented in Equations (2)–(4), is obtained minimizing the energy  $U^\eta(u, \xi_n)$  with the boundary conditions  $u(0) = 0$  and  $u(L) = \eta$ . Note that, with the simple one dimensional cohesive law here adopted, the incremental problem is explicit with respect to the internal variable  $\xi$ , therefore this variable can be updated independently at the end of the step, when  $u_{n+1}$  is known.

*Proof.* Assume that  $u$  is a stationary point of  $U^\eta(u, \xi_n)$  and consider the variations of the form  $u + \lambda v$ , where  $\lambda$  is a scalar variable and  $v : [0, L] \rightarrow \mathfrak{R}$  a test function, satisfying homogeneous boundary conditions, which may have a jump in  $z_v \in S_v$ . The stationarity condition is given in terms of the first

variation of  $U^\eta(u, \xi_n)$  by the inequality

$$\begin{aligned} \lim_{\lambda \rightarrow 0^+} \frac{1}{\lambda} (U^\eta(u + \lambda v, \xi_n) - U^\eta(u, \xi_n)) &= \lim_{\lambda \rightarrow 0^+} \frac{1}{2\lambda} \int_I \left[ E \left( \frac{du}{dx} + \lambda \frac{dv}{dx} \right)^2 - E \left( \frac{du}{dx} \right)^2 \right] dx \\ &+ \lim_{\lambda \rightarrow 0^+} \frac{1}{\lambda} \sum_{z \in S_u \cup S_v} \left( a(z) \tilde{G}([u + \lambda v], \xi_n) - a(\bar{z}) \tilde{G}([u], \xi_n) \right) - \int_I b v \, dx \geq 0. \end{aligned}$$

Making use of the same arguments discussed in the previous section, the previous condition can be rewritten as

$$\int_I \left( E \frac{du}{dx} \right) \frac{dv}{dx} \, dx + a(z_v) \frac{d\tilde{G}([u], \xi_n)}{d[u]} [v] - \int_I b v \, dx \geq 0.$$

Now we consider some particular variations  $v$  in order to obtain the governing equations.

- Assuming  $[v] = 0$ , following the same path of the previous section one can obtain equilibrium conditions in the bulk and across the interface in  $\bar{z}$ .
- Now we can choose a variation  $v$  having a unit discontinuity at  $\bar{z}$ . Consider again the form of the functional given in Equation (8) obtained by integrating by parts the body force integral. Taking into account the bulk equilibrium, the stationarity conditions of Equation (8) read

$$-\sigma^\eta + B(\bar{z}) + a(\bar{z}) \frac{d\tilde{G}([u], \xi_n)}{d[u]} \geq 0. \tag{14}$$

Accounting for the definition of  $\tilde{G}([u], \xi_n)$  in Equation (5) and noting that  $\sigma^\eta - B(\bar{x}) = \sigma(\bar{z}) = p$  is the stress acting on the crack, from Equation (14) one obtains

$$-p + a(\bar{z}) \frac{g(\xi_n)}{\xi_n} [u] \geq 0, \quad \text{for } [u] \leq \xi_n, \tag{15}$$

$$-p + a(\bar{z}) g([u]) \geq 0, \quad \text{for } [u] \geq \xi_n. \tag{16}$$

When  $[u] = 0 < \xi_n$ , condition in Equation (15) gives  $p \leq 0$ , meaning that, if the crack has been already activated ( $\xi_n > 0$ ), a complete closure of the crack ( $[u] = 0$ ) corresponds to zero or negative stress. Assume now  $[u] > 0$ , in this case also a perturbation  $u - \lambda v$  is admissible for small  $\lambda$ , and inequalities opposite to Equations (15)–(16) are obtained. Therefore one has

$$p = a(\bar{z}) \frac{g(\xi_n)}{\xi_n} [u], \quad \text{for } [u] \leq \xi_n, \tag{17}$$

$$p = a(\bar{z}) g([u]), \quad \text{for } [u] \geq \xi_n. \tag{18}$$

From Equation (17) one obtains

$$p \leq a(\bar{z}) g(\xi_n), \quad \text{for } [u] \leq \xi_n. \tag{19}$$

- Consider a variation  $v$  having a unit discontinuity in  $z_v \notin S_u$ . Having in mind that, for  $x \neq \bar{z}$ ,  $[u](x) = \xi_n(x) = 0$ , one has

$$a(z_v) \frac{d\tilde{G}([u](z_v), \xi_n(z_v))}{d[u]} = a(z_v) g(0) = \bar{p}(z_v)$$

and the stationarity conditions simply give the consistency condition in the bulk  $-\sigma(x) + \bar{p}(x) \geq 0$ .

Noting that, by definition, at the end of the step  $\Delta\xi = 0$  if  $[u] \leq \xi_n$  while  $\Delta\xi = [u] - \xi_n$  if  $[u] \geq \xi_n$ , one obtains that : (i) Equations (17) and (18) define the traction-crack opening displacement relation (3); (ii) Equations (18) and (19) can be rewritten in the Kuhn–Tucker form seen in Equation (4) and thus provide the finite-step loading-unloading conditions for the cohesive crack.  $\square$

### 6. Algorithmic aspects

One of the important features of the present finite-step formulation is that the governing equations and the nonreversibility of damage growth are enforced only at the end of the step. In view of the nonconvex character of the energy functional, this implies that solutions may exist which minimize the energy but could not be reached in a continuous process due to the existence of energy barriers. These solutions appears to be an artifact of the algorithmic formulation of the finite-step problem and does not reflect the physical behavior. Therefore, it seems necessary to complement the algorithm with criteria for the exclusion of nonphysical solutions.

Let us consider first the crack initiation problem. At the end of Section 4, it has been proven that for  $\eta \rightarrow \bar{\eta}^+$ , the position of the first crack minimizes the functional  $U^{\eta \rightarrow \bar{\eta}^+}(u, 0)$ . We now consider the more general case where  $\eta$  can assume arbitrary values with respect to  $\bar{\eta}$ . The solution of the step problem is sought by searching for minimizers of the energy  $U^\eta(u, 0)$ . A classical approach consists of computing first an elastic trial, that is, a tentative solution assuming unlimited elastic behavior. If this is not a minimizer, then a better solution is found minimizing the energy along a descent direction, defined by the local gradient. The procedure is repeated until a minimizer is found.

Let  $u^{tr}$  be the elastic (trial) solution, that is, the minimizer of  $U^\eta$  restricted to the space of admissible displacements without cracks. Equilibrium in the bulk is clearly satisfied, that is,  $(E(u^{tr})' + B)' = (\sigma^{\eta, tr})' = 0$ ; hence for every admissible variation  $v$  with jump  $[v](z_v) > 0$ , from Equation (10) one has

$$\lim_{\lambda \rightarrow 0^+} \frac{1}{\lambda} (U^\eta(u^{tr} + \lambda v, 0) - U^\eta(u^{tr}, 0)) = (-\sigma^{\eta, tr} + B(z_v) + a(z_v)g(0))[v]. \tag{20}$$

If the variation of  $U^\eta$  given in Equation (20), computed in  $u^{tr}$  and with respect to every variation  $v$ , is positive, that is, if

$$\lim_{\lambda \rightarrow 0^+} \frac{1}{\lambda} (U^\eta(u^{tr} + \lambda v, 0) - U^\eta(u^{tr}, 0)) \geq 0,$$

then  $u^{tr}$  is a local minimizer. As discussed in Section 4, (Equations (11) and (12)), since  $[v](z_v) > 0$ , from Equation (20) it follows that  $-\sigma^{\eta, tr} + B(z_v) + a(z_v)g(0) > 0$  and thus  $\sigma^{\eta, tr}(z_v) < \bar{p}(z_v)$ . This means that the stress associated to  $u^{tr}$  is everywhere below the limit strength and therefore  $u_{n+1} = u^{tr}$  will be the solution of the step. On the contrary, if there exists a variation  $v$  such that

$$\lim_{\lambda \rightarrow 0^+} \frac{1}{\lambda} (U^\eta(u^{tr} + \lambda v, 0) - U^\eta(u^{tr}, 0)) = (-\sigma^{\eta, tr} + B(z_v) + a(z_v)g(0))[v] < 0, \tag{21}$$

then a new solution  $u_{n+1} \neq u^{tr}$  will be computed along a descent direction. From the physical point of view it seems reasonable to consider that a fracture could appear in any of the points  $z_v$  where the limit strength is exceeded, that is, where Equation (21) holds (for a variation  $v$  with a single discontinuity in  $z_v$ ).

In Section 4 it has been shown that for crack initiation (that is, for  $\eta = \bar{\eta}$ ) it is energetically convenient to open just one crack. It is shown below that the same result is obtained also in a computational procedure starting from the trial solution. Let us assume to be using a solution algorithm capable to deal with multiple cracks. Starting from the trial solution, it may happen that for a suitable variation  $v$  with two jumps in  $z_v^1$  and  $z_v^2$ , we get

$$\begin{aligned} \lim_{\lambda \rightarrow 0^+} \frac{1}{\lambda} (U^\eta(u^{tr} + \lambda v, 0) - U^\eta(u^{tr}, 0)) \\ = (-\sigma^{\eta, tr} + B(z_v^1) + a(z_v^1)g(0))[v](z_v^1) + (-\sigma^{\eta, tr} + B(z_v^2) + a(z_v^2)g(0))[v](z_v^2) < 0 \end{aligned}$$

with

$$(-\sigma^{\eta, tr} + B(z_v^2) + a(z_v^2)g(0)) > 0. \tag{22}$$

This means that a solution with multiple cracks may appear as energetically convenient with respect to the trial solution, and therefore reachable along a descent direction, even if at one of the points of activation ( $z_v^2$  in this case) a local energy barrier (that is, a local stress below the limit strength) prevents the actual opening of the crack. Such a solution seems not acceptable from a physical point of view and since fracture is a phenomenon governed by the local state of the material, it seems more reasonable to exclude from the search those locations where Equation (22) holds. Therefore, starting from the trial solution, only those points  $z_v$  where

$$(-\sigma^{\eta, tr} + B(z_v) + a(z_v)g(0)) < 0, \tag{23}$$

that is, points where the trial stress exceeds the local strength, will be considered as possible locations of the cracks in the search algorithm. Note that this argument in general does not exclude solutions with multiple cracks. There may be cases where solutions with multiple cracks can be reached along descending paths where condition in Equation (23) is satisfied at each crack location. These solutions are ruled out by the minimality, as for the crack initiation problem the concavity of the inelastic potential  $G([u])$  makes it convenient to open only one crack. Its correct position  $\bar{z}$  can be obtained searching for the solution along the steepest descent direction  $v$  from  $u^{tr}$ , that is, looking for the lowest value of the derivative of  $U^\eta$  computed in  $u^{tr}$ . It can be readily seen that this is obtained when the crack position minimizes the quantity  $B(z_v) + a(z_v)g(0)$ .

Let us consider now the crack opening problem. Assume that at time  $t_n$  only the first crack at  $\bar{z}$  is open. A displacement  $\eta > \eta_n$  be assigned at the bar end.

As in the previous case, let  $u^{tr}$  be the “elastic” trial solution. Since a damage model is used for the description of the cohesive crack behavior, it is appropriate to compute the trial solution using a secant elastic modulus. This allows to obtain the exact solution in the case of unloading. The following unlimited elastic behavior is assumed for the active cohesive crack (see Figure 4):

$$p^{tr}(\bar{z}) = a(\bar{z}) \frac{g(\xi_n)}{\xi_n} [u^{tr}](\bar{z}).$$

In this case, given  $\eta > \eta_n$  we have  $[u^{tr}] > \xi_n$  and

$$p^{tr}(\bar{z}) = \sigma^{\eta, tr} - B(\bar{z}) > a(\bar{z})g([u^{tr}](\bar{z})). \tag{24}$$

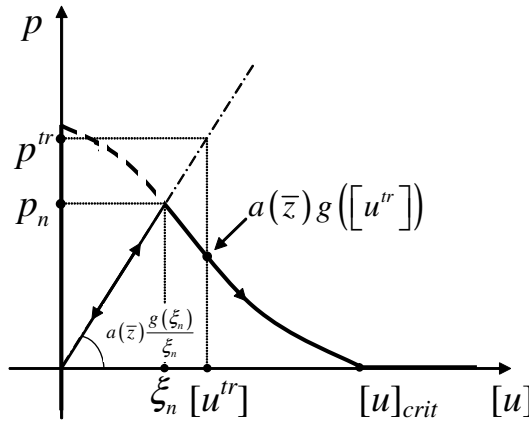


**Figure 4.** Unlimited elastic cohesive law used for computing the trial solution.

Hence,  $u^{tr}$  is not stable with respect to variations  $v$  with  $[v](\bar{z}) > 0$ . Indeed

$$\lim_{\lambda \rightarrow 0^+} \frac{1}{\lambda} (U^\eta(u^{tr} + \lambda v, \xi_n) - U^\eta(u^{tr}, \xi_n)) = (-\sigma^{n, tr} + B(\bar{z}) + a(\bar{z})g([u^{tr}](\bar{z}))) [v](\bar{z}) < 0. \quad (25)$$

A possible minimizer has to be sought within one of the following situations that may arise: (i) the crack at  $\bar{z}$  closes and one or more new cracks open; (ii) the crack at  $\bar{z}$  grows and one or more new cracks initiate; (iii) the crack at  $\bar{z}$  remains constant and one or more new cracks initiate; (iv) the crack at  $\bar{z}$  grows and no other cracks initiate.

As done for the crack initiation case, the physical feasibility of possible solutions is tested considering variations with a single jump. Variations  $v$  which close the crack, that is, with  $[v](\bar{z}) < 0$ , lead to a positive derivative in Equation (25) and therefore are not energetically convenient with respect to the trial solution. For this reason, case (i) can be ruled out and only displaced configurations such that  $[u](\bar{z}) \geq [u^{tr}](\bar{z})$  will be considered henceforth.

Now we will show that, starting from the trial solution, both closing the active crack and/or initiating new cracks are energetically less convenient than further opening the existing crack (that is, situation (iv)). Let us consider first the situation (ii). According to the criterion in Equation (21) of negative derivative for the selection of possible locations  $z_v \neq \bar{z}$  of new cracks, variations with  $[v](z_v) > 0$  lead to the local condition  $\sigma^{n, tr} > a(z_v)g(0) + B(z_v)$ . Denote by  $w_1 \geq 0$  the incremental opening of the crack at  $\bar{z}$ , that is,  $[u](\bar{z}) = [u^{tr}](\bar{z}) + w_1$ , and by  $w_2 = [v](z_v) = w - w_1 \geq 0$  the opening of a new crack at  $z_v \neq \bar{z}$ ,  $w$  being the total incremental opening with respect to the trial solution. As  $\bar{G}([u^{tr}](\bar{z}) + w_1, \xi_n(\bar{z}))$  is concave in the variable  $w_1$ , the argument used in Section 4 allows to state that a single active fracture (corresponding to  $w_1 = 0$  or  $w_2 = 0$ ) is always energetically more convenient, which rules out case (ii).

It remains to show that the minimizer is given by  $w_2 = 0$  and hence that also case (iii) can be ruled out. Assume by contradiction that  $u$  is a minimizer with  $w_1 = 0$ , so that

$$[u](\bar{z}) = [u^{tr}](\bar{z}) \quad \text{and} \quad [u](z_v) = w_2 = w > 0.$$

In this case, the total energy (see Equation (8)) would be given by

$$U^\eta(u, \xi_n) = \int_I \frac{du}{dx} \left( \frac{1}{2} E \frac{du}{dx} + B \right) dx + a(\bar{z}) \tilde{G}([u^{tr}](\bar{z}), \xi_n(\bar{z})) + B(\bar{z})[u^{tr}](\bar{z}) + a(z_v)G(w_2) + B(z_v)w_2 - B(L)\eta. \quad (26)$$

In view of the results of Proposition 4, assuming that  $u$  is a minimizer implies that equilibrium has to be satisfied. Imposing equilibrium we obtain  $a(z_v)g(w_2) + B(z_v) = a(\bar{z})g([u^{tr}](\bar{z})) + B(\bar{z}) = \sigma^\eta$ . Being  $a(z_v)g(w) + B(z_v)$  a nonincreasing function, in the variable  $w$ , we get

$$a(z_v)g(w_2) + B(z_v) = a(\bar{z})g([u^{tr}](\bar{z})) + B(\bar{z}) \geq a(\bar{z})g([u^{tr}](\bar{z}) + \hat{w}_1) + B(\bar{z}), \quad (27)$$

for every choice of  $\hat{w}_1 \geq 0$ . Taking  $\hat{w}_1 = w_2$ , one has

$$\begin{aligned} a(z_v)G(w_2) + B(z_v)w_2 &= \int_0^{w_2} \left( a(z_v)g(w) + B(z_v) \right) dw \geq \int_{[u^{tr}](\bar{z})}^{[u^{tr}](\bar{z})+w_2} \left( a(\bar{z})g(w) + B(\bar{z}) \right) dw \\ &= a(\bar{z}) \left( G([u^{tr}](\bar{z}) + w_2) - G([u^{tr}](\bar{z})) \right) + B(\bar{z})w_2. \end{aligned}$$

By this inequality and taking into account that from Equation (5) one has  $G([u^{tr}](\bar{z}) + w_2) - G([u^{tr}](\bar{z})) = \tilde{G}([u^{tr}](\bar{z}) + w_2, \xi_n(\bar{z})) - \tilde{G}([u^{tr}](\bar{z}), \xi_n(\bar{z}))$ , it turns out that the total energy corresponding to the opening  $w_2 = w$  concentrated in the first crack, that is, with  $[u](\bar{z}) = [u^{tr}](\bar{z}) + w$  and  $[u](z_v) = 0$ , is

$$U^\eta(u, \xi_n) = \int_I \frac{du}{dx} \left( \frac{1}{2} E \frac{du}{dx} + B \right) dx + a(\bar{z}) \tilde{G}([u^{tr}](\bar{z}) + w_2, \xi_n(\bar{z})) + B(\bar{z})([u^{tr}](\bar{z}) + w_2) - B(L)\eta,$$

and is smaller than the energy in Equation (26). This proves that the situation (iv) is the one which minimizes the energy.

In conclusion, provided that criterion in Equation (23) is used at each step to assess the feasibility of a point as location of a new crack, it can be stated that also in the present finite-step computational approach, for monotonically increasing imposed displacement, it is always energetically more convenient to open only one crack.

### 7. An explicit computation

The quasistatic evolution, defined in terms of local minimizers of the potential energy, is verified on a simple one-dimensional example whose step-by-step solution can be obtained analytically.

Consider a bar of length  $L = 10$  mm and uniform elastic modulus  $E = 1$  MPa, subject to a constant body force  $b = 0.2E/L$  and a monotonically increasing imposed displacement  $\eta(t)$ . The bar is assumed to have a fracture strength  $\bar{p}(x) = a(x)g(0) = a(x)\bar{g}$  varying along the bar with  $a(x) = 1 + 100(x/L - 1/2)^2$  and  $\bar{p}(L/2) = \bar{g} = 0.1E$ . Denoting by  $w$  the displacement discontinuity, a linear cohesive crack model is considered

$$g(w) = \begin{cases} \bar{g} \left( 1 - \frac{1}{w_{\text{crit}}} w \right), & \text{for } w \leq w_{\text{crit}}, \\ 0, & \text{for } w > w_{\text{crit}}, \end{cases}$$

where  $w_{\text{crit}} = 0.15L$  is the critical opening beyond which no traction can be transmitted across the crack. The potential  $G(w)$  is then given by

$$G(w) = \begin{cases} \bar{g}(w - \frac{1}{2w_{\text{crit}}}w^2), & \text{for } w \leq w_{\text{crit}}, \\ \bar{g}\frac{w_{\text{crit}}}{2}, & \text{for } w \geq w_{\text{crit}}. \end{cases}$$

Let  $\mathcal{A}(\eta, w)$  be the set of displacements such that  $u(0) = 0, u(L) = \eta$  and  $[u] = w$ . Assuming a holonomic process ( $\xi = 0$ ) and imposing equilibrium in the bulk, one can express the displacements along the bar in terms of the assigned end displacement  $\eta$ , the crack opening  $w$  and the crack position  $\bar{z}$ . Equivalently one can minimize  $U^\eta$  with respect to  $u \in \mathcal{A}(\eta, w)$ , thus obtaining the energy function  $\mathcal{U}(\eta, w, \bar{z})$

$$\mathcal{U}(\eta, w, \bar{z}) = \min\{U^\eta(u, 0) : u \in \mathcal{A}(\eta, w)\}. \tag{28}$$

For this simple example the solution  $u(x)$  can be explicitly computed and is given by

$$u(x) = \begin{cases} -\frac{b}{2E}x^2 + \left(\eta - w + \frac{bL^2}{2E}\right)\frac{x}{L}, & \text{for } x < \bar{z}, \\ -\frac{b}{2E}x^2 + \left(\eta - w + \frac{bL^2}{2E}\right)\frac{x}{L} + w, & \text{for } x > \bar{z}. \end{cases} \tag{29}$$

The energy function is then obtained substituting Equation (29) into Equation (8) and working out the integrals

$$\mathcal{U}(\eta, w, \bar{z}) = \frac{E(\eta - w)^2}{2L} + \frac{b(2w\bar{z} - L(\eta + w))}{2} - \frac{b^2L^3}{24E} + \left[1 + 100\left(\frac{\bar{z}}{L} - \frac{1}{2}\right)^2\right]G(w). \tag{30}$$

Note that  $\mathcal{U}(\eta, w, \bar{z})$  is differentiable with respect to  $w$  and  $\bar{z}$ . Local minimizers are found from

$$\begin{aligned} \frac{\partial \mathcal{U}}{\partial w} &= -\frac{E(\eta - w)}{L} + \frac{b(2\bar{z} - L)}{2} + \left[1 + 100\left(\frac{\bar{z}}{L} - \frac{1}{2}\right)^2\right]g(w) = 0, \\ \frac{\partial \mathcal{U}}{\partial \bar{z}} &= bw + \frac{100}{L}\left(\frac{2\bar{z}}{L} - 1\right)G(w) = 0. \end{aligned} \tag{31}$$

The second stationarity condition reflects the requirement that the crack must initiate in a position which minimizes the potential energy. At crack initiation ( $w \rightarrow 0^+$ ),  $G(w)$  behaves like  $g(0)w$  and the second condition in Equation (31) requires that

$$b + \frac{100}{L}\left(\frac{2\bar{z}}{L} - 1\right)g(0) = 0,$$

which is solved for  $\bar{z} = 0.49L$ . From the first condition in Equation (31), for  $\bar{z} = 0.49L$  and  $w = 0$ , one obtains the value  $\bar{\eta} = 0.099L$  of the imposed displacement at crack initiation.

Figure 5a shows the plot of  $\mathcal{U}$  as a function of the crack position and opening displacement for  $\eta = \bar{\eta}$  (for representation convenience values of  $\mathcal{U} > 0.2$  have been cut in this plot). It should be noted that for  $\eta = \bar{\eta}$ ,  $\bar{z} = 0.49L$  is the position of the point where the curve representing the stress along the bar is tangent to the curve representing the fracture strength  $\bar{p}(x) = \bar{g}[1 + (x - \frac{1}{2}L)^2]$ , see Figure 5b.

For  $\eta > \bar{\eta}$  the minimizers of Equation (30) give a position of the crack different from  $\bar{z} = 0.49L$ , which is not feasible for the real problem: once the material is broken at a certain position it cannot heal and

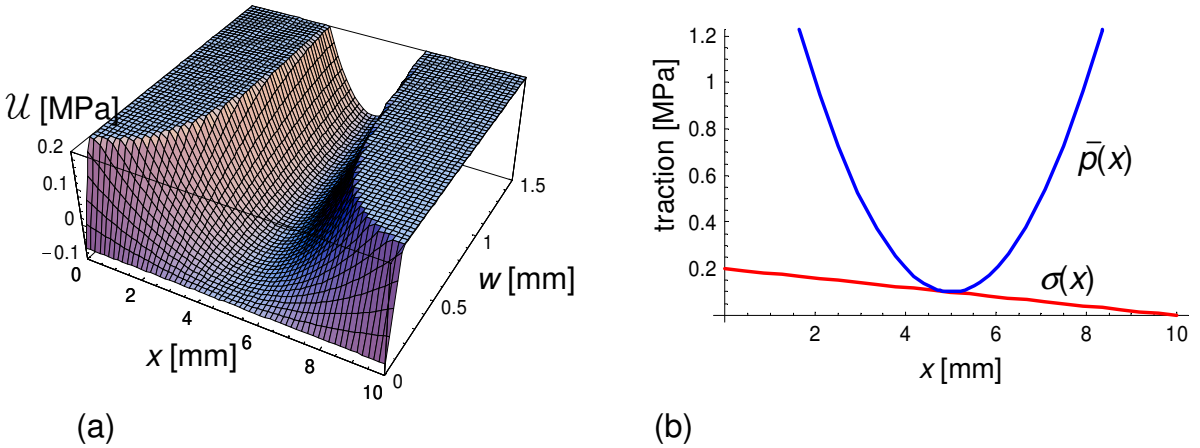


**Figure 5.** (a) Energy function for  $\eta = \bar{\eta}$ ; (b) crack position.

the crack position cannot change. In this case, the solution has to be sought solving the first condition of Equation (31) for  $\bar{z} = 0.49L$ .

The history of the assigned end displacement is shown in Figure 6a together with the corresponding computed crack opening. After initiation, the crack position is kept fixed at  $\bar{z} = 0.49L$ . The damage variable  $\xi$  is updated at the end of each step. The solution at each step is computed analytically minimizing the updated functional  $U^\eta(u, \xi_n)$  according to the step-by-step procedure outlined in Section 5. Since in each step the bar is either monotonically loaded or unloaded, the computed and exact solutions coincide. The computed history of cohesive traction is shown in Figure 6b. The values of the crack opening displacement and the explicit expressions of the energy functionals to be minimized at each step are reported in Table 1.

Contour plots of the minimized functionals are shown in Figure 7. The computed solutions are denoted by a white dot. As expected, the dots do not coincide with the absolute minimum of the functionals, since the crack position has to remain fixed.

The optimal value of the energy  $^0U$  as a function of the imposed displacement  $\eta$  is plotted in Figure 8. The curve from point 0 to point 1 represents the bulk energy, while the curve from 1 to 2 corresponds to

step	$\eta$ [mm]	functional to be minimized	$w$ [mm]
1	0.99	$U^{\eta=0.99}(u, \xi = 0) = \text{bulk energy} + a(\bar{z})G(w)$	0.00
2	1.20	$U^{\eta=1.20}(u, \xi = 0) = \text{bulk energy} + a(\bar{z})G(w)$	0.64
3	0.90	$U^{\eta=0.90}(u, \xi = 0.64) = \text{bulk energy} + a(\bar{z})\frac{g(0.64)}{2 \cdot 0.64}w^2$	0.48
4	1.30	$U^{\eta=1.30}(u, \xi = 0.64) = \text{bulk energy} + a(\bar{z})(G(w) - G(0.64) + 0.64\frac{g(0.64)}{2})$	0.95

**Table 1.** Energy functionals to be minimized at each step.



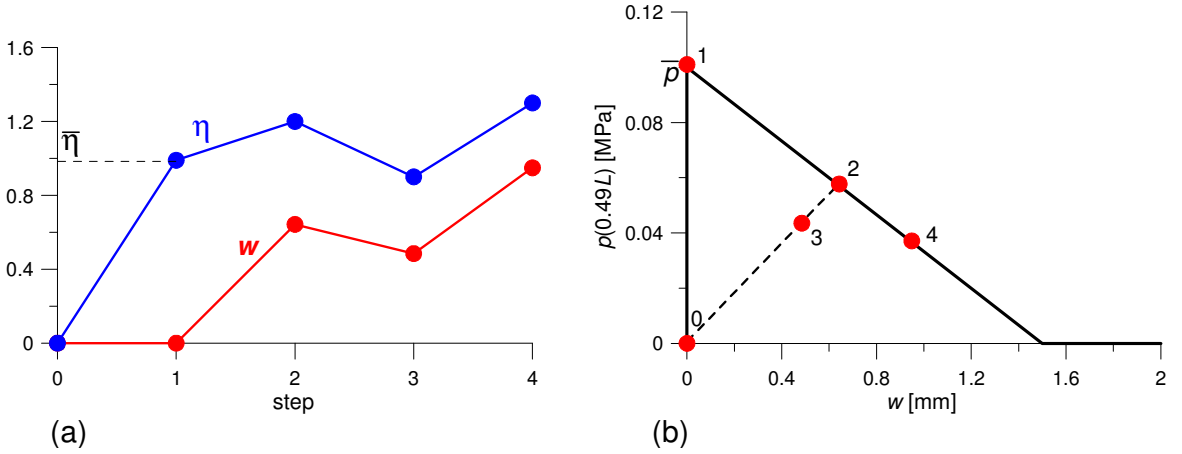


**Figure 6.** (a) History of assigned end displacement and corresponding computed crack opening; (b) history of cohesive traction across the crack.

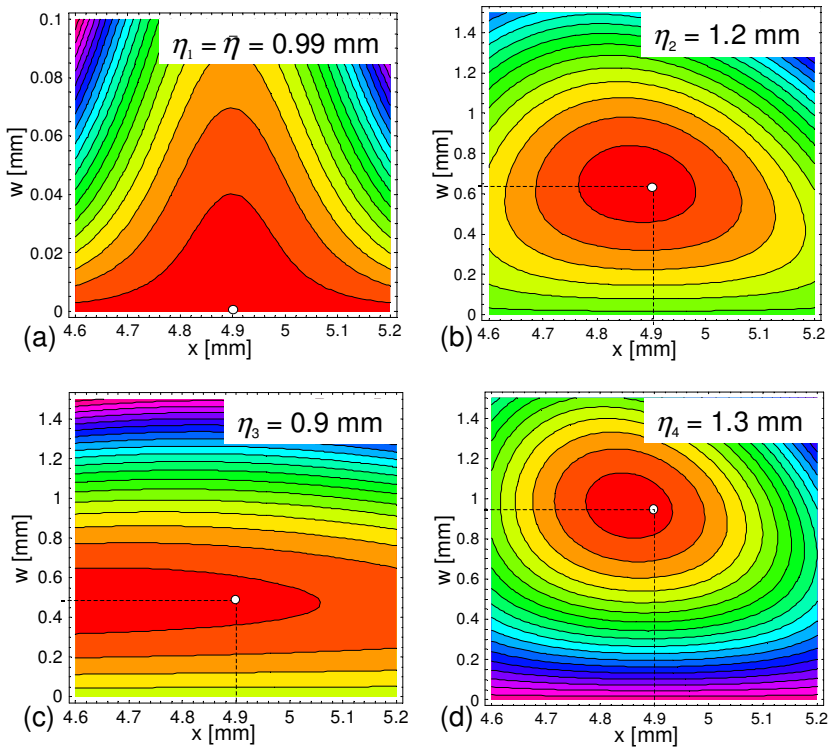


**Figure 7.** Contour plots of functionals to be minimized at each step. White dots denote computed solutions.

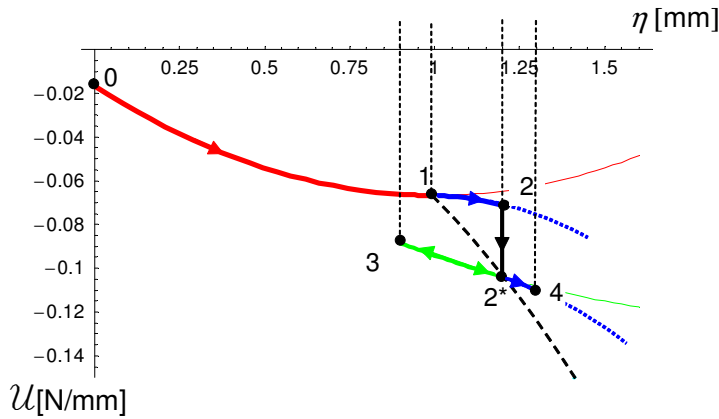


**Figure 8.** Evolution of energy  $\mathcal{U}$  as a function of imposed displacement  $\eta$ . Solid curves denote real path.

the sum of bulk and surface energies, defined only for  $\eta \geq \bar{\eta}$ . The picture shows clearly how, for  $\eta \geq \bar{\eta}$ , it becomes energetically more convenient to activate the crack at  $\bar{z}$ . When  $\eta_2 = 1.2$  mm is reached, the functional is modified updating damage and its value passes from point 2 to point 2\*. The dashed curve from 1 to 2\* represents the exact solution corresponding to continuous increase of damage  $\xi$ , as it occurs in the real process. As already pointed out, the computed and exact solution coincide at the end of the step, after damage updating. From 2\* to 3, the imposed displacement decreases (unloading) while from 3 to 4 further loading occurs.

### 8. Conclusions

The problem of a bar constrained at both ends and subject to an axial body force and an imposed displacement at one end has been studied. A linear elastic bulk material with limited strength, varying along the bar axis, has been assumed. When the axial stress exceeds the material strength at a point, a cohesive damaging crack opens producing a localized displacement jump. The possibility of a variational characterization of the solution has been investigated leading to the following results.

Assuming an ideally reversible material behavior (the material heals upon unloading and crack closure), it has been shown that the problem solution minimizes the total potential energy, which includes a bulk term (elastic energy) and a surface term (cohesive fracture energy). It has also been shown that the position of crack initiation can be obtained from a minimality condition for zero crack opening.

If the evolution problem is approximated as a sequence of finite holonomic steps, where the nondecreasing damage internal variable is updated only at the end of each step, it is shown that the finite-step solution can be obtained from the minimum conditions of a suitable functional.

The issue of the opening of multiple cracks has also been addressed. In the finite-step formulation, after crack initiation it is not possible to state that the opening of multiple cracks is not energetically convenient. However, solutions with multiple cracks appear to be a consequence of the finite-step context, and not reachable in a continuous process. An algorithmic criterion has been proposed for the exclusion of solutions which are classified as unphysical. If solutions which do not satisfy this criterion are excluded,

then it has been shown that the energy is always minimized by opening only one crack. In our opinion, this discussion may provide a useful insight also in view of possible extensions of the present computational approach to 2 or 3-dimensional problems, where, however, the appropriate underlying mathematical setting is still debated in the current literature on the subject. A simple example with a uniform axial body force has been used to illustrate the theoretical results obtained.

## References

- [Ambrosio et al. 2000] L. Ambrosio, N. Fusco, and D. Pallara, *Functions of bounded variation and free discontinuity problems*, Oxford University Press, Oxford, 2000.
- [Angelillo et al. 2003] M. Angelillo, E. Babilio, and A. Fortunato, “A computational approach to fracture of brittle solids based on energy minimization”, Preprint, Università di Salerno, 2003.
- [Askes and Sluys 2000] H. Askes and L. J. Sluys, “Remeshing strategies for adaptive ALE analysis of strain localisation”, *Eur. J. Mech. A: Solids* **19**:3 (2000), 447–467.
- [Bourdin et al. 2000] B. Bourdin, G. Francfort, and J. J. Marigo, “Numerical experiments in revisited brittle fracture”, *J. Mech. Phys. Solids* **48**:4 (2000), 797–826.
- [Braides et al. 1999] A. Braides, G. Dal Maso, and A. Garroni, “Variational formulation of softening phenomena in fracture mechanics: the one-dimensional case”, *Arch. Ration. Mech. An.* **146**:1 (1999), 23–58.
- [Chambolle 2003] A. Chambolle, “A density result in two-dimensional linearized elasticity and applications”, *Arch. Ration. Mech. An.* **167**:3 (2003), 211–233.
- [Dal Maso and Toader 2002] G. Dal Maso and R. Toader, “A model for the quasi-static growth of brittle fractures: existence and approximation results”, *Arch. Ration. Mech. An.* **162**:2 (2002), 101–135.
- [Dal Maso and Zanini 2007] G. Dal Maso and C. Zanini, “Quasistatic crack growth for a cohesive zone model with prescribed crack path”, *Proc. R. Soc. Edin. A Math.* **137** (2007), 1–27.
- [Del Piero and Truskinovsky 2001] G. Del Piero and L. Truskinovsky, “Macro- and micro-cracking in one-dimensional elasticity”, *Int. J. Solids Struct.* **38**:6-7 (2001), 1135–1148.
- [Dumstorff and Meschke 2005] P. Dumstorff and G. Meschke, “Modelling of cohesive and non-cohesive cracks via X-FEM based on global energy criteria”, pp. 565–568 in *COMPLAS VIII, VIII International Conference on Computational Plasticity*, edited by E. Oñate and D. R. J. Owen, CIMNE, Barcelona (Spain), 2005.
- [Francfort and Larsen 2003] G. A. Francfort and C. J. Larsen, “Existence and convergence for a quasi-static evolution in brittle fracture”, *Commun. Pur. Appl. Math.* **56**:10 (2003), 1465–1500.
- [Francfort and Marigo 1998] G. Francfort and J. J. Marigo, “Revisiting brittle fracture as an energy minimization problem”, *J. Mech. Phys. Solids* **46**:8 (1998), 1319–1342.
- [Mariani and Perego 2003] S. Mariani and U. Perego, “Extended finite element method for quasi-brittle fracture”, *Int. J. Numer. Methods Eng.* **58**:1 (2003), 103–126.
- [Moës and Belytschko 2002] N. Moës and T. Belytschko, “Extended finite element method for cohesive crack growth”, *Eng. Fract. Mech.* **69**:7 (2002), 813–833.
- [Moës et al. 1999] N. Moës, J. Dolbow, and T. Belytschko, “A finite element method for crack growth without remeshing”, *Int. J. Numer. Methods Eng.* **46**:1 (1999), 131–150.
- [Negri 2003] M. Negri, “A finite element approximation of the Griffith’s model in fracture mechanics”, *Numer. Math.* **95**:4 (2003), 653–687.
- [Oliver et al. 2002] J. Oliver, A. E. Huespe, M. D. G. Pulido, and E. Chaves, “From continuum mechanics to fracture mechanics: the strong discontinuity approach”, *Eng. Fract. Mech.* **69**:2 (2002), 113–136.
- [Oliver et al. 2003] J. Oliver, A. E. Huespe, and E. Samaniego, “A study on finite elements for capturing strong discontinuities”, *Int. J. Numer. Methods Eng.* **56**:14 (2003), 2135–2161.
- [Pandolfi and Ortiz 2002] A. Pandolfi and M. Ortiz, “An efficient adaptive procedure for three-dimensional fragmentation simulations”, *Eng. Comput.* **18**:2 (2002), 148–159.

- [Rodríguez-Ferran and Huerta 2000] A. Rodríguez-Ferran and A. Huerta, “Error estimation and adaptivity for nonlocal damage models”, *Int. J. Solids Struct.* **37**:48-50 (2000), 7501–7528.
- [Simo et al. 1993] J. C. Simo, J. Oliver, and F. Armero, “An analysis of strong discontinuities induced by strain softening in rate-independent inelastic solids”, *Comput. Mech.* **12**:5 (1993), 277–296.
- [Wells and Sluys 2001] G. N. Wells and L. J. Sluys, “A new method for modelling cohesive cracks using finite elements”, *Int. J. Numer. Methods Eng.* **50**:12 (2001), 2667–2682.

Received 21 Nov 2005.

CLAUDIA COMI: [claudia.comi@polimi.it](mailto:claudia.comi@polimi.it)

*Dipartimento di Ingegneria Strutturale, Politecnico di Milano, Piazza L. da Vinci 32, 20133 Milano, Italy*

STEFANO MARIANI: [stefano.mariani@polimi.it](mailto:stefano.mariani@polimi.it)

*Dipartimento di Ingegneria Strutturale, Politecnico di Milano, Piazza L. da Vinci 32, 20133 Milano, Italy*

MATTEO NEGRI: [matteo.negri@unipv.it](mailto:matteo.negri@unipv.it)

*Dipartimento di Matematica, Università degli Studi di Pavia, Via Ferrata 1, 27100 Pavia, Italy*

UMBERTO PEREGO: [umberto.perego@polimi.it](mailto:umberto.perego@polimi.it)

*Dipartimento di Ingegneria Strutturale, Politecnico di Milano, Piazza L. da Vinci 32, 20133 Milano, Italy*

## DYNAMIC BUCKLING OF IMPULSIVELY LOADED PRISMATIC CORES

ENRICO FERRI, EMILIO ANTINUCCI, MING Y. HE, JOHN W.  
HUTCHINSON, FRANK W. ZOK AND ANTHONY G. EVANS

When sandwich panels with prismatic cores are impulsively loaded, the stresses imposed by the core on the front face, as well as those transmitted through the core govern the response metrics, especially the center displacement, resistance to tearing, and loads transmitted to the supports. This article presents a basic study of the dynamic response with emphasis on the I-core. A prior assessment revealed bucklewaves induced because of inertial phenomena accompanying the rapid compression of the members. The development of these waves is an integral aspect of the dynamic response. One objective of this investigation is to ascertain the characteristics governing such waves in I-core configurations through a combined experimental and numerical study. A particular emphasis is on the influence of manufacturing imperfections in the core members on the formation and propagation of the buckles. A second goal is to examine the stresses associated with the dynamic compression of the core, again through a combined experimental and numerical investigation.

The investigation is conducted for stainless steel I-core panels supported at the back face and subjected to a constant velocity at the front. Imperfections to be included in the numerical study have been ascertained by comparing buckle patterns with those found experimentally over the relevant velocity range. The simulations reveal that the stresses induced differ on the front and back faces. On the front they are higher and velocity dependent. On the rear they are velocity invariant and scale with the relative density and material yield strength. The duration of the stress pulses, which is essentially the same on both faces, scales linearly with the core height. It correlates with the time needed for bucklewaves to propagate through the core to the back face. After the pulse terminates, the core continues to compress at a stress level about an order of magnitude smaller.

### 1. Introduction

Insights regarding the response of metallic sandwich panels to water blast have been gained by recent assessments of the fluid/structure interaction (FSI). Most crucial has been the discovery of soft and strong core responses, dependent on such factors as the dynamic strength of the core, its thickness, and the magnitude of the impulse [Liang et al. 2007]. When a soft response can be elicited through the appropriate design of the core, the performance metrics are beneficially affected. In particular, the forces transmitted to the supports, the center deflection, and the strains induced in the faces are all reduced. This happens because the time required to crush the core exceeds that needed for the plastic deformation to propagate laterally from the supports to the center of the panel. However, the soft design must assure

---

*Keywords:* dynamic buckling, impulse loads, prismatic core.

This work was supported by the ONR MURI program on blast resistant structures through a subcontract from Harvard University to the University of California, Santa Barbara (Contract No. 123163-03).

that the front face does not slap into the back. Otherwise the performance inverts and the metrics become adversely affected.

Fundamental mechanics guiding the selection of soft cores (while averting slapping) has been devised for cores that crush at constant dynamic strength (such as foams and multilayer truss configurations) [Fleck and Deshpande 2004; Tilbrook et al. 2006; Wei et al. 2007]. The situation differs for prismatic cores such as I-, X-, Y- and Z- cores because these do not exhibit constant dynamic crush strength [Radford et al. 2007]. The purpose of this article is to contribute to the understanding of the dynamic crushing of prismatic cores with the eventual goal of using this knowledge to distinguish between soft and strong responses.

Progress toward the objective of understanding the dynamics of core compression has been made by examining the response of slender columns to a velocity,  $v_0$ , abruptly imposed at one end [Abrahamson and Goodier 1966; Vaughn et al. 2005; Vaughn and Hutchinson 2006]. Short wavelength buckles have been shown to form (Figure 1) having wavelength that depends on  $v_0$  as well as the slenderness of the members. These bucklewaves influence the strains that can be induced in the members, as well as the stresses transmitted into the supporting structure. Building upon the insights provided by the bucklewave analysis, a combined experimental and numerical investigation is pursued in this article.

Since transitions between soft and strong responses can be induced in I-cores [Liang et al. 2007], this geometry provides a convenient test bed to examine the concepts. In the present study, cores are fabricated from stainless steel and tested under conditions that impose a constant velocity at one end.

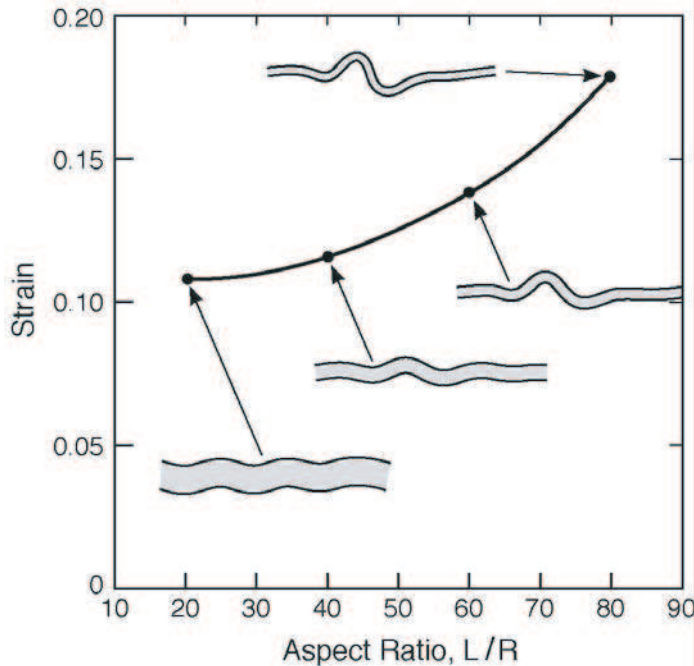


**Figure 1.** Buckle waves generated in free standing slender columns subject to a constant velocity at one end (the left). The plot indicates the terminal value of the nominal plastic strain [Vaughn and Hutchinson 2006].

Since the response is sensitive to the buckling modes, as well as to the wavelength and amplitude of imperfections, one focus of the experiments is on a classification of the preferred dynamic modes. For this purpose, a high speed camera is used to monitor the bucklewaves. Thereafter, the classification is used to select the modes relevant to realistic numerical simulations conducted using ABAQUS Explicit.

Ultimately, the stresses transmitted through the members are most relevant to the assessment of prismatic sandwich structures. These stresses are measured using a Hopkinson bar and the results used to validate the numerical simulations. Thereafter, simulations are used to provide basic understanding of the stress wave propagation and buckling phenomena, and of the magnitude and duration of the transmitted pressure pulse. The results provide the insight needed for analytic models.

To achieve the preceding objectives, this article is organized in the following manner. In [Section 2](#), the experimental methods are described. In [Section 3](#), the measurements and observations are presented. In [Section 4](#), the dynamic modes are ascertained and the sensitivity of the simulations to imperfections is established. The buckle patterns are also determined. In [Section 5](#), the dynamic stresses are characterized and related to such variables as the imposed velocity, core thickness and its relative density, as well as the strain-rate sensitivity of the material. Comparisons between measurements and simulations are presented in [Section 6](#).

## 2. Test protocol

All test specimens were fabricated from 304 stainless steel. To produce the test configurations, an array of slotted strips was assembled in a rectangular wine box configuration ([Figure 2](#)). The web dimensions were  $h = 0.25$  mm and  $H = 25$  mm, with slenderness characterized by  $H/h = 100$  and relative density  $\bar{\rho} = h/L_1 = 0.02$ . Once assembled, the core members were attached to top and bottom face sheets (each 1.5 mm thick) by placing small amounts of braze material at the intersection points (a mixture of

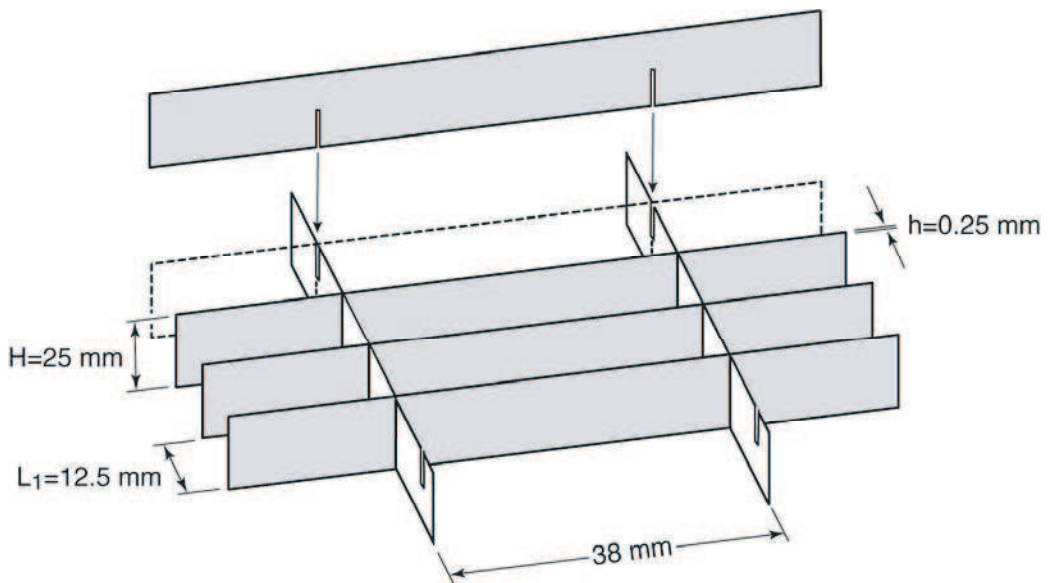


**Figure 2.** Schematic of core assembly method and pertinent dimensions.

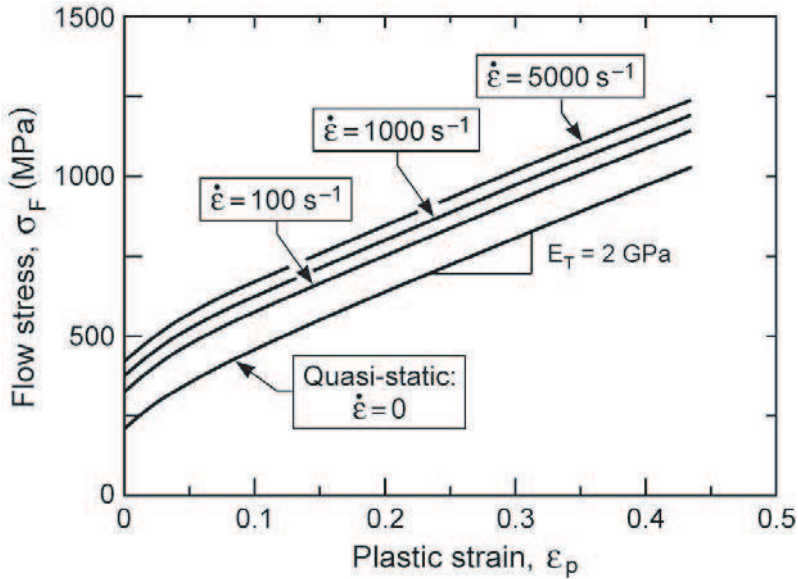


**Figure 3.** Quasistatic and dynamic flow characteristics of 304 stainless steel.

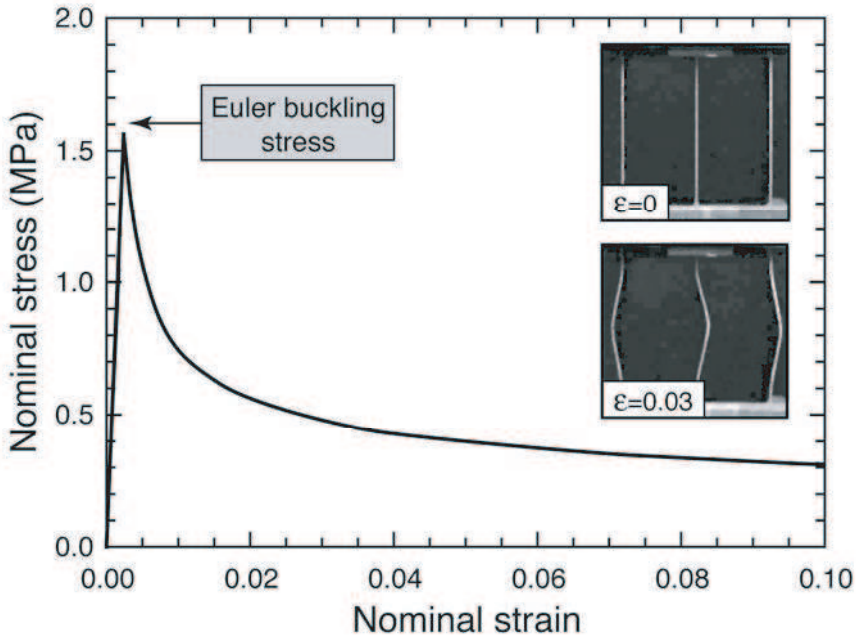


**Figure 4.** Quasistatic compressive response of I-core specimen.



Nicrobraz Cement 520 and Nicrobraz 31 braze powder, provided by Wal Colmonoy, Madison Heights, MI) and heating the assembly in vacuum for 2 hours at 1075° C. Specimens were cut from the panels using electro-discharge machining. Each was 32 mm square and contained three parallel web members, spaced 12.5 mm apart. Regions containing the transverse, widely spaced, web members were discarded (these members were used solely to provide support to the longitudinal members during assembly and brazing).

Dynamic through-thickness compression tests were performed in a gas gun using cylindrical Al 7075-T6 projectiles 45 mm in diameter and 50 mm long. The test specimens were mounted onto a 2.6 m long Hopkinson bar, instrumented with two 350 strain gauges in a half Wheatstone bridge configuration, positioned at mid-length. The event window was  $\sim 500 \mu\text{s}$ , dictated by the time required for the incident pulse to reflect off the back surface and return to the gauge location. This duration is significantly greater than that needed for core crushing under the test conditions employed. The impact velocity was measured by three pairs of laser diodes at the end of the gun barrel. It was varied between 75 and 160 m/s. For comparison, quasistatic compression tests were also performed, at a nominal strain rate of  $10^{-4} \text{ s}^{-1}$ .

Images obtained using a high speed camera (Imacon 200, DRS Technologies) were used for two purposes: (a) the sequences confirmed that the imposed velocity was constant over the relevant time period and consistent with that measured by the laser diodes, and (b) buckling patterns were recorded at periodic time intervals and subsequently used for assessment of the numerical simulations.

The quasistatic and dynamic plastic properties of the alloy were obtained from previous studies [Stout and Follansbee 1986; Xue and Hutchinson 2006; Zok et al. 2005] and are reproduced in Figure 3. The rate sensitivity of the initial yield stress is characterized by

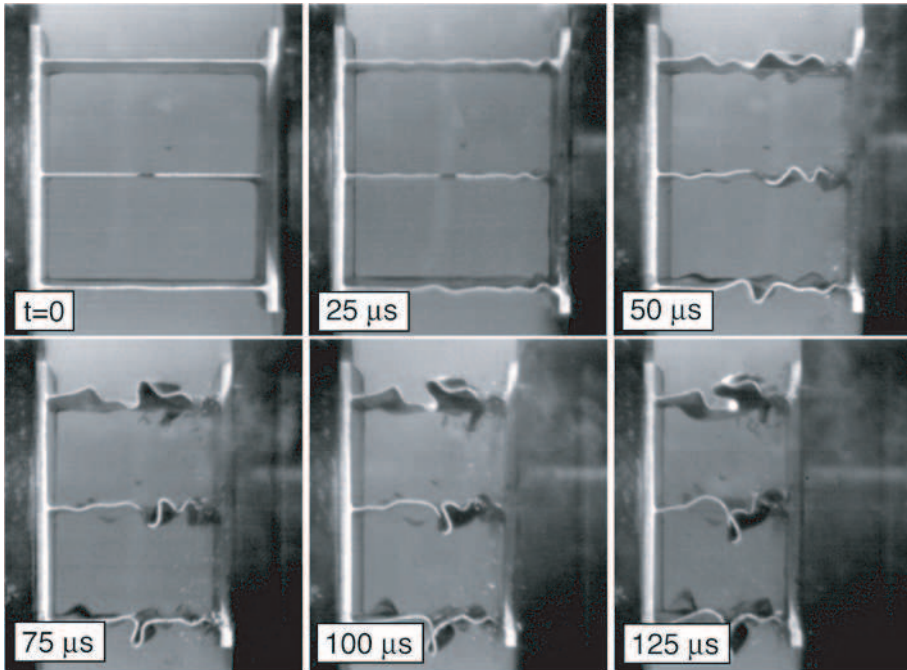
$$k \equiv \sigma_y(\dot{\epsilon}_p)/\sigma_y^o = 1 + (\dot{\epsilon}_p/\dot{\epsilon}_0)^m, \quad (1)$$

where  $\sigma_y^o$  is the quasistatic yield stress (200 MPa),  $\dot{\epsilon}_p$  is the plastic strain-rate,  $\dot{\epsilon}_0 = 4,920 \text{ s}^{-1}$  and  $m = 0.154$ . The rate-independent, quasistatic limit has  $\dot{\epsilon}_p/\dot{\epsilon}_0 \rightarrow 0$ , or, equivalently,  $k = 1$ . The hardening rate is strain rate independent. Additionally, in the domain  $\epsilon_p > 0.05$ , the hardening rate is constant, characterized by a tangent modulus  $E_T \approx 2 \text{ GPa}$ .

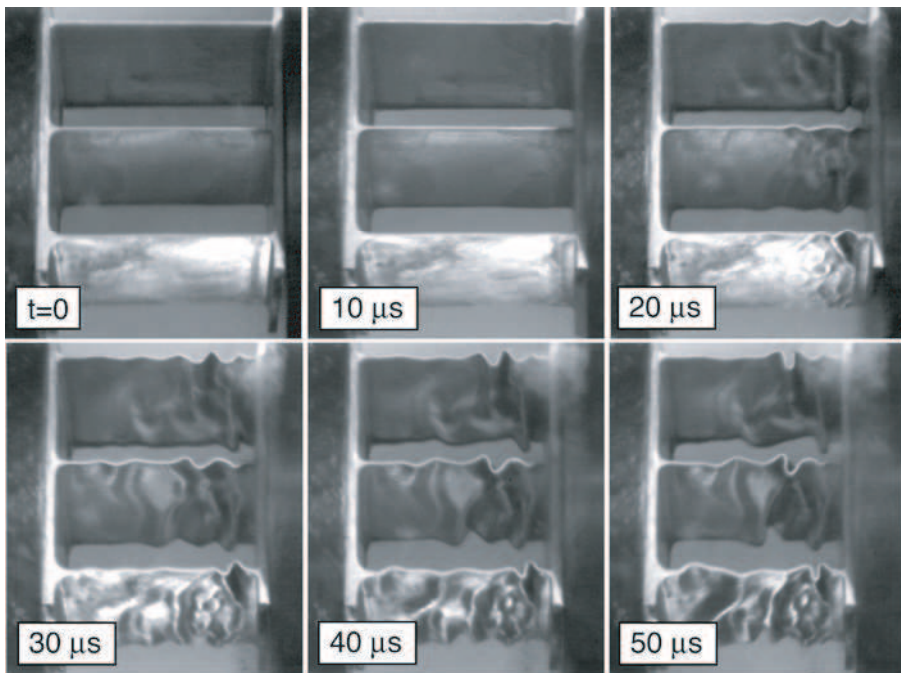
### 3. Experimental results

Results from a representative quasistatic compression test (Figure 4) reveal a stress maximum and subsequent rapid softening caused by elastic buckling. The peak value (1.5 MPa) correlates well with that predicted by the Euler buckling formula (assuming clamped ends) and well below the predicted yield stress:  $\sigma_Y \bar{\rho} \approx 4 \text{ MPa}$ . Moreover, the buckling pattern (shown in the inset) is consistent with the shape of the fundamental mode.

In contrast, the dynamic buckling response involves short wavelength buckles, typically an order of magnitude smaller. Two representative sets of images of the buckling sequence are presented in Figure 5. In one case, the specimen is viewed parallel to the plane of the web members; in the other, the viewing direction is at 20° to this plane, thereby revealing the faces. These complementary views show the progression of short wavelength buckles, initiating near the impacted face and propagating as a wave towards the opposite face. For the projectile velocity employed (95 m/s), the time required for this bucklewave to reach the back face is about 30  $\mu\text{s}$ . In the inclined orientation, the images also reveal the



(a)



(b)

**Figure 5.** Buckle wave formation in I-cores at imposed velocity  $v_0 = 95$  m/s. Specimens viewed (a) parallel to, and (b) at  $20^\circ$  to the web members. In both sequences, the projectile just makes contact with the right side of the specimen in the first frame (labeled  $t = 0$ ).

presence of transverse buckles, manifested as undulations normal to the direction of imposed velocity. This feature highlights the three-dimensional nature of the bucklewaves and motivates the subsequent numerical investigation.

Additional features of the bucklewaves are gleaned from detailed comparisons of the buckle patterns (when viewed on-edge) at various time intervals. Representative profiles for three web members for an incident velocity of 95 m/s are plotted on Figures 6a—6c. In each case, the buckle pattern at short times exhibits 4—5 peaks. As buckling proceeds, some of the buckles grow more rapidly than others, essentially consuming adjacent buckles of smaller amplitude (examples indicated by open circles). One manifestation of this process is an apparent reduction in bucklewavelength with increasing time. Eventually, at large strains, only one or two buckles survive. These features are also apparent from the crushed samples, which exhibit only one or two dominant folds in each web member. The implications are twofold. First, the bucklewavelength at prescribed velocity is not ordained, but rather evolves with time. Similar features emerge from the numerical simulations presented in the next section as well as from an analytical model for bucklewave evolution [Vaughn and Hutchinson 2006]. Second, postmortem examinations of crushed specimens provide no information on the evolution of buckle patterns, especially

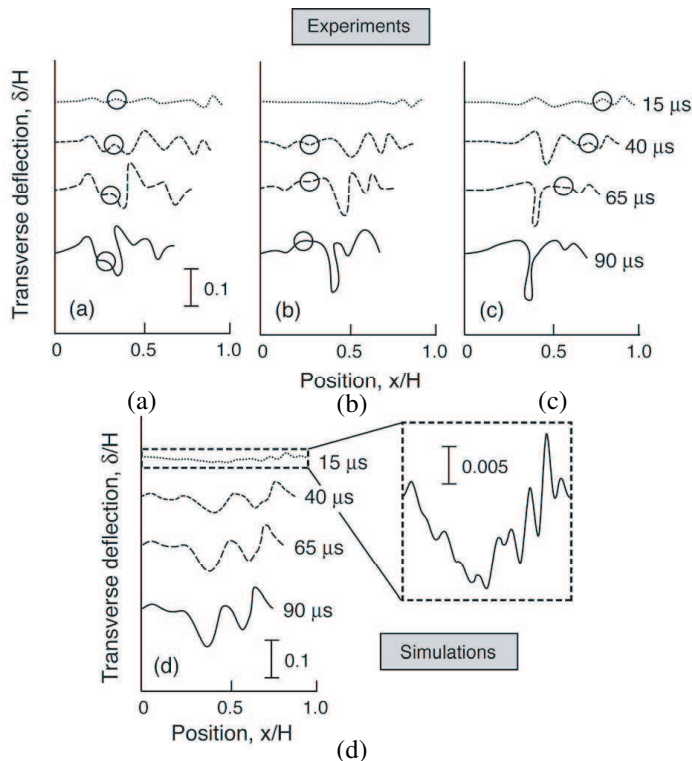
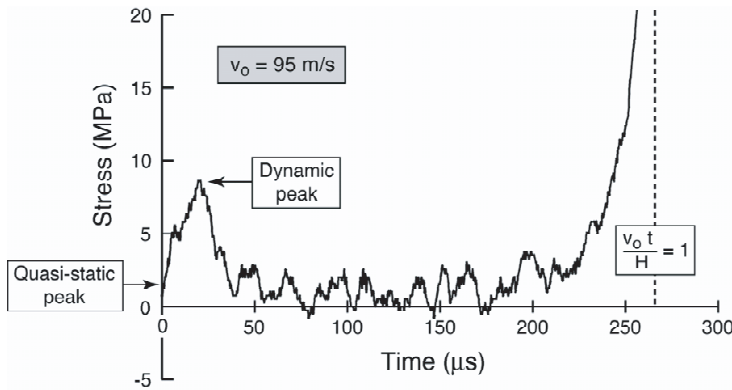


**Figure 6.** (a)–(c) Buckle patterns obtained from high speed photography at imposed velocity  $v_0 = 95$  m/s at several times after impact. The circles show examples of buckles that were well defined in the early stages but were subsequently consumed by the growth of adjacent buckles. (d) Simulations corresponding to experimental measurements. Inset shows detail of the buckle pattern at the earliest time.

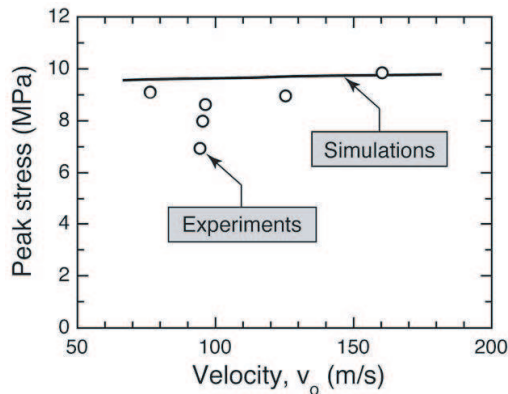
those that were present in the early stages of crushing and dominated the loading response. In situ observations are crucial in this regard.

The corresponding back face response is characterized by three stages (Figure 7a): (i) a rapid rise, peak, and decay in stress over a period of about  $30 \mu s$ , coincident with the time for bucklewave propagation; (ii) an extended irregular plateau at significantly reduced stress level, accompanying the large scale collapse of the web members; and (iii) a rapid hardening domain as the compressive strain approaches unity, characterized by  $v_0 t / H \approx 1$ . The initial peak is essentially independent of the imposed velocity (over the range 75–165 m/s), but exceeds the quasistatic stress by a factor of about 5 (Figure 7b). This elevation is attributable to both strain rate sensitivity of the plastic response and inertial stabilization of long wavelength buckles at high velocities [Vaughn et al. 2005; Vaughn and Hutchinson 2006; Wei et al. 2007]. These effects will become apparent in the ensuing numerical assessment.

#### 4. Establishing the buckling modes



(a)



(b)

**Figure 7.** Dynamic compressive response of I-core specimen.

**4.1. Geometry and boundary conditions.** The geometric variables used in the numerical investigation are depicted in Figure 8. A unit cell is defined with periodic boundary conditions. In most cases the cell is square in plan view, such that  $L_1 = L_2 = L$ , and has cross sectional shape with fixed ratio of edge length  $L$ , to core height  $H$  (specified as  $H/L = 2$ ). Most calculations use a slenderness  $H/h = 100$ , with relative density  $\bar{\rho} = h/L \equiv 2h/H = 0.02$ . In some instances, the slenderness is varied in the range  $50 \leq H/h \leq 400$  (while retaining the shape  $H/L = 2$ ).

**4.2. Finite element method.** The unit cell has been analyzed by the commercial code, ABAQUS/Explicit. Four-node shell elements (S4R) with five integration points through the thickness are used to model both the faceplates and the core members. Manufacturing imperfections are incorporated into the calculations. Periodic boundary conditions are applied, except at the front and back faces. A uniform velocity boundary condition is imposed on the front. To encompass the responses of interest, the parameter ranges have been selected in accordance with the following four considerations. First, in typical panels subject to water blast, front face velocities up to  $v_0 = 100$  m/s are induced [Fleck and Deshpande 2004; Xue and Hutchinson 2004]. Velocities from 10 to 500 m/s capture most of the realistic possibilities. Unless stated otherwise, the results are for 100 m/s. Second, the core thickness,  $H$ , is varied between the small values used for the experiments (25 mm) to the large values expected for actual panels (0.3 m). Unless stated otherwise, the thickness is taken to be  $H = 0.2$  m. Third, within the slenderness range  $50 \leq H/h \leq 400$ , the core relative density is varied over  $0.005 \leq \bar{\rho} \leq 0.04$ , thereby spanning the transition from soft to strong responses. Unless stated otherwise, the results are for  $H/h = 100$  ( $\bar{\rho} = 0.02$ ). Fourth, the responses are somewhat dependent on the strain rate sensitivity of the material. Most results include this sensitivity. In a few cases, where fundamental insights are needed, a strain rate insensitive material has been used.

In most cases, to be as close as possible to the experimental arrangement, the back face is placed on a rigid foundation. This support will cause the responses to differ from those for a free back face, such as the center of a panel subject to blast.

**4.3. Buckling modes.** Before embarking on detailed dynamic calculations, the distribution of imperfections capable of duplicating the experimentally measured buckle patterns over the complete velocity

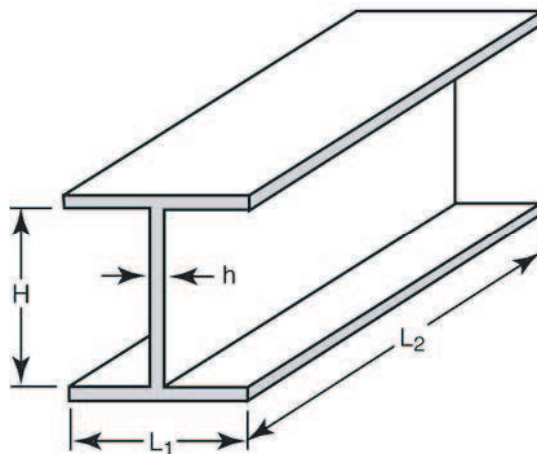


**Figure 8.** Cell model used in finite element calculations.

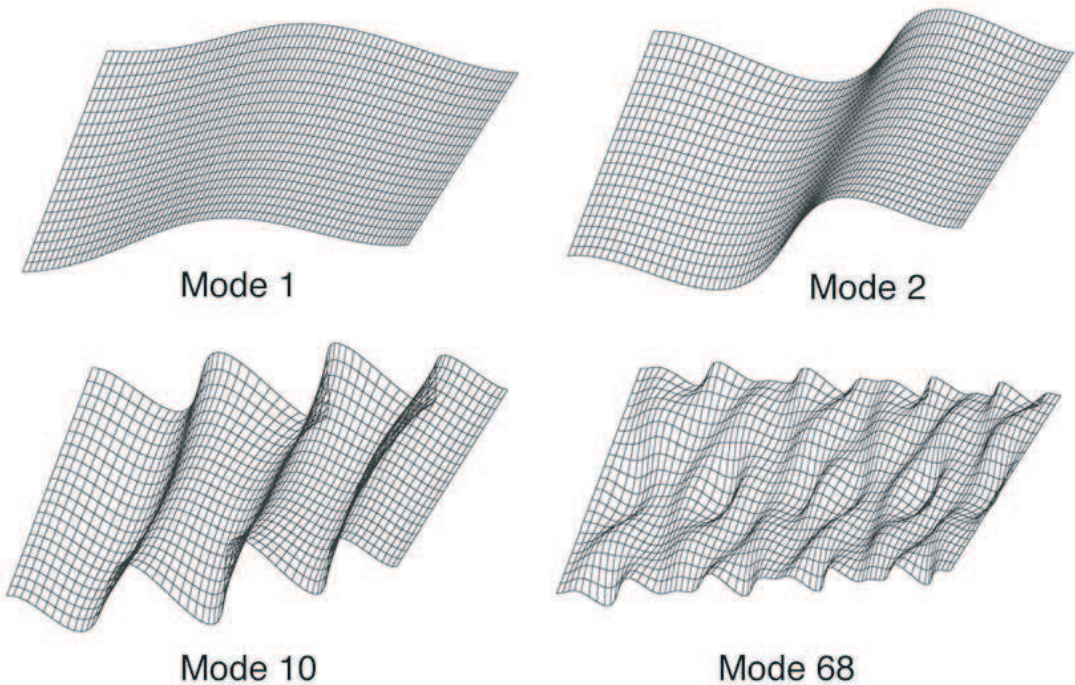


**Figure 9.** Examples of the buckle patterns calculated for four eigenmodes (1, 2, 10, 68).

range (from quasistatic to the highest velocity,  $v_0 = 500$  m/s) must be ascertained, commencing with insight gained from the experimental observations (Figures 4 and 5). The following three steps have been undertaken.

- (i) The eigen-modes have been ascertained and those having features similar to the experiments are identified. Four selected modes are summarized on Figure 8. Evidently, among these, mode 68 exhibits buckle patterns most similar to the dynamic bucklewaves, including both axial and lateral wavelengths. This combination of orthogonal wavelengths provides a sufficient number density of imperfections that the dynamic modes are reproduced with acceptable fidelity.
- (ii) Dynamic calculations of the stresses transmitted into the back face are performed using various modes, incorporating a range of imperfection amplitudes. The salient results are summarized on Figure 10. Note that all imperfections have a dramatic influence on the stress, so that calculations without imperfections are inadequate. Once imperfections are introduced, thereafter the effects are less pronounced. The perspective taken for this investigation is that, since the amplitudes of imperfections present in actual I-core panels are difficult to specify or measure, a realistic choice is made that gives acceptable agreement with the present experimental observations. Thereafter, the amplitudes are held constant. An independent, more detailed, investigation of the influence of imperfection amplitude will be reported elsewhere.
- (iii) To adequately encompass the buckling response over the full velocity range, it is not sufficient to use modes that provide buckle patterns representative of the highest velocities, because these

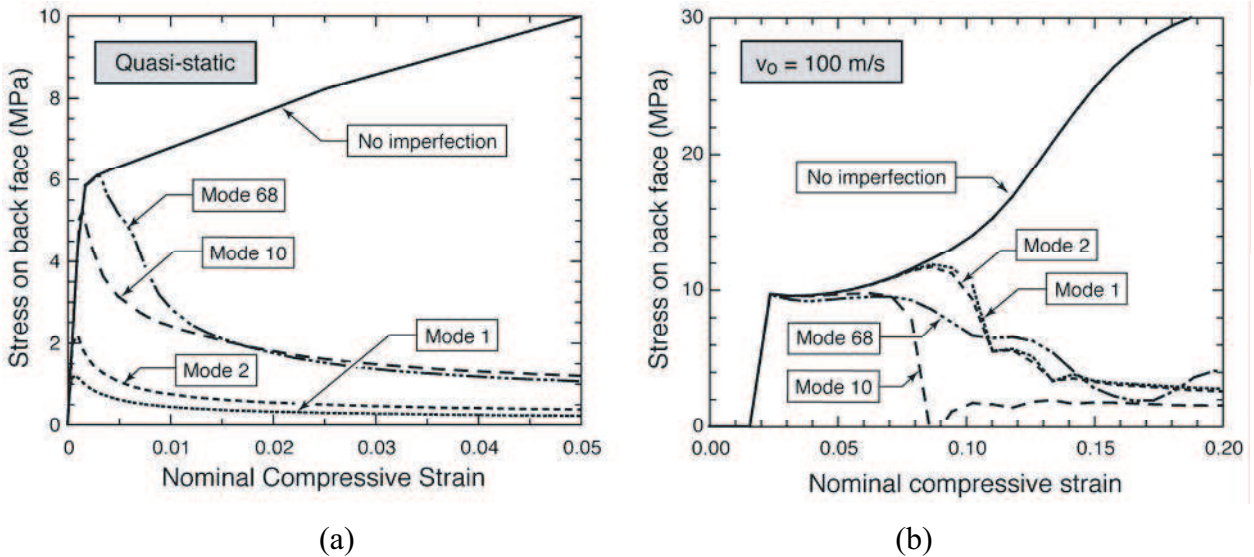


**Figure 10.** Effects of imperfection mode on (a) quasistatic and (b) dynamic response. (Imperfection amplitude  $\xi = 0.15$ ).

do not reproduce the quasistatic response, and vice versa. For instance, for quasistatic loading (Figure 10a), the mode 1 imperfection yields the lowest buckling stress (at 1.2 MPa comparable to the measurements) and a buckling mode consistent with that observed experimentally. In contrast, under dynamic conditions, to capture the buckle patterns (Figure 9) and peak stresses (Figure 10b), higher modes are required. Consequently, to embrace all possible responses, several representative modes are combined. But, before proceeding, the sensitivity of the buckling response is ascertained, both to the modes selected and the way in which they are combined. The objective is to assure that the calculations have generality and are insensitive to the specific choices. Overall, the results reveal that the most important to include are mode 1 plus one high mode (such as 68). For smooth trends with velocity, two intermediate modes (2 and 10) are also included in subsequent simulations.

To be consistent with the nature of manufacturing imperfections, the amplitude  $\delta$  corresponding to each mode is taken to be proportional to the respective longitudinal wavelength. For instance, if the amplitude for mode 1 is selected as  $\xi \equiv \delta/h = 1$ , the amplitude for mode 68 is  $\delta/h = 1/7$  (refer to the buckle pattern on Figure 9), and so on. Using this approach, the buckle wavelengths emerging from the calculations at the highest velocity are smaller than those associated with the highest eigen-mode (compare, for example, the buckle pattern at 500 m/s in Figure 11 with the mode 68 imperfection in Figure 9). Visually, these modes appear similar to those found experimentally at comparable velocity (Figures 5 and 7). The ability of ABAQUS to select the short wavelengths is attributed to the through-width variation in buckle shape associated with the highest modes (Figure 9). This variation provides an infinite number of permutations in available wavelength in any direction. These results provide some assurance that the dynamic modes selected are not excessively constrained by the initial imperfections.

In all ensuing calculations, combined imperfections are used. The stress/strain curves used as input are those applicable to 304 stainless steel, plotted on Figure 3 and described by Equation (1). In a few cases,

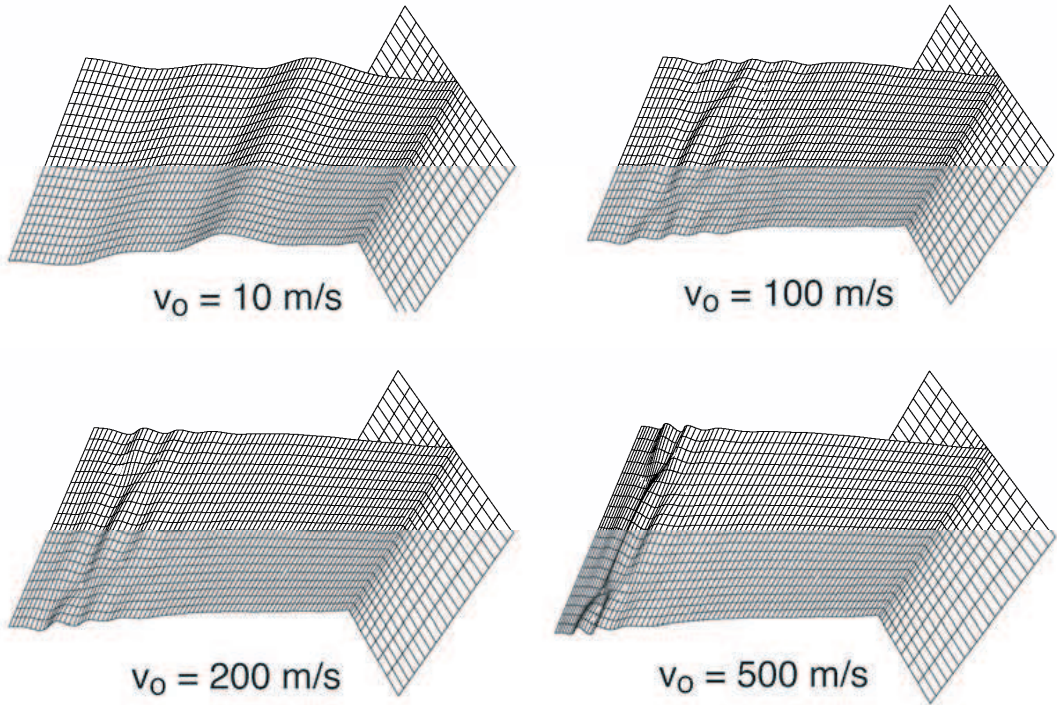


**Figure 11.** Buckle waves induced at several imposed velocities. Note that the wavelengths at the highest velocities are shorter than those of the initial imperfections (Figure 9). ( $H = 25$  mm,  $\bar{\rho} = 0.02$ ).

to gain insight, the strain rate dependence has been excluded. With a Young's modulus  $E = 200$  GPa and a mass density  $\rho = 7,800$  kg/m<sup>3</sup>, the elastic wave speed through this material is  $c_{el} = \sqrt{E/\rho} \approx 5,000$  m/s. All calculations are performed by imposing a constant velocity  $v_0$  at one end.

**4.4. Stress wave propagation.** Stress wave propagation down the core members is characterized by performing calculations without imperfections, because the members remain straight (no buckling) up to large strains (Figure 10). The plastic strain distribution at various times after the velocity is imposed is presented in Figure 12 ( $H = 25$  mm). Results determined for the rate-independent material (Figure 12a) reveal the propagation of a plastic front with velocity  $v_{pl} \approx 800$  m/s and constant strain in the wake. The response is similar to that reported for annealed Cu [Von Karman and Duwez 1950], except that the velocity and plastic strain are higher.

When the elastic wave reaches the back face, at  $t = H/c_{el} \approx 5$   $\mu$ s, a secondary plastic front with small plastic strain emerges from the back face and advances towards the incident front. Neglecting the short time associated with the transmission of the elastic wave, the time for convergence of the plastic fronts is  $t_{pl} \approx H/2v_{pl}$ . Convergence of the two waves causes a slight increase in the plastic strain in the wake of the incident front. Significant elevations in plastic strain develop only after the incident plastic front reaches the back face, at  $t = H/v_{pl} \approx 40$   $\mu$ s. Repeating the calculations with a rate-dependent material (Figure 12b) indicates that the plastic front is now much more diffuse, with a broader distribution of



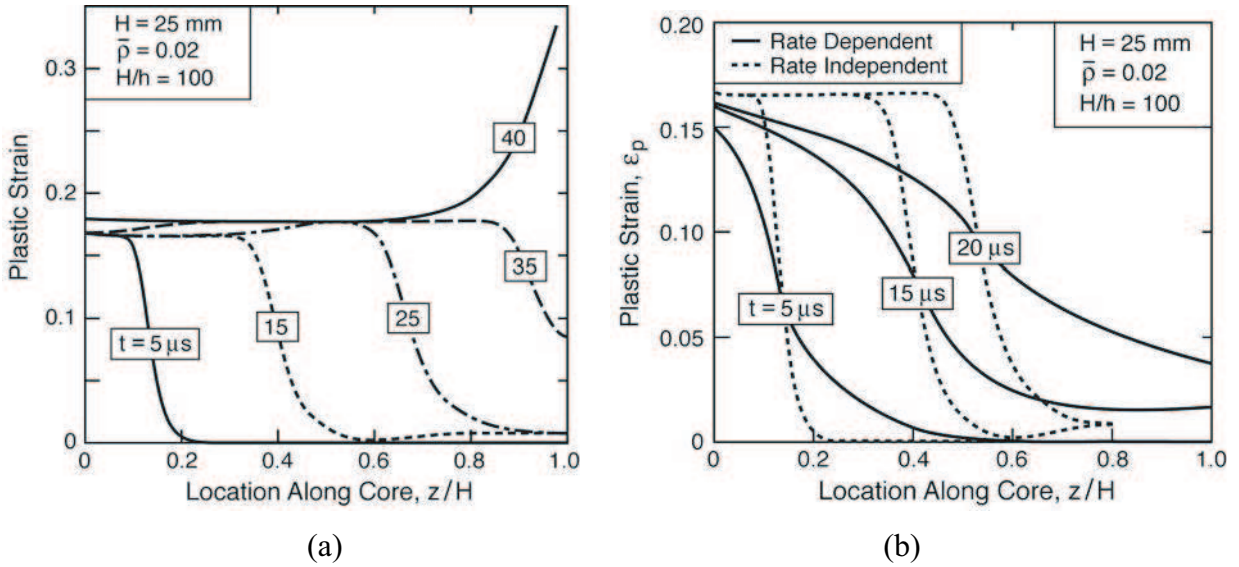


**Figure 12.** Temporal variation in plastic strain distribution calculated for a core without imperfections (to suppress buckling) subject to velocity  $v_0 = 100$  m/s. (a) Rate independent material, and (b) Comparison between rate dependent and rate independent materials.

plastic strain. Moreover, the plastic front propagates more rapidly than in the rate insensitive material. If a plastic strain of 1% is specified to define this front, its velocity is computed to be  $v_{pl} \approx 1,800$  m/s. The consequences will become apparent when the stresses are discussed below.

**4.5. Buckle wavelengths.** When imperfections are present, bucklewaves become evident in the wake of the plastic front shortly after the velocity is imposed (Figure 11). Their subsequent evolution, characterized by lateral displacement profiles, is illustrated in Figure 6d for one specific case. In the early stages ( $\leq 20 \mu s$  after the velocity is imposed), the profile exhibits about 10 peaks with an average wavelength  $L_c/h \approx 10$ . Thereafter, the number of peaks diminishes as some peaks are consumed by growth of adjacent ones. For instance, after  $100 \mu s$ , only 3 or 4 peaks remain with an average wavelength  $L_c/h \approx 20 - 30$ .

For comparison, the wavelengths predicted from a free-flight model are calculated [Vaughn and Hutchinson 2006]. The model predicts that  $L_c$  scales with the length  $L_o$  of a clamped plate at the onset of buckling when compressed quasistatically into the plastic range. Tangent-modulus theory gives  $L_o$  as:

$$\frac{L_o}{h} = \pi \sqrt{\frac{E_T}{3\sigma}} \tag{2}$$

In the present context,  $\sigma$  is taken as the dynamic stress in the plastic region prior to buckling. For a rate-independent material with bilinear stress/strain characteristics, this stress is uniform over the length

and is accurately described by the relation [Vaughn and Hutchinson 2006]:

$$\frac{\sigma}{\sigma_Y \bar{\rho}} \approx 1 + \sqrt{\frac{E_T}{E}} \left( \frac{v_0}{c_{el} \varepsilon_Y} - 1 \right). \tag{3}$$

Upon combining Equations (2) and (3), the critical length becomes:

$$\frac{L_o}{h} = \pi \left\{ \frac{3\sigma_y}{E_T} \left[ 1 + \sqrt{\frac{E_T}{E}} \left( \frac{v_o}{c_{el} \varepsilon_y} - 1 \right) \right] \right\}^{-1/2}.$$

For  $v_o = 100$  m/s, the predicted wavelength is  $L_o/h \approx 3$ . The corresponding wavelength ascertained from the numerical simulations (Figure 7d) at the same incident velocity is initially  $L_o/h \approx 10$ , increasing to 30 in the later stages of buckling. The discrepancy between the analytic and numerical results is an indication of the highly nonlinear nature of the problem and the consequent difficulties in obtaining an accurate analytic solution.

### 5. Dynamic stresses

**5.1. General observations.** Representative results for the computed stress/time response in the presence of imperfections are plotted in Figure 13. The following general features emerge:

- (i) The front face stress achieves a peak  $\sigma_{max}^f$  almost instantaneously and remains at this level for a characteristic pulse time,  $t_{pulse}$ , before dropping abruptly to a much lower steady-state plateau (Figure 13a).

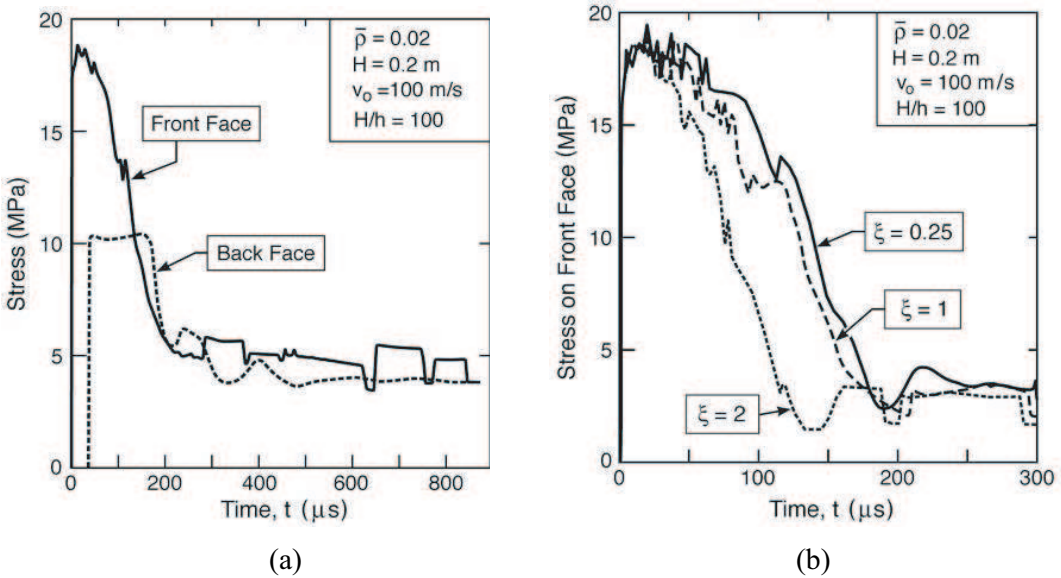


**Figure 13.** The temporal dependence of the stresses induced on the back and front face when a velocity  $v_0 = 100$  m/s is imposed at one end. (Imperfection amplitude  $\xi = 1$ ).

- (ii) The back face exhibits similar features, with two notable exceptions. First, the initial plateau stress,  $\sigma_{\max}^b$ , is achieved after a short delay, due to the time for transmission of the pressure pulse through the core, given by  $t = H/c_{el}$ . Second, this plateau is lower than the peak on the front face ( $\sigma_{\max}^b < \sigma_{\max}^f$ ). Otherwise, the pulse time  $t_{\text{pulse}}$  and the steady-state plateau stress are comparable on both faces.
- (iii) The imperfection magnitude has minimal effect on the peak stresses on both faces. However,  $t_{\text{pulse}}$  is altered, decreasing as the imperfections become large (Figure 13b).

The governing phenomena and their dependence on core characteristics, material behavior and imposed velocity are elucidated below.

**5.2. Front face stresses.** The maximum front face stress attained at short times,  $\sigma_{\max}^f$ , increases linearly with imposed velocity (Figure 14a). Comparisons of  $\sigma_{\max}^f$  with the result in (Equation (3)) for a rate-independent material affirms the fidelity of the analytic model (Figure 14b). Upon incorporating strain rate sensitivity, the stress increases, but when normalized by the appropriate  $\sigma_Y$ , at  $\dot{\epsilon} = v_0/H$ , Equation (3) retains accuracy adequate for most purposes.

**5.3. Transmitted stresses and pulse duration.** Stresses induced on the back face determined over a wide range of velocity, core thickness, and core member slenderness have the characteristics presented in Figures 15–17. Comparison with and without strain-rate sensitivity (Figure 15) reveals two differences. The rate dependence increases  $\sigma_{\max}^b$  by about a factor 2 (from 5 to 10 MPa) and decreases the pulse duration (from 30 to 20  $\mu\text{s}$ ). The former is attributed to the strain rate sensitivity while the latter is associated with the more rapid propagation of the plastic front (Figure 12b). Hereafter, to provide a common basis for comparison, the temporal coordinate is normalized by the core height  $t/H$ . In some

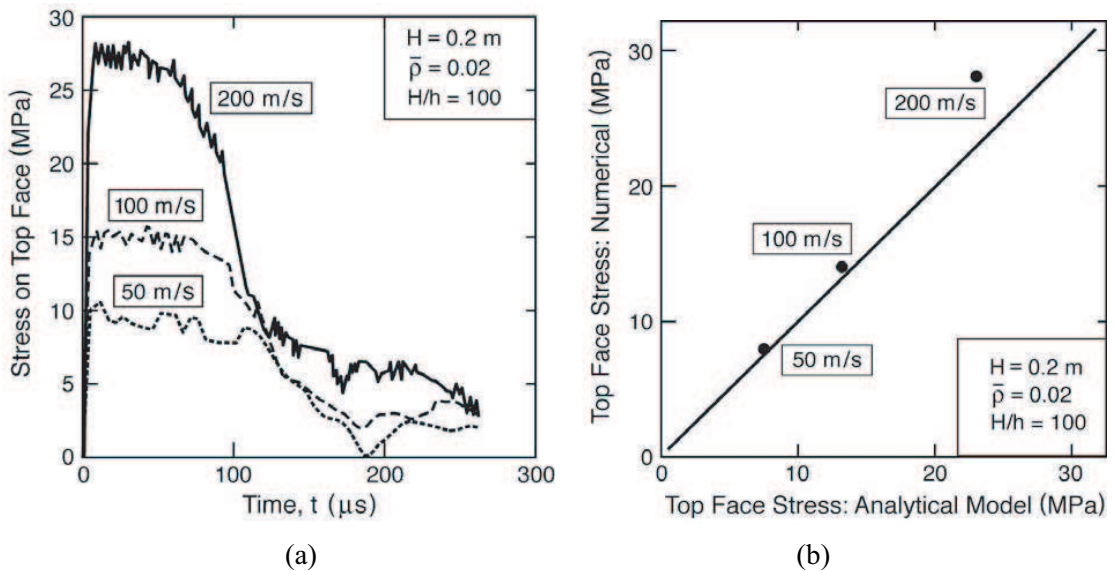


**Figure 14.** A comparison of the peak front face stress obtained from the numerical simulations with the value estimated from the analytic formula.

plots, the actual stress is used. In others, the stress is normalized:  $\sigma/\bar{\rho}\sigma_Y$ , where  $\sigma_Y$  is again the yield strength at the nominal strain rate ( $\dot{\epsilon} = v_0/H$ ). The key observations are as follows:

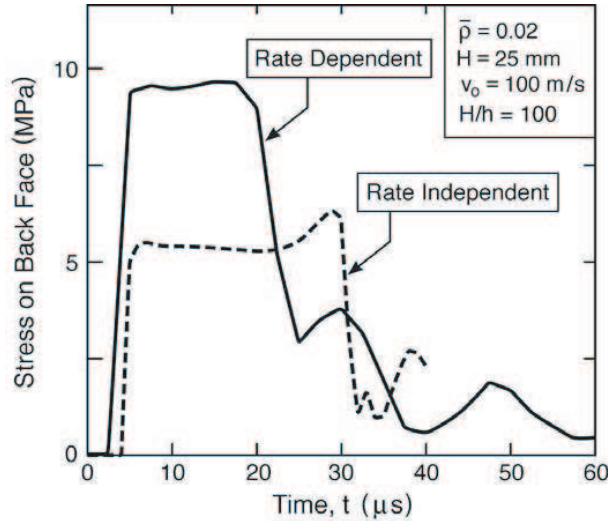


**Figure 15.** The temporal dependence of the stresses induced on the back face when a velocity  $v_0 = 100$  m/s is imposed at one end, including comparison between rate dependent and rate independent materials. Note that the former results in a higher stress but shorter pulse duration.

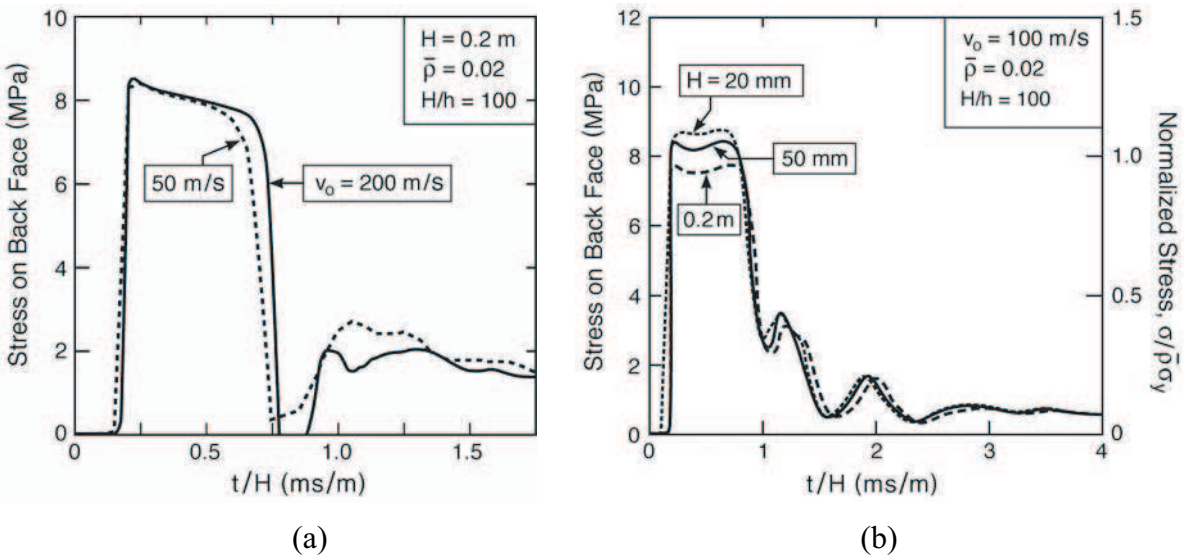


**Figure 16.** The temporal trends in the stress pulse transmitted through the core, with time coordinate normalized by the core height. (a) Effect of imposed velocity at fixed core height. (b) Effects of core height at fixed velocity.

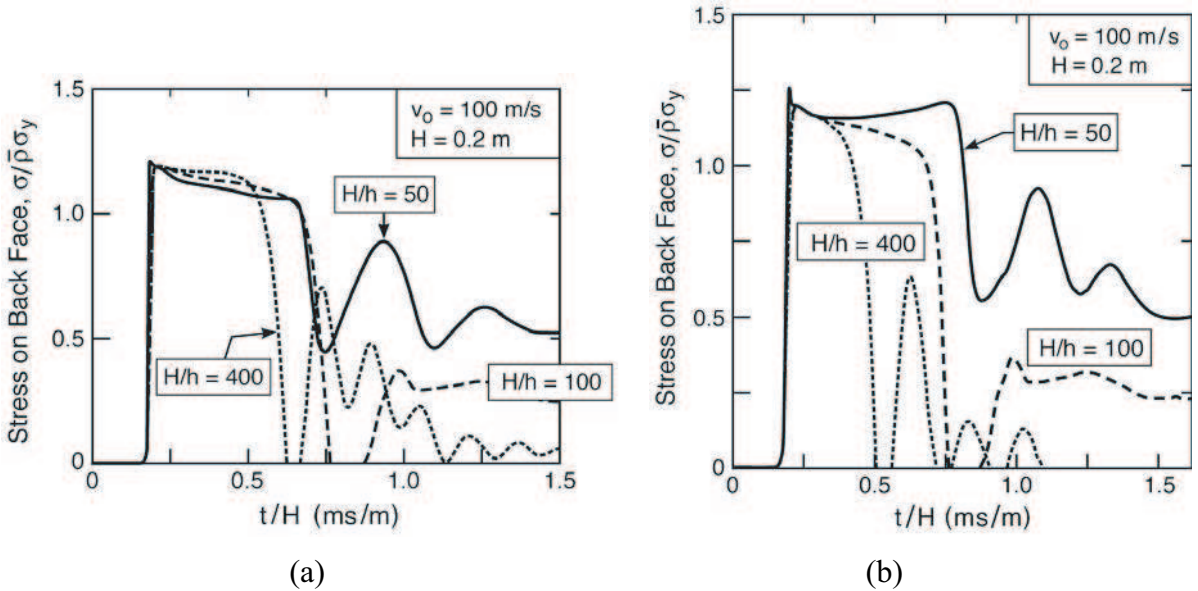


**Figure 17.** The influence of core member slenderness on the stress pulse transmitted through the core. (a) Imperfection amplitude scaled with the member thickness:  $\delta/h = 1$ . (b) Constant imperfection amplitude,  $\delta = 1$  mm.

- (i) For fixed core thickness, the plateau stress and pulse duration are independent of velocity for rate-independent materials (Figure 16a). Moreover, when rate sensitivity is included, the amplitude is larger and the duration shorter (Figure 15).
- (ii) Upon varying the core thickness at fixed velocity and slenderness (Figure 16b), the pulse durations become coincident when the time is core thickness normalized. That is,  $t_{\text{pulse}}$  scales with  $H$ . In contrast,  $\sigma_{\text{max}}^b$  is almost independent of  $H$ .
- (iii) The effects of slenderness at fixed velocity and core height depend on the scaling used for the imperfection amplitude. The issues are elucidated by two sets of simulations. One set uses amplitudes that scale linearly with member thickness,  $\delta/h = 1$  (Figure 17a), while the other uses amplitudes independent of the slenderness (Figure 17b). In all examples, the normalized peak stress,  $\sigma_{\text{max}}^b/\bar{\rho}\sigma_Y$ , is unaffected. But there are effects on the pulse duration,  $t_{\text{pulse}}/H$ . When the imperfection amplitudes are scaled,  $t_{\text{pulse}}/H$  is almost invariant with slenderness, decreasing slightly for the most slender members. However, when the amplitudes are fixed,  $t_{\text{pulse}}/H$  decreases systematically with slenderness.

**5.4. Interpretation.** That the pulse duration scales linearly with core thickness indicates a phenomenon dictated by a wave front propagating through the core. To reveal the source, contours of plastic strain are plotted in a time sequence after the imposition of the velocity (Figures 19). These reveal the propagation of a diffuse plastic front from the end exposed to the velocity, as well as the formation of an opposing front

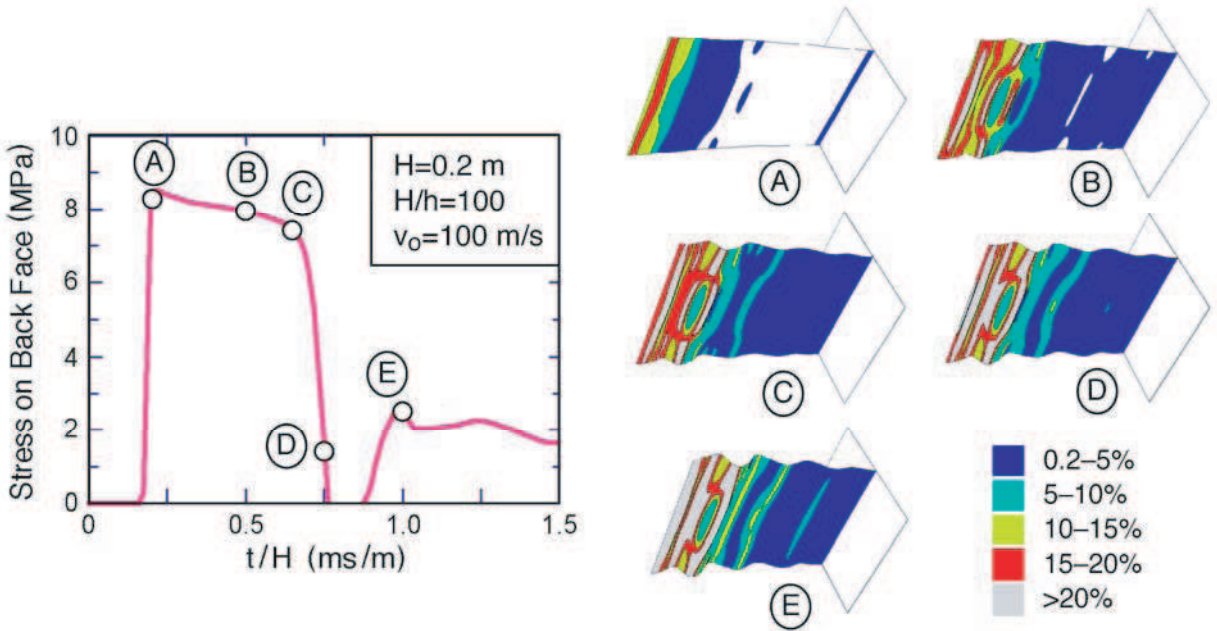


**Figure 18.** Montage of deformed core members at different times after impact. The colors refer to levels of plastic strain. (Imperfection amplitude:  $\xi = 1$ ).

after the elastic wave reflects from the back face. This is consistent with the behavior obtained for the straight (imperfection-free) core (Figure 12). The bucklewave behind the outgoing plastic front initiates in regions where the strain has exceeded about 10%. These waves propagate at velocity,  $v_{bw} \approx v_{pl}$  and reach the back face at time,  $t_{bw} = H/v_{bw}$ . Inspection of the figures indicates that the stresses remain at the plateau level on both front and back faces, even when bucklewaves are in evidence. That is, buckling near the top face does not immediately cause a reduction in the stresses. Additionally, the pulse terminates approximately at a time when the bucklewave front essentially reaches the back face, at  $t \approx t_{bw}$  (Figure 14a). The associated wave velocity is  $v_{bw} \approx 800$  m/s for the rate independent material and  $v_{bw} \approx 1,200$  m/s for the rate dependent material. These values are consistent with the velocities of the plastic front (Figure 12). They suggest an approximate scaling for pulse duration of the form

$$t_{\text{pulse}} = \lambda(\delta/h) H/v_{pl},$$

where  $\lambda(\delta/h)$  is a nondimensional parameter of order unity.

In an attempt to provide additional insight into the pulse duration, the evolution of the buckles is monitored by evaluating the spatial variations in the nominal compressive strain along a line parallel to the imposed velocity (Figure 19). The results re-affirm that the buckles become prominent (manifested in large strain undulations) while the stress on the back face is still at its plateau level (see, for example, point A in Figures 18 and 19). However, there is no apparent change in the buckling features at the moment the stress drops from the plateau, between points C and D.

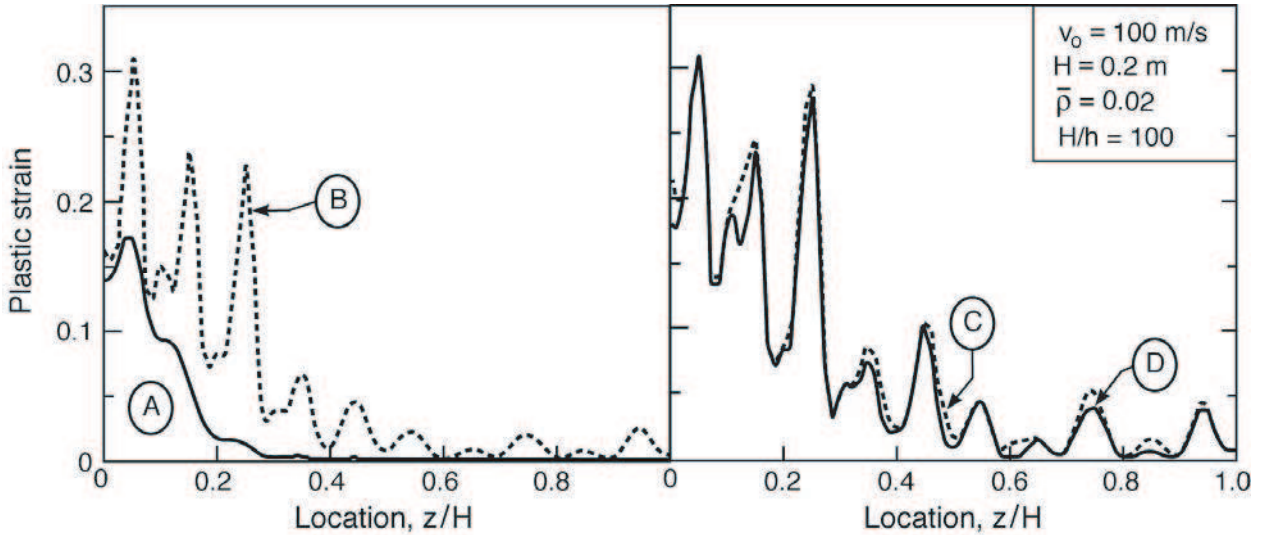


**Figure 19.** Distribution of plastic strains at various durations after the velocity is imposed. Labels correspond to points in Figure 18.

An understanding of the role of imperfection amplitude and the details of the critical event that triggers the stress drop awaits further numerical investigations. The results of these investigations will be reported elsewhere.

## 6. Comparison with measurements

An assessment of the numerical results has been made by comparison with the experimental measurements, using the actual test geometries in the simulations. The metrics for this assessment include the peak back face stress, the peak duration and the buckle patterns.

Simulated stress/time curves are presented in Figure 20. Upon comparison with the measurements (Figures 7a), both the peak stress and the pulse duration are captured well, with predicted values of  $\sigma_{\max}^b \approx 9 - 10$  MPa and  $t_{\text{pulse}} \approx 30 \mu\text{s}$ . Moreover, the simulations predict a velocity independent peak in accord with the measurements (Figure 7b). However, a discrepancy exists in the rise time of the initial peak. That is, the simulations predict that the rise should be almost instantaneous (over time  $\ll 1 \mu\text{s}$ ) whereas the measured values are typically  $10\text{--}20 \mu\text{s}$ . The difference can be attributed to nonuniform loading during the early stages of contact, caused by a small degree of projectile misalignment. For instance, a  $1^\circ$  misalignment at typical velocities would create a  $10 \mu\text{s}$  delay between the point of first contact and that at which contact is complete. Such misalignment is also expected to reduce the peak stresses. Indeed, the measured values fall slightly below the predictions (Figure 7b).

The predicted buckle patterns are compared with the measured ones in Figure 6. When viewed at the same resolution as the measurements, the initial computed profile (at  $15 \mu\text{s}$ ) exhibits about 5 peaks: comparable to the measurements. In contrast, when magnified (inset in Figure 6d), the profile exhibits about twice as many peaks. For longer times, the number of peaks diminishes, as some peaks are consumed by growth of adjacent ones. Overall, the predicted buckle evolution is deemed to be a reasonably

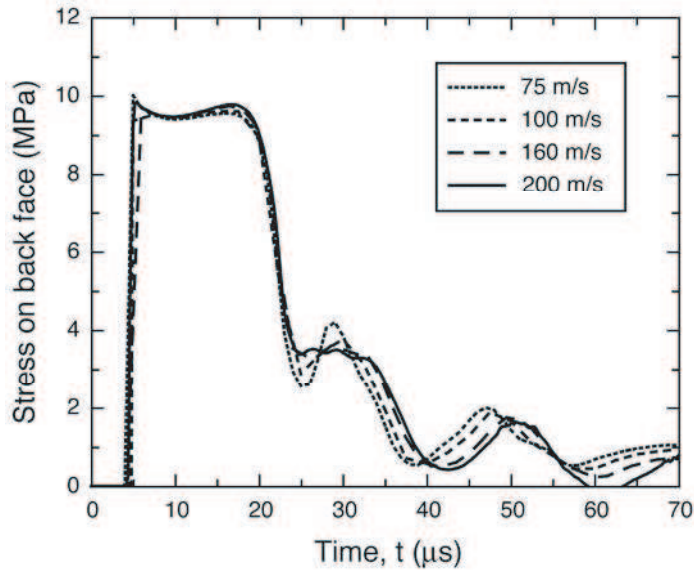


**Figure 20.** Simulated response of tested I-core specimens ( $H = 25$  mm,  $h = 0.25$  mm,  $\xi = 1$ ).

accurate representation of that observed experimentally. The inherent variations in the observed patterns (Figures 6a–c) preclude a more rigorous quantitative assessment.

## 7. Conclusions

Combined measurements and simulations have been used to characterize the response of stainless steel I-core panels supported at the back face and subjected to a constant velocity at the front. Finding a means to incorporate appropriate imperfections has been a major aspect of the assessment. The preferred method combines several prominent buckling modes and assigns imperfection amplitudes proportional to wavelengths. The procedure has been motivated and substantiated by comparing buckle patterns with those found experimentally over the relevant velocity range.

The simulations reveal that the stresses induced differ on the front and back faces. The push-back stress exerted by the core members on the front face are higher and velocity dependent. They are consistent with an analytical formula for straight (nonbuckling) columns. The stresses transmitted through the core to the back face are velocity invariant. They also scale linearly with the product of the relative density and material yield strength. The latter has been substantiated by experimental measurements.

The duration of the stress peak  $t_{\text{pulse}}$  has been assessed. This duration is essentially the same on both faces, and independent of the incident velocity. Moreover, it scales linearly with the core height  $H$ , indicative of a wave propagation phenomenon. Inspection of the numerical results indicates that the pulse terminates when the bucklewave, propagating at velocity  $v_{bw}$ , reaches the back face. Accordingly, the pulse time is related to core thickness and bucklewave velocity, such that  $t_{\text{pulse}} = H/v_{bw}$ . After the pulse terminates, the core continues to compress at a stress level about an order of magnitude smaller.



## References

- [Abrahamson and Goodier 1966] G. R. Abrahamson and J. N. Goodier, "Dynamic flexural buckling of rods within an axial plastic compression wave", *J. Appl. Mech. (Trans. ASME)* **33** (1966), 241–247.
- [Fleck and Deshpande 2004] N. A. Fleck and V. Deshpande, "The resistance of clamped sandwich beams to shock loading", *J. Appl. Mech. (Trans. ASME)* **71**:3 (2004), 386–401.
- [Liang et al. 2007] Y. Liang, A. V. Spuskanyuk, S. E. Flores, D. R. Hayhurst, J. W. Hutchinson, R. M. McMeeking, and A. G. Evans, "The response of metallic sandwich panels to water blast", *J. Appl. Mech. (Trans. ASME)* **74**:1 (2007), 81–99.
- [Radford et al. 2007] D. D. Radford, G. J. McShane, V. S. Deshpande, and N. A. Fleck, "Dynamic compressive response of stainless steel square-honeycombs", *J. Appl. Mech. (Trans. ASME)* (2007). To appear.
- [Stout and Follansbee 1986] M. G. Stout and P. S. Follansbee, "Strain rate sensitivity, strain hardening, and yield behavior of 304L stainless steel", *J. Eng. Mater. Technol. (Trans. ASME)* **108** (1986), 344–353.
- [Tilbrook et al. 2006] M. T. Tilbrook, V. S. Deshpande, and N. A. Fleck, "The impulsive response of sandwich beams: analytical and numerical investigation of regimes of behaviour", *J. Mech. Phys. Solids* **54**:11 (2006), 2242–2280.
- [Vaughn and Hutchinson 2006] D. G. Vaughn and J. W. Hutchinson, "Bucklewaves", *Eur. J. Mech. A:Solids* **25**:1 (2006), 1–12.
- [Vaughn et al. 2005] D. G. Vaughn, J. M. Canning, and J. W. Hutchinson, "Coupled plastic wave propagation and column buckling", *J. Appl. Mech. (Trans. ASME)* **72**:1 (2005), 139–146.
- [Von Karman and Duwez 1950] T. Von Karman and P. Duwez, "The propagation of plastic deformation in solids", *J. Appl. Phys.* **21**:10 (1950), 987–994.
- [Wei et al. 2007] Z. Wei, M. Y. He, and A. G. Evans, "Application of a dynamic constitutive law to multilayer metallic sandwich panels subject to impulsive loads", *J. Appl. Mech. (Trans. ASME)* (2007). To appear.
- [Xue and Hutchinson 2004] Z. Xue and J. W. Hutchinson, "A comparative study of impulse-resistant metal sandwich plates", *Int. J. Impact Eng.* **30**:10 (2004), 1283–1305.
- [Xue and Hutchinson 2006] Z. Xue and J. W. Hutchinson, "Crush dynamics of square honeycomb sandwich cores", *Int. J. Numer. Methods Eng.* **65**:13 (2006), 2221–2245.
- [Zok et al. 2005] F. W. Zok, H. Rathbun, M. He, E. Ferri, C. Mercer, R. M. McMeeking, and A. G. Evans, "Structural performance of metallic sandwich panels with square honeycomb cores", *Philos. Mag.* **85**:26-27 (2005), 3207–3234.

Received 26 Apr 2006.

ENRICO FERRI: [ef99@engineering.ucsb.edu](mailto:ef99@engineering.ucsb.edu)

Department of Mechanical Engineering, University of California, Santa Barbara, CA 93106-5050, United States

EMILIO ANTINUCCI: [emilio@engineering.ucsb.edu](mailto:emilio@engineering.ucsb.edu)

Materials Department, University of California, Santa Barbara, CA 93106-5050, United States

MING Y. HE: [ming@engineering.ucsb.edu](mailto:ming@engineering.ucsb.edu)

Materials Department, University of California, Santa Barbara, CA 93106-5050, United States

JOHN W. HUTCHINSON: [hutchinson@husm.harvard.edu](mailto:hutchinson@husm.harvard.edu)

Division of Engineering and Applied Sciences, Harvard University, Cambridge, MA 02138, United States

FRANK W. ZOK: [zok@engineering.ucsb.edu](mailto:zok@engineering.ucsb.edu)

Materials Department, University of California, Santa Barbara, CA 93106-5050, United States

ANTHONY G. EVANS: [agevans@engineering.ucsb.edu](mailto:agevans@engineering.ucsb.edu)

Materials Department, University of California, Santa Barbara, CA 93106-5050, United States

# AXIALLY SYMMETRIC CONTACT PROBLEM OF FINITE ELASTICITY AND ITS APPLICATION TO ESTIMATING RESIDUAL STRESSES BY CONE INDENTATION

HAO TIAN-HU

We discuss the axially symmetric contact problem of finite elasticity (theory of small deformation on initial stress body) and its application to estimating residual stresses by cone indentation. In particular, we determine the relation among the penetration depth, the contact radius and the residual stress.

## 1. Introduction

The residual stress problem is very important in engineering. [Suresh and Giannakopoulos \[1998\]](#) have pointed out that in the classical theory of elasticity the penetration depth, contact radius, and contact pressure are all independent of the residual stress and, thus, cannot be used to determine it. This independence can be explained as follows. In the linear theory of elasticity two independent solutions can be superposed to form a new solution according to the principle of superposition. Therefore, the cone indentation stress solution without residual stress and the residual (homogeneous) stress solution can be superposed to form a new solution. This new superposed solution is for the cone indentation stress field with residual stress and is unique due to the uniqueness of the linear theory of elasticity. It is apparent that the cone indentation stress field is independent of the residual stress in this solution. Therefore, the residual stress cannot be determined from it. In order to avoid this independence one has to deviate from the classical theory of elasticity. The theory of finite elasticity, that is, the theory of small deformations with initial stress body, is nonlinear so that two independent stress fields cannot be superposed. On the basis of it, one can deal with the residual stress. Naturally, the theory of plasticity is also nonlinear. However, according to it one can deal with the problem of unloading, that is, tension residual stress and indentation, which is difficult to discuss. Therefore, the results in this paper are only an initial effort in studying the plasticity behavior. Further developments will be discussed in another paper.

Here we address the theory of small deformation with initial stress body, which has been studied for a long time [[Southwell 1913](#); [Green and Shield 1951](#); [Ericksen 1953](#); [Bernstein and Toupin 1960](#); [Payne and Weinberger 1961](#); [Truesdell 1961](#); [Hayes and Rivlin 1961](#); [Pearson 1950](#); [Holden 1964](#); [Beatty 1971](#); [Savwers and Rivlin 1973](#); [1977](#); [1978](#); [Lurie 1990](#), Chapter 8; [1986](#); [Hwang 1989](#)]. [Lurie \[1990\]](#) and [Hwang \[1989\]](#) summarize the known results prior to 1989. On the basis of the theory of finite elasticity, that is, the theory of small deformations with initial stress body, we discuss in this paper the axially symmetric contact problem. Its application to estimating residual stresses by cone indentation

---

*Keywords:* finite elasticity, axially symmetric, residual stress, cone indentation.

Thanks to Professors B. L. Wang, Chuanzeng Zhang and Shen Ziyuan for their valuable help on English. This work has been supported by the National Natural Science Foundation of China.

is considered. Specifically, we have determined the relation among the penetration depth, the contact radius, and the residual stress.

**2. Axially symmetric deformation and strain energy function**

For the axially symmetric case let  $(x_1, x_2)$  be the position of a point before the deformation, where  $x_1 = z$ ,  $x_2 = r$ , and  $(y_1, y_2)$  after the deformation.  $\lambda_1, \lambda_2, \lambda_\theta$  denote the initial stretches due to residual stress with  $y_j = \lambda_j x_j + u_j$ , for  $j = 1, 2$ . For comparison, in the classical theory,  $y_j = x_j + u_j$ . Then,

$$F_{ij} = \frac{\partial y_i}{\partial x_j} = \lambda_i \delta_{ji} + u_{i,j}, \quad (u_\theta = 0),$$

where there is no sum over  $i$ ,  $u_{i,j} = \partial u_i / \partial x_j$  and  $|u_{i,j}| = O(\varepsilon) \ll 1$ .

Consider the components  $\lambda_\theta$  and  $F_{\theta\theta}$ . Since  $\lambda_\theta$  is the length after the initial deformation (residual stress) divided by the length before the deformation, and  $F_{\theta\theta}$  is the same ratio after the deformation, one has

$$\lambda_\theta = \frac{\lambda_2 x_2 \theta}{x_2 \theta} = \lambda_2, \quad F_{\theta\theta} = \frac{(\lambda_2 x_2 + u_2) \theta}{x_2 \theta} = \frac{\lambda_2 x_2 + u_2}{x_2} = \lambda_2 + \frac{u_2}{x_2}.$$

For the deformation tensor components  $C_{ij}$  we have

$$C_{ij} = \frac{\partial y_k}{\partial x_i} \frac{\partial y_k}{\partial x_j} = \lambda_j u_{j,i} + \lambda_i u_{i,j} + \lambda_i \lambda_j \delta_{ij} + O(\varepsilon^2),$$

no sum over  $i$  or  $j$  implied.

Expanding  $C_{ij} = C_{ij0} + \delta C_{ij} + O(\varepsilon^2)$  one has

$$C_{ij0} = \lambda_i \lambda_j \delta_{ij} \quad \text{and} \quad \delta C_{ij} = \lambda_j u_{j,i} + \lambda_i u_{i,j}.$$

For the deformation tensor component  $C_{\theta\theta}$ ,

$$\begin{aligned} C_{\theta\theta} &= C_{\theta\theta 0} + \delta C_{\theta\theta} = \lambda_2^2 + 2\lambda_2 \frac{u_2}{x_2}, \\ C_{\theta\theta 0} &= \lambda_2^2, \\ \delta C_{\theta\theta} &= 2\lambda_2 \frac{u_2}{x_2}, \\ \delta C_{\theta k} &= 0 \quad (\theta \neq k), \\ C_{kk} &= \lambda_r^2 + \lambda_1^2 + \lambda_\theta^2 + \delta C_{11} + \delta C_{22} + \delta C_{\theta\theta}, \\ C_{kk0} &= \lambda_r^2 + \lambda_1^2 + \lambda_\theta^2 = 2\lambda_r^2 + \lambda_1^2. \end{aligned}$$

According to [Lurie \[1990\]](#), the strain energy function can utilize a variety of materials, for example, the Money material, the Monahan material, the Blats–Ko material, semi-linear material, the neo-Hook material, and others. It must be pointed out that [Ranht et al. \[1978\]](#) used the neo-Hook material for the incompressible case. This result can only be considered as a preliminary attempt to deal with the plasticity behavior, which we will discuss in another paper. Here, for convenience, we use the semi-linear

material as follows:

$$W = \frac{1}{8}\lambda(C_{kk} - 3)^2 + \frac{1}{4}\mu(C_{ij} - \delta_{ij})(C_{ij} - \delta_{ij}), \quad W(\lambda_i = 1, u_j = 0) = 0,$$

where  $\lambda$  and  $\mu$  are material constants to be discussed later.

Setting  $\lambda_1 = \lambda_2 = \lambda_\theta = 1$ , one has

$$\begin{aligned} \delta C_{ij} &= \lambda_i u_{i,j} + \lambda_j u_{j,i} + O(\varepsilon^2) = u_{i,j} + u_{j,i} + O(\varepsilon^2) = 2\varepsilon_{ij}, \\ \delta C_{\theta\theta} &= 2\lambda_\theta \frac{u_r}{x_2} = 2\frac{u_r}{x_2} = 2\varepsilon_{\theta\theta}, \\ C_{ij0} &= \delta_{ij}, \\ C_{\theta\theta0} &= 1, \\ (C_{kk} - 3) &= \delta_{kk} + 2\varepsilon_{kk} - 3 = 2\varepsilon_{kk} = 2(\varepsilon_{11} + \varepsilon_{22} + \varepsilon_{\theta\theta}), \\ (C_{ij} - \delta_{ij}) &= \delta_{ij} + 2\varepsilon_{ij} - \delta_{ij} = 2\varepsilon_{ij}, \\ W &= \frac{1}{8}\lambda(C_{kk} - 3)^2 + \mu\frac{1}{4}(C_{ij} - \delta_{ij})(C_{ij} - \delta_{ij}) \\ &= \frac{1}{2}\lambda(\varepsilon_{11} + \varepsilon_{22} + \varepsilon_{\theta\theta})^2 + \mu(\varepsilon_{11}^2 + \varepsilon_{22}^2 + \varepsilon_{\theta\theta}^2 + \varepsilon_{12}\varepsilon_{12} + \varepsilon_{21}\varepsilon_{21}). \end{aligned}$$

This coincides with the classical theory. In it  $\mu$  is the shear modulus and  $\lambda = E\nu/((1 + \nu)(1 - 2\nu))$  is Lamé's constant, where  $E$  is the Young's modulus and  $\nu$  is the Poisson ratio.

### 3. Stresses and equilibrium

The Piola stress is given by

$$\sigma_{ij} = 2\frac{\partial y_i}{\partial x_k} \frac{\partial W}{\partial C_{kj}}, \quad \sigma_{\theta\theta} = 2\left(\lambda_\theta + \frac{u_r}{x_2}\right) \frac{\partial W}{\partial C_{\theta\theta}}.$$

It is not symmetric, but on the basis of moment equilibrium satisfies the identity

$$\sigma_{k2} \frac{\partial x_1}{\partial y_k} = \sigma_{k1} \frac{\partial x_2}{\partial y_k} \quad (k = 1, 2).$$

Using the Taylor series expansion  $f(a + \delta) = f(a) + f'(a)\delta + O(\delta^2)$ , one has

$$\frac{\partial W}{\partial C_{kj}} = W_{kj} + W_{kjlm}\delta C_{lm} + O(\varepsilon^2),$$

where  $W_{ij} = (\partial W/\partial C_{ij})_0$ ,  $W_{ijkl} = (\partial^2 W/\partial C_{ij}\partial C_{kl})_0$ . Here the notation  $( )_0$  means that  $W$  is a function of the initial stretches  $\lambda_i$  due to residual stress, but not a function of  $\delta C_{lm}$ .

The expansion of  $\sigma_{ij}$  is given by

$$\begin{aligned} \sigma_{ij} &= \sigma_{ij0} + \delta\sigma_{ij}, & \sigma_{ij0} &= 2\lambda_i W_{ij}, & \delta\sigma_{ij} &= 2W_{kj}u_{i,k} + 2\lambda_i W_{ijkl}\delta C_{kl}, \\ \sigma_{\theta\theta} &= \sigma_{\theta\theta0} + \delta\sigma_{\theta\theta}, & \sigma_{\theta\theta0} &= 2\lambda_\theta W_{\theta\theta}, & \delta\sigma_{\theta\theta} &= 2W_{\theta\theta}u_{2,2} + 2\lambda_\theta W_{\theta\theta kl}\delta C_{kl}. \end{aligned}$$

In order to clarify the stress components, we now turn to the coefficients  $W_{ij}$  and  $W_{ijkl}$ . Since we are interested in the axially symmetric case,  $\lambda_\theta = \lambda_2$ ,  $u_\theta = 0$ , and  $u_1, u_2$  are functions of  $x_1, x_2$ . Altogether, the coefficients are

$$W_{ij} = \left( \frac{\partial W}{\partial C_{ij}} \right)_0, \quad W_{ijkl} = \left( \frac{\partial^2 W}{\partial C_{ij} \partial C_{kl}} \right)_0,$$

$$W_{11} = \frac{1}{4}\lambda(\lambda_2^2 + \lambda_1^2 + \lambda_\theta^2 - 3) + \frac{1}{2}\mu(\lambda_1^2 - 1),$$

$$W_{22} = W_{\theta\theta} = \frac{1}{4}\lambda(\lambda_2^2 + \lambda_1^2 + \lambda_\theta^2 - 3) + \frac{1}{2}\mu(\lambda_2^2 - 1),$$

$$W_{12} = W_{21} = W_{1\theta} = W_{\theta 1} = W_{2\theta} = W_{\theta 2} = 0,$$

$$W_{1111} = W_{2222} = W_{\theta\theta\theta\theta} = \frac{1}{4}\lambda + \frac{1}{2}\mu, \quad W_{2211} = W_{\theta\theta 11} = W_{22\theta\theta} = \frac{1}{4}\lambda,$$

$$W_{1212} = W_{2121} = W_{1\theta 1\theta} = W_{\theta 1\theta 1} = W_{2\theta 2\theta} = W_{\theta 2\theta 2} = \frac{1}{2}\mu.$$

Since the surface of the half plane is free of traction before the press of the cone, the stress component  $\sigma_{110}$  must be zero. Therefore, one has

$$\sigma_{110} = 2\lambda_1 W_{11} = \frac{1}{2}\lambda_1(\lambda(2\lambda_2^2 + \lambda_1^2 - 3) + 2\mu(\lambda_1^2 - 1)) = 0.$$

Setting  $W_{11} = 0$  and solving for  $\lambda_1$  we get

$$\lambda_1^2 = 1 - 2\lambda \left( \frac{\lambda_2^2 - 1}{\lambda + 2\mu} \right). \tag{1}$$

Similarly, one can obtain the relation between  $\lambda_2$  and the residual stress  $\sigma_R = \sigma_{220}$ :

$$\sigma_R = \sigma_{220} = \lambda_2\mu(\lambda_2^2 - 1) \left( \frac{3\lambda + 2\mu}{\lambda + 2\mu} \right) \quad \text{or} \quad \lambda_2^3 - \lambda_2 = \sigma_{220} \left( \frac{\lambda + 2\mu}{3\lambda\mu + 2\mu^2} \right). \tag{2}$$

The homogeneous residual stress  $\sigma_R$  leads to residual stresses  $\sigma_x = \sigma_y = \sigma_R$  when the  $xy$  plane is parallel to the surface.

Let us now look at the stress components  $\sigma_{ij}, \sigma_{\theta\theta}$ . Using  $\lambda_2 = \lambda_\theta$ ,  $u_\theta = 0$  and the fact that  $u_1, u_2$  are functions of  $x_1, x_2$ , one obtains

$$\begin{aligned} \sigma_{\theta\theta} = \lambda_2\mu(\lambda_2^2 - 1) & \left( \frac{3\lambda + 2\mu}{\lambda + 2\mu} \right) + 2\frac{u_2}{x_2} \left( \frac{\lambda}{4}(\lambda_2^2 + \lambda_1^2 + \lambda_\theta^2 - 3) + \frac{\mu}{2}(\lambda_\theta^2 - 1) \right) \\ & + 2\lambda_\theta \left( \left( \frac{\lambda}{2} + \mu \right) \lambda_\theta \frac{u_2}{x_2} + \frac{\lambda}{4}(2\lambda_2 u_{2,2} + 2\lambda_1 u_{1,1}) \right), \end{aligned}$$

$$\sigma_{\theta\theta 0} = \lambda_2\mu(\lambda_2^2 - 1) \left( \frac{3\lambda + 2\mu}{\lambda + 2\mu} \right),$$

$$\begin{aligned}
 \delta\sigma_{\theta\theta} &= \left(\frac{\lambda}{2}(2\lambda_2^2 + \lambda_1^2 - 3) + \mu(\lambda_2^2 - 1) + \lambda_2^2(\lambda + 2\mu)\right)\frac{u_2}{x_2} + \lambda_2\lambda(\lambda_2 u_{2,2} + \lambda_1 u_{1,1}); \\
 \sigma_{22} &= \lambda_2\left(\frac{\lambda}{2}(2\lambda_2^2 + \lambda_1^2 - 3) + \mu(\lambda_2^2 - 1)\right) + u_{2,2}\left(\frac{\lambda}{2}(2\lambda_2^2 + \lambda_1^2 - 3) + \mu(\lambda_2^2 - 1)\right) \\
 &\quad + \lambda_2\left((\lambda + 2\mu)\lambda_2 u_{2,2} + \lambda\left(\lambda_1 u_{1,1} + \lambda_2\frac{u_2}{x_2}\right)\right), \\
 \sigma_{220} &= \lambda_2\left(\frac{\lambda}{2}(2\lambda_2^2 + \lambda_1^2 - 3) + \mu(\lambda_2^2 - 1)\right), \\
 \delta\sigma_{22} &= \left(\frac{\lambda}{2}(2\lambda_2^2 + \lambda_1^2 - 3) + \mu(\lambda_2^2 - 1) + \lambda_2^2(\lambda + 2\mu)\right)u_{2,2} + \lambda\lambda_2\left(\lambda_1 u_{1,1} + \lambda_2\frac{u_2}{x_2}\right), \\
 \sigma_{11} &= \left(\frac{\lambda}{2}(2\lambda_2^2 + \lambda_1^2 - 3) + \mu(\lambda_1^2 - 1) + \lambda_1^2(\lambda + 2\mu)\right)u_{1,1} + \lambda\lambda_1\left(\lambda_2 u_{2,2} + \lambda_2\frac{u_2}{x_2}\right), \\
 \sigma_{110} &= 0, \\
 \delta\sigma_{11} &= \left(\frac{\lambda}{2}(2\lambda_2^2 + \lambda_1^2 - 3) + \mu(\lambda_1^2 - 1) + \lambda_1^2(\lambda + 2\mu)\right)u_{1,1} + \lambda\lambda_1\lambda_2\left(u_{2,2} + \frac{u_2}{x_2}\right); \\
 \sigma_{21} &= 2\lambda_2 W_{21} + 2u_{2,1} W_{zz} + 2\lambda_2 W_{2121} \delta C_{21} = \lambda_2 \mu (\lambda_2 u_{2,1} + \lambda_1 u_{1,2}), \\
 \sigma_{210} &= 0, \quad \delta\sigma_{21} = \lambda_2 \mu (\lambda_2 u_{2,1} + \lambda_1 u_{1,2}); \\
 \sigma_{12} &= 2u_{1,2} W_{22} + \left(\frac{\lambda_1}{\lambda_2}\right)\sigma_{21}, \quad \sigma_{120} = 0, \quad \delta\sigma_{12} = 2u_{1,2} W_{22} + \left(\frac{\lambda_1}{\lambda_2}\right)\delta\sigma_{21}. \tag{3}
 \end{aligned}$$

We also have the equilibrium equations

$$\frac{\partial\sigma_{22}}{\partial x_2} + \frac{\partial\sigma_{21}}{\partial x_1} + \frac{\sigma_{22} - \sigma_{\theta\theta}}{x_2} = 0 \quad \text{and} \quad \frac{\partial\sigma_{12}}{\partial x_2} + \frac{\partial\sigma_{11}}{\partial x_1} + \frac{\sigma_{12}}{x_2} = 0 \quad \text{for } \sigma_{12} \neq \sigma_{21}.$$

Using the equalities  $\sigma_{220} = \sigma_{\theta\theta 0}$  and  $\sigma_{120} = \sigma_{210} = 0$ , and the fact that the components  $\sigma_{ij0}$  are not functions of  $x_1$  and  $x_2$ , we have

$$\frac{\partial\delta\sigma_{22}}{\partial x_2} + \frac{\partial\delta\sigma_{21}}{\partial x_1} + \frac{\delta\sigma_{22} - \delta\sigma_{\theta\theta}}{x_2} = 0 \quad \text{and} \quad \frac{\partial\delta\sigma_{12}}{\partial x_2} + \frac{\partial\delta\sigma_{11}}{\partial x_1} + \frac{\delta\sigma_{12}}{x_2} = 0 \quad \text{for } \delta\sigma_{12} \neq \delta\sigma_{21}.$$

Substituting the expressions for  $\sigma_{\theta\theta 0}$ ,  $\sigma_{220}$  and  $\sigma_{21}$  into the first equilibrium equation, we obtain

$$A\nabla^2 u_2 - (A - \lambda_2^2 \mu)u_{2,11} + (\lambda + \mu)\lambda_2 \lambda_1 u_{1,12} - A\left(\frac{u_2}{x_2}\right) = 0, \tag{4}$$

where  $A = (2\lambda + 3\mu)(\lambda_2^2 - 1) + \frac{\lambda}{2}(\lambda_1^2 - 1) + \lambda + 2\mu$  and  $\nabla^2 f = f_{,22} + f_{,2}/x_2 + f_{,11}$ . Introduce the function  $\Phi$  such that

$$u_2 = -C\Phi_{21} \quad \text{and} \quad u_1 = A\nabla^2\Phi - B\Phi_{11}, \tag{5}$$

where  $B = A - \lambda_2^2 \mu$  and  $C = (\lambda + \mu)\lambda_2 \lambda_1$ . Then (4) is satisfied automatically.

Using the equalities

$$\begin{aligned} \delta\sigma_{12} &= 2u_{1,2}W_{22} + (\lambda_1/\lambda_2)\delta\sigma_{21}, \\ \delta\sigma_{21} &= \lambda_2\mu(\lambda_2u_{2,1} + \lambda_1u_{1,2}), \\ \delta\sigma_{11} &= (2W_{11} + \lambda_1^2(\lambda + 2\mu))u_{1,1} + \lambda_z\lambda(\lambda_2u_{2,2} + \lambda_2u_{2}/x_2), \end{aligned}$$

the second equilibrium equation becomes

$$D\nabla^2u_1 + C\left(u_{2,12} + \frac{u_{2,1}^2}{x_2}\right) + (2W_{11} - 2W_{22} + (\lambda + \mu)\lambda_1^2)u_{1,11} = 0, \tag{6}$$

where  $D = (\lambda + 2\mu)(\lambda_1^2 - 1)/2 + (\lambda + \mu)(\lambda_2^2 - 1) + \mu$ .

We can rewrite the above equation substituting (5) into (6) and considering Equations (4)–(6) with the result

$$DA\nabla^4\Phi - DB\nabla^2\Phi_{11} - C^2\nabla^2\Phi_{11} + C^2\Phi_{1111} + EA\nabla^2\Phi_{11} - EB\Phi_{1111} = 0, \tag{7}$$

where  $E = 2W_{11} - 2W_{22} + (\lambda + \mu)\lambda_1^2$ .

Using the Hankel transform of zeroth order, one obtains

$$DA\xi^4G(\xi, x_1) + (DB - EA - 2DA + C^2)\xi^2G(\xi, x_1)_{11} + (-EB + DA - DB + EA)G(\xi, x_1)_{1111} = 0,$$

where  $G(\xi, x_1) = \int_0^\infty x_2J_0(\xi x_2)\Phi dx_2$  and  $J_0(\xi x_2)$  is the zeroth order Bessel function. The subscript notation used here means  $G_{11} = d^2G/dx_1^2$ .

Letting  $G(\xi, x_1) = F(\xi)e^{H(\xi)x_1}$  we can rewrite this as a quadratic equation in  $H^2/\xi^2$ :

$$p_1 + \frac{p_2H^2}{\xi^2} + \frac{p_3H^4}{\xi^4} = 0, \tag{8}$$

where  $p_1 = DA$ ,  $p_2 = (DB - EA - 2DA + C^2)$ , and  $p_3 = (-EB + DA - DB + EA)$ .

For the classical case  $\lambda_j = 1$ , the characteristic equation becomes

$$\frac{H^4}{\xi^4} - \frac{2H^2}{\xi^2} + 1 = 0. \tag{9}$$

When the determinant  $\Delta = p_2^2 - 4p_1p_3$  of (8) vanishes, the equation has two equal positive roots. One can consider that  $\lambda_j = 1 + \delta_j$ ,  $\Delta \rightarrow 0$  but  $\Delta < 0$  or  $\Delta > 0$  and the equation has two complex roots ( $\Delta < 0$ ) or two positive real roots ( $\Delta > 0$ ). Now one only deals with the case with two different real positive roots  $r_1^2$  and  $r_2^2$ , where  $r_1 > 0$  and  $r_2 > 0$ . The other cases will be discussed in detail in Section A1, page 1376. In the limit  $x_1 \rightarrow \infty$ ,  $G \rightarrow 0$ , we have

$$G(\xi, x_1) = N_1(\xi)e^{-r_1\xi x_1} + N_2(\xi)e^{-r_2\xi x_1}. \tag{10}$$

In what follows we write  $N_1(\xi)$  and  $N_2(\xi)$  simply as  $N_1$  and  $N_2$ , respectively.

Now we turn our attention to the stress component  $\delta\sigma_{21}$ . Using Equations (27) and (30) from the Appendix as well as (10), one has

$$\delta\sigma_{21} = \lambda_2\mu P \int_0^\infty \xi^4(N_1(r_1^2 + w)e^{-r_1\xi x_1} + N_2(r_2^2 + w)e^{-r_2\xi x_1})J_1(\xi x_2) d\xi, \tag{11}$$

where

$$P = \lambda_2 C + \lambda_1 B - \lambda_1 A \quad \text{and} \quad w = \lambda_1 A / (\lambda_2 C + \lambda_1 B - \lambda_1 A).$$

With  $x_1 = 0$  and  $\delta\sigma_{21} = 0$ , the above equation simplifies to

$$\delta\sigma_{21} = \lambda_2 \mu P \int_0^\infty \xi^4 (N_1(r_1^2 + w) + N_2(r_2^2 + w)) J_1(\xi x_2) d\xi = 0, \tag{12}$$

which gives

$$N_2 = - \left( \frac{r_1^2 + w}{r_2^2 + w} \right) N_1. \tag{13}$$

Substituting (13) into (10), we get

$$G(\xi, x_1) = N_1 (e^{-r_1 \xi x_1} - Q e^{-r_2 \xi x_1}), \tag{14}$$

where

$$Q = \frac{r_1^2 + \lambda_1(A/P)}{r_2^2 + \lambda_1(A/P)}.$$

Let us now discuss the stress component  $\delta\sigma_{11}$  and displacement component  $u_1$ . Substituting (14) into (10), one obtains

$$\delta\sigma_{11} = R(A\nabla^2\Phi_1 - B\Phi_{111}) - C\lambda\lambda_2\lambda_1(\nabla^2\Phi_1 - \Phi_{111}), \tag{15}$$

where

$$R = \frac{1}{2}\lambda(2\lambda_2^2 + \lambda_1^2 - 3) + \mu(\lambda_1^2 - 1) + \lambda_1^2(\lambda + 2\mu) = 2W_{11} + \lambda_1^2(\lambda + 2\mu).$$

The zeroth order Hankel transform of (15) is

$$\int_0^\infty x_2 J_0(\xi x_2) \delta\sigma_{11} dx_2 = (RA - RB)G_{111} + (C\lambda\lambda_2\lambda_1 - RA)\xi^2 G_1. \tag{16}$$

Similarly, the zeroth order Hankel transform of  $u_1$  in (9) is

$$\int_0^\infty x_2 J_0(\xi x_2) u_1 dx_2 = (A - B)G_{11} - A\xi^2 G. \tag{17}$$

Setting  $x_1 = 0$  and using Equations (14), (16) and (17), one has

$$\delta\sigma_{11} = (-(RA - RB)(r_1^3 - Qr_2^3) - (C\lambda\lambda_2\lambda_1 - RA)(r_1 - Qr_2)) \int_0^\infty \xi^4 J_0(\xi x_2) N_1 d\xi,$$

$$u_1 = ((A - B)(r_1^2 - Qr_2^2) - A(1 - Q)) \int_0^\infty \xi^3 J_0(\xi x_2) N_1 d\xi.$$

The boundary conditions are

$$\begin{aligned} ((A - B)(r_1^2 - Qr_2^2) - A(1 - Q)) \int_0^\infty \xi^3 J_0(\xi x_2) N_1 d\xi &= [u_1(x_2)]_{x_1=0}, & x_2 \leq a, \\ \int_0^\infty \xi^4 J_0(\xi x_2) N_1 d\xi &= 0, & x_2 > a, \end{aligned}$$

where  $a$  is the radius of contact area, which will be discussed in detail later.



Setting  $\xi a = p, x_2 = a\rho, p^3 N_1 = f(p)$ , and

$$a^4 [u_1(x_2)]_{x_1=0} = ((A - B)(r_1^2 - Qr_2^2) - A(1 - Q))g(\rho),$$

one has

$$\begin{aligned} \int_0^\infty f(p) J_0(p\rho) dp &= g(\rho), & 0 \leq \rho \leq 1, \\ \int_0^\infty f(p) p J_0(p\rho) dp &= 0, & \rho > 1. \end{aligned} \tag{18}$$

Let  $g(\rho) = \sum_{n=0}^\infty A_n \rho^n (0 \leq \rho \leq 1)$ . Then from [Sneddon 1951] the solution of (18) is

$$f(p) = \frac{1}{\sqrt{\pi}} \sum_{n=0}^\infty A_n \left( \cos p + p \int_0^1 u^{n+1} \sin(pu) du \right) \frac{\Gamma(1 + n/2)}{\Gamma(3/2 + n/2)}, \tag{19}$$

where  $\Gamma$  is the gamma function (recall that  $\Gamma(1) = 1$  and  $\Gamma(3/2) = \sqrt{\pi}/2$ ).

We can write

$$[u_1(\rho)]_{x_1=0} = b + a \cot \alpha (1 - \rho)$$

for  $0 \leq \rho \leq 1$  and  $g(\rho) = A_0 + A_1 \rho$ , where  $\alpha$  is the angle of the circular cone (the angle between the asymmetric axis  $Ox_1(Oz)$  and the mother line of the surface of the circular cone). Then, one has

$$a^4 [u_1(x_2)]_{x_1=0} = ((A - B)(r_1^2 - Qr_2^2) - A(1 - Q))(A_0 + A_1 \rho),$$

where

$$A_0 = \frac{(b + a \cot \alpha) a^4}{(A - B)(r_1^2 - Qr_2^2) - A(1 - Q)}, \quad A_1 = \frac{-a^5 \cot \alpha}{(A - B)(r_1^2 - Qr_2^2) - A(1 - Q)}.$$

Considering that  $A_n = 0$  for  $n \geq 2$ , from Equation (19), we get

$$f(p) = 2 \left( \frac{A_0}{\pi} + \frac{A_1}{2} \right) \frac{\sin p}{p} + A_1 \frac{(\cos p - 1)}{p^2},$$

$$\begin{aligned} \delta\sigma_{11} &= -(RA - RB)(r_1^3 - Qr_2^3) - (C\lambda\lambda_2\lambda_1 - RA)(r_1 - Qr_2) \\ &\quad \times \left( \left( \frac{2A_0}{\pi} + A_1 \right) a^{-5} \int_0^\infty J_0(p\rho) \sin p dp + A_1 a^{-5} \int_0^\infty J_0(p\rho) \frac{(\cos p - 1)}{p} dp \right). \end{aligned}$$

Since the integral  $\int_0^\infty J_0(p) \sin p dp$  is divergent, to make sure the stress component  $\delta\sigma_{11}$  is finite at the edge of the punch we require  $(2A_0/\pi + A_1) = 0$ , which means  $b = a \cot \alpha (\pi/2 - 1)$  and

$$[u(z, x_2)]_{x_1=0, x_2=0} = \frac{\pi}{2} a \cot \alpha, \quad f(p) = A_1 \frac{\cos p - 1}{p^2}. \tag{20}$$

Noting that

$$\int_0^\infty J_0(p\rho) \frac{\cos p - 1}{p} dp = -\cosh^{-1}(1/\rho),$$

we get

$$\delta\sigma_{11} = ((RA - RB)(r_1^3 - Qr_2^3) + (C\lambda\lambda_2\lambda_1 - RA)(r_1 - Qr_2))\frac{A_1}{a^5} \cosh^{-1}(1/\rho). \tag{21}$$

We prove in the Appendix (see (59)) that the compressive force  $T$  is given by

$$T = a^2 \frac{\pi(RA - RB)(p_1 + w(-p_2 + \sqrt{p_1 p_3})) - \pi(C\lambda\lambda_2\lambda_1 - RA)(\sqrt{p_1 p_3} - wp_3)}{((A - B)w + A)(-p_2 p_3 + 2p_1^{1/2} p_3^{3/2})^{1/2}}, \tag{22}$$

where the  $p_j$  are the coefficients in the characteristic equation (8).

The contact radius  $a$  is therefore

$$a = \left( \frac{T \tan \alpha ((A - B)w + A)(-p_2 p_3 + 2p_1^{1/2} p_3^{3/2})^{1/2}}{\pi(RA - RB)p_1 + \pi(RA - RB)w(-p_2 + \sqrt{p_1 p_3}) - \pi(C\lambda\lambda_2\lambda_1 - RA)(\sqrt{p_1 p_3} - wp_3)} \right)^{1/2}. \tag{23}$$

By (20), the penetration depth  $[u_1(x_1, x_2)]_{x_1=x_2=0}$  equals  $(\pi/2)a \cot \alpha$ , that is,

$$u_1(x_1, x_2)|_{x_1=x_2=0} = \frac{\pi}{2} \left( \frac{T \cot \alpha ((A - B)w + A)(-p_2 p_3 + 2p_1^{1/2} p_3^{3/2})^{1/2}}{\pi(RA - RB)p_1 + \pi(RA - RB)w(-p_2 + \sqrt{p_1 p_3}) - \pi(C\lambda\lambda_2\lambda_1 - RA)(\sqrt{p_1 p_3} - wp_3)} \right)^{1/2}. \tag{24}$$

Using Equations (1) and (2), we can solve for  $\lambda_1$  and  $\lambda_2$  given the constants  $\mu$ ,  $\lambda$  and the residual stress  $\sigma_{22,0}$ . We can then find the values of coefficients  $A, B, C, D, E, p_1, p_2, p_3, P, w, Q, R$  using Equations (4)–(8), (11), (14) and (15). We can find the contact radius  $a$  and penetration depth  $[u(x_1, x_2)]_{x_1=0, x_2=0}$  with the help of (23) and (24).

We have obtained the relation between the residual stress, the contact radius and the penetration depth. As a result, we can determine the residual stress from the contact radius or the penetration depth.

We now look at a numerical example. The result for  $\lambda = 30\text{--}50$  GPa,  $\mu = 60\text{--}80$  GPa,  $T = 0.23$  kg and  $\alpha = \pi/12$  according to (23), is plotted in Figure 1.

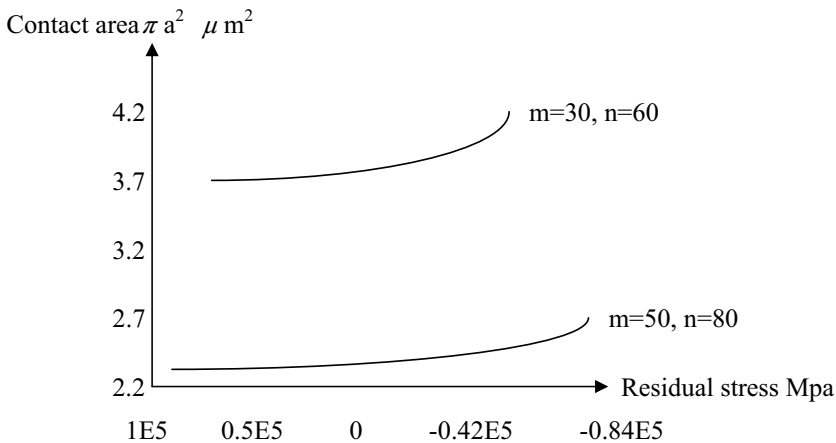


**Figure 1.** Relation between the area and residual stress:  $\lambda = m$  GPa and  $\mu = n$  GPa. The Poisson ratio is  $\nu = m/(2n + 2m)$  and Young’s modulus is  $E = (2n + 3m)\mu/(n + m)$ .

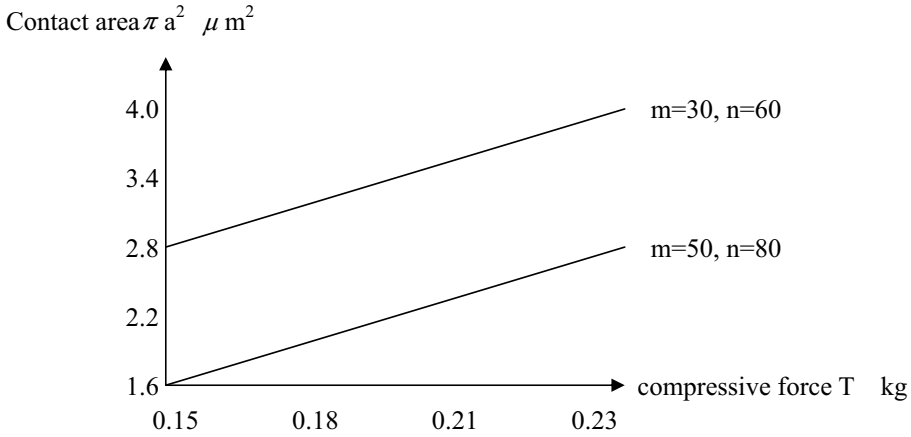


**Figure 2.** Relation between contact area and compressive force for zero residual stress:  $\lambda = m$  GPa,  $\mu = n$  GPa,  $\nu = m/(2n + 2m)$ ,  $E = (2n + 3m)\mu/(n + m)$ .

We see that a body under tensile residual stress behaves like a string under tension. That leads to a decrease of the contact area so that it is smaller than without the stress. However, for compressive residual stress the opposite effect is obtained. These results coincide with those obtained in [Hao 1986].

To check the numerical results, consider the case of zero residual stress. For  $\lambda = 30\text{--}50$  GPa,  $\mu = 60\text{--}80$  GPa, and  $\alpha = \pi/12$  the relation between the contact area and the compressive force  $T$  for zero residual stress is given in Figure 2. We see that it agrees with the numerical results in Figure 1.

#### 4. Concluding remarks

We have studied the axially symmetric contact problem in the framework of the theory of finite elasticity, that is, the theory of small deformation on initial stress body. We have also considered its application to estimating residual stresses by cone indentation. In particular, we have been able to determine the relation among the penetration depth, the contact radius and the residual stress. Further study must focus on the more general method to solve the residual stress problems and consider the plasticity behavior.

#### Appendix

**A1. The complex root case.** We consider the complex root case, where

$$\begin{aligned}
 H^2 &= \xi^2(r \pm is) = \xi^2 \eta e^{\pm i\vartheta}, & &= \pm \xi \eta^{1/2} (\cos \vartheta/2 \pm i \sin \vartheta/2) - \pi \leq \vartheta \leq \pi \quad \text{with } \cos \vartheta/2 > 0, \\
 G(\xi, x_1) &= K(\xi) e^{\xi \eta^{1/2} (\cos \vartheta/2 + i \sin \vartheta/2) x_1} + L(\xi) e^{\xi \eta^{1/2} (\cos \vartheta/2 - i \sin \vartheta/2) x_1} \\
 &\quad + M(\xi) e^{-\xi \eta^{1/2} (\cos \vartheta/2 + i \sin \vartheta/2) x_1} + N(\xi) e^{-\xi \eta^{1/2} (\cos \vartheta/2 - i \sin \vartheta/2) x_1}.
 \end{aligned}$$

The case  $x_1 \geq 0$  is considered, where  $x_1 \rightarrow \infty$  and  $u, \sigma_{ij} \rightarrow 0$ :

$$G(\xi, x_1) = M e^{-\xi \eta^{1/2} (\cos \vartheta/2 + i \sin \vartheta/2) x_1} + N e^{-\xi \eta^{1/2} (\cos \vartheta/2 - i \sin \vartheta/2) x_1}. \tag{25}$$

For convenience,  $M(\xi)$  and  $N(\xi)$  are replaced by  $M$  and  $N$  but they are functions of  $\xi$ .

It is apparent that  $G(\xi, x_1)$  is real; therefore,

$$G(\xi, x_1) = Me^{-\xi dx_1} + \bar{M}e^{-\xi \bar{d}x_1}, \tag{26}$$

where  $d = \eta^{1/2}(\cos \vartheta/2 + i \sin \vartheta/2)$  and  $\bar{d} = \eta^{1/2}(\cos \vartheta/2 - i \sin \vartheta/2)$ .

Next we deal with the stress component  $\delta\sigma_{21}$ :

$$\begin{aligned} \sigma_{21} &= \lambda_2\mu(\lambda_2u_{r,1} + \lambda_1u_{1,2}) = \lambda_2\mu(-\lambda_2C\Phi_{211} + \lambda_1(A\nabla^2\Phi - B\Phi_{11})_2) \\ &= \lambda_2\mu(-(\lambda_2C + \lambda_1B)\Phi_{211} + \lambda_1(A\nabla^2\Phi)_2) \end{aligned} \tag{27}$$

From Equation (54) in the Appendix, one knows that

$$\begin{aligned} &-(\lambda_2C + \lambda_zB)\lambda_2\mu \int_0^\infty x_2J_1(\xi x_2) d\Phi_{11} + \lambda_1A\lambda_2\mu \int_0^\infty x_2J_1(\xi x_2) d\nabla^2\Phi \\ &= (\lambda_2C + \lambda_zB)\lambda_2\mu\xi \int_0^\infty \Phi_{11}x_2J_0(\xi x_2) dx_2 - \lambda_1A\lambda_2\mu\xi \int_0^\infty \nabla^2\Phi x_2J_0(\xi x_2) dx_2. \end{aligned} \tag{28}$$

Hence

$$\begin{aligned} \int_0^\infty x_2J_1(\xi x_2)\delta\sigma_{21}dx_2 &= \lambda_2\mu \int_0^\infty x_2J_1(\xi x_2)(-\lambda_2C + \lambda_zB)\Phi_{211} + \lambda_1(A\nabla^2\Phi)_2) dx_2 \\ &= -(\lambda_2C + \lambda_zB)\lambda_2\mu \int_0^\infty x_2J_1(\xi x_2)\Phi_{211}dx_2 + \lambda_1A\lambda_2\mu \int_0^\infty x_2J_1(\xi x_2)(\nabla^2\Phi)_2 dx_2 \\ &= -(\lambda_2C + \lambda_zB)\lambda_2\mu \int_0^\infty x_2J_1(\xi x_2) d\Phi_{11} + \lambda_1A\lambda_2\mu \int_0^\infty x_2J_1(\xi x_2) d\nabla^2\Phi \\ &= (\lambda_2C + \lambda_zB)\lambda_2\mu\xi \int_0^\infty \Phi_{11}x_2J_0(\xi x_2) dx_2 - \lambda_1A\lambda_2\mu\xi \int_0^\infty \nabla^2\Phi x_2J_0(\xi x_2) dx_2 \\ &= \lambda_2\mu(\lambda_2C + \lambda_1B)\xi(d^2/dx_1^2)G(\xi, x_1) - \lambda_2\mu\lambda_1A\xi(d^2/dx_1^2 - \xi^2)G(\xi, x_1) \\ &= (\lambda_2\mu(\lambda_2C + \lambda_1B) - \lambda_2\mu\lambda_1A)\xi G(\xi, x_1)_{11} + \lambda_2\mu\lambda_1A\xi^3G(\xi, x_1), \end{aligned} \tag{29}$$

which leads to

$$\begin{aligned} \delta\sigma_{21} &= \int_0^\infty \xi^2(\lambda_2\mu PG(\xi, x_1)_{11} + \lambda_2\mu\lambda_1A\xi^2G(\xi, x_1))J_1(\xi x_2) d\xi, \\ G(\xi, x_1) &= G(\xi, x_1) = Me^{-\xi dx_1} + \bar{M}e^{-\xi \bar{d}x_1}, \quad G(\xi, x_1)_{11} = \xi^2(Md^2e^{-\xi dx_1} + \bar{M}\bar{d}^2e^{-\xi \bar{d}x_1}). \end{aligned} \tag{30}$$

When  $x_1 = 0$ , one obtains, denoting by  $M_{re}$  the real part of  $M$ ,

$$\begin{aligned} G(\xi, 0) &= M + \bar{M} = 2M_{re}, \quad [G(\xi, z)_{11}]_{x_1=0} = \xi^2(Md^2 + \bar{M}\bar{d}^2), \\ \delta\sigma_{21} &= \int_0^\infty \xi^2(\lambda_2\mu P\xi^2(Md^2 + \bar{M}\bar{d}^2) + 2\lambda_2\mu\lambda_1A\xi^2M_{re})J_1(\xi x_2) d\xi. \end{aligned}$$

When  $x_1 = 0$ ,  $\delta\sigma_{21} = 0$  ( $x_1 = z, x_2 = r$ ), one obtains  $(Md^2 + \bar{M}\bar{d}^2) + 2wM_{re} = 0$ , leading to

$$M_{re}(d^2 + 2w + \bar{d}^2) + iM_{im}(d^2 - \bar{d}^2) = 0,$$

$$M = M_{re} \left( \frac{1 - (d^2 + 2w + \bar{d}^2)}{(d^2 - \bar{d}^2)} \right) = \frac{-2M_{re}(\bar{d}^2 + w)}{(d^2 - \bar{d}^2)},$$

$$\bar{M} = M_{re} \left( \frac{1 + (d^2 + 2w + \bar{d}^2)}{(d^2 - \bar{d}^2)} \right) = \frac{2M_{re}(d^2 + w)}{(d^2 - \bar{d}^2)}; \tag{31}$$

$$G(\xi, x_1) = \frac{2M_{re}(-\bar{d}^2 + w)e^{-\xi dx_1} + (d^2 + w)e^{-\xi \bar{d}x_1}}{(d^2 - \bar{d}^2)},$$

$$G_1 = \frac{-2M_{re}\xi(-\bar{d}^2 + w)de^{-\xi dx_1} + (d^2 + w)\bar{d}e^{-\xi \bar{d}x_1}}{(d^2 - \bar{d}^2)},$$

$$G_{11} = \frac{2M_{re}\xi^2(-\bar{d}^2 + w)d^2e^{-\xi dx_1} + (d^2 + w)\bar{d}^2e^{-\xi \bar{d}x_1}}{(d^2 - \bar{d}^2)},$$

$$G_{111} = \frac{-2M_{re}\xi^3(-\bar{d}^2 + w)d^3e^{-\xi dx_1} + (d^2 + w)\bar{d}^3e^{-\xi \bar{d}x_1}}{(d^2 - \bar{d}^2)}. \tag{32}$$

Now the stress component  $\delta\sigma_{11}$  and displacement component  $u_1$  are discussed. On the basis of equations (16)–(17), one obtains

$$\delta\sigma_{11} = \int_0^\infty \xi J_0(\xi x_2) ((RA - RB)G_{111} + (C\lambda\lambda_2\lambda_1 - RA)\xi^2 G_1) d\xi, \tag{33}$$

$$u_1 = \int_0^\infty \xi J_0(\xi x_2) ((A - B)G_{11} - A\xi^2 G) d\xi. \tag{34}$$

For  $x_1 = 0$ , one has

$$G(\xi, x_1) = 2M_{re},$$

$$G_1 = -2M_{re}\xi \frac{-(\bar{d}^2 + w)d + (d^2 + w)\bar{d}}{d^2 - \bar{d}^2} = 2M_{re}\xi \frac{(\bar{d}d - w)(d - \bar{d})}{d^2 - \bar{d}^2} = 2M_{re}\xi \frac{\bar{d}d - w}{d + \bar{d}},$$

$$G_{11} = 2M_{re}\xi^2 \frac{-(\bar{d}^2 + w)d^2 + (d^2 + w)\bar{d}^2}{d^2 - \bar{d}^2} = -2M_{re}\xi^2 w, \tag{35}$$

$$G_{111} = -2M_{re}\xi^3 \frac{-(\bar{d}^2 + w)d^3 + (d^2 + w)\bar{d}^3}{d^2 - \bar{d}^2} = -2M_{re}\xi^3 \frac{\bar{d}^2 d^2 (d - \bar{d}) + w(d^3 - \bar{d}^3)}{d^2 - \bar{d}^2}$$

$$= -2M_{re}\xi^3 \frac{\bar{d}^2 d^2 + w(d^2 + \bar{d}d + \bar{d}^2)}{d + \bar{d}}.$$

Substituting these into Equations (33)–(34), one obtains

$$\begin{aligned} \delta\sigma_{11} &= \int_0^\infty \xi J_0(\xi x_2) \frac{-(RA-RB)2M_{re}\xi^3(\bar{d}^2d^2 + w(d^2+\bar{d}d+\bar{d}^2))}{d+\bar{d}} + \frac{(C\lambda\lambda_2\lambda_1-RA)\xi^22M_{re}\xi(\bar{d}d-w)}{d+\bar{d}} d\xi \\ &= -2(RA-RB)\frac{\bar{d}^2d^2 + w(d^2+\bar{d}d+\bar{d}^2)}{d+\bar{d}} \int_0^\infty \xi M_{re}J_0(\xi x_2)\xi^3 d\xi \\ &\quad + 2(C\lambda\lambda_2\lambda_1-RA)\frac{\bar{d}d-w}{d+\bar{d}} \int_0^\infty \xi M_{re}J_0(\xi x_2)\xi^3 d\xi \\ &= \frac{-2(RA-RB)(\bar{d}^2d^2 + w(d^2+\bar{d}d+\bar{d}^2)) + 2(C\lambda\lambda_2\lambda_1-RA)(\bar{d}d-w)}{d+\bar{d}} \int_0^\infty \xi M_{re}J_0(\xi x_2)\xi^3 d\xi; \end{aligned} \tag{36}$$

$$u_1 = \int_0^\infty \xi J_0(\xi x_2)(-(A-B)2M_{re}\xi^2w - 2A\xi^2M_{re}) d\xi = -(A-B)2w - 2A \int_0^\infty \xi J_0(\xi x_2)M_{re}\xi^2 d\xi. \tag{37}$$

The boundary conditions are

$$\begin{aligned} -(A-B)2w - 2A \int_0^\infty \xi J_0(\xi x_2)M_{re}\xi^2 d\xi &= [u_1(x_2)]_{x_1=0}, \quad x_1 = 0, \quad 0 \leq x_2 \leq a, \\ \int_0^\infty \xi^4 J_0(\xi x_2)M_{re}d\xi &= 0, \quad x_1 = 0, \quad x_2 > a, \end{aligned} \tag{38}$$

where  $a$  is the radius of the contact area, which will be discussed later.

Let  $\xi a = p$ ,  $x_2 = a\rho$ ,  $a^4[u_1(x_2)]_{x_1=0} = -2((A-B)w + A)g(\rho)$ ,  $p^3M_{re} = f(\rho)$ . Then

$$\begin{aligned} \int_0^\infty f(\rho)J_0(p\rho) d\rho &= g(\rho), \quad 0 \leq \rho \leq 1, \\ \int_0^\infty f(\rho)pJ_0(p\rho) d\rho &= 0, \quad \rho > 1. \end{aligned} \tag{39}$$

Let  $g(\rho) = \sum_{n=0}^\infty A_n\rho^n$ , with  $0 \leq \rho \leq 1$ ; by [Sneddon 1951](#), the solution of the equations is

$$f(\rho) = \pi^{-1/2} \sum_{n=0}^\infty A_n \left( \cos p + p \int_0^1 u^{n+1} \sin(pu) du \right) \frac{\Gamma(1+n/2)}{\Gamma(3/2+n/2)}. \tag{40}$$

Let  $[u_1(\rho)]_{x_1=0} = b + a \cot \alpha(1 - \rho)$  with  $0 \leq \rho \leq 1$ ; that is,  $g(\rho) = A_0 + A_1\rho$ , so

$$\begin{aligned} -2((A-B)w + A)(A_0 + A_1\rho) &= a^4[u_1(\rho)]_{x_1=0} = a^4(b + a \cot \alpha(1 - \rho)), \\ A_0 &= -a^4(b + a \cot \alpha)/2((A-B)w + A), \\ A_1 &= a^4a \cot \alpha/2((A-B)w + A). \end{aligned} \tag{41}$$

On the basis of equation (40), one obtains

$$f(\rho) = 2(A_0/\pi + A_1/2)\frac{\sin p}{p} + A_1\frac{\cos p - 1}{p^2}; \tag{42}$$

hence

$$\begin{aligned}
 \delta\sigma_{11} &= \frac{-2(RA-RB)(\bar{d}^2d^2 + w(d^2+\bar{d}d+\bar{d}^2)) + 2(C\lambda\lambda_2\lambda_1-RA)(\bar{d}d-w)}{d+\bar{d}} \int_0^\infty \xi^4 M_{re} J_0(\xi x_2) d\xi \\
 &= \frac{-2(RA-RB)(\bar{d}^2d^2 + w(d^2+\bar{d}d+\bar{d}^2)) + 2(C\lambda\lambda_2\lambda_1-RA)(\bar{d}d-w)}{a^5(d+\bar{d})} \int_0^\infty pf(p) J_0(p\rho) dp \\
 &= \frac{-2(RA-RB)(\bar{d}^2d^2 + w(d^2+\bar{d}d+\bar{d}^2)) + 2(C\lambda\lambda_2\lambda_1-RA)(\bar{d}d-w)}{a^5(d+\bar{d})} \\
 &\quad \times \int_0^\infty p \left( (2A_0/\pi + A_1) \frac{\sin p}{p} + A_1 \frac{\cos p - 1}{p^2} \right) J_0(p\rho) dp \\
 &= \frac{-2(RA-RB)(\bar{d}^2d^2 + w(d^2+\bar{d}d+\bar{d}^2)) + 2(C\lambda\lambda_2\lambda_1-RA)(\bar{d}d-w)}{d+\bar{d}} \\
 &\quad \times \left( \frac{2A_0/\pi + A_1}{a^5} \int_0^\infty J_0(p\rho) \sin p dp + \frac{A_1}{a^5} \int_0^\infty J_0(p\rho) \frac{\cos p - 1}{p} dp \right). \tag{43}
 \end{aligned}$$

As the integral  $\int_0^\infty J_0(p) \sin p dp$  is divergent, for the finiteness of stress component  $\delta\sigma_{11}$  at the edge of the punch, we have  $(2A_0/\pi + A_1) = 0$ , that is,  $b = a \cot \alpha(\pi/2 - 1)$ . Hence

$$u(x_1, x_2)_{x_1=0, x_2=0} = b + a \cot \alpha = \frac{\pi}{2} a \cot \alpha, \quad f(p) = A_1 \frac{\cos p - 1}{p^2}, \tag{44}$$

$$\begin{aligned}
 \delta\sigma_{11} &= \frac{-2(RA-RB)(\bar{d}^2d^2 + w(d^2+\bar{d}d+\bar{d}^2)) + 2(C\lambda\lambda_2\lambda_1-RA)(\bar{d}d-w)}{a^5(d+\bar{d})} A_1 \int_0^\infty J_0(p\rho) \frac{\cos p - 1}{p} dp \\
 &= \frac{-2(RA-RB)(\bar{d}^2d^2 + w(d^2+\bar{d}d+\bar{d}^2)) + 2(C\lambda\lambda_2\lambda_1-RA)(\bar{d}d-w)}{a^5(d+\bar{d})} A_1 \cosh^{-1}(1/\rho), \tag{45}
 \end{aligned}$$

$$\begin{aligned}
 T &= -2\pi \int_0^a [\delta\sigma_{11}]_{x_1=0} x_2 dx_2 \\
 &= -2\pi \frac{-2(RA-RB)(\bar{d}^2d^2 + w(d^2+\bar{d}d+\bar{d}^2)) + 2(C\lambda\lambda_2\lambda_1-RA)(\bar{d}d-w)}{a^5(d+\bar{d})} A_1 \\
 &\quad \int_0^a (\cosh^{-1}(a/x_2) x_2) dx_2. \tag{46}
 \end{aligned}$$

The integral on the right is equal to

$$\int_{1/a}^\infty \frac{\cosh^{-1}(av)}{v^3} dv = a^2 \int_1^\infty \frac{\cosh^{-1} u}{u^3} du = a^2 \int_0^\infty \frac{w \sin hw}{(\cosh w)^3} dw = \frac{a^2}{2};$$

therefore

$$T = -\pi a^2 \frac{-2(RA-RB)(\bar{d}^2d^2 + w(d^2+\bar{d}d+\bar{d}^2)) + 2(C\lambda\lambda_2\lambda_1-RA)(\bar{d}d-w)}{a^5(d+\bar{d})} A_1. \tag{47}$$

Substituting the value of  $A_1$  from (41), we obtain

$$T = \pi a^2 \frac{(RA - RB)(\bar{d}^2 d^2 + w(d^2 + \bar{d}d + \bar{d}^2)) - (C\lambda\lambda_2\lambda_1 - RA)(\bar{d}d - w)}{d + \bar{d}} \frac{\cot \alpha}{(A - B)w + A}. \tag{48}$$

The contact radius  $a$  is thus

$$a = \left( \frac{P \tan \alpha ((A - B)w + A)(d + \bar{d})}{\pi(RA - RB)(\bar{d}^2 d^2 + w(d^2 + \bar{d}d + \bar{d}^2)) - \pi(C\lambda\lambda_2\lambda_1 - RA)(\bar{d}d - w)} \right)^{1/2}. \tag{49}$$

The penetration depth is

$$[u(x_1, x_2)]_{x_1=0, x_2=0} = \frac{\pi}{2} a \cot \alpha, \tag{50}$$

where  $a$  is given by the previous equation.

Using the equalities  $\bar{d}^2 d^2 = p_1/p_3$  and  $\bar{d}^2 + d^2 = p_2/p_3$ , we obtain successively

$$\bar{d}d = \sqrt{p_1/p_3}, \quad \bar{d} + d = \sqrt{-p_2/p_3 + 2\sqrt{p_1/p_3}}, \quad d^2 + \bar{d}d + \bar{d}^2 = -p_2/p_3 + \sqrt{p_1/p_3}. \tag{51}$$

With this one can find the value of  $a$  in (49).

**A2. About  $Q$ .** It is known that  $Q = (r_1^2 + w)/(r_2^2 + w)$ , where  $w = \lambda_1 A / (\lambda_2 C + \lambda_1 B - \lambda_1 A)$ . Therefore,

$$\begin{aligned} 1 - Q &= 1 - \frac{r_1^2 + w}{r_2^2 + w} = \frac{r_2^2 - r_1^2}{r_2^2 + w}, \\ r_1 - Qr_2 &= r_1 - r_2 \frac{r_1^2 + w}{r_2^2 + w} = \frac{(r_2 - r_1)(r_1 r_2 - w)}{r_2^2 + w}, \\ r_1^2 - Qr_2^2 &= \frac{(r_2^2 r_1^2 + w r_1^2) - (r_1^2 r_2^2 + w r_2^2)}{r_2^2 + w} = w \frac{r_1^2 - r_2^2}{r_2^2 + w}, \\ r_1^3 - Qr_2^3 &= \frac{r_1^3(r_2^2 + w) - r_2^3(r_1^2 + w)}{r_2^2 + w} = \frac{(r_1 - r_2)r_1^2 r_2^2 + w(r_1^3 - r_2^3)}{r_2^2 + w} \\ &= (r_1 - r_2) \frac{r_1^2 r_2^2 + w(r_1^2 + r_1 r_2 + r_2^2)}{r_2^2 + w}, \end{aligned} \tag{52}$$

**A3. Research on some integrals.** When the integrals

$$\int_0^\infty x_2 J_1(\xi x_2) d\Phi_{11} \quad \text{and} \quad \int_0^\infty x_2 J_1(\xi x_2) \nabla^2 \Phi$$

are calculated, it is supposed that

$$x_2 J_1(\xi x_2) \Phi_{11} \rightarrow 0 \quad \text{and} \quad x_2 J_1(\xi x_2) \nabla^2 \Phi \rightarrow 0$$

by letting  $(x_1^2 + x_2^2)^{1/2} = r \rightarrow \infty$ .

It is known that

$$x \gg 1 \quad J_n(r) \rightarrow O(r^{-1/2}) \quad \text{and} \quad x_2 J_1(\xi x_2) \rightarrow O(r^{1/2}).$$



In our problem,  $u_1$  and  $u_2 \rightarrow 0$  when  $r \rightarrow \infty$ . In [Sneddon 1951], it is found that  $u_1$  and  $u_2 \rightarrow O(1/r)$  when  $r \rightarrow \infty$ .

On view of the relation between the displacements  $u_j$  and the function  $\Phi$ ,

$$\begin{aligned} u_2 &= -C\Phi_{21}, \\ u_1 &= A\nabla^2\Phi - B\Phi_{11}, \end{aligned}$$

one can deem that  $\Phi \rightarrow O(r)$ ; that is to say,

$$\Phi_{11} \rightarrow O(1/r) \quad \text{and} \quad \nabla^2\Phi \rightarrow O(1/r).$$

From this, one obtains

$$x_2J_1(\xi x_2)\Phi_{11} \rightarrow O(1/r^{-1/2}) \quad \text{and} \quad x_2J_1(\xi x_2)\nabla^2\Phi \rightarrow O(1/r^{-1/2}). \tag{53}$$

Therefore

$$\begin{aligned} & -(\lambda_2C + \lambda_zB)\lambda_2\mu \int_0^\infty x_2J_1(\xi x_2) d\Phi_{11} + \lambda_1A\lambda_2\mu \int_0^\infty x_2J_1(\xi x_2) d\nabla^2\Phi \\ &= -(\lambda_2C + \lambda_zB)\lambda_2\mu \left( \int_0^\infty dx_2J_1(\xi x_2)\Phi_{11} - \frac{1}{\xi} \int_0^\infty \Phi_{11} d\xi x_2J_1(\xi x_2) \right) \\ & \quad + \lambda_1A\lambda_2\mu \left( \int_0^\infty dx_2J_1(\xi x_2)\nabla^2\Phi - \frac{1}{\xi} \int_0^\infty \nabla^2\Phi d\xi J_1(\xi x_2)x_2 \right) \\ &= (\lambda_2C + \lambda_zB)\lambda_2\frac{\mu}{\xi} \int_0^\infty \Phi_{11} d\xi x_2J_1(\xi x_2) - \lambda_1A\lambda_2\frac{\mu}{\xi} \int_0^\infty \nabla^2\Phi d\xi J_1(\xi x_2)x_2 \\ &= (\lambda_2C + \lambda_zB)\lambda_2\mu\xi \int_0^\infty \Phi_{11}x_2J_0(\xi x_2) dx_2 - \lambda_1A\lambda_2\mu\xi \int_0^\infty \nabla^2\Phi x_2J_0(\xi x_2) dx_2, \tag{54} \end{aligned}$$

because  $d(vJ_1(v)) = vJ_0(v)dv$ .

**A4. Force on the cone, contact radius and penetration depth.** For the compressive force  $T$  on the cone, from (21), one obtains

$$\begin{aligned} T &= -2\pi \int_0^a [\delta\sigma_{11}]_{x_1=0} x_2 dx_2 \\ &= -2\pi ((RA - RB)(r_1^3 - Qr_2^3) + (C\lambda\lambda_2\lambda_1 - RA)(r_1 - Qr_2)) \frac{A_1}{a^5} \int_0^a (\cosh^{-1}(a/x_2)x_2) dx_2 \\ &= -\pi a^2 ((RA - RB)(r_1^3 - Qr_2^3) + (C\lambda\lambda_2\lambda_1 - RA)(r_1 - Qr_2)) \frac{A_1}{a^5} \\ &= \pi a^2 \frac{(RA - RB)(r_1^3 - Qr_2^3) + (C\lambda\lambda_2\lambda_1 - RA)(r_1 - Qr_2)}{(A - B)(r_1^2 - Qr_2^2) - A(1 - Q)} \cot \alpha. \tag{55} \end{aligned}$$

The contact radius  $a$  is thus

$$a = \left( \frac{T \tan \alpha ((A - B)(r_1^2 - Qr_2^2) - A(1 - Q))}{\pi (RA - RB)(r_1^3 - Qr_2^3) + \pi (C\lambda\lambda_2\lambda_1 - RA)(r_1 - Qr_2)} \right)^{1/2}, \tag{56}$$

and we know from (20) that the penetration depth is given by

$$[u_1(x_1, x_2)]_{x_1=0, x_2=0} = \frac{\pi}{2} a \cot \alpha. \tag{57}$$

For convenience,  $r_1, r_2$  and  $Q$  will be replaced by the coefficients of the characteristic equation. First the expressions in  $Q$  are replaced by expressions in  $r_1, r_2$ , using (52). We obtain

$$T = a^2 \frac{\pi(RA - RB)(r_1^2 r_2^2 + w(r_1^2 + r_1 r_2 + r_2^2)) - \pi(C\lambda\lambda_2\lambda_1 - RA)(r_1 r_2 - w)}{((A - B)w + A)(r_2 + r_1)} \cot \alpha, \tag{58}$$

$$a = \left( \frac{T \tan \alpha ((A - B)w + A)(r_2 + r_1)}{\pi(RA - RB)(r_1^2 r_2^2 + w(r_1^2 + r_1 r_2 + r_2^2)) - \pi(C\lambda\lambda_2\lambda_1 - RA)(r_1 r_2 - w)} \right)^{1/2},$$

from which we also obtain the penetration depth via (57).

From (8), one knows that  $p_j$  are the coefficients of characteristic equation; therefore, the relations between  $p_j$  and  $r_1, r_2$  are exactly as in Equation (51), with  $r_1, r_2$  replacing  $d, \bar{d}$ .

Substituting this into (58), one obtains

$$T = a^2 \frac{\pi(RA - RB)(p_1/p_3 + w(-p_2/p_3 + \sqrt{p_1/p_3})) - \pi(C\lambda\lambda_2\lambda_1 - RA)(\sqrt{p_1/p_3} - w)}{((A - B)w + A)(-p_2/p_3 + 2\sqrt{p_1/p_3})^{1/2}} \cot \alpha$$

$$= a^2 \frac{\pi(RA - RB)(p_1 + w(-p_2 + \sqrt{p_1 p_3})) - \pi(C\lambda\lambda_2\lambda_1 - RA)(\sqrt{p_1 p_3} - w p_3)}{((A - B)w + A)(-p_2 p_3 + 2p_1^{1/2} p_3^{3/2})^{1/2}},$$

$$a = \left( \frac{T \tan \alpha ((A - B)w + A)(-p_2 p_3 + 2p_1^{1/2} p_3^{3/2})^{1/2}}{\pi(RA - RB)(p_1 + w(-p_2 + \sqrt{p_1 p_3})) - \pi(C\lambda\lambda_2\lambda_1 - RA)(\sqrt{p_1 p_3} - w p_3)} \right)^{1/2} \tag{59}$$

and

$$[u(x_1, x_2)]_{x_1=0, x_2=0} = \frac{\pi}{2} a \cot \alpha.$$

### References

[Beatty 1971] M. E. Beatty, "Estimate of ultimate safe loads in elastic stability theory", *J. Elasticity* **1**:2 (1971), 95–120.

[Bernstein and Toupin 1960] B. Bernstein and R. A. Toupin, "Korn inequalities for the sphere and circle", *Arch. Rational Mech. Anal.* **6** (1960), 51–64.

[Ericksen 1953] K. N. Ericksen, "On the propagation of wavees in isotropic incompressible perfect elastic materials", *J. Rational Mech. Anal. (Indiana Univ.)* **2**:2 (1953), 329–337.

[Green and Shield 1951] A. E. Green and R. T. Shield, "Finite extension and torsion of cylinders", *Phil. Trans. Roy. Soc. London Ser. A* **244** (1951), 47–86.

[Hao 1986] T. H. Hao, "The opening displacement of a crack in an infinite plate subjected to crack parallel initial stress", pp. 185–191 in *Fracture control of engineering structures* (Amsterdam, 1986), vol. 1, edited by H. C. van Elst and A. Bakker, Engineering Materials Advisory Services Ltd., Warley, West Midlands, UK, 1986.

[Hayes and Rivlin 1961] M. Hayes and R. S. Rivlin, "Propagation of a plane wave in an isotropic elastic material subject to pure homogeneous deformation", *Arch. Rational Mech. Anal.* **8** (1961), 15–22.

[Holden 1964] J. T. Holden, "Estimation of critical loads in elastic stability theory", *Arch. Rational Mech. Anal.* **17** (1964), 171–183.

- [Hwang 1989] K. C. Hwang, *Nonlinear continuum mechanics*, Science Press, Beijing, 1989. In Chinese.
- [Lurie 1990] A. I. Lurie, *Nonlinear theory of elasticity*, Series in Applied Mathematics and Mechanics **36**, North-Holland, Amsterdam, 1990.
- [Payne and Weinberger 1961] L. E. Payne and H. F. Weinberger, “On Korn’s inequality”, *Arch. Rational Mech. Anal.* **8** (1961), 89–98.
- [Pearson 1950] C. E. Pearson, “General theory of elastic stability”, *Quart. Appl. Math.* **14** (1950), 133–144.
- [Ranht et al. 1978] S. Ranht, Dhaliwal, and B. M. Singh, “The axisymmetric Boussinesq problem of an initially stressed neo-Hookean half-space for a punch with arbitrary profile”, *Internat. J. Engrg. Sci.* **16** (1978), 379–385.
- [Savwers and Rivlin 1973] K. N. Savwers and R. S. Rivlin, “Instability of an elastic material”, *Int. J. Solids Struct.* **9** (1973), 607–613.
- [Savwers and Rivlin 1977] K. N. Savwers and R. S. Rivlin, “On the speed of propagation of waves in a deformed elastic material”, *J. Appl. Math. Phys. (ZAMP)* **28**:6 (1977), 1045–1057.
- [Savwers and Rivlin 1978] K. N. Savwers and R. S. Rivlin, “A note on the Hadamard criterion for an incompressible isotropic elastic material”, *Mech. Res. Comm.* **5**:4 (1978), 211–244.
- [Sneddon 1951] I. N. Sneddon, *Fourier transforms*, McGraw-Hill, New York, 1951.
- [Southwell 1913] R. V. Southwell, “On the general theory of elastic stability”, *Phil. Trans. Roy. Soc. London Ser. A* **213** (1913), 187–244.
- [Suresh and Giannakopoulos 1998] S. Suresh and A. E. Giannakopoulos, “A new method for estimating residual stresses by instrumented sharp indentation”, *Acta Mater.* **46**:16 (1998), 5755–5767.
- [Truesdell 1961] C. Truesdell, “General and exact theory of waves in finite elastic strain”, *Arch. Rational Mech. Anal.* **8** (1961), 263–296.

Received 29 Sep 05.

HAO TIAN-HU: [haoth0000@yahoo.com.cn](mailto:haoth0000@yahoo.com.cn)

P.O. Box 220, China Textile University, Shanghai 200051, P. R. China

## CRACK INITIATION PREDICTION FOR V-NOTCHES UNDER MIXED-MODE LOADING IN BRITTLE MATERIALS

JIA LI AND XIAO-BING ZHANG

In this work, crack initiation from a notch tip in elements subjected to a mixed mode loading was studied. Two phenomenological criteria, based on a concept of Leguillon, were proposed and applied to predict crack initiation from a  $V$ -notch tip in a brittle or quasibrittle material. The first criterion, called in this paper the  $G$ - $\sigma$  criterion, makes use of the critical strain energy release rate and the ultimate tensile stress as the main parameters of fracture. It requires calculations of strain energy release rate after an infinitesimal crack kinking. By means of some numerical effort, we established the indispensable relationships between the strain energy release rate after crack kinking and the remote mixed mode loads. These relationships enabled us to apply directly the proposed criterion to mixed-mode loaded notches. We also modified the strain energy density criterion proposed by Sih on the basis of Leguillon's concept to form a criterion capable of predicting the crack initiation from a  $V$ -notch tip. This criterion, which we call the  $S$ - $\sigma$  criterion, benefits from its simplicity in applications. Confrontation with experimental data shows that both the criteria enable reasonably accurate prediction of fracture in elements with  $V$ -notches subjected to mixed mode loading. Consequently, they can be effectively applied in practical engineering applications.

### 1. Introduction

In engineering applications, the failure prediction of a structure depends not only on the strengths of the materials with which it is built, but also on the local stress concentrations [Bazant 2000]. For brittle or quasibrittle elastic materials, it is clear that the crack initiation from a stress concentration area is a critical moment in the structure service life. In the case where a  $V$ -shaped notch exists in a structure component, the crack initiation from the notch tip requires careful analyses because the stress field near the notch tip is a singular one and therefore this area is a potential origin of the crack initiation.

Different crack initiation criteria for  $V$ -notches have been reported in the literature. A fairly obvious choice consists in establishing notch fracture criteria on the basis of the critical values of the notch stress intensity factors [Reedy and Guess 1995; Dunn et al. 1997b; Dunn et al. 1997a]. Recently, attention has been focused on finite-fracture based criteria in which a finite-length crack or a finite damage zone is introduced. In general, these criteria have been drawn from the work of [McClintock 1958] on crack growth in ductile materials. The initial idea of McClintock was that in order to avoid the singularity of the near-tip fields, one can choose the normal strain  $\varepsilon_{\theta\theta}$  at some small distance  $l$  measured from the crack tip as a fracture parameter: the crack propagates once it reaches its critical value. Subsequently, numerous variants of this criterion were reported in the literature. For crack propagations, several criteria were proposed by choosing the normal tensile stress  $\sigma_{\theta\theta}$  [Ritchie et al. 1973; Kosai et al. 1993] or the

---

*Keywords:* fracture criteria, brittle fracture, v-shaped notches, mixed mode loading, crack initiation.

tensile stress  $\sigma_{\theta\theta}$  and the shear stress  $\sigma_{r\theta}$  [Mroz and Seweryn 1998], at a finite distance  $l$  from the crack tip as fracture parameters. For crack onset from a notch tip, similar criteria were established (see the summary made in [Seweryn and Lukaszewicz 2002]). Apart from these criteria, the strain energy release rate at a virtually created crack tip of a finite length  $l$  and the strain energy density factor  $S$  have also been introduced into the fracture criteria [Palaniswamy and Knauss 1972; Seweryn and Lukaszewicz 2002]. In all these criteria, the finite length  $l$  is an inevitable parameter that enables us to deal with stress singularities different from  $-1/2$ . However, the physical interpretation of this length is rather vague. It was often considered as a material parameter related to the microstructure of the material, as in the grain size in metals. In common practice, this characteristic length is often calculated by the Irwin concept [Irwin 1968] which gives rise to formulas such as  $l = EG_c/\sigma_c^2$ , with  $E$  being the Young modulus,  $G_c$  the critical value of strain energy release rate,  $\sigma_c$  the limit failure stress.

[Leguillon 2002] pointed out that if the concept of the finite fracture mechanics is applicable to the crack initiation analysis, the finite characteristic length  $l$  is not only a material-dependent constant. In fact, it depends also on the stress distribution in the structure, that is, on the structure geometry and the remote loading. In his analysis of crack onset at a  $V$ -notch tip, he argued that an admissible length  $l$  can be determined by  $l = EG_c/(\bar{K}\sigma_c^2)$ , where  $\bar{K}$  depends on the notch opening angle. This analysis enabled him to propose a crack onset criterion, in which both the tensile stress and the incremental strain energy release rate at a finite distance  $l$  should reach their critical values  $\sigma_c$  and  $G_c$  simultaneously. This criterion is self-consistent. In fact, these conditions are sufficient to determine both the characteristic distance  $l$  and the critical remote loads. This criterion provides good results in the prediction of crack onset in  $V$ -notched structures under pure mode  $I$  loading [Leguillon 2002; Leguillon and Yosibash 2003].

In this paper, we apply the concept developed by Leguillon to the crack onset analysis for  $V$ -notched plates subjected to mixed-mode loading. A criterion based on the calculation of the strain energy release rate at a virtual crack tip issued from the notch tip and the tensile stress at the same point in the configuration without the virtual crack, named in this paper the  $G$ - $\sigma$  criterion, is first proposed. The main difficulty in the application of this criterion is to evaluate the strain energy release rate. Important numerical effort has been made to this end.

In order to avoid too much numerical computation, another crack onset criterion, which we designate the  $S$ - $\sigma$  criterion, is here proposed on the basis of the strain energy density criterion of Sih [Sih 1974]. The main idea is to modify Sih's criterion by using the Leguillon concept in order to deal with stress singularities different from  $-1/2$ . This criterion provides a simpler technique to the prediction of crack initiation from a notch tip. Comparing with the experimental data, both criteria give satisfactory predictions for the limit loads as well as for the crack deviation angles. Finally, the efficiency of these criteria is discussed at the end of this paper.

## 2. Experimental basis

Numerous experimental studies have been published in the topic of evaluating structure failures with  $V$ -shaped notches [Broughton et al. 1990; Seweryn et al. 1997; Bansal and Kumosa 1998]. In this work, the experimental results obtained by [Seweryn et al. 1997] were chosen to verify the efficiency of the proposed criteria. In [Seweryn et al. 1997], symmetric plane specimens with  $V$ -shaped notches were made of polymethyl methacrylate (PMMA). The selection of the PMMA material was essentially due

to its brittle characteristics, since it allows the possibility of cutting notches of a small radius (about 0.01 mm). The mechanical properties of the material are as follows:

- (i) Young’s modulus:  $E = 3300 \text{ MPa}$ ;
- (ii) Poisson ratio:  $\nu = 0.35$ ;
- (iii) limit failure stress:  $\sigma_c = 102.8 \text{ MPa}$ ;
- (iv) critical strain energy release rate:  $G_c = 0.384 \text{ MPa}\cdot\text{mm}$ .

The geometry of the specimens is shown in [Figure 1](#). Imposed displacements were applied at two ends of the specimens by using a specially designed device. The mode mixity was adjusted by varying the proportion of the horizontal and vertical displacement components, that is, the ratio of shear to tensile forces.

### 3. Leguillon’s and modified Sih’s criteria for notches under mode-I loading

In this section, we first review the crack onset criterion proposed by [\[Leguillon 2002\]](#). Then the Leguillon concept is used to modify the criterion of Sih in order to form another crack onset criterion for a V-shaped notch under pure tensile loading. Finally, the critical loads for crack onset predicted by using these criteria are compared with the experimental data.

Consider first a plane sharp notch in a linear elastic medium with vertex angle  $2\alpha$  and a polar coordinate system  $(r, \theta)$  with the origin at the tip of the notch ([Figure 2](#)). The dominant displacements  $u_i$  and stresses  $\sigma_{ij}$  near the notch tip can be written as follows:

$$\begin{aligned}
 u_i &= \frac{k_1 r^{\lambda_1}}{2\mu(2\pi)^{1-\lambda_1}} \tilde{u}_{1i}(\theta) + \frac{k_2 r^{\lambda_2}}{2\mu(2\pi)^{1-\lambda_2}} \tilde{u}_{2i}(\theta) \\
 \sigma_{ij} &= \frac{k_1}{(2\pi r)^{1-\lambda_1}} \tilde{\sigma}_{1ij}(\theta) + \frac{k_2}{(2\pi r)^{1-\lambda_2}} \tilde{\sigma}_{2ij}(\theta),
 \end{aligned}
 \tag{1}$$

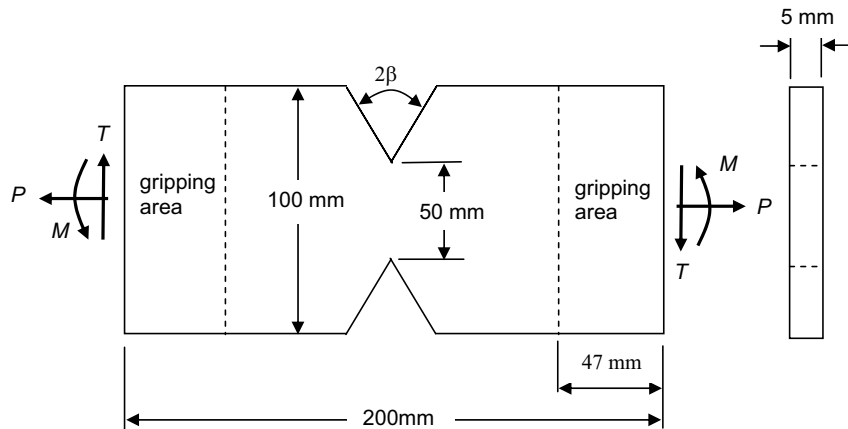


**Figure 1.** Geometry of specimens with V-notches.

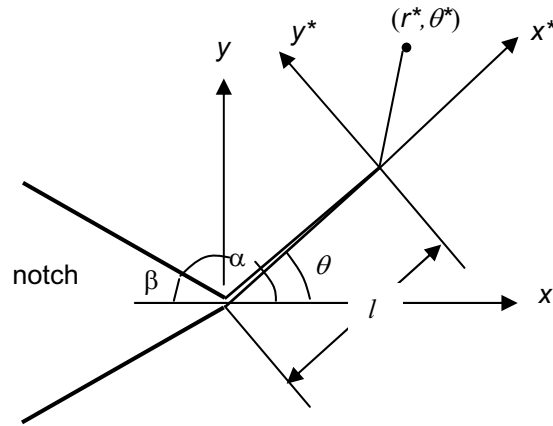


**Figure 2.** Notch geometry, virtual crack and coordinate systems.

where  $\mu$  is the shear modulus,  $\tilde{u}_{1i}(\theta)$ ,  $\tilde{u}_{2i}(\theta)$ ,  $\tilde{\sigma}_{1ij}(\theta)$  and  $\tilde{\sigma}_{2ij}(\theta)$  are trigonometric functions of  $\theta$ . The exponents  $\lambda_1$  and  $\lambda_2$  describe the near-tip stress singularities and are given by the characteristic equations

$$\begin{aligned}\lambda_1 \sin 2\alpha + \sin 2\lambda_1\alpha &= 0, \\ \lambda_2 \sin 2\alpha - \sin 2\lambda_2\alpha &= 0.\end{aligned}\quad (2)$$

The coefficients  $k_1$  and  $k_2$  are the so-called notch stress intensity factors, defined as

$$\begin{aligned}k_1 &= \lim_{r \rightarrow 0} (2\pi r)^{1-\lambda_1} \sigma_{\theta\theta}(r, \theta = 0), \\ k_2 &= \lim_{r \rightarrow 0} (2\pi r)^{1-\lambda_2} \sigma_{r\theta}(r, \theta = 0).\end{aligned}\quad (3)$$

Among these components, we give the explicit expression of  $\sigma_{\theta\theta}$  that is useful in later formulations:

$$\begin{aligned}\sigma_{\theta\theta} &= \frac{k_1}{(2\pi r)^{1-\lambda_1} C_1} (\cos(1+\lambda)\alpha \cos(1-\lambda)\theta - \cos(1-\lambda)\alpha \cos(1+\lambda)\theta) \\ &\quad + \frac{k_2(1+\lambda)}{(2\pi r)^{1-\lambda_2} C_2} (-\sin(1-\lambda)\alpha \sin(1+\lambda)\theta + \sin(1+\lambda)\alpha \sin(1-\lambda)\theta)\end{aligned}\quad (4)$$

with

$$\begin{aligned}C_1 &= \cos(1+\lambda_1)\alpha - \cos(1-\lambda_1)\alpha, \\ C_2 &= (1+\lambda_2) \sin(1-\lambda_2)\alpha - (1-\lambda_2) \sin(1+\lambda_2)\alpha.\end{aligned}$$

In general,  $\lambda_1$  and  $\lambda_2$  are larger than 0.5, therefore, the singularities at a V-shaped notch tip are weaker than that at a crack tip. As a consequence, the criteria for crack growth, such as the strain energy release rate criterion, are not directly applicable. Moreover, the criteria usually used for nonsingular stresses such like the maximum tensile stress criterion are not appropriate. Special criteria have to be developed for this class of problems.

**3.1. Leguillon's criterion.** Leguillon [2002] proposed a criterion to predict the crack initiation from a notch tip. In fact, under pure tensile loading, the incremental strain energy release rate of a newly created

crack originated from the notch tip can be developed in the form

$$\bar{G} = -\frac{W}{l} = ck_1^2 l^{2\lambda_1-1} + \dots, \tag{5}$$

where  $l$  is the crack length,  $W$  is the potential strain energy needed to create the crack,  $c$  is a constant depending on the notch-opening angle and the material parameters. Its values have been tabulated by Leguillon [2002]. The crack onset condition, according to the incremental Griffith criterion, requires that

$$\bar{G} = ck_1^2 l^{2\lambda_1-1} \geq G_c. \tag{6}$$

It is clear that  $\bar{G}$  tends to zero if  $l$  is infinitesimally small. Therefore, there must be a jump from 0 to  $l$  when crack onset occurs. From Equation (6), the length of this jump must satisfy the condition

$$l^{2\lambda_1-1} \geq \frac{G_c}{ck_1^2}. \tag{7}$$

On the other hand, under pure tensile loading, the tensile stress at the point ( $r = l, \theta = 0$ ) is, according to (4),

$$\sigma_{\theta\theta} = k_1(2\pi l)^{\lambda_1-1}. \tag{8}$$

It is clear that the tensile stress tends to the infinity when  $l$  tends to zero. According to the maximal tensile stress criterion, we have, for small  $l$ ,

$$\sigma_{\theta\theta} = k_1(2\pi l)^{\lambda_1-1} \geq \sigma_c, \tag{9}$$

which leads to

$$(2\pi l)^{1-\lambda_1} \leq \frac{k_1}{\sigma_c}. \tag{10}$$

For a small load represented by  $k_1$ , the conditions (7) and (10) are incompatible. When the load increases monotonically, it reaches a critical value  $k_c$  for which both the conditions (7) and (10) hold. This leads us to determine the increment length:

$$l = \frac{1}{(2\pi)^{2-2\lambda_1}} \frac{G_c}{c\sigma_c^2}. \tag{11}$$

Once the incremental length  $l$  determined, the critical remote load  $k_c$  can be calculated from either (6) or (9).

**3.2. Modified Sih's criterion.** Sih [1974] assumed that the crack bifurcation direction from a crack tip is determined by the minimum value of strain energy density factor  $S$ , and the crack propagation occurs once the strain energy density factor reaches a critical value  $S_c$ . In a polar coordinate system with the origin at the crack tip, the elastic strain energy  $dU$  stored in the elementary volume  $dV = r d\theta dr$  is given by the relation

$$\frac{dU}{dV} = \frac{1}{2}(\sigma_{rr}\epsilon_{rr} + \sigma_{\theta\theta}\epsilon_{\theta\theta} + 2\sigma_{r\theta}\epsilon_{r\theta}). \tag{12}$$

The factor  $S$  is defined as

$$S = \frac{dU}{dV} r. \tag{13}$$



The critical value of  $S$  can be related to the critical strain energy release rate  $G_c$  [Sih 1974], namely

$$S_c = \frac{\kappa - 1}{\kappa + 1} \frac{1}{\pi} G_c, 0, \quad (14)$$

where

$$\begin{cases} \kappa = (3 - \nu)/(1 + \nu) & \text{for plane stress,} \\ 3 - 4\nu & \text{for plane strain.} \end{cases}$$

Therefore Sih's criterion for crack propagation can be written as follows:

- the crack bifurcation direction  $\varphi$  is determined by

$$\left. \frac{\partial S}{\partial \theta} \right|_{\theta=\varphi} = 0, \quad \left. \frac{\partial^2 S}{\partial \theta^2} \right|_{\theta=\varphi} > 0; \quad (15)$$

- the crack propagates once

$$S \geq S_c. \quad (16)$$

Consider now a  $V$ -shaped notch under pure tensile loading. According to Equation (13), the strain energy density factor takes the form

$$S = k_1^2 (2\pi r)^{2\lambda_1 - 1} \tilde{S}(\theta), \quad (17)$$

where  $\tilde{S}(\theta)$  is a dimensionless angular function that can easily be determined by means of Equations (1) and (12). In the case of pure tensile loading, the crack initiation angle from the notch tip is  $\varphi = 0$ . In such a case,  $\tilde{S}(0)$  becomes a constant  $K$  depending on the notch-opening angle. For plane stress, for example, we can write

$$\begin{aligned} K &= \frac{1 - 2\nu\sigma + \sigma^2}{4\pi E} \\ \sigma &= \frac{(3 - \lambda_1) \cos(1 + \lambda_1)\alpha + (1 + \lambda_1) \cos(1 - \lambda_1)\alpha}{(1 + \lambda_1)(\cos(1 + \lambda_1)\alpha - \cos(1 - \lambda_1)\alpha)}. \end{aligned} \quad (18)$$

It is clear that  $\lim_{r \rightarrow 0} S(r, 0) = 0$ . In order to be able to use Sih's criterion, we adopt a nonlocal length  $r = l$ , at this distance the crack onset condition (16) becomes

$$S(l) = K k_1^2 (2\pi l)^{2\lambda_1 - 1} \geq S_c. \quad (19)$$

Therefore

$$(2\pi l)^{2\lambda_1 - 1} \geq \frac{S_c}{K k_1^2}. \quad (20)$$

Consider now the tensile stress at the ligament. According to the maximum tensile stress criterion, Equation (9) must hold.

Similarly to Leguillon's criterion, both Equations (20) and (9) must hold for a crack onset. Therefore we can obtain the crack onset length  $l$  as

$$l = \frac{1}{2\pi} \frac{S_c}{K \sigma_c^2} \quad (21)$$

and the critical remote load, represented by  $k_1$ , can easily be determined from either (19) or (9).

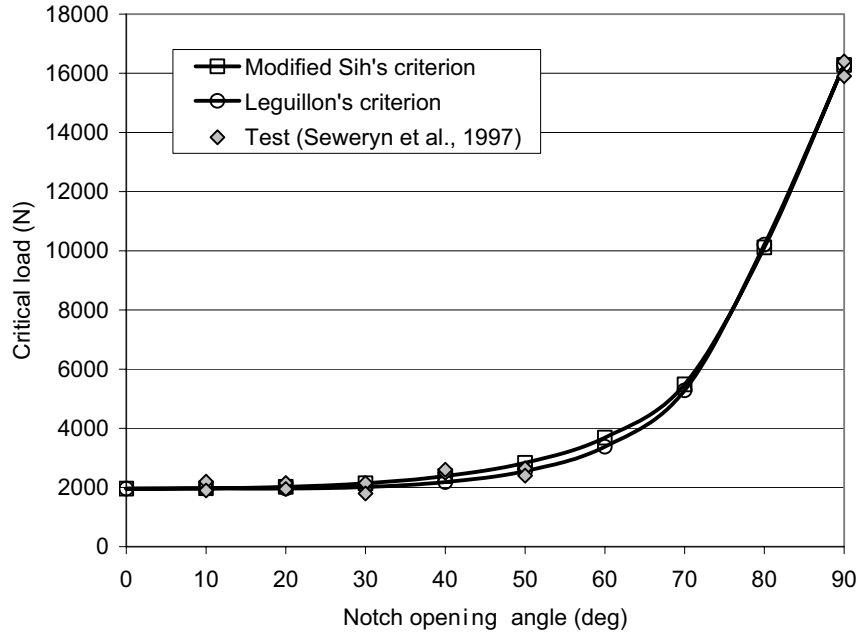


**Figure 3.** Failure load versus notch opening angle for *V*-notched plates under pure tensile loading

Figure 3 illustrates the comparison between the critical loads at fracture of the specimens recorded in the experimentation [Seweryn et al. 1997] and those predicted by using respectively Leguillon’s criterion and modified Sih’s criterion. It is shown that both criteria provide good agreement with respect to the experimental data.

**4. The  $G$ - $\sigma$  criterion for mixed-mode loaded notches**

The concept developed by Leguillon is physically reasonable and self-consistent. The main difficulty remains the evaluation of the incremental strain energy release rate  $\bar{G}$ . Consider the *V*-notch illustrated in Figure 2 with a crack of length  $l$  issued from the notch tip in an arbitrary direction  $\theta$ . The incremental strain energy release rate  $\bar{G}$  during the creation of this crack is the average work done by the stresses in front of the crack on the displacements of the crack edge:

$$\bar{G} = -\frac{1}{l} \int_0^l (\sigma_{\theta\theta}(r, \theta)u_{\theta}^*(l - r, \pi) + \sigma_{r\theta}(r, \theta)u_r^*(l - r, \pi)) dr. \tag{22}$$

However, the evaluation of  $\bar{G}$  is associated with considerable computational difficulties. A basic problem is to determine displacements along the edges of an assumed crack. In the original work of Leguillon [2002], the evaluation of  $\bar{G}$  is relied on the possibility of its expansion in an asymptotic series involving the crack length  $l$ . In the present work, we will not attempt to perform such an asymptotic analysis, and a different method is adopted.

Let us consider the same *V*-shaped notch. We assume that under mixed mode loading, there exists a small crack issued from the notch tip and characterized by its length  $l$  and its orientation  $\theta$ . The

assumption of this finite-length crack can be justified as follows [Seweryn and Lukaszewicz 2002]: due to large stresses, intensive microcracking occurs near the notch tip. This microcrack network can be replaced by an equivalent crack in order to produce a mathematically manageable model. The size of this equivalent crack is essentially within a mesoscopic scale (about several tens of microns for the used PMMA). In brittle materials, the instable propagation of this equivalent crack leads to a macroscopic crack onset.

The energy release rate of this virtual crack is defined by

$$G = - \lim_{\Delta l} \frac{1}{\Delta l} \int_0^{\Delta l} (\sigma_{\theta\theta}^*(0)u_{\theta}^*(\pi) + \sigma_{r\theta}^*(0)u_r^*(\pi)) dr, \quad (23)$$

where  $(r^*, \theta^*)$  are the polar coordinates with an origin at the crack tip and  $\sigma_{\theta\theta}^*$ ,  $\sigma_{r\theta}^*$ ,  $u_{\theta}^*$  and  $u_r^*$  are the stress and displacement components in the above coordinates. Taking into consideration only the first terms of the asymptotic expansion of the stress and displacement fields near the crack tip, one obtains

$$G = \frac{K_I^2 + K_{II}^2}{E'}, \quad (24)$$

where  $K_I$  and  $K_{II}$  are the stress intensity factors at the newly created crack tip, with

$$E' = \begin{cases} E & \text{for plane stress,} \\ \frac{E}{1-\nu^2} & \text{for plane strain.} \end{cases} \quad (25)$$

A criterion of a macroscopic crack initiation can therefore be established on the basis of the energy release rate at the tip of the virtual crack. By adopting the Leguillon's concept, this criterion can be described as follows:

Crack onset occurs from the notch tip if at a neighboring point  $(\varphi, l)$ ,

- (i) the circumferential tensile stress reaches the material critical strength  $\sigma_c$ ;
- (ii) the strain energy release rate of a virtual crack, emanated from the notch tip to this point, reaches the critical toughness  $G_c$ ;
- (iii) the strain energy release rate reaches a maximal value among all possible crack onset directions.

Therefore, the application of this criterion consists in evaluating the crack initiation angle  $\varphi$ , the crack onset length  $l$  and the critical remote load  $F$  from the relationships

$$\begin{aligned} \sigma_{\theta\theta}(F, l, \varphi) &= \sigma_c \\ G(F, l, \varphi) &= G_c \\ \frac{\partial G(F, l, \varphi)}{\partial \varphi} &= 0, \quad \frac{\partial^2 G(F, l, \varphi)}{\partial \varphi^2} < 0. \end{aligned} \quad (26)$$

This criterion is called hereafter the  $G$ - $\sigma$  criterion.

The key factor in applying this criterion is to evaluate the strain energy release rate for the virtual crack emanating from the  $V$ -notch tip. To this end, we write, from a dimensional analysis, the relationships

between the stress intensity factors  $(k_1, k_2)$  at the  $V$ -notch tip and  $(K_I, K_{II})$ , those at the virtual crack tip, for infinitesimal  $l$ :

$$\begin{aligned} K_I &= b_{11}k_1l^{\lambda_1-\frac{1}{2}} + b_{12}k_2l^{\lambda_2-\frac{1}{2}}, \\ K_{II} &= b_{21}k_1l^{\lambda_1-\frac{1}{2}} + b_{22}k_2l^{\lambda_2-\frac{1}{2}}, \end{aligned} \quad (27)$$

where  $b_{ij}$  are dimensionless functions depending on the crack deviation angle  $\varphi$ .

From Equations (24) and (27) we obtain

$$E'G = c_1(\varphi)k_1^2l^{2\lambda_1-1} + c_2(\varphi)k_1k_2l^{\lambda_1+\lambda_2-1} + c_3(\varphi)k_2^2l^{2\lambda_2-1}, \quad (28)$$

where  $c_1(\varphi)$ ,  $c_2(\varphi)$  and  $c_3(\varphi)$  result from combination of  $b_{ij}$  and therefore are  $\varphi$ -dependent functions. In order to determine these functions, we carried out detailed numerical calculations by establishing finite element models. The idea is to mesh carefully a notched plate with a branched crack. Then we calculate accurately the strain energy release rates at the crack tip by varying the crack length, the crack direction, and the mode mixity of the remote loads. These numerical data are correlated with Equation (28) by using a least square procedure in order to determine accurately the functions  $c_i(\varphi)$ . This approach seems to be somewhat onerous and lacking in elegance. However, with the extraordinary capacity of actual computers and finite element codes, a linear elastic calculation is quite rapid. Combining this with an automatic meshing procedure, the entire computational work is not extensively time-consuming.

In the numerical simulations, the specimens used in [Seweryn et al. 1997] were meshed as illustrated in Figure 4. The lower specimen edge was fixed while along the upper specimen edge the enforced displacements were prescribed in the direction of  $y$ -axis for tension and  $x$ -axis for shear. The tensile and shearing load components  $P$  and  $T$  were calculated by integrating the resulting stresses across the

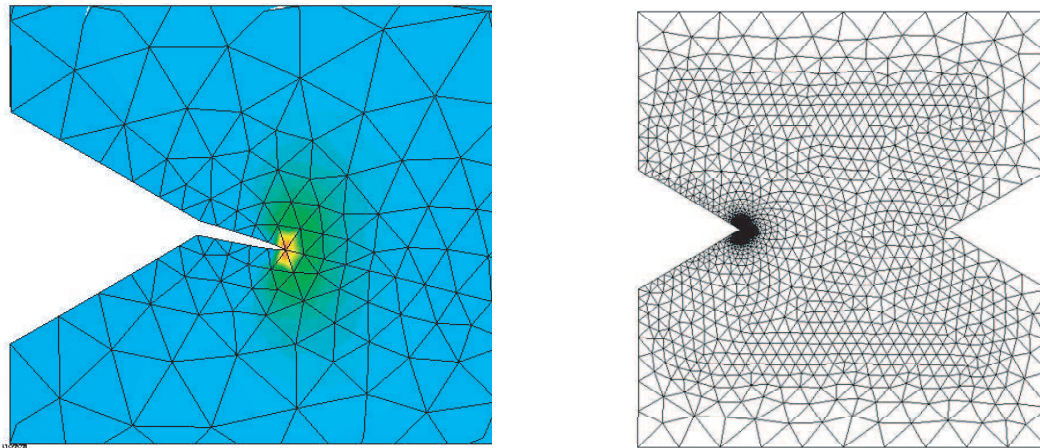


**Figure 4.** Typical meshing of the specimens and the zoom around the branched crack.

specimen width. Therefore the resulting force  $F$  is related to  $P$  and  $T$  by

$$F = \sqrt{P^2 + T^2}, \quad P = F \cos \psi, \quad T = F \sin \psi, \quad (29)$$

where  $\psi$  denotes the application angle of the resulting force. The notch stress intensity factors  $k_1$  and  $k_2$  are related to the remote loading by

$$\begin{aligned} k_1 &= \xi_1 P = \xi_1 F \cos \psi \\ k_2 &= \xi_2 T = \xi_2 F \sin \psi, \end{aligned} \quad (30)$$

where the coefficients  $\xi_1$  and  $\xi_2$  for these specimens have been computed and tabulated by [Seweryn and Lukaszewicz 2002].

A highly accurate method, the so-called  $G$ - $\Theta$  method [Destuynder et al. 1983; Suo and Combes-cure 1992] and implemented in the finite element code CAST3M (software edited by the Commissariat d'Énergie Atomique of France), was used to calculate the strain energy release rates for branched cracks. To be precise, 30 values of  $G$  were calculated for each crack initiation angle with 5 crack lengths, varying from 0.05 mm to 0.5 mm, and 6 load mixities, varying from pure tension to pure shear. These values of  $G$  were then input into a least square program to obtain  $c_i(\varphi)$ . An example of the fitting procedure is given in Figure 5 that shows the correlation between the numerical values of  $G$  and Equation (28) for a  $60^\circ$  notch under pure mode I loading. In this Figure, the circles represent the FE results, and the line represents the fitting curve according to (28). We can see that the fitting is highly accurate. This accuracy can be obtained for nearly all the cases we treated. Consequently, we can confirm that the present numerical correlation method is suitable.

The numerical values of  $c_i(\varphi)$  are plotted in Figures 6 and 7. For reasons of symmetry, i.e.  $c_1(\varphi) = c_1(-\varphi)$ ,  $c_2(\varphi) = -c_2(-\varphi)$ ,  $c_3(\varphi) = c_3(-\varphi)$ , only  $c_i(\varphi)$  in the interval  $[-\alpha, 0]$  are presented. From these

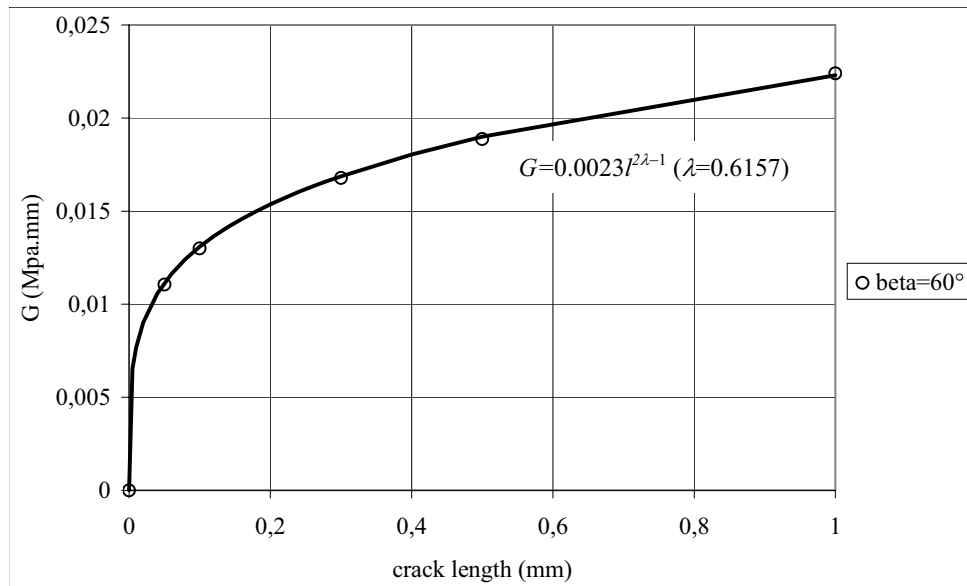


**Figure 5.** Correlation between the numerical values of  $G$  and Equation (28).

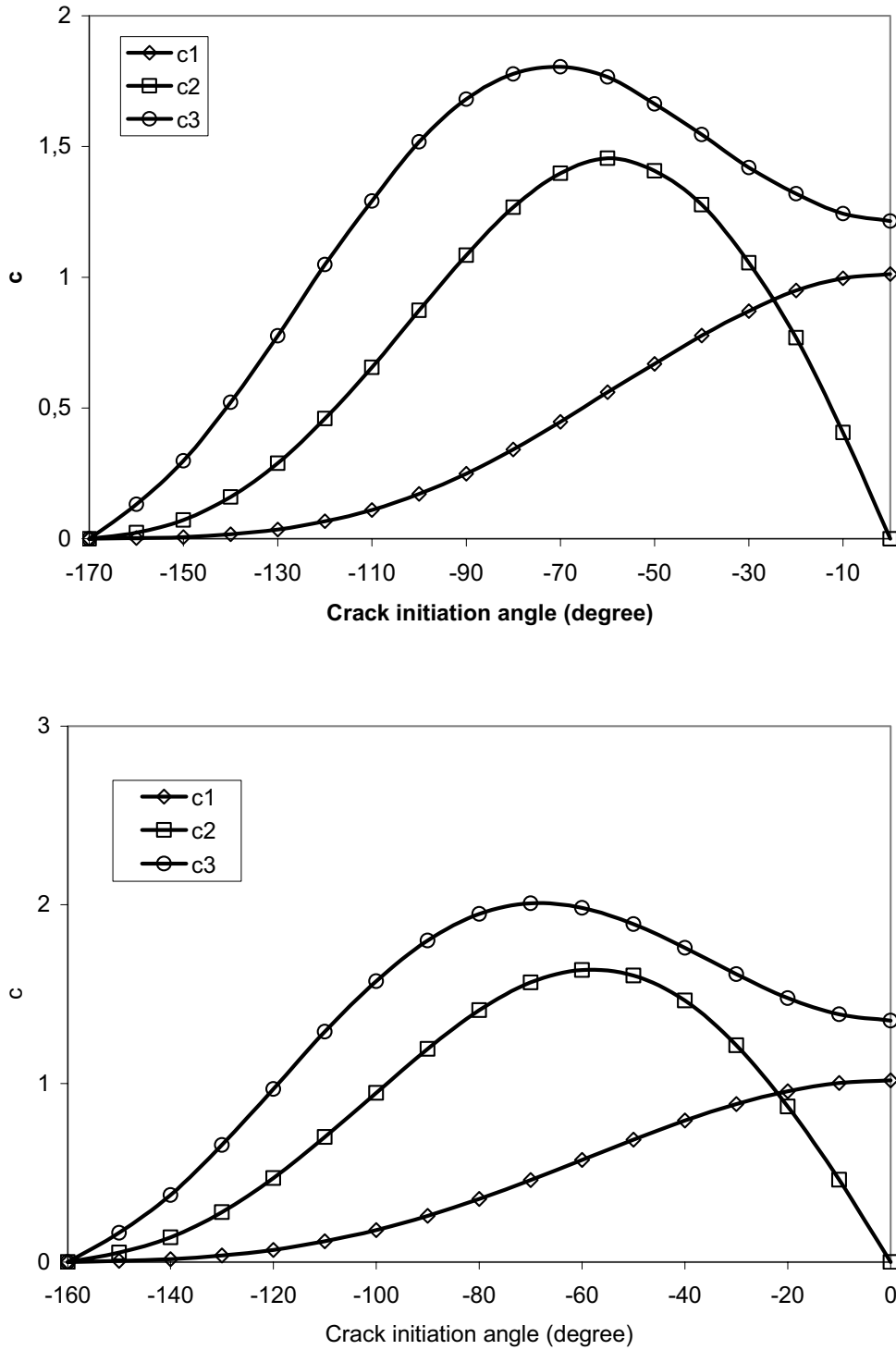


**Figure 6.** Variation of  $c_i$  as function of crack initiation angle: (top)  $\beta = 10^\circ$ , (bottom)  $\beta = 20^\circ$ .

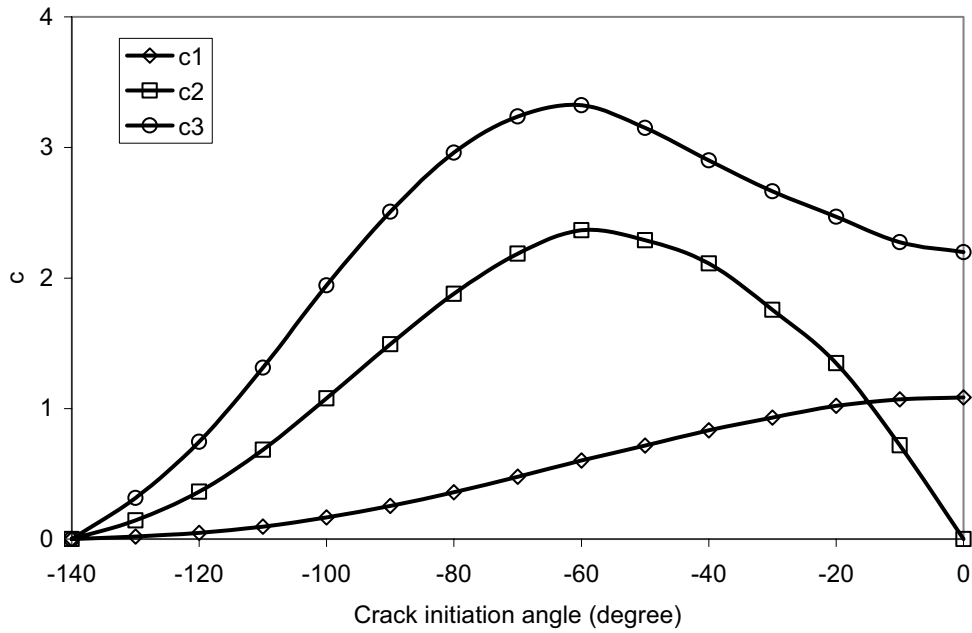
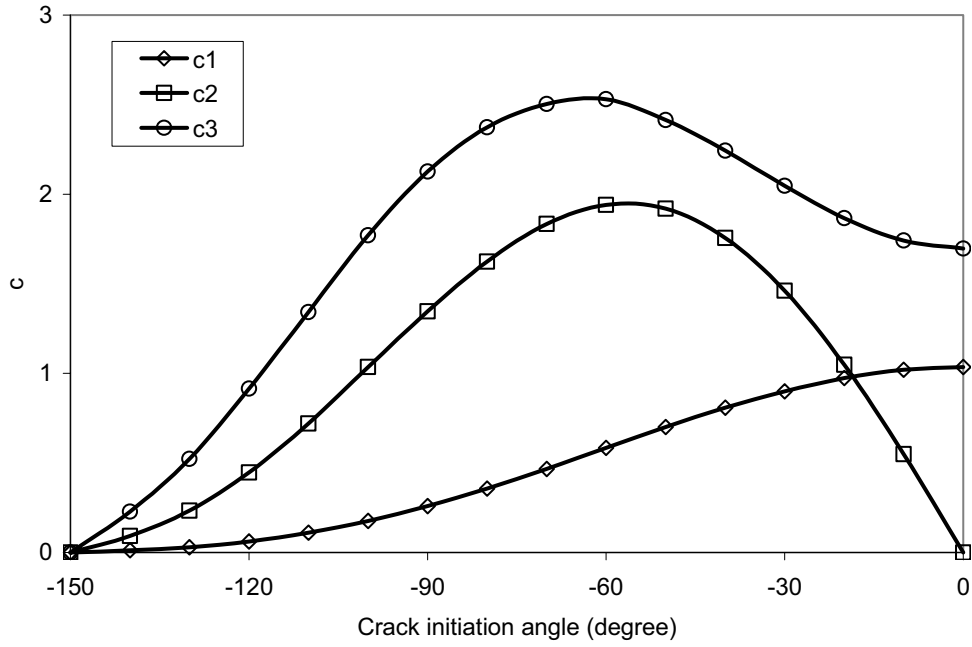


**Figure 7.** Variation of  $c_i$  as function of crack initiation angle: (top)  $\beta = 30^\circ$ ; (bottom)  $\beta = 40^\circ$ .

results, the strain energy release rate for any branched crack from the notch tip of a small length can easily be calculated from Equation (28).

By introducing Equations (4), (28) and (29) into Equation (26), we rewrite explicitly the conditions in the  $G$ - $\sigma$  criterion:

$$\begin{aligned} & \frac{\xi_1 \cdot F \cos \psi}{(2\pi l)^{1-\lambda_1} C_1} (\cos(1+\lambda)\alpha \cos(1-\lambda)\theta + \cos(1-\lambda)\alpha \cos(1+\lambda)\theta) \\ & + \frac{\xi_2 \cdot F \sin \psi (1+\lambda)}{(2\pi l)^{1-\lambda_2} C_2} (-\sin(1-\lambda)\alpha \sin(1+\lambda)\theta + \sin(1+\lambda)\alpha \sin(1-\lambda)\theta) = \sigma_c, \\ & F^2 \left( (\xi_1 \cos \psi)^2 c_1(\varphi) l^{2\lambda_1-1} + \xi_1 \xi_2 \cos \psi \sin \psi c_2(\varphi) l^{\lambda_1+\lambda_2-1} + (\xi_2 \sin \psi)^2 c_3(\varphi) l^{2\lambda_2-1} \right) = G_c, \\ & (\xi_1 \cos \psi)^2 c'_1(\varphi) l^{2\lambda_1-1} + \xi_1 \xi_2 \cos \psi \sin \psi c'_2(\varphi) l^{\lambda_1+\lambda_2-1} + (\xi_2 \sin \psi)^2 c'_3(\varphi) l^{2\lambda_2-1} = 0, \\ & (\xi_1 \cos \psi)^2 c''_1(\varphi) l^{2\lambda_1-1} + \xi_1 \xi_2 \cos \psi \sin \psi c''_2(\varphi) l^{\lambda_1+\lambda_2-1} + (\xi_2 \sin \psi)^2 c''_3(\varphi) l^{2\lambda_2-1} < 0. \end{aligned} \tag{31}$$

These transcendental equations can be resolved by using numerical methods such like the Newton–Raphson method.

### 5. The $S$ - $\sigma$ criterion for mixed-mode loaded notches

The modified Sih criterion is attractive by its simplicity in applications. Under mixed mode loading, this criterion, named the  $S$ - $\sigma$  criterion hereafter, can be described as follows: crack onset occurs from the notch tip if at a neighbouring point  $(\varphi, l)$ ,

- (i) the circumferential tensile stress reaches the material critical strength  $\sigma_c$ ;
- (ii) the strain energy density factor reaches the critical value  $S_c$ ;
- (iii) the strain energy density factor reaches a minimal value among all possible crack onset directions.

In plane stress, the strain energy density factor  $S$  is given by

$$\begin{aligned} S &= \frac{1}{2} (\sigma_{rr} \varepsilon_{rr} + \sigma_{\theta\theta} \varepsilon_{\theta\theta} + 2\sigma_{r\theta} \varepsilon_{r\theta}) r \\ &= \frac{1}{2E} (\sigma_{rr}^2 + \sigma_{\theta\theta}^2 - 2\nu \sigma_{rr} \sigma_{\theta\theta} + (1+\nu) \sigma_{r\theta}^2) r. \end{aligned} \tag{32}$$

At a characteristic distance  $l$  from the notch tip, the strain energy density can be written as follows:

$$S(l, \theta) = d_1(\theta) k_1^2 l^{2\lambda_1-1} + d_2(\theta) k_1 k_2 l^{\lambda_1+\lambda_2-1} + d_3(\theta) k_2^2 l^{2\lambda_2-1}, \tag{33}$$

where the angular functions  $d_1(\theta)$ ,  $d_2(\theta)$ , and  $d_3(\theta)$  can readily be calculated from Equation (1). The direction of crack propagation angle  $\varphi$  is defined by

$$\begin{aligned} \left. \frac{\partial S}{\partial \theta} \right|_{\theta=\varphi} &= \left( d'_1(\theta) k_1^2 l^{2\lambda_1-1} + d'_2(\theta) k_1 k_2 l^{\lambda_1+\lambda_2-1} + d'_3(\theta) k_2^2 l^{2\lambda_2-1} \right)_{\theta=\varphi} = 0 \\ \left. \frac{\partial^2 S}{\partial \theta^2} \right|_{\theta=\varphi} &= \left( d''_1(\theta) k_1^2 l^{2\lambda_1-1} + d''_2(\theta) k_1 k_2 l^{\lambda_1+\lambda_2-1} + d''_3(\theta) k_2^2 l^{2\lambda_2-1} \right)_{\theta=\varphi} > 0. \end{aligned} \tag{34}$$



Consequently, the  $S$ - $\sigma$  criterion is explicitly written as follows:

Find  $(\varphi, l, F)$  satisfying

$$\begin{aligned} & \frac{\xi_1 \cdot F \cos \psi}{(2\pi l)^{1-\lambda_1} C_1} (\cos(1+\lambda)\alpha \cos(1-\lambda)\theta + \cos(1-\lambda)\alpha \cos(1+\lambda)\theta) \\ & + \frac{\xi_2 \cdot F \sin \psi (1+\lambda)}{(2\pi l)^{1-\lambda_2} C_2} (-\sin(1-\lambda)\alpha \sin(1+\lambda)\theta + \sin(1+\lambda)\alpha \sin(1-\lambda)\theta) = \sigma_c \\ & F^2 ((\xi_1 \cos \psi)^2 d_1(\varphi) l^{2\lambda_1-1} + \xi_1 \xi_2 \cos \psi \sin \psi d_2(\varphi) l^{\lambda_1+\lambda_2-1} + (\xi_2 \sin \psi)^2 d_3(\varphi) l^{2\lambda_2-1}) = S_c \\ & (\xi_1 \cos \psi)^2 d_1'(\varphi) l^{2\lambda_1-1} + \xi_1 \xi_2 \cos \psi \sin \psi d_2'(\varphi) l^{\lambda_1+\lambda_2-1} + (\xi_2 \sin \psi)^2 d_3'(\varphi) l^{2\lambda_2-1} = 0 \\ & (\xi_1 \cos \psi)^2 d_1''(\varphi) l^{2\lambda_1-1} + \xi_1 \xi_2 \cos \psi \sin \psi d_2''(\varphi) l^{\lambda_1+\lambda_2-1} + (\xi_2 \sin \psi)^2 d_3''(\varphi) l^{2\lambda_2-1} > 0 \end{aligned} \quad (35)$$

We solved these nonlinear equations by using the Newton–Raphson method.

## 6. Results and discussions

The results obtained for the prediction of the failure loads of  $V$ -notched plates subjected to mixed loading by using the above-mentioned criteria were compared with the experimental data in [Seweryn et al. 1997]. Since the material used, the PMMA, is of brittle character, initiation of a macrocrack often leads to global failure of the element. As a consequence, a critical load to initiate a crack was considered as the fracture load of the plate.

Figures 8 and 9 presents the variation of the direction of crack initiation angles  $\varphi$  versus the load application angle  $\psi$  for different values of the notch-opening angle  $\beta$ . Experimental data were marked by points and the predicted results were presented by continue lines with points. From these figures we can observe that the predicted crack initiation directions by both the criteria agree well with the experimental results for small opening angles  $\beta \leq 30^\circ$ . However, the predicted results are less accurate for specimens with a notch opening angle  $\beta = 40^\circ$ .

In Figures 10 and 11, we plot the ratios of the critical mixed mode loads  $F_c$  to the critical tensile load  $P_c$  determined from both the criteria as function of load application angle  $\psi$ . Experimental results are also represented for comparison. These figures show that both the criteria provide us with good prediction if the notch opening angle  $\beta > 10^\circ$ . For  $\beta = 10^\circ$ , the  $S$ - $\sigma$  criterion still agrees quite well with the test data, while the  $G$ - $\sigma$  criterion gives somewhat conservative predictions when the shear loads dominate.

A common advantage of both the proposed criteria is that they are all self-consistent. No additional conditions are required in their application. This differs from the early-proposed local criteria such as the RKR criterion [Ritchie et al. 1973] or McClintock's criterion [McClintock 1958] in which a virtual process distance from the crack tip was introduced but can't be determined by the criteria themselves. This distance, however, is clearly defined with the criteria used in the present work. In general, it depends not only upon the material mechanical properties (strength and toughness), but also upon the structure configuration (geometry, loading). In the present notch cases, this characteristic length varies from 0.02 mm to 0.035 mm.

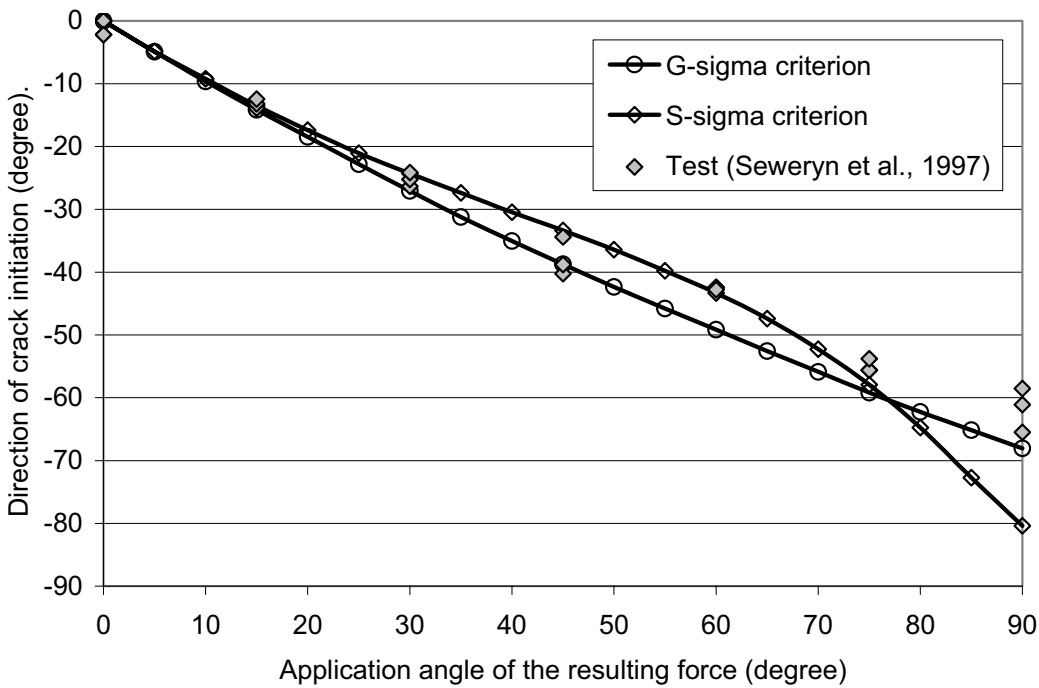
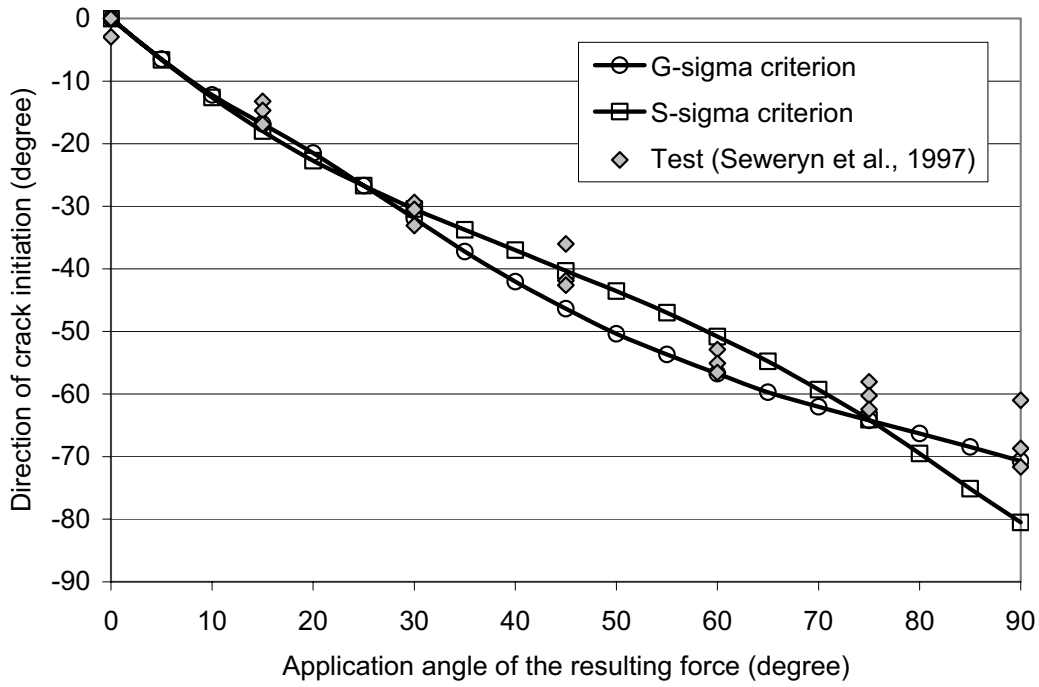


**Figure 8.** Direction of crack initiation versus application angle of resulting force: (top)  $\beta = 10^\circ$ ; (bottom)  $\beta = 20^\circ$ .

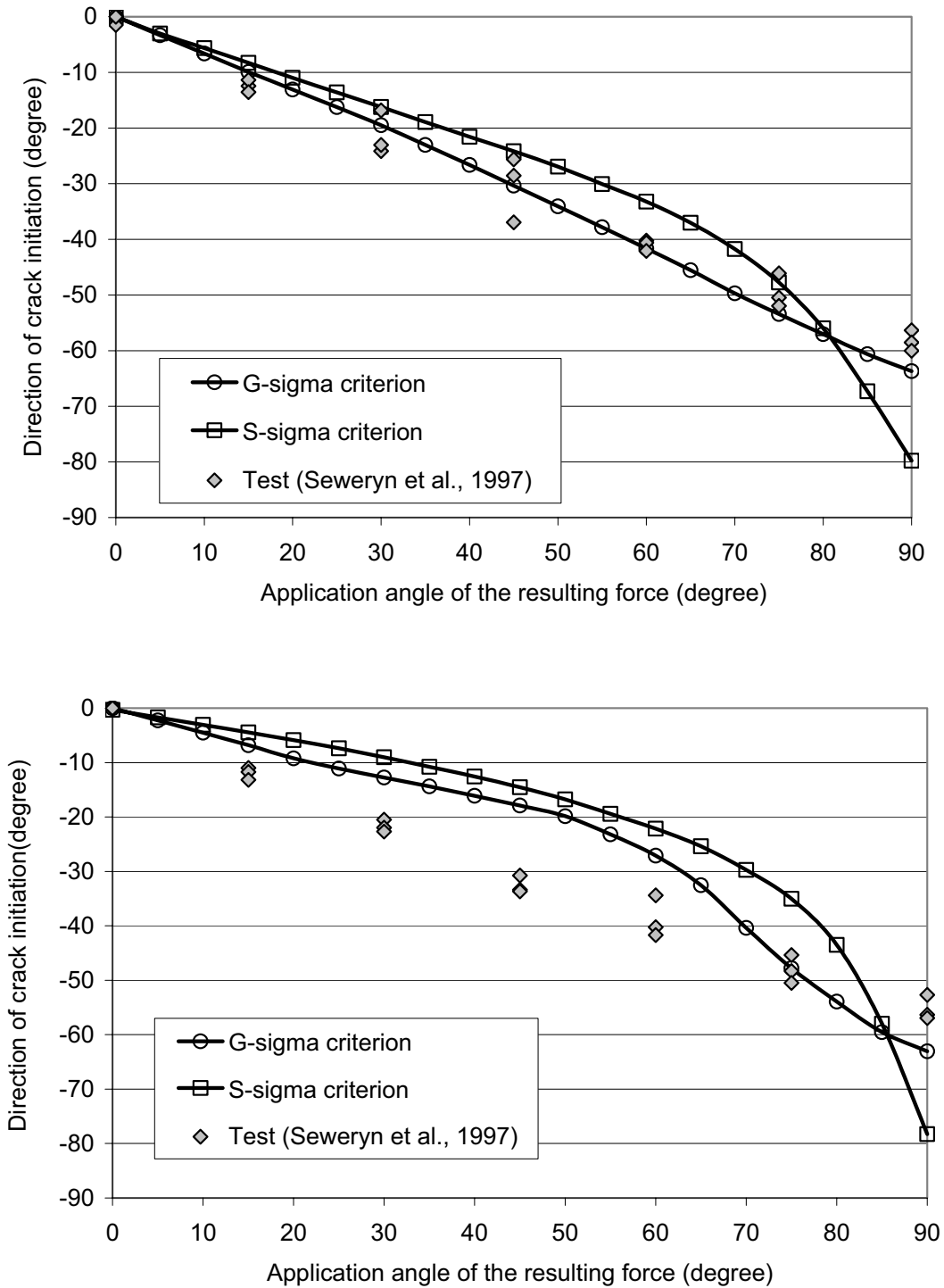


**Figure 9.** Direction of crack initiation versus application angle of resulting force: (top)  $\beta = 30^\circ$ ; (bottom)  $\beta = 40^\circ$ .

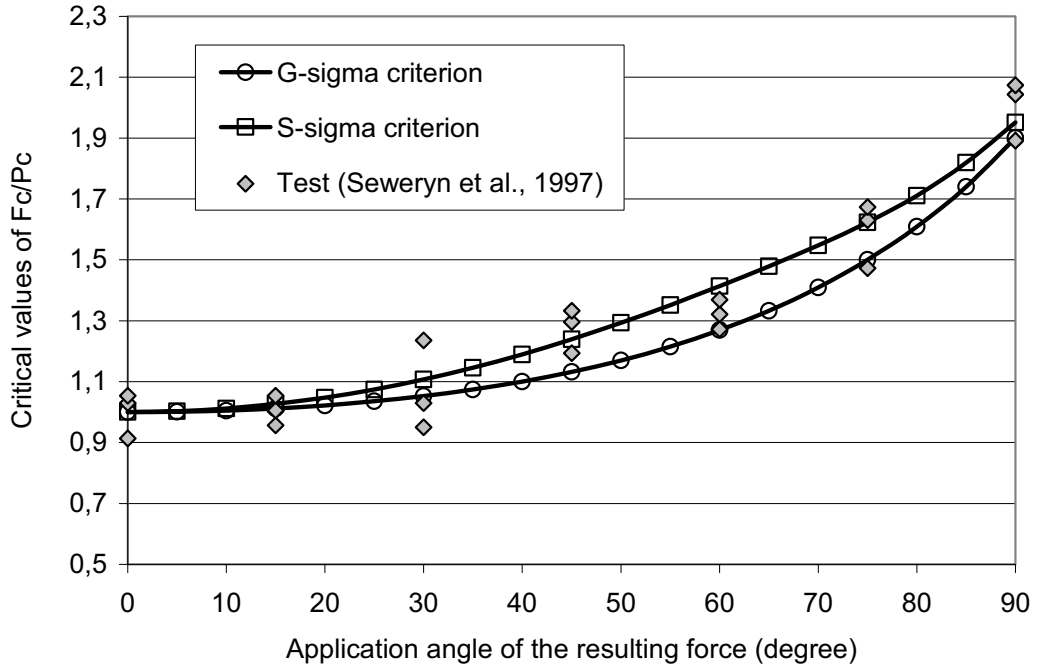
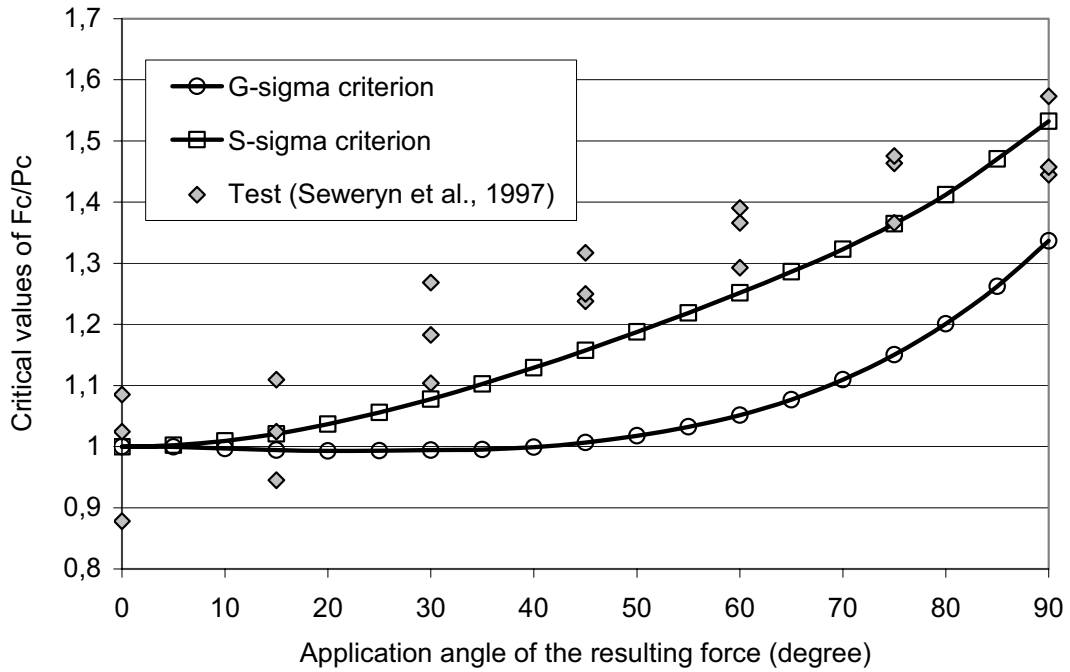


**Figure 10.** Critical values of  $F_c/P_c$  versus application angle of resulting force: (top)  $\beta = 10^\circ$ ; (bottom)  $\beta = 20^\circ$ .

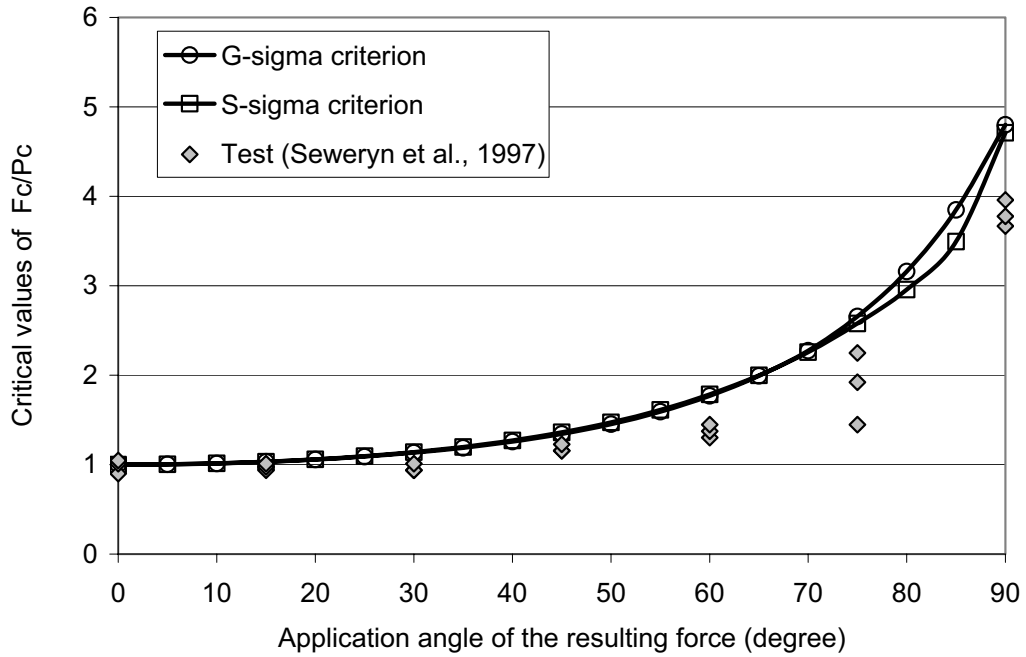
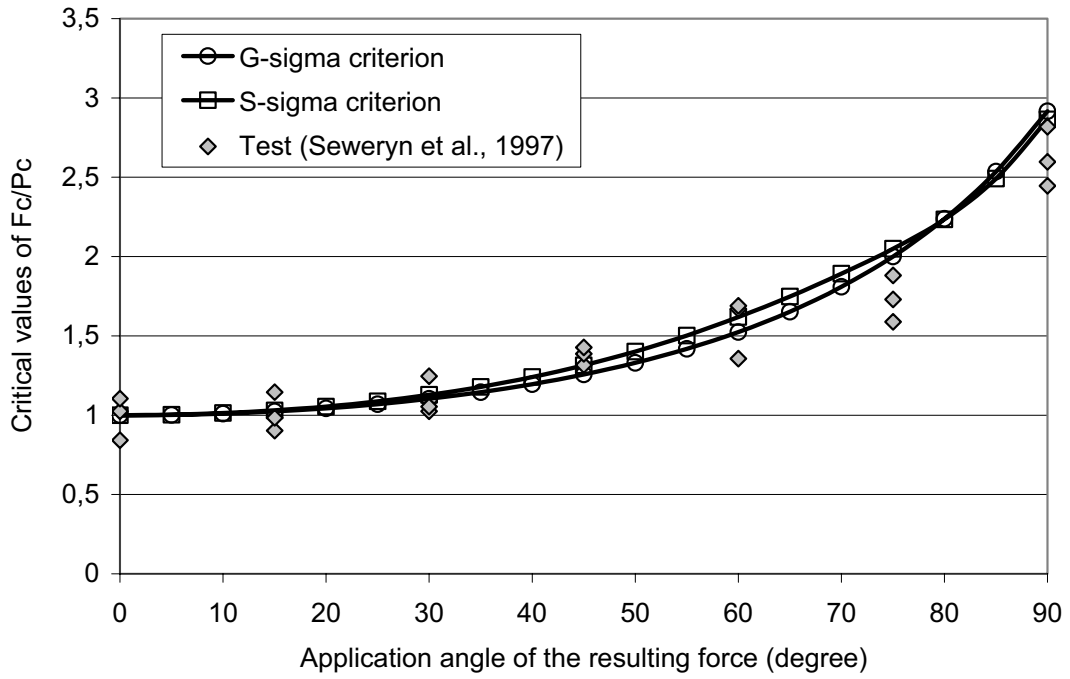


**Figure 11.** Critical values of  $F_c/P_c$  versus application angle of resulting force: (top)  $\beta = 30^\circ$ ; (bottom)  $\beta = 40^\circ$ .

## 7. Concluding remarks

In this work, the crack initiation from a notch tip under mixed loads was considered. Two phenomenological criteria were applied to predict the crack initiation. These two criteria, namely the  $G$ - $\sigma$  criterion and the  $S$ - $\sigma$  criterion, were established by using the concept proposed by [Leguillon 2002], in which both the stress and the energy balances are taken into consideration in the simulation of the crack initiation. The common advantage of the criteria is their self-consistency.

The  $G$ - $\sigma$  criterion was established on the analysis of up and low bounds of the critical loading, as a consequence, is physically reasonable. In the present work, by means of an important numerical effort, we have established the indispensable relationships between the strain energy release rate after a crack kinking and the remote loads for a  $V$ -notch under mixed mode loading. These relationships enable us to apply the  $G$ - $\sigma$  in a straightforward manner.

The strain energy density criterion was proposed for crack propagation and bifurcation with successful applications. In the present work, this criterion was modified on the basis of Leguillon's concept to form a criterion capable to predict the crack initiation from a  $V$ -notch tip. Even though its physical interpretation is less evident, this criterion benefits from its simplicity in applications.

Confrontation with experimental data shows that both the criteria enable reasonably accurate prediction of fracture in elements with  $V$ -notches subjected to mixed mode loading. Consequently, they can be effectively applied in practical engineering applications.

## References

- [Bansal and Kumosa 1998] A. Bansal and M. Kumosa, "Analysis of double edge-cracked Iosipescu specimens under biaxial loads", *Eng. Fract. Mech.* **59**:1 (1998), 89–100.
- [Bazant 2000] Z. P. Bazant, "Size effect", *Int. J. Solids Struct.* **37**:1-2 (2000), 69–80.
- [Broughton et al. 1990] W. Broughton, M. Kumosa, and D. Hull, "Analysis of the Iosipescu shear test as applied to unidirectional carbon-fibre reinforced composites", *Compos. Sci. Technol.* **38**:4 (1990), 299–325.
- [Destuynder et al. 1983] P. Destuynder, M. Djaoua, and S. Lescure, "Quelques remarques sur la mécanique de la rupture élastique", *J. Mec. Theor. Appl.* **2** (1983), 113–135.
- [Dunn et al. 1997a] M. Dunn, W. Suwito, and S. Cunningham, "Fracture initiation at sharp notches: correlation using critical stress intensities", *Int. J. Solids Struct.* **34**:29 (1997), 3873–3883.
- [Dunn et al. 1997b] M. Dunn, W. Suwito, S. Cunningham, and C. May, "Fracture initiation at sharp notches under mode I, mode II and mild mixed mode loading", *Int. J. Fract.* **84**:4 (1997), 367–381.
- [Irwin 1968] G. Irwin, "Linear fracture mechanics, fracture transition and fracture control", *Eng. Fract. Mech.* **1**:2 (1968), 241–257.
- [Kosai et al. 1993] M. Kosai, A. Kobayashi, and M. Ramulu, *Tear straps in airplane fuselage, durability of metal aircraft structures*, edited by S. Atluri et al., Atlanta Technology Publishers, 1993.
- [Leguillon 2002] D. Leguillon, "Strength or toughness? A criterion for crack onset at a notch", *Eur. J. Mech. A Solids* **21**:1 (2002), 61–72.
- [Leguillon and Yosibash 2003] D. Leguillon and Z. Yosibash, "Crack onset at a v-notch. Influence of the notch tip radius", *Int. J. Fract.* **122**:1-2 (2003), 1–21.
- [McClintock 1958] F. McClintock, "Ductile fracture instability in shear", *J. Appl. Mech. (Trans. ASME)* **25** (1958), 582–588.
- [Mroz and Seweryn 1998] Z. Mroz and A. Seweryn, "Non-local failure and damage evolution rule: application to a dilatant crack model", *J. Phys.* **8** (1998), 257–268.
- [Palaniswamy and Knauss 1972] K. Palaniswamy and W. Knauss, "Propagation of a crack under general in-plane tension", *Int. J. Fract.* **8**:1 (1972), 114–117.

- [Reedy and Guess 1995] J. E. Reedy and T. Guess, “Butt tensile joint strength: interface corner stress intensity factor prediction”, *J. Adhes. Sci. Technol.* **9** (1995), 237–251.
- [Ritchie et al. 1973] R. Ritchie, J. Knott, and J. Rice, “On the relationship between critical tensile stress and fracture toughness in mild steel”, *J. Mech. Phys. Solids* **21**:6 (1973), 395–410.
- [Seweryn and Lukaszewicz 2002] A. Seweryn and A. Lukaszewicz, “Verification of brittle fracture criteria for elements with V-shaped notches”, *Eng. Fract. Mech.* **69**:13 (2002), 1487–1510.
- [Seweryn et al. 1997] A. Seweryn, S. Poskrobko, and Z. Mroz, “Brittle fracture in plane elements with sharp notches under mixed-mode loading”, *J. Eng. Mech.* **123**:6 (1997), 535–543.
- [Sih 1974] G. Sih, “Strain-energy-density factor applied to mixed mode crack problems”, *Int. J. Fract.* **10**:3 (1974), 305–321.
- [Suo and Combescure 1992] X. Suo and A. Combescure, “On the application of  $G-\theta$  method and its comparison with De Lorenzi’s approach”, *Nucl. Eng. Des.* **135**:2 (1992), 207–224.

Received 2 Dec 2005.

JIA LI: [jia.li@lpmtm.univ-paris13.fr](mailto:jia.li@lpmtm.univ-paris13.fr)

LPMTM, CNRS UPR 9001, Institut Galilée, Université Paris 13, 99 Avenue Jean-Baptiste Clément, 93430 Villetaneuse, France

XIAO-BING ZHANG: [zang@moniut.univ-bpclermont.fr](mailto:zang@moniut.univ-bpclermont.fr)

LAMI, Université Blaise Pascal de Clermont-Ferrand, Avenue Aristide Briand, 03100 Montluçon, France

## A CLOSED-FORM SOLUTION FOR A CRACK APPROACHING AN INTERFACE

BORIS NULLER, MICHAEL RYVKIN AND ALEXANDER CHUDNOVSKY

A closed-form solution is presented for the stress distribution in two perfectly bonded isotropic elastic half-planes, one of which includes a fully imbedded semi-infinite crack perpendicular to the interface. The solution is obtained in quadratures by means of the Wiener–Hopf–Jones method. It is based on the residue expansion of the contour integrals using the roots of the Zak–Williams characteristic equation. The closed-form solution offers a way to derive the Green’s function expressions for the stresses and the SIF (stress intensity factor) in a form convenient for computation. A quantitative characterization of the SIF for various combinations of elastic properties is presented in the form of function the  $c(\alpha, \beta)$ , where  $\alpha$  and  $\beta$  represent the Dundurs parameters. Together with tabulated  $c(\alpha, \beta)$  the Green’s function provides a practical tool for the solution of crack-interface interaction problems with arbitrarily distributed Mode I loading. Furthermore, in order to characterize the stability of a crack approaching the interface, a new *interface parameter*  $\chi$ , is introduced, which is a simple combination of the shear moduli  $\mu_s$  and Poisson’s ratios  $\nu_s$  ( $s = 1, 2$ ) of materials on both sides of the interface. It is shown that  $\chi$  uniquely determines the asymptotic behavior of the SIF and, consequently, the crack stability. An estimation of the interface parameter prior to detailed computations is proposed for a qualitative evaluation of the crack-interface interaction. The propagation of a stable crack towards the interface with a vanishing SIF is considered separately. Because in this case the fracture toughness approach to the material failure is unsuitable an analysis of the complete stress distribution is required.

### 1. Introduction

Determining the stress field in the vicinity of a crack tip approaching a bimaterial interface has important applications for layered elastic materials. [Zak and Williams \[1963\]](#) proposed the first formulation and solution of the problem for a semi-infinite crack perpendicular to a bimaterial interface with the crack tip at the interface. [Khrapkov \[1968\]](#) offered a closed-form solution for the problem of a finite crack with its tip at the interface. [Cook and Erdogan \[1972\]](#) and [Erdogan and Bircikoglu \[1973\]](#) derived the integral equations and provided the numerical solutions for fully imbedded semi-infinite and finite cracks, and for cracks either terminating at or crossing the material interface. A similar dislocation approach was employed by [Wang and Stahle 1998\]](#) for the study of stress fields in the vicinity of a finite crack approaching the interface. Using the exact solution obtained for Mode III as a prototype, [Atkinson \[1975\]](#) introduced an asymptotic solution for the SIF with respect to a small distance  $\varepsilon$  between the crack tip and the interface. Here the SIF is presented as  $K_I = \varepsilon^{p_1-1/2} f(\alpha, \beta)$ , with  $p_1$ ,  $\alpha$ , and  $\beta$  representing the first root of the Zak–Williams characteristic equation and the Dundurs parameters respectively. Later, [He and Hutchinson \[1989\]](#) considered a set of more general problems related to crack arrest and to penetration through or deflected by the interface.

---

*Keywords:* stress intensity factor, crack stability, bimaterial plane, analytic function.



Employing the amplitude factor  $k_I$  for the boundary value problem with a crack terminating at the interface, He and Hutchinson were able to improve the representation of  $K_I$  to

$$K_I = k_I \varepsilon^{p_1 - 1/2} c(\alpha, \beta),$$

where the function  $c(\alpha, \beta)$  is a solution of a system of singular integral equations. [Romeo and Ballarini \[1995\]](#) evaluated the function  $c(\alpha, \beta)$  and applied the results to finite and semi-infinite cracks. For certain values of  $\alpha$  and  $\beta$ , however, the evaluation of the function  $c(\alpha, \beta)$  results in an uncertainty of  $0 \cdot \infty$  type that cannot be resolved numerically. [Leguillon et al. \[2000\]](#) investigated of the competition between three fracture scenarios – primary crack growth, interface debonding, and a new crack nucleation beyond the interface – by means of asymptotic analysis.

In this paper we construct a closed-form solution for the problem of a semi-infinite crack perpendicular to an interface between two isotropic elastic half-planes under Mode I loading by the Winner–Hopf–Jones method [\[Noble 1958\]](#). While [Nuller et al. \[2001\]](#) summarized some of the results earlier, here we present the complete solution along with an analysis of the closed-form representation of the function  $c(\alpha, \beta)$ . For convenience of application, the values of the function  $c(\alpha, \beta)$  are computed and reported in [Table 2](#). Romeo and Ballarini’s results coincide with the closed-form solution only in the case when  $\alpha = \beta = 0$  and diverge significantly when  $\alpha$  approaches  $\pm 1$ .

In [Section 2](#) we present the general formulation and closed-form solution of an auxiliary problem on a crack fully imbedded in the left half-plane and perpendicular to the interface, which is conjugate (the same Wiener–Hopf equation) to the problem considered by [\[Khrapkov 1968\]](#). Using this solution in [Section 3](#), we evaluate the Green’s function for the SIF. [Section 4](#) is dedicated to an assessment of crack stability through an analysis of the asymptotic expression of the SIF. We introduce a new parameter of the interface,  $\chi$ , to characterize the stability of a crack approaching the interface. The parameter  $\chi$  is a simple combination of shear moduli and Poisson’s ratios on both sides of the interface. Addressed separately is the case of stable crack propagation when the SIF concept of fracture mechanics does not apply.

The first root of the Zak–Williams characteristic equation  $p_1$  is a cornerstone of crack stability analysis and, as such, of the asymptotic representations of the solution. A proof of the existence and uniqueness of the  $p_1$  value in the strip  $0 < \operatorname{Re} p < 1$  of the complex plane of the Mellin transform parameter  $p$  for all possible values of elastic constants is presented in [Appendix A](#). The dependence of the first root location on the real axis upon the interface parameter  $\chi$  is also analyzed there.

## 2. General formulation

Consider a semi-infinite crack perpendicular to the interface between two perfectly bonded dissimilar elastic half-planes [Figure 1](#). The distance of the crack tip from the interface is  $\varepsilon$ . The elastic properties of the materials are defined by the shear moduli  $\mu_s$  and Poisson’s ratio’s  $\nu_s$ . The values of the index  $s = 1, 2$  correspond to the uncracked and the cracked half-planes respectively. We introduce the system of polar coordinates  $R, \theta$  in which the origin lies at the intersection of the crack axis and the interface such that the crack is located along the line  $\theta = \pi$ . Formulating the problem with the non-dimensional radial coordinate  $r = R/\varepsilon$ , the crack tip is associated with the point  $r = 1, \theta = \pi$ .

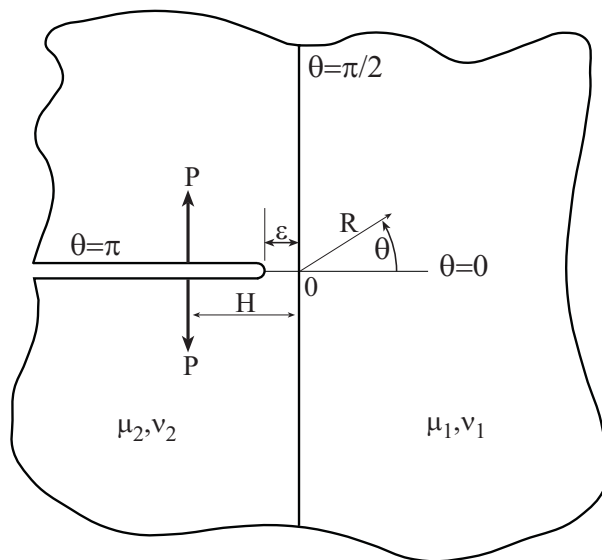


**Figure 1.** Perpendicular to the interface crack, fully imbedded in the left half-plane.

We assume that the loading corresponds to the Mode I, the stress field vanishes at  $r \rightarrow \infty$ , and the local strain energy is bounded in the crack tip vicinity. Using the apparent symmetry, we formulate the boundary value problem for the upper half-plane  $0 < \theta < \pi$ ,  $0 < r < \infty$  as follows. The radial and angular displacements  $u(r, \theta)$ ,  $v(r, \theta)$  and the stresses  $\sigma_\theta(r, \theta)$  satisfy the continuity conditions at the interface

$$[v(r, \pi/2)] = [u(r, \pi/2)] = 0; \quad [\sigma_\theta(r, \pi/2)] = [\tau_{r\theta}(r, \pi/2)] = 0, \quad 0 < r < \infty, \quad (1)$$

where  $[f(r, \theta)]$  denotes the jump of  $f(r, \theta)$  in the  $\theta$  direction. At the boundary of the half-plane

$$v(r, 0) = 0, \quad \tau_{r\theta}(r, 0) = \tau_{r\theta}(r, \pi) = 0, \quad 0 < r < \infty, \quad (2)$$

$$v(r, \pi) = v(r), \quad 0 < r \leq 1, \quad (3)$$

$$\sigma_\theta(r, \pi) = \sigma(r), \quad 1 < r < \infty. \quad (4)$$

Here the function  $\sigma(r)$  represents the applied load and  $v(r) \equiv 0$  for the problem under consideration. However, we write condition in Equation (3) in a more general form for future consideration. We seek the solution as Papkovitch–Neuber functions presented in the form of the Mellin integrals

$$2\mu_s v(r, \theta) = \frac{1}{2\pi i} \int_{L_0} [A_s(p)(p - \kappa_s) \sin(p + 1)\theta + B_s(p)(p - 1) \sin(p - 1)\theta + C_s(p)(p - \kappa_s) \cos(p + 1)\theta + D_s(p)(p - 1) \cos(p - 1)\theta] r^{-p} dp, \quad (5)$$

$$2\mu_s u(r, \theta) = \frac{1}{2\pi i} \int_{L_0} [A_s(p)(p + \kappa_s) \cos(p + 1)\theta + B_s(p)(p - 1) \cos(p - 1)\theta - C_s(p)(p + \kappa_s) \sin(p + 1)\theta - D_s(p)(p - 1) \sin(p - 1)\theta] r^{-p} dp, \quad (6)$$

where the integration path  $L_0$  is a contour parallel to the imaginary axis of the plane of the complex Mellin transform parameter  $p$ , and  $\kappa_s = 3 - 4\nu_s$ . The subscript  $s = 1, 2$  denotes the quantities related to the right ( $0 < \theta < \pi/2$ ) and left ( $\pi/2 < \theta < \pi$ ) quadrants respectively. The unknown functions  $A_s, B_s, C_s, D_s$  are to be defined from the boundary conditions.

Using Jones method [Noble 1958] we introduce “-” and “+” transforms

$$v^-(p) = \int_1^\infty v(r, \pi)r^{p-1}dr, \quad \sigma^+(p) = \int_0^1 \sigma_\theta(r, \pi)r^p dr,$$

which are analytical in the respective left and right half-planes separated by the contour  $L_0$ . Other functions analytical in these half-planes will be also denoted by the superscripts “+” and “-”. The boundary conditions given by Equations (3) and (4) may now be presented as

$$v(r, \pi) = \frac{1}{2\pi i} \int_{L_0} [v^-(p) + v^+(p)]r^{-p}dp, \quad 0 < r < \infty \tag{7}$$

$$\sigma_\theta(r, \pi) = \frac{1}{2\pi i} \int_{L_0} [\sigma^-(p) + \sigma^+(p)]r^{-p-1}dp, \quad 0 < r < \infty \tag{8}$$

$$\sigma^-(p) = \int_1^\infty \sigma(r)r^p dr, \quad v^+(p) = \int_0^1 v(r)r^{p-1}dr. \tag{9}$$

Substitution of Equations (5) and (6) into the boundary conditions in Equations (1), (2), (7) and in Equations (1), (2), (8) yields two systems of eight linear algebraic equations, each with coefficients  $a_{ik}(p)$  with respect to the unknowns  $A_1(p), B_1(p), \dots, D_2(p)$ . In both systems the first seven equations are identical and homogeneous. The only nonhomogeneous equations are the last ones obtained from conditions in Equations (7) and (8). Denoting the determinants of the first and second systems as  $N_v(p)$  and  $N_\sigma(p)$  respectively, the expression for the function  $A_1(p)$  may be presented in the following alternative forms

$$A_1(p) = \frac{[v^-(p) + v^+(p)]M(p)}{N_v(p)}, \quad A_1(p) = \frac{[\sigma^-(p) + \sigma^+(p)]M(p)}{N_\sigma(p)}, \tag{10}$$

where  $M(p)$  is the cofactor of the element  $a_{81}(p)$ , which is the same in both systems, and where

$$N_v(p) = \mu_2^{-1}b_0b_1b_2(1 - p)^2 \sin^2 \pi p, \quad N_\sigma(p) = 2p(1 - p)^2 \sin \pi p N(p), \tag{11}$$

$$N(p) = 2b_1(b_2 \cos \pi p + b_3p^2) + b_4, \tag{12}$$

where

$$b_0 = 1 + \kappa_2, \quad b_1 = 1 + \kappa_1\mu, \quad b_2 = \mu + \kappa_2, \quad b_3 = 2(\mu - 1),$$

$$b_4 = -2\kappa_1\mu^2 - (\kappa_1 - 1)(\kappa_2 - 1)\mu + \kappa_2^2 + 1, \quad \mu = \frac{\mu_2}{\mu_1}.$$

Equating the right hand sides of Equations (10) we obtain the Wiener–Hopf equation

$$\sigma^- + \sigma^+ = K(p)[v^-(p) + v^+(p)], \quad K(p) = \frac{N_\sigma(p)}{N_v(p)}, \quad p \in L_0, \tag{13}$$

for the two unknown functions  $\sigma^+(p)$  and  $v^-(p)$ . The solution is constructed using the technique developed by [Nuller 1976]. The function  $K(p)$  can be presented in the form of a product  $K(p) = K_1(p)K_2(p)$ ,

where

$$K_1(p) = 4\mu_2 b_0^{-1} p \cot \pi p, \quad K_2(p) = \frac{2b_1(b_2 \cos \pi p + b_3 p^2) + b_4}{2b_1 b_2 \cos \pi p}.$$

Factorization with respect to the contour  $L_0$ , which is taken to be the imaginary axis, yields

$$K_m(p) = \frac{K_m^+(p)}{K_m^-(p)}, \quad m = 1, 2.$$

For the function  $K_1(p)$ , the factorization is trivial. For the function  $K_2(p)$  the factorization is carried out by the use of the Cauchy-type integrals, see [Gakhov 1966] and can be performed due to the following properties of this function on  $L_0$ : (1) it is Hölder continuous; (2) it has no zeros, see Appendix A; (3) it has zero index; and (4)  $\ln K_2(p)$  decays exponentially as  $|p| \rightarrow \infty$ , which follows from the asymptotic relation  $K_2(it) \sim 1 + O[t^2 \exp(-\pi|t|)]$ , as  $|t| \rightarrow \infty$ . Hence, the factorization  $K(p) = K^+(p)[K^-(p)]^{-1}$  is given by

$$\begin{aligned} K^+(p) &= \frac{4\mu_2 \Gamma(p+1)}{b_0 \Gamma(p+1/2)} K_2^+(p), \\ K^-(p) &= \frac{\Gamma(1/2-p)}{\Gamma(1-p)} K_2^-(p), \\ K_2^\pm(p) &= \exp \left[ -\frac{1}{2\pi i} \int_{-i\infty}^{i\infty} \frac{\ln K_2(t) dt}{t-p} \right], \quad p \notin L_0 \\ K_2^\pm(p) &= K_2^{\pm 1/2}(p) \exp \left[ -\frac{1}{2\pi i} \int_{-i\infty}^{i\infty} \frac{\ln K_2(t) dt}{t-p} \right], \quad p \in L_0, \end{aligned} \tag{14}$$

where  $\Gamma(p)$  is the Gamma function.

Now the Wiener–Hopf Equation (13) can be rewritten in the following form

$$\frac{\sigma^-(p) + \sigma^+(p)}{K^+(p)} = \frac{v^-(p) + v^+(p)}{K^-(p)}, \quad p \in L_0. \tag{15}$$

Let the external conditions be given by the power form expressions

$$\sigma(r) = ar^{-\gamma-1}, \quad v(r) = br^\delta, \tag{16}$$

with  $\gamma > 0$ ,  $\delta > 0$ , and  $a < 0$ , which corresponds to Mode I loading. For this case Equations (9) yield

$$\sigma^-(p) = \frac{-a}{p-\gamma}, \quad v^+(p) = \frac{b}{p+\delta}, \tag{17}$$

and the nonhomogeneous Wiener–Hopf Equation (15) can be factorized as follows

$$\begin{aligned} \frac{\sigma^+(p)}{K^+(p)} + \frac{a}{p-\gamma} \left[ \frac{1}{K^+(\gamma)} - \frac{1}{K^+(p)} \right] - \frac{b}{(p+\delta)K^-(-\delta)} = \\ \frac{v^-(p)}{K^-(p)} + \frac{b}{p+\delta} \left[ \frac{1}{K^-(p)} - \frac{1}{K^-(-\delta)} \right] + \frac{a}{(p-\gamma)K^+(\gamma)}. \end{aligned} \tag{18}$$

Both parts of the last equality are analytical in their respective half-planes separated by the contour  $L_0$  and decrease at least as  $p^{-1}$  or faster when  $|p| \rightarrow \infty$ . Employing now Liouville’s theorem, we conclude

that each side of Equation (18) is equal to zero. Consequently, we find the stress transform to be

$$\sigma^+(p) = K^+(p) \left[ \frac{b}{(p + \delta)K^-(-\delta)} - \frac{a}{(p - \gamma)K^+(\gamma)} \right] + \frac{a}{p - \gamma}. \tag{19}$$

The asymptotic stress distribution at the crack tip is defined by the stress transform behavior for large  $|p|$ . From Equations (14) and (19) it is evident that for  $|p| \rightarrow \infty$

$$\sigma^+(p) \sim -\frac{4\mu_2}{1 + \kappa_2} \left[ \frac{a}{K^+(\gamma)} - \frac{b}{K^-(-\delta)} \right] p^{-1/2}. \tag{20}$$

As a result,

$$\sigma_\theta(r, \pi) \sim -\frac{4\mu_2}{1 + \kappa_2} \left[ \frac{a}{K^+(\gamma)} - \frac{b}{K^-(-\delta)} \right] \frac{1}{\sqrt{\pi(1-r)}}, \quad r \rightarrow 1 - 0.$$

In view of the accepted length scale normalization, the actual displacements  $v(R)$  are obtained from the scaled displacements derived in the solution by multiplying by  $\varepsilon$ , that is,  $v(R) = \varepsilon v(r)$ . Consequently, the relation between the scaled and the non-scaled stresses is

$$\sigma(R, \theta) = \frac{\sigma(r, \theta)}{\varepsilon}. \tag{21}$$

### 3. Green’s function for SIF

The study of crack stability near the interface requires solutions for arbitrarily distributed loads, which can be obtained using the Green’s function of the particular problem, namely the solution for the two unit forces  $P = 1$  applied to the crack faces symmetrically at some point  $R = H$ ; see Figure 1. This solution is defined by the boundary conditions in Equations (1), (2) and (4) with

$$\sigma_\theta(r) = -\delta(r - h),$$

where  $\delta(r)$  is the delta function and  $h = H/\varepsilon$ .

Through the superposition principle this problem may be considered as the sum of the following two problems. The first is the problem seen in Equations (1), (2) and (4) with  $\sigma_\theta(r) = -\delta(r - h)$  for  $0 < r < \infty$ . The second is a mixed problem defined by the conditions given in Equations (1)–(4) with  $\sigma(r) = 0$  and  $v(r) = -v_\delta(r)$ , where  $v_\delta(r)$  represents the displacements obtained in the first problem. The solution of the first problem clearly has no singularity at the point of interest  $r = 1$ ,  $\theta = \pi$  as the stresses  $\sigma(r, \theta)$  are equal to zero for  $0 < r < 1$ . Therefore the singularity at this point for the Green’s function of the initial problem is completely defined by the stress field of the second problem.

In the first problem the transforms of the applied loading are given by  $\sigma^+(p) = 0$ , and  $\sigma^-(p) = -h^p$ . Consequently, from Equations (10) and (11) we obtain

$$v_\delta(r) = -\frac{1}{2\pi i} \int_{L_0} \frac{Q(p)h^p}{N(p)r^p} dp, \quad Q(p) = \frac{b_0 b_1 b_2 \sin \pi p}{2p\mu_2}.$$

Employing the residue theorem and closing the integration path to the left of the contour  $L_0$  we find that for  $r < 1$

$$v_\delta(r) = \sum_{k=1}^{\infty} \frac{Q(-p_k)r^{p_k}}{N'(-p_k)h^{p_k}}. \tag{22}$$

Here  $p = -p_k$  are the roots of the Zak–Williams characteristic equation, see Equation (12):

$$N(p) = 0 \tag{23}$$

which are located in the left half-plane  $\text{Re } p < 0$ . The numbering is in accord with the increasing distance from the imaginary axis.

It follows from Equations (9), (16), (17), and (22) that for the second problem

$$v_\delta^+(p) = - \sum_{k=1}^{\infty} \frac{Q(-p_k)}{N(-p_k)(p + p_k)h^{p_k}} .$$

Taking into account that  $\sigma^-(p) = 0$  and reapplying the procedure (17)–(20), we obtain

$$\sigma^+(p) \sim 2b_1b_2 \left[ \sum_{k=1}^{\infty} \frac{\sin \pi p_k}{p_k N'(-p_k) K^-(-p_k) h^{p_k}} \right] p^{-1/2}, \quad |p| \rightarrow \infty . \tag{24}$$

Consequently, the asymptote of the singular stresses in the initial problem that also defines the Green’s function for the SIF  $K_I$  is given by

$$\sigma_\theta(r, \pi) \sim 2b_1b_2 \left[ \sum_{k=1}^{\infty} \frac{\sin \pi p_k}{p_k N'(-p_k) K^-(-p_k) h^{p_k}} \right] \frac{1}{\sqrt{\pi(1-r)}}, \quad r \rightarrow 1 - 0 . \tag{25}$$

The Cauchy-type integral representing the function  $K^-(-p_k)$  converges exponentially. The series in the brackets of Equation (25) has the same type of convergence due to the multiplier  $h^{-p_k}$  and because the remaining terms have the order  $O(\sqrt{p_k})$ . The values  $p_k$  can be found from the characteristic equation (23) by the Newton’s method using the asymptotics

$$p_k = k \pm i \frac{2}{\pi} \ln k + O(1)$$

for large  $k$ . In order to obtain the non-scaled form of the above result we have to replace  $r$  and  $h$  by  $R/\varepsilon$  and  $H/\varepsilon$  respectively and use the relation in Equation (21).

An asymptotic expression for the SIF Green’s function for the problem at hand proceeds from the asymptotic representation given by Equation (25) of the hoop stress component:

$$K_I = c(\alpha, \beta) H^{-p_1} \varepsilon^{p_1-1/2} . \tag{26}$$

Here  $c(\alpha, \beta)$  is a smooth and finite function of the Dundurs parameters  $\alpha$  and  $\beta$ :

$$c(\alpha, \beta) = \frac{2\sqrt{2}b_1b_2 \sin \pi p_1}{p_1 N'(-p_1) K^-(-p_1)}, \tag{27}$$

$$\alpha = \frac{\mu(\kappa_1 + 1) - \kappa_2 - 1}{\mu(\kappa_1 + 1) + \kappa_2 + 1}, \quad \beta = \frac{\mu(\kappa_1 - 1) - \kappa_2 + 1}{\mu(\kappa_1 + 1) + \kappa_2 + 1} .$$

When  $\varepsilon \rightarrow 0$ , the SIF  $K_I$  apparently behaves as  $\varepsilon^{p_1-1/2}$  and, depending on the value of  $p_1$ , tends to 0 or  $\infty$ . The values of the first root  $p_1(\alpha, \beta)$  and the function  $c(\alpha, \beta)$  for various combinations of  $\alpha$  and  $\beta$  are presented in Tables 1 and 2. From these values the asymptote of the SIF for arbitrary material parameters combination can be obtained by interpolation. The values of  $p_1$  agree with the graphical

$\alpha \setminus \beta$	-0.45	-0.4	-0.3	-0.2	-0.1	0.0	0.1	0.2	0.3	0.4	0.45	
-0.95	0.872	0.803	0.717	0.661	0.622	0.592						
-0.9	0.868	0.799	0.713	0.657	0.618	0.589						
-0.8		0.789	0.704	0.650	0.611	0.583						
-0.7		0.777	0.694	0.641	0.604	0.576						
-0.6		0.764	0.683	0.631	0.5951	0.568	0.548					
-0.5			0.670	0.621	0.586	0.560	0.540					
-0.4			0.656	0.609	0.575	0.550	0.532					
-0.3			0.641	0.595	0.563	0.540	0.522					
-0.2			0.624	0.580	0.550	0.528	0.512	0.5				
-0.1				0.564	0.535	0.515	0.5	0.489				
0.0				0.545	0.519	0.5	0.486	0.477				
0.1				0.524	0.5	0.483	0.471	0.463				
0.2				0.5	0.479	0.464	0.453	0.447	0.443			
0.3					0.454	0.441	0.433	0.428	0.426			
0.4					0.427	0.416	0.409	0.405	0.405			
0.5					0.395	0.386	0.381	0.379	0.380			
0.6					0.357	0.351	0.347	0.347	0.349	0.355		
0.7						0.308	0.306	0.307	0.311	0.318		
0.8						0.255	0.254	0.256	0.261	0.268		
0.9							0.183	0.183	0.185	0.189	0.195	0.200
0.95							0.130	0.130	0.132	0.135	0.140	0.144

**Table 1.** Values of the first root  $p_1$  of the Zak–Williams characteristic equation; see Equations (23) and (12).

results of [Romeo and Ballarini 1995] and with the results for several specific material pairs reported by [Cook and Erdogan 1972].

### 4. Stability analysis

Based on the analysis presented in Appendix A, we see that the Zak–Williams Equation (23) always possesses a single first root  $p_1$  in the strip  $0 \leq \text{Re } p \leq 1$  which is simple and real. Furthermore,  $0 < p_1 < 1/2$  when

$$\chi = \frac{\mu_1 \kappa_2}{\mu_2 \kappa_1}$$

the combination of elastic coefficients of both materials is less than unity.

Consequently, if  $\chi < 1$  then, in view of Equation (26),  $\lim_{\varepsilon \rightarrow 0} K_I = \infty$ , and the crack is unstable in the vicinity of the interface. Similarly, when  $\chi > 1$  then  $1/2 < p_1 \leq 1$ ,  $\lim_{\varepsilon \rightarrow 0} K_I = 0$ , and the crack is stable. In this paper we consider only linear crack propagation. The stability of a crack with curvilinear path was investigated by [Gunnars et al. 1997]. We refer to the above combination of elastic coefficients “ $\chi$ ” as the crack stability factor (CSF). From the structure of the CSF we can see that the stability of the crack in the vicinity of an interface depends on the combination of Poisson ratios  $\nu_1$  and  $\nu_2$  as well as

$\alpha \setminus \beta$	-0.45	-0.4	-0.3	-0.2	-0.1	0	0.1	0.2	0.3	0.4	0.45
-0.95	0.330	0.406	0.466	0.487	0.492	0.487					
-0.9	0.352	0.425	0.481	0.5004	0.504	0.498					
-0.8		0.467	0.514	0.5285	0.529	0.521					
-0.7		0.513	0.549	0.5592	0.556	0.546					
-0.6		0.564	0.588	0.5926	0.587	0.574	0.555				
-0.5			0.630	0.6288	0.619	0.604	0.583				
-0.4			0.675	0.6678	0.655	0.636	0.613				
-0.3			0.724	0.7098	0.693	0.672	0.646				
-0.2			0.774	0.7546	0.734	0.711	0.683	0.651			
-0.1				0.8021	0.778	0.753	0.723	0.689			
0				0.8519	0.826	0.798	0.767	0.731			
0.1				0.9035	0.876	0.846	0.814	0.777			
0.2				0.9565	0.928	0.898	0.865	0.828	0.784		
0.3					0.982	0.953	0.921	0.884	0.840		
0.4					1.038	1.010	0.980	0.944	0.902		
0.5					1.095	1.070	1.042	1.009	0.970		
0.6					1.152	1.131	1.108	1.079	1.044	1.000	
0.7						1.194	1.176	1.153	1.125	1.088	
0.8						1.260	1.248	1.232	1.211	1.185	
0.9						1.333	1.326	1.318	1.307	1.292	1.283
0.95						1.376	1.373	1.369	1.363	1.354	1.349

**Table 2.** Values of  $c(\alpha, \beta)$ ; see Equation (27).

the ratio of shear moduli  $\mu_1/\mu_2$ . Since the stress state in the problem under consideration is completely defined by the Dundurs parameters it is useful to exhibit the stability/instability zones in the plane  $(\alpha, \beta)$ ; see Figure 2. It is clear that the stability condition  $\alpha > 0$  employed by [Leguillon et al. 2000] holds true only for the specific case when  $\beta = 0$ .

The effect of the Poisson ratios  $\nu_1$  and  $\nu_2$  on crack stability at the interface is often overlooked. Typically the crack stability is determined on the basis of the shear moduli ratio only. If the crack exists in a more rigid material and approaches an interface with the softer material ( $\mu_2 > \mu_1$  in Figure 1), it is regarded as unstable, see [Romeo and Ballarini 1995]. Consider, however, the case when the crack is in the more rigid material,  $\mu_1/\mu_2 = 2/3$ ,  $\nu_1 = 0.4$ , and  $\nu_2 = 0.2$ . Calculation of the CSF for the plane strain case ( $\kappa_s = 3 - 4\nu_s$ ,  $s = 1, 2$ ) yields  $\chi > 1$ . Hence, in contrast to the conclusion based on  $\mu_1/\mu_2 < 1$ , the crack is stable. In the  $(\alpha, \beta)$  plane the points corresponding to the material combinations possessing the above property are located within the lower sector generated by the lines  $\alpha = \beta$  and  $\alpha = -\beta$ ; see Figure 2. Examples of the corresponding engineering materials combinations can be identified using the data presented by [Suga et al. 1988].

As we noted at the beginning of the previous section, the stresses between the crack tip and the interface are non-zero only in the second problem taking part in the superposition. Their transform  $\sigma(r, \pi)$  can



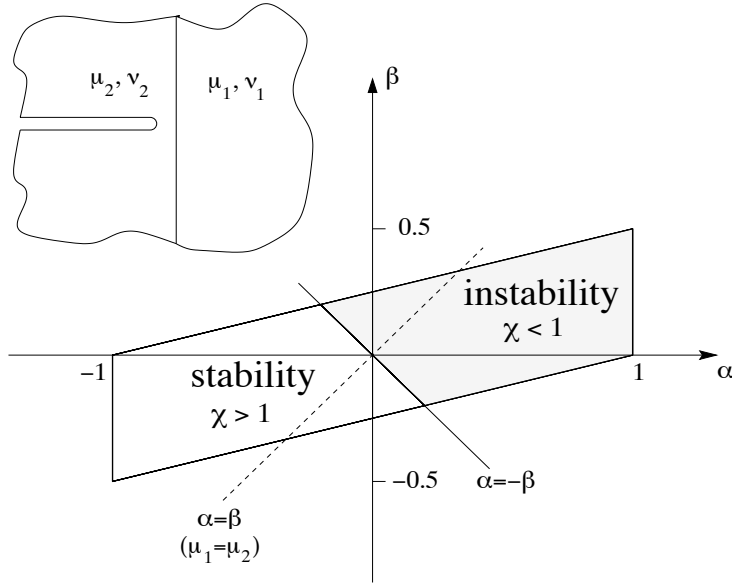


**Figure 2.** Crack stability and instability regions in the  $\alpha, \beta$  plane. The dashed line corresponds to the equal shear moduli of the materials on both sides of the interface.

be determined in the same way we derived the asymptote in Equation (24). Hence,

$$\sigma_\theta(r, \pi) = \frac{1}{2\pi i} \int_{L_0} K^+(p) \sum_{k=1}^{\infty} \frac{Q(-p_k)}{(p + p_k)K^-(-p_k)N'(-p_k)h^{p_k}} r^{-p-1} dp .$$

After closing the integration path to the left of the contour  $L_0$  we employ the residue theorem which leads to the formula for the stresses in front of the crack. In view of Equation (21) and using the nonscaled variables, we obtain

$$\sigma_\theta(R, \pi) = -\frac{1}{\pi \varepsilon} \sum_{n=1}^{\infty} \sum_{k=1}^{\infty} \frac{(-1)^n n \sin \pi p_k N(-n) K^-(-n) (R/\varepsilon)^{n-1}}{p_k (p_k - n) N'(-p_k) K^-(-p_k) (H/\varepsilon)^{p_k}} , \quad 0 < R < \varepsilon . \quad (28)$$

The stress distribution between the crack tip and the interface is depicted in Figure 3. As an illustration, consider the aluminum-epoxy composite. The material parameters needed for the computations are provided in Table 3. The dashed curves represent the inverse square root asymptotes obtained from

**Table 3.** Material properties.

	Young modulus $E$ (GPa)	Poisson ratio $\nu$
Epoxy	3	0.345
Aluminum	70	0.333
Boron	380	0.2

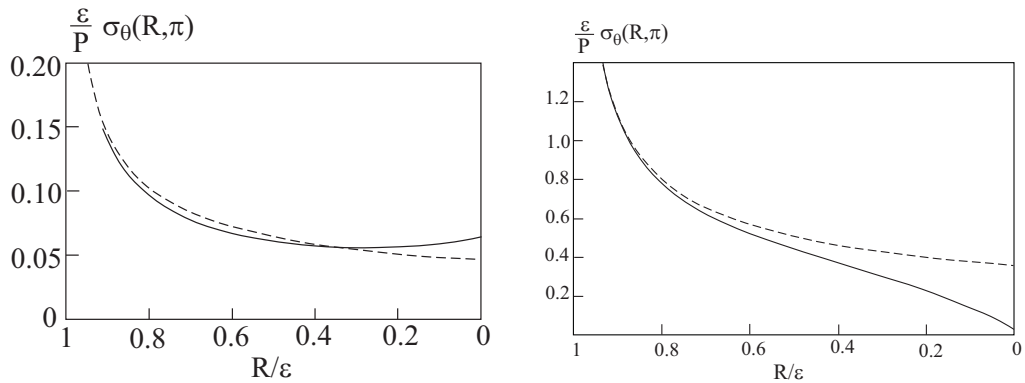


**Figure 3.** Hoop stress distribution between the crack tip and the interface in the aluminum-epoxy composite for the crack located in the epoxy (left) and in the aluminum (right). The dashed lines denote the inverse square root asymptotes.

Equation (25) and correspond to the case of a homogeneous plane. In the first case (Figure 3, left) the crack is imbedded in the soft (epoxy) constituent and is stable ( $\chi = 22.7 > 1$ ). As expected, the stresses near tip are less than for a crack in a homogeneous plane. Somewhat surprisingly, however, the stresses near the interface increase and are nonmonotonic. The quantitative analysis of the results reveals that: (1) the inverse square root asymptote agrees well with the exact solution only within about  $0.1\varepsilon$  from the crack tip; (2) within roughly  $0.7\varepsilon$  the asymptote has the same trend as the exact solution; (3) the asymptote underestimates by approximately 30% the value of stress at the interface ( $R = 0$ ), where the hoop stress reaches the local maximum. When the materials are reversed (Figure 3, right) the crack is located within the aluminum and is unstable ( $\chi = 1/22.7$ ). In this case: (1) the inverse square root asymptote also agrees well with the exact solution within about  $0.15\varepsilon$  from the crack tip; (2) however, the asymptote increasingly overestimates stresses as the distance from the crack tip grows, reaching about 30% at  $R = 0.7\varepsilon$ ; and (3) it grossly overestimates the values of stresses near the interface ( $R = 0$ ). The observed stress distributions agree with the data reported by [Wang and Stahle 1998] who investigated the crack approaching the interface by means of the semi-analytical dislocation approach.

The actual size of the K-dominance zone, which is proportional to  $\varepsilon$ , decreases for the crack approaching the interface. Thus at some point it becomes comparable to the fracture process zone of the cracked material. As a result, the standard fracture toughness criterion of crack propagation becomes invalid even for brittle materials and a nonasymptotic analysis of the stress field in the crack tip vicinity is required. This point is discussed in detail in [Ryvkin et al. 1995] and is illustrated in [Ryvkin 2000] in the problem of a crack close to a bimaterial interface. In the case of an unstable crack, which has no reason to stop after it begins to move for some finite value of  $\varepsilon$ , the above remark probably does not apply. The stable crack, on the other hand, may be arrested for vanishingly small  $\varepsilon$ . Consequently, the analysis of the complete stress distribution in front of a stable crack is of primary interest.

The influence of the elastic mismatch (the aluminum-epoxy and the boron-epoxy composites) on the stress distribution in front of a stable crack is illustrated in Figure 4.

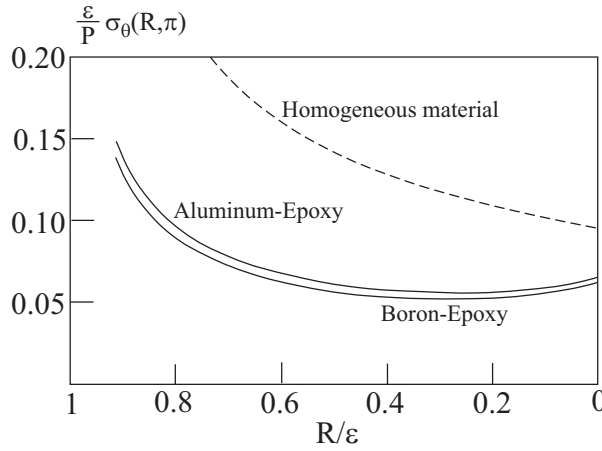


**Figure 4.** Stresses in front of the crack in the aluminum-epoxy and boron-epoxy composites. The dashed line is associated with the stresses in front of a crack in a homogeneous material.

For reference, the stress distribution for the crack in a homogeneous material is also shown by a dashed line. As expected, a greater mismatch of the materials leads to decrease in the stress. In spite of the fact that the stiffness of boron is greater than aluminum, the difference in stresses is nominal. This is attributable to the large mismatch between the epoxy and both of the above materials. Therefore the difference between them is of secondary importance and the bimaterial systems approach the limiting case of the epoxy half-plane bonded to a rigid substrate.

In order to examine the stress distribution on both sides of the interface, we need to derive the expression for the stress  $\sigma(r, 0)$  in the uncracked material. In contrast to the stress  $\sigma(r, \pi)$  here we have to superpose the stresses in both problems formulated in the beginning of the previous section. After some manipulation and employing the residue theorem, we obtain for  $0 < r < 1$

$$\sigma_{\theta}(r, 0) = \frac{1}{\pi} \sum_{n=1}^{\infty} \sum_{k=1}^{\infty} \frac{(-1)^n n \sin \pi p_k U(-n) K^{-}(-n) r^{n-1}}{p_k(p_k - n) N'(-p_k) K^{-}(-p_k) h^{p_k}},$$

where

$$U(p) = (1 + \kappa_2)[\kappa_2(2p - 1) - 1 - 2p - \mu(1 + \kappa_1 - 2p + 2\kappa_1 p)].$$

The nonscaled expression is determined in a manner similar to Equation (28). The stresses in the  $\varepsilon$  vicinity of the interface in the aluminum-epoxy composite are depicted in Figure 5. As before, the dashed line corresponds to the crack in a homogeneous material.

In accord with the continuity of the hoop strain component, the stresses beyond the interface in the relatively stiff aluminum jump to a value higher than that in the epoxy. For some material combinations this phenomenon may lead to a new crack nucleation within the stiff constituent, see [Leguillon et al. 2000].

As noted above, the SIF vanishes in the case of a stable crack approaching the interface. However, this does not suggest that the stable crack can not reach the interface. In order to examine this opportunity, a

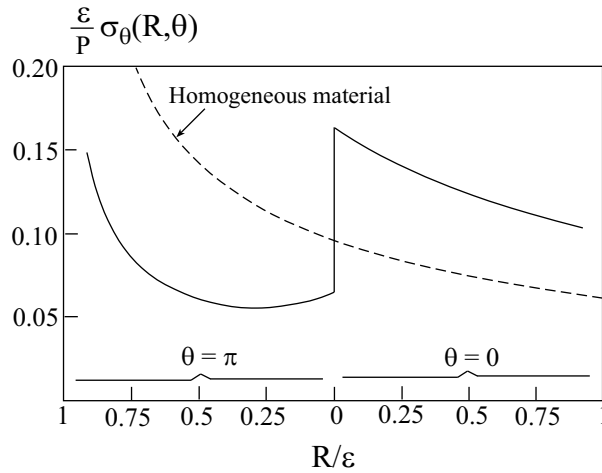


**Figure 5.** Stresses in the  $\varepsilon$ -vicinity of the interface.

critical stress-based criterion such as the Neuber–Novozhilov criterion [Neuber 1937; Novozhilov 1969] or the criterion indicated in [Cook and Erdogan 1972] needs to be employed rather than the fracture toughness criterion. After a crack has reached the interface, further crack propagation is defined by the competition between two possibilities: the penetration of the interface or deflection into it, see [He and Hutchinson 1989]. The need for a stress-based criterion is supported by the fact that the leading term in the expression given by Equation (28) for the stresses in front of a crack is proportional to  $\varepsilon^{p_1-1}$  and becomes unbounded when  $\varepsilon \rightarrow 0$ . Consequently, when the crack approaches the interface the stresses in the interface vicinity increase. Two opposite trends in the dependence of the stresses upon  $\varepsilon$  near the crack tip and near the interface are illustrated in Figure 6. Unlike the previous graphs, the coordinate system located at the crack tip is employed as shown in the insert.

Therefore the crack tip is associated with the left side of the graph and the crack propagation corresponds to the different positions of the interface denoted in the figure by the dashed lines. Since the results for several crack locations are depicted, the parameter employed for the length scale normalization here is  $H$  and not  $\varepsilon$  as it was previously. The stress distributions for three different distances between the crack tip and the interface ( $\varepsilon/H = 0.1, 0.05$  and  $0.02$ ) are presented. The limiting values of stress at the interface are derived in an accurate manner from a simple formula given by the first term of the infinite sum in Equation (28). Thus,

$$\sigma_{\theta}(0, \pi) = \frac{1}{\pi \varepsilon} \frac{\sin \pi p_1 N(-1) K^{-}(-1)}{p_1(p_1 - n) N'(-p_1) K^{-}(-p_1)(H/\varepsilon)^{p_1}} .$$

These values are denoted in the figure by the circles. As the distance between the crack tip and the interface decreases, so does the stress singularity in the crack tip vicinity. On the other hand, the non-monotonic stress behavior becomes more pronounced and the stresses near the interface increase, which at some point may lead to nucleation of a new microcrack located on the crack line and terminating at the interface.

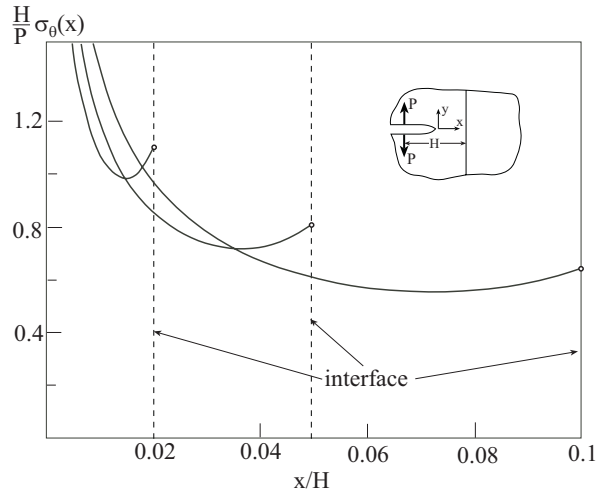


**Figure 6.** Stress distribution for the different distances between the tip of a stable crack and the interface.

The above approach is numerically very efficient. In order to reach less than one percent accuracy, 100 terms of the series in  $n$  and 3 terms of the series in  $k$  need to be taken into account. This is not surprising since, as it was noted, the series in  $k$  converges exponentially.

## 5. Conclusion

In this paper, we obtained a closed-form solution for the stress distribution in two perfectly bonded isotropic elastic half-planes with a fully imbedded semi-infinite crack orthogonal to the interface under Mode I loading by means of the Winner–Hopf–Jones method. The Green’s functions for the stresses and the SIF are constructed using auxiliary problems solved in quadratures. The closed-form solution of the problem offers a way to express the result in a form convenient for computation. A quantitative characterization of the SIF for various combinations of elastic parameters via the function  $c(\alpha, \beta)$  provides a practical tool for the solution of crack-interface interaction problems for arbitrarily distributed Mode I loading. The values of the function  $c(\alpha, \beta)$  computed from the closed-form solution reported herein, when compared with those obtained previously by the numerical solution of singular integral equations [Romeo and Ballarini 1995], suggest an error in the later procedure.

In order to characterize the stability of a crack approaching the interface, we introduced a new *interface parameter*,  $\chi$ , which is a simple combination of the shear moduli  $\mu_s$  and the Poisson ratios  $\nu_s$  ( $s = 1, 2$ ) of the materials on both sides of the interface. The crack stability or instability in the vicinity of the interface is associated with a decrease or increase of the energy release rate, that is, SIF with  $\varepsilon \rightarrow 0$ . Since  $K_I$  behaves as  $\varepsilon^{p_1-1/2}$ , the crack stability or instability depends on  $p_1$  being greater or less than  $1/2$ . This result agrees with the former asymptotic investigations of the problem, but we established here for the first time the exact condition of crack stability in terms of material parameters. The interface parameter  $\chi$  uniquely determines the sign of inequality for the first root  $p_1$  of the Zak–Williams characteristic equation and thus indicates the asymptotic behavior of the SIF. An estimation of the interface parameter prior to

detailed computations may serve as a qualitative evaluation of the strength of the stress singularity in the vicinity of the interface.

It appears that the propagation of a stable crack cannot be predicted in the framework of the SIF approach. In this case the critical stress criterion can be employed in conjunction with the solution obtained.

**Appendix A: Study of the first root of Zak–Williams characteristic equation**

The dependence of the stress distribution and the SIF on the material properties in two perfectly bounded isotropic elastic half-planes with a crack approaching the interface is conventionally expressed in terms of the Dundurs parameters  $\alpha$  and  $\beta$ .

$$\alpha = \frac{\mu(\kappa_1 + 1) - \kappa_2 - 1}{\mu(\kappa_1 + 1) + \kappa_2 + 1}, \quad \beta = \frac{\mu(\kappa_1 - 1) - \kappa_2 + 1}{\mu(\kappa_1 + 1) + \kappa_2 + 1}.$$

The crack stability in the vicinity of the interface is determined by the value of the first root  $p = p_1$  of the Zak–Williams characteristic equation [1963]. Specifically, the crack is stable when  $1/2 < p_1 < 1$  or unstable when  $0 < p_1 < 1/2$ . In what follows we analyze the value of  $p_1$  and the dependence of the crack stability on the material properties of both sides of the interface. The Zak–Williams equation can be presented in terms of the function  $N(p)$  in Equation (23). According to Equation (12)  $N(p)$  can be explicitly written as

$$N(p) = 2(1 + \kappa_1)[(\mu + \kappa_2) \cos \pi p + 2(\mu - 1)p^2] - 2\kappa_1\mu^2 - (\kappa_1 - 1)(\kappa_2 - 1)\mu + \kappa_2^2 + 1. \quad (29)$$

Therefore it may be considered as a function of one complex variable  $p$  and three real variables  $\kappa_1, \kappa_2$ , and  $\mu$ :  $N(p) \equiv N(\omega, p)$ ,  $\omega = (\kappa_1, \kappa_2, \mu)$ . Let us denote

$$p = \eta + i\xi, \quad \eta = \text{Re } p, \quad \xi = \text{Im } p; \quad N(p) = U(p) + iV(p), \quad U(p) = \text{Re } N(p), \quad V(p) = \text{Im } N(p). \quad (30)$$

The expressions of the material parameters through the Poisson ratios and shear moduli  $\kappa_s = 3 - 4\nu_s$ ,  $s = 1, 2$ , and  $\mu = \mu_2/\mu_1$  indicate the limits  $1 < \kappa_s < 3$ ,  $0 < \mu < \infty$ . Consequently, we assume that  $\omega \in \Omega$ , where  $\Omega = \{\omega : 1 < \kappa_s < 3, 0 < \mu < M\}$  is a 3-dimensional parallelepiped and  $M$  is an arbitrary large number. Furthermore, we define a rectangle domain  $D = \text{Re } p \in (0, 1)$ ,  $\text{Im } p \in (-q, q)$  in the complex plane with the boundary  $\Gamma$ . The barred symbols  $\bar{\Omega}$  and  $\bar{D}$  denote the closed sets and  $\Omega \times D$  represents the Cartesian product.

**Lemma 1.** The function  $N(\omega, p)$  does not vanish on the imaginary axis  $\text{Re } p = 0$  for any  $\omega \in \bar{\Omega}$ .

*Proof.* In view of Equations (29) and (30) we obtain

$$\begin{aligned} U(0) &= \mu(1 + \kappa_1 + \kappa_2 + \kappa_1\kappa_2) + (\kappa_2 + 1)^2 > 0, \\ \frac{\partial U(i\xi)}{\partial \xi} &= 2(1 + \kappa_1\mu)[\pi(\mu + \kappa_2) \sinh \pi \xi - 4(\mu - 1)\xi] \geq 2(1 + \kappa_1\mu)[\pi^2(\mu + \kappa_2)\xi - 4(\mu - 1)\xi] \\ &= 2(1 + \kappa_1\mu)[(\pi^2 - 4)\mu + \kappa_2\pi^2 + 4]\xi \geq 0, \quad \xi \geq 0. \end{aligned}$$

Since  $U(0) > 0$  and  $\partial U(i\xi)/\partial \xi \geq 0$  for  $\xi \geq 0$ , the function  $U(i\xi)$  increases monotonically for positive  $\xi$  and  $U(i\xi) > 0$  for  $\xi \geq 0$ . From the evenness of function  $U(i\xi)$  it follows that  $N(i\xi) > 0$  for any  $\xi$ .  $\square$

**Lemma 2.** The function  $N(\omega, p)$ ,  $\omega \in \bar{\Omega}$ , does not vanish on the line  $p = 1 + i\xi$  for any  $\omega \in \bar{\Omega}$ .

*Proof.* For  $\mu \neq 1$  and  $|\xi| > 0$  we have  $V(1 + i\xi) = 8(1 + \kappa_1\mu)(\mu - 1)\xi \neq 0$ . Taking into account that  $\kappa_1, \kappa_2 \in [1, 3]$ , for  $\mu = 1$  and  $|\xi| \neq 0$  we the have

$$U(1 + i\xi) = -2(1 + \kappa_1)(1 + \kappa_2) \cosh \pi \xi - 2\kappa_1 - (\kappa_1 - 1)(\kappa_2 - 1) + \kappa_2^2 + 1 < -8 \cosh \pi \xi - 2 + \kappa_2^2 + 1 < 0.$$

For the case when  $\xi = 0$ ,  $\omega \in \bar{\Omega}$  we find  $U(1) = \mu(1 + \kappa_1)(1 - 3\kappa_1) + (\kappa_2 - 1)^2 - 4 \leq \mu(1 + \kappa_2)(1 - 3\kappa_1) < 0$ . Consequently,  $N(1 + i\xi) \neq 0$  for all  $\xi \in (-\infty, \infty)$ . □

**Lemma 3.** It is possible to find a positive number  $c$  defined by the following condition: the function  $N(\omega, p)$ ,  $\omega \in \hat{\Omega}$ , is not vanishing on the segments  $\text{Re } p \in [0, 1]$ ,  $\text{Im } p = \pm q$  for any  $q > c$ .

*Proof.* The lower bound for  $c$  may be easily found by estimating the function  $\cos \pi p$  by the first three terms of the Maclaurin series expansion in the rectangular domain  $0 \leq \eta \leq 1$ ,  $-c \leq \xi \leq c$ . □

**Lemma 4.** For the case when  $\kappa_1 = \kappa_2$  and  $\mu = 1$ , function  $N(\omega, p)$  has the only zero  $p_1 = 1/2$  in the strip  $\text{Re } p \in [0, 1]$ .

*Proof.* For this case  $N(\omega, p) = (1 + \kappa_1)^2 \cos \pi p$ . □

**Theorem 1.** The function  $N(\omega, p)$ ,  $\omega \in \bar{\Omega}$  has a single, simple and real zero in the strip  $0 \leq \text{Re } p \leq 1$ .

*Proof.* For any  $\omega \in \hat{\Omega}$  the function  $N(\omega, p)$  of the complex variable  $p$  is analytic for  $p \in D$ , is continuous with its derivative on  $\Gamma$ , and, following Lemmas 1–3, does not vanish on this contour. Therefore, in accord with the principle of the argument, an integral along the closed contour  $\Gamma$

$$I(\omega) = \frac{1}{2\pi i} \int_{\Gamma} \frac{N'_p(\omega, p)}{N(\omega, p)} dp \tag{31}$$

is equal to the total number (with regard to multiplicity) of zeros of the function  $N(\omega, p)$  in  $D$ .

Changing the elastic parameters along some path in  $\Omega$ , let us assume that for some point  $\omega_*$  an  $r$ -order zero of the function  $N(\omega, p)$  appears (or disappears) in  $D$ . Then the function  $I(\omega)$  will have a finite  $r$ -units discontinuity at this point. However, the integrand in Equation (31) is continuous in  $\bar{\Omega} \times \Gamma$  since the absolute values of its partial derivatives with respect to  $p$  and  $\omega$  are bounded in this domain. Therefore the integral  $I(\omega)$ ,  $\omega \in \bar{\Omega}$  also represents a continuous function of  $\omega$ .

The above contradiction leads to the conclusion that for any  $\omega \in \Omega$  the function  $N(\omega, p)$  has the same number of zeros in  $D$ , that is,  $I(\omega) = \text{const} = n$ . Since Lemma 4 implies that for  $\omega = \omega_0 = (\kappa_1, \kappa_2, 1)$  there is the only simple zero is  $p_1 = 1/2$ , we then find that  $n = 1$ . Clearly this single zero can not become complex valued for some  $\omega$  because in that case the conjugate number  $\bar{p}_1$  also satisfies Equation (29).

Finally, since  $q > 0$  is unbounded, the above result obtained for  $p \in D$  holds for the entire strip  $0 \leq \text{Re } p \leq 1$ .

Since for every  $\omega \in \Omega$  corresponds some value of the first zero  $p_1$  of the function  $N(\omega, p)$ ,  $(\omega, p) \in \bar{\Omega} \times \bar{D}$ , we can consider an implicit function  $p = f(\omega)$ ,  $\omega \in \bar{\Omega}$ . This function must fulfill the equation  $N(\omega, p) = 0$ ,  $(\omega, p) \in \hat{\Omega} \times \hat{D}$  and, in accord with Lemma 4, meet the condition  $f(\omega_0) = 1/2$ . □

**Remark 1.** Theorem 1 can be now formulated as follows: The function  $p = f(\omega)$ ,  $\omega \in \bar{\Omega}$  exists, it is real valued, and it varies in a domain  $P \subset (0, 1)$ .

**Remark 2.** The function  $N(\omega, p)$  and its derivative  $\partial/\partial p[N(\omega, p)]$  do not vanish simultaneously in any point of the domain  $\bar{\Omega} \times \bar{D}$ .

*Proof.* The existence of such a point implies that function  $N(\omega, p)$  has a multiple zero at this point, which violates [Theorem 1](#). □

**Theorem 2.** The implicit function  $p = f(\omega)$ ,  $\omega \in \bar{\Omega}$  defined by the equation  $N(\omega, p) = 0$ ,  $(\omega, p) \in \bar{\Omega} \times \bar{D}$  and condition  $f(\omega_0) = 1/2$  exists. It is unique, continuous, and has continuous bounded partial derivatives.

*Proof.* In accord with [Theorem 1](#) there exists a unique implicit function  $p = f(\omega)$ ,  $\omega \in \bar{\Omega}$  which is defined by a zero of the function  $N(\omega, p)$  for a given  $\omega$ . Since the partial derivatives of the function  $N(\omega, p)$  of the first and second order in any bounded domain are bounded, function  $N(\omega, p)$  and its derivative are continuous in the 4-dimensional parallelepiped  $\bar{\Omega} \times [0, 1]$ . Furthermore, following [Remark 2](#), the functions  $N(\omega, p)$  and  $\partial/\partial p[N(\omega, p)]$  do not vanish simultaneously. The theorem of implicit functions then establishes that function  $p = f(\omega)$  is continuous and its first derivatives

$$\frac{\partial p}{\partial \mu} = -\frac{\partial N(\omega, p)}{\partial \mu} \left[ \frac{\partial N(\omega, p)}{\partial p} \right]^{-1}, \quad \frac{\partial p}{\partial \kappa_s} = -\frac{\partial N(\omega, p)}{\partial \kappa_s} \left[ \frac{\partial N(\omega, p)}{\partial p} \right]^{-1}, \quad s = 1, 2 \quad (32)$$

exist and are continuous and bounded. □

**Lemma 5.** Consider a surface  $S$  in  $\Omega$  defined by the equation  $\kappa_1\mu - \kappa_2 = 0$ . Then every point  $(\omega, 1/2)$ ,  $\omega \in S$  from  $\bar{\Omega} \times [0, 1]$  is zero of the function  $N(\omega, p)$  and for the points with  $\omega \in \bar{S}$ ,  $N(\omega, 1/2) \neq 0$ .

*Proof.* The proof is obvious from the relation  $N(\omega, 1/2) = (\kappa_2 - \kappa_1\mu)(\mu + \kappa_2)$ . □

**Lemma 6.** For arbitrary fixed  $\kappa_1, \kappa_2 \in [1, 3]$  the function  $p = f(\kappa_1, \kappa_2, \mu)$  represents a decreasing function of  $\mu$  in the vicinity of the point  $\mu_1 = \kappa_2/\kappa_1$ .

*Proof.* In accord with [Theorem 2](#), the partial derivatives of the function  $N(\omega, p)$  in  $\bar{\Omega} \times \bar{D}$  exist and are bounded. At the point  $(\omega_1, 1/2)$ ,  $\omega_1 = (\kappa_1, \kappa_2, \kappa_2\kappa_1^{-1})$ , the partial derivatives are negative:

$$\begin{aligned} \frac{\partial N(\omega_1, 1/2)}{\partial \mu} &= -\kappa_2(1 + \kappa_1) < 0, \\ \frac{\partial N(\omega_1, 1/2)}{\partial p} &= 2(1 + \kappa_2)\kappa_1^{-1}[\pi(1 + \kappa_1)\kappa_2 - 2(\kappa_2 - \kappa_1)] < 2(1 + \kappa_2)\kappa_1^{-1}(4 - 2\pi) < 0. \end{aligned}$$

Recalling [Equation \(32\)](#) we conclude that  $\partial f(\omega_1)/\partial \mu < 0$  and the function  $f(\omega)$  decreases with respect to  $\mu$  at the point  $\omega_1$ . The surface  $S$  separates the parallelepiped  $\bar{\Omega}$  into two parts:  $\bar{\Omega}^-$  for  $\mu < \kappa_2\kappa_1^{-1}$  and  $\bar{\Omega}^+$  for  $\mu > \kappa_2\kappa_1^{-1}$ . □

**Theorem 3.** If  $\omega \in \bar{\Omega}^+$ , then  $f(\omega) < 1/2$ . If  $\omega \in \bar{\Omega}^-$ , then  $f(\omega) > 1/2$ .

*Proof.* Let us assume the opposite, that is, for some point  $\omega_2 = (\kappa_1, \kappa_2, \mu)$  from  $\bar{\Omega}^+$   $p_2 = f(\omega_2) \geq 1/2$ . [Lemma 5](#) states that the case of equality is impossible since  $\omega_2 \notin S$ , so we consider the case when  $p_2 > 1/2$ . We connect the points  $\omega_1 = (\kappa_1, \kappa_2, \kappa_2\kappa_1^{-1})$  and  $\omega_2$  by a line segment  $\gamma$  and consider the function  $p = f(\omega) = \varphi(\mu)$  on  $\gamma$ . By [Lemma 6](#) this function is decreasing in the vicinity of the point  $\omega_1$ . By [Lemma 5](#)  $\varphi(\mu_1) = 1/2$ . Consequently, there is a point  $\mu_3$  where  $p_3 = \varphi(\mu_3) < 1/2$ . Continuous in accord with [Theorem 2](#), the function  $\varphi(\mu)$  takes on the segment  $(\mu_3, \mu_2)$  all the intermediate values



between  $p_3$  and  $p_2$ . Therefore the point  $\mu_4 \in (\mu_3, \mu_2)$  exists where  $\varphi(\mu_4) = 1/2$ . But this results in a contradiction with [Lemma 5](#) since the point  $(\kappa_1, \kappa_2, \mu_4) \in \bar{\Omega}^+$  is not located on  $S$  and cannot be a zero of the function  $N(\omega, 1/2)$ . The proof of the second part of the theorem is carried out in a similar manner.  $\square$

**Summary.** Initially we sought zeros of the function  $N(\omega, p)$  in the 5-dimensional domain  $\Omega \times D$  characterized by five real valued parameters two of which ( $\mu$  and  $\xi$ ) are unbounded. Answering the question on the existence of zeros and their number, [Theorem 1](#) reduced substantially the range of possible locations for  $p_1$ . [Theorem 2](#) and [Lemma 5](#) provided the foundation for developing a simple iterative procedure with respect to  $\mu$  based on the continuous dependence of  $p_1$  upon all the parameters  $\omega(\kappa_1, \kappa_2, \mu)$  and the known initial value  $p_1 = 1/2$  for  $\mu = \kappa_2 \kappa_1^{-1}$ . Finally, [Theorem 3](#) allows us to answer the question of whether the crack will be stable ( $\mu < \kappa_2 \kappa_1^{-1}$ ,  $\chi > 1$ ,  $p_1 > 1/2$ ) or unstable ( $\mu > \kappa_2 \kappa_1^{-1}$ ,  $\chi < 1$ ,  $p_1 < 1/2$ ) for  $\varepsilon \rightarrow 0$  a priori, without any calculations. We only need to know the elastic parameters of the composite body, namely, the ratio  $\mu = \mu_2/\mu_1$  and  $\kappa_s = 3 - 4\nu_s$ .

### Acknowledgements

This work was supported by Shell E&P Technology Applications & Research. We would like to express our gratitude to Dr. G. Wong and J. W. Dudley of Shell International Exploration & Production for their attention and encouragement. We would also like to thank Professor R. Ballarini for useful discussions with him regarding this work.

### Homage

On September 5, 2002, after a long fight with cancer, Professor Boris M. Nuller passed away.

Born in 1934, Boris Nuller survived the winter of 1941 in Leningrad under the siege. He received his Ph.D. and D.Sci. degrees from Leningrad Polytechnic Institute, and during the last few years served as head of the Mathematics Department of the Leningrad Forestry Academy. Publishing over 200 scientific papers in his lifetime, many of which found industrial application, Professor Nuller dedicated his exceptional mathematical talent to applied mechanics. He developed a method of piecewise homogeneous solutions for problems with mixed boundary conditions, improved the methods of solution of Gilbert–Riemann and Wiener–Hopf functional equations, and advanced the technique of discrete Fourier transforms for domains possessing cyclic or translational symmetry. Among his numerous contributions are solutions of various contact problems related mainly to fracture mechanics, the development of nonlinear poro-elasticity and a mathematical model of cutting.

Professor Nuller’s friendship, his commitment to research, his creativity, and his insight into the problems of mathematical physics will be missed.

### References

- [Atkinson 1975] C. Atkinson, “[On the stress intensity factors associated with cracks interacting with an interface between two elastic media](#)”, *Int. J. Eng. Sci.* **13**:5 (1975), 489–504.
- [Cook and Erdogan 1972] T. S. Cook and F. Erdogan, “[Stress in bonded materials with a crack perpendicular to the interface](#)”, *Int. J. Eng. Sci.* **10**:8 (1972), 677–697.

- [Erdogan and Biricikoglu 1973] F. Erdogan and V. Biricikoglu, “Two bonded half-planes with a crack going through the interface”, *Int. J. Eng. Sci.* **11**:7 (1973), 745–766.
- [Gakhov 1966] F. D. Gakhov, *Boundary value problems*, Pergamon Press, London, UK, 1966.
- [Gunnars et al. 1997] J. Gunnars, P. Stahle, and T. C. Wang, “On crack path stability in a layered material”, *Comput. Mech.* **19**:6 (1997), 545–552.
- [He and Hutchinson 1989] M.-Y. He and J. W. Hutchinson, “Crack deflection at an interface between dissimilar elastic materials”, *Int. J. Solids Struct.* **25**:9 (1989), 1053–1067.
- [Khrapkov 1968] A. A. Khrapkov, “First fundamental problem for a piecewise-homogeneous plane with a slit perpendicular to the line of separation”, *J. Appl. Math. Mech.* **32**:4 (1968), 666–678.
- [Leguillon et al. 2000] D. Leguillon, C. Lacroix, and E. Martin, “Interface debonding ahead of a primary crack”, *J. Mech. Phys. Solids* **48**:10 (2000), 2137–2161.
- [Neuber 1937] H. Neuber, *Kerbspannungslehre*, Springer, Berlin, Germany, 1937.
- [Noble 1958] B. Noble, *Method based on the Wiener-Hopf technique for solution of partial differential equations*, Pergamon Press, Oxford, UK, 1958.
- [Novozhilov 1969] V. V. Novozhilov, “On a necessary and sufficient criterion for brittle strength”, *J. Appl. Math. Mech.* **33**:2 (1969), 201–210.
- [Nuller 1976] B. M. Nuller, “Contact problem for an elastic wedge reinforced by a bar of uniform resistance”, *Sov. Phys. Doklady* **20** (1976), 789–790.
- [Nuller et al. 2001] B. Nuller, M. Ryvkin, A. Chudnovsky, J. W. Dudley, and G. K. Wong, “Crack interaction with an interface in laminated elastic media”, pp. 289–296 in *Proceedings: Rock Mechanics in the National Interest*, edited by D. Elsworth and et. al, Washington, DC, July 2001.
- [Romeo and Ballarini 1995] A. Romeo and R. Ballarini, “A crack very close to a bimaterial interface”, *J. Appl. Mech. (Trans. ASME)* **62** (1995), 614–619.
- [Ryvkin 2000] M. Ryvkin, “K–dominance zone for a semi–infinite mode I crack in a sandwich composite”, *Int. J. Solids Struct.* **37**:35 (2000), 4825–4840.
- [Ryvkin et al. 1995] M. Ryvkin, L. Slepyan, and L. Banks-Sills, “On the scale effect in the thin layer delamination problem”, *Int. J. Fract.* **71**:3 (1995), 247–271.
- [Suga et al. 1988] T. Suga, G. Elssner, and S. Schmauder, “Composite parameters and mechanical compatibility of material joints”, *J. Compos. Mater.* **22**:10 (1988), 917–934.
- [Wang and Stahle 1998] T. C. Wang and P. Stahle, “Stress state in front of a crack perpendicular to bimaterial interface”, *Eng. Fract. Mech.* **59**:4 (1998), 471–485.
- [Zak and Williams 1963] A. R. Zak and M. L. Williams, “Crack point stress singularities at a bi-material interface”, *J. Appl. Mech. (Trans. ASME)* **30** (1963), 142–143.

Received 1 Feb 2006.

BORIS NULLER: Deceased 5 Sep 2002

*Department of Applied Mathematics, Kirov Academy of Wood Technology, St. Petersburg 195220, Russia*

MICHAEL RYVKIN: [arikr@eng.tau.ac.il](mailto:arikr@eng.tau.ac.il)

*School of Mechanical Engineering, Iby and Aladar Fleischman Faculty of Engineering, Tel Aviv University, Tel Aviv 69978, Israel*

ALEXANDER CHUDNOVSKY: [achudnov@uic.edu](mailto:achudnov@uic.edu)

*Department of Civil and Materials Engineering, The University of Illinois at Chicago, 842 West Taylor Street, Chicago, Illinois 60607-7023, United States*

## STATISTICAL STRENGTH OF A TWISTED FIBER BUNDLE: AN EXTENSION OF DANIELS EQUAL-LOAD-SHARING PARALLEL BUNDLE THEORY

PANKAJ K. PORWAL, IRENE J. BEYERLEIN AND S. LEIGH PHOENIX

In this work, we extend the statistical strength model of Daniels for a parallel fiber bundle to a twisted bundle with an ideal helical structure. The bundle is clamped at each end in such a way that it has no slack fibers in the unloaded state. The fibers are linearly elastic and continuous, and have random strengths following a Weibull distribution with Weibull shape parameter  $\rho$ . We calculate the stress redistribution from failed to surviving fibers according to a twist-modified equal load sharing (TM-ELS) rule, introduced here. The effect of the twist is modeled analytically by two approaches, one called *geometrical averaging*, in which the fiber helix angles are averaged, and the other called *statistical averaging*, in which the fiber failure probabilities are averaged. In both probability models, the bundle strength distributions remain asymptotically Gaussian, as in Daniels' original model; however, the associated mean and standard deviation are additionally altered by the surface twist angle. To validate these theories, a Monte Carlo model is developed to simulate fiber break initiation and progression within a cross-sectional plane under tension. For all values of surface twist angle  $\alpha_s$ ,  $\rho$  and bundle size studied, the simulated strength distributions are shown to be strongly Gaussian. Transitions in failure mode from diffuse, across the bundle cross-section, to localized near the center of the bundle occur when  $\alpha_s$  and  $\rho$  increase and the bundle size decreases, in spite of application of a diffuse-type loading sharing rule, TM-ELS. Both analytical models provide similar results which are in excellent agreement with the simulated results. For the most part, we consider the bundle to be short enough that interfiber friction plays no role in the stress redistribution. However, to demonstrate its importance in long bundles, we mimic the effects of interfiber friction by considering a chain of such bundles where the bundle length is chosen to approximate the characteristic length of unloading around breaks.

### 1. Introduction

Yarns, ropes, and cables, generically called twisted mechanical structures, have been used for centuries as load-bearing structures. When fabricated from ultrastrong, high-performance polymer-based or carbon-based fibers, such as Kevlar, PBO, graphite, and even carbon nanotubes (see, for example, [Vigolo et al. 2000; Zhang et al. 2004]) such structures can be made with superior strengths and can possibly be used in many technically advanced aerospace and defense applications. Like traditional fibers, such as wool, cotton and polyester, these advanced fibers exhibit a substantial variation in strength as well

---

*Keywords:* twisted fiber bundle or yarn, Monte Carlo simulation, statistical strength, twist modified equal load sharing (TM-ELS), ideal helical structure, interfiber friction, chain-of-bundles model.

The authors gratefully acknowledge the support of the Science and Technology-based Distinguished Student Award provided to graduate student Pankaj K. Porwal by Los Alamos National Laboratory (LANL) and the support of a LANL-directed Research and Development project (No. 20030216) provided to IJB. This work has been supported in part under the *Institute for Future Space Transport*, a NASA University Institute funded under Cooperative Agreement NCC3-994.

as size (length and number of fibers) effects. Consequently the strength of the twisted structure made from such fibers will also exhibit similar characteristics, although it may be much weaker depending on the extent of variability and the stiffness of the fibers. Thus, there is a need for structural strength predictions, particularly in the high reliability regime, that is, only one failure out of thousands or millions of specimens under a design load. In other words, an average strength determined from a few tests will not be sufficient. Such predictive capability, however, is not in place for these twisted structures.

In these structures, the local material strengths vary from point to point and from fiber to fiber within the bundle. As a consequence, the failure processes can be quite random and the strengths can statistically vary among twisted bundles of otherwise identical descriptions. As the bundle volume increases (either in diameter or length) the likelihood of finding a weak region or defect that can lead to failure will increase as well, leading to a lower average strength among many specimens. Fiber strengths are commonly described by the Weibull distribution, an empirical statistical model that was built upon weakest-link concepts [Phoenix and Beyerlein 2000]. However, the strength distribution and size effect for a twisted fiber bundle are generally more complicated and unknown.

These twisted structures are also heterogeneous in microstructure. To see this, envision fibers in layers following concentric helical paths about the central axis of the fiber ‘bundle’ (for example, yarn, rope, cable) with helical angles varying from zero, for the central fiber, to  $\alpha_s$ , for fibers at the surface. Under the action of an applied load, the stresses or strains sustained by individual fibers differ depending on their helical angle with respect to the loading direction and the angles of the surrounding fibers. In addition, their stresses will depend on the actual distribution of neighboring fiber breaks.

Unlike the initial or elastic modulus, the strength of a heterogeneous material cannot be predicted by a rule-of-mixtures type calculation. Strength is best predicted by considering failure mechanisms involving various initiation phenomena and subsequent propagation behavior to catastrophic collapse. The two primary mechanisms in a twisted fiber bundle are fiber failure and fiber slipping (for example, unraveling), which may occur simultaneously. This interplay of failure mechanisms is a favorable situation, which can theoretically lead to optimal strengths without compromising ductility.

In this work, we develop analytical models for bundle strength based only on the first mechanism, fiber breaks and load redistribution. They allow for a stochastic progression of fiber breaks within a cross-sectional plane of an ideal helical structure. Under the initial application of strain or stress, breaks occur first in the weakest or most highly stressed fibers. As the stress level increases, breaks increase in number until an unstable pattern of breaks and the maximum stress that can be sustained, is achieved.

To validate the simplifying assumptions made in the analytical models, a Monte Carlo computational model is developed. This computational model simulates more accurately the ‘true’ failure progression in many replications, sufficient for generating empirical statistical strength distributions. This useful tool provides insight into the mathematical form of the bundle strength distributions, characteristics of the failure modes, and dependencies on statistical fiber strength properties and surface twist angle,  $\alpha_s$ . In this work, both the Monte Carlo and analytical models consider Weibull fiber strengths and a nonlocalized load sharing rule among broken and intact fibers called the twist-modified equal load sharing (TM-ELS) rule. In TM-ELS, failed fibers carry zero stress and surviving fibers share the applied bundle load but carry individual stresses depending on their radial positions in the bundle. As a consequence, fiber breaks will propagate based not only on their strengths and the total number of breaks, but on their helix angle as well. Like the conventional ELS rule, no direct enhancements result from the relative proximity of

one break to another. Pure ELS is well known to apply to dry bundles of parallel fibers when there is negligible friction between the fibers, which causes load build-up from the fiber ends to be rather inefficient. For a twisted bundle, however, we show that in spite of the TM-ELS assumption, the Monte Carlo model forecasts transitions in failure mode from ductile-like to brittle-like due to the twist angles and fiber strength variation.

While very important, incorporating the effects of friction and slipping is beyond the scope of the current work and will be considered in a sequel. Nonetheless, as a preview of the expected behavior we perform a simple chain-of-bundles calculation, using results of [Alexander 1952] for the stress recovery length around a fiber discontinuity in terms of yarn tension and twist. However, in the actual yarn the stress transfer length around a broken fiber depends on its radial position because the radial pressure distribution is nonuniform.

## 2. Theoretical background

Most theories for yarns, ropes, and cables operate within a deterministic strength paradigm with the goal of determining the optimal surface twist angle at which the highest bundle strength is achieved. In fact, fiber manufacturers often apply twist to varying degrees (not necessarily the same from one lot to the next) to determine fiber strength to meet some acceptance criteria or minimum standard. The optimal twist angle is generally related to a single-valued fiber strength, fiber diameter and length, and the magnitude of frictional forces in shear acting along fibers to resist sliding. For an excellent summary of the earlier, classical theoretical and experimental works, we refer the reader to [Hearle et al. 1969]. Other more recent attempts in this category, including work on impregnated yarns, can be found in [Naik et al. 2001], where the strength of impregnated yarn was estimated using an effective shear traction and fiber obliquity factor.

On the other hand, most statistical strength models treat a parallel array of fibers rather than a twisted bundle. These models generally focus on the influence of fiber strength, bundle length, bundle size, fiber packing, and interface properties, in the case when matrix is present in the parallel fiber bundle. For a recent review of these parallel bundle theories, we refer the reader to [Phoenix and Beyerlein 2000]. Among these we mention only the classical theory of Daniels [1945], which is relevant to this work. Through a long and complicated proof, Daniels showed that when the load from fiber breaks is redistributed equally among the remaining intact fibers (ELS), the strength of a large bundle asymptotically approaches a Gaussian distribution. He derived expressions for the asymptotic mean  $\mu_D$  and standard deviation  $\gamma_D$  as a function of the underlying strength distribution of the fibers and bundle size in terms of number of fibers.

There are, however, a few notable statistical strength theories for twisted fiber bundles [Phoenix 1979; Pan 1993]. Although using different approaches, they both have extended Daniels' parallel bundle theory. Phoenix [1979] in particular studied the influence of slack as a result of incomplete migration, that is, the deviation of fibers from an ideal helical path, that occurs after the twisting process. He proposed a statistical model for random fiber slack, which has two characteristic parameters reflecting the extent and uniformity of the migration process, and applied it to an ideal helical structure where the fiber strength itself followed a Weibull distribution. An asymptotically Gaussian distribution for the strength of the twisted yarn was argued to apply, as in Daniels' case, and the associated mean and standard deviation

were derived. We compare the results of [Phoenix 1979] to that of the present work. Pan [1993] derived and directly applied an orientation efficiency factor to Daniels' mean  $\mu_D$  and standard deviation  $\gamma_D$  to account for the effect of an average twist. Up to now, twisted bundle strength studies have not used Monte Carlo simulation to investigate the nature of the yarn strength distribution or to validate the Gaussian form of the distribution, which had been assumed upfront to apply to twisted structures and in fact many other structures outside of the parallel ELS bundle.

### 3. Modeling approach

**3.1. Parallel bundle.** Our models for the strength of a twisted bundle will build upon Daniels' well-known theory for a parallel ELS bundle. His model is briefly reviewed here.

Daniels [1945] considered  $n$  parallel fibers that are evenly clamped at each end and have the same cross-sectional area  $A$  and linear elastic constitutive law with Young's modulus  $E_f$ . The fiber strengths  $X_1, X_2, \dots, X_n$  (in units of stress) are independent and identically distributed (i.i.d.) random variables following a cumulative distribution function (cdf)  $F(s)$ ,  $s \geq 0$ , where  $s$  is the stress in the fiber along the direction of loading. When the fibers are parallel to the direction of loading,  $s$  is also the axial stress in the fibers. The corresponding strain to failure of fiber  $i$ ,  $\xi_i$ , is simply  $\xi_i = X_i/E_f$ .

A nominal stress  $\sigma$  is uniformly applied to this  $n$ -sized bundle, and as  $\sigma$  is increased, the fibers start to break whenever and wherever the fiber stress exceeds the fiber strength. Due to the strength variation, fiber breaks tend to initiate and spread in a random manner. According to the ELS rule of Daniels' model, when a fiber breaks, its lost load is instantaneously redistributed in equal portions to all surviving fibers. Consequently, the individual axial stresses, denoted here as  $s$ , in the remaining intact fibers will be equal, and will be higher than  $\sigma$  for the bundle. If  $N_b$  is the current number of breaks in the bundle, then according to ELS,  $s$  is

$$s = \left( \frac{n}{n - N_b} \right) \sigma.$$

The strength of the bundle  $S$  is the maximum stress borne by the bundle, and is given by

$$S = \max \left\{ X_{1,n}, \left( \frac{n-1}{n} \right) X_{2,n}, \dots, \left( \frac{1}{n} \right) X_{n,n} \right\},$$

where  $X_{1,n} \leq X_{2,n} \leq \dots \leq X_{n,n}$  are the order statistics of the strengths of the  $n$  fibers. Daniels proved that  $S$  asymptotically follows a Gaussian (that is, normal) distribution, with probability density function (pdf)  $g_n(s)$  given by

$$g_n(s) = \frac{1}{\sqrt{2\pi}\gamma_D^2} \exp \left\{ -\frac{(s - \mu_D)^2}{2\gamma_D^2} \right\}, \quad (1)$$

where  $\mu_D$  is the mean and  $\gamma_D$  is the standard deviation of the bundle strength.

In general the bundle can be loaded in a stress-controlled or strain-controlled manner. In the latter, with increasing strain  $\epsilon_y$  on the bundle, the resulting bundle stress fluctuates randomly. For a large bundle (that is,  $n \rightarrow \infty$ )  $\sigma(s)$ , the nominal bundle stress as a function of  $s$  asymptotically approaches the function  $\mu(s)$  given by

$$\mu(s) = s[1 - F(s)], \quad s \geq 0.$$

The  $\mu_D$  in Equation (1) is the maximum of  $\mu(s)$ , formally called the asymptotic mean strength, and is

$$\mu_D = \max_s \{\mu(s) : s \geq 0\}. \tag{2}$$

$\mu(s) = \mu_D$  occurs when  $s = s^*$ , that is,  $s^* = \{s : \mu(s) = \mu_D\}$ . The variance function for the bundle stress is given by

$$\Sigma(s) = s^2 F(s)[1 - F(s)], \quad s \geq 0,$$

and the asymptotic standard deviation  $\gamma_D$  of the bundle strength is

$$\gamma_D = \frac{s^*}{\sqrt{n}} \sqrt{F(s^*)[1 - F(s^*)]}. \tag{3}$$

Note that the asymptotic value  $\mu_D$  is independent of  $n$ . Smith [1982] derived a correction factor for  $\mu_D$  that depends on  $n$  to improve the accuracy of  $\mu_D$  for relatively small bundles. The correction factor is given by

$$\Delta_n^* = \frac{0.996}{n^{2/3}} \left\{ \frac{F'(s^*)^2 s^{*4}}{2F'(s^*) + s^* F''(s^*)} \right\}^{1/3}, \tag{4}$$

where prime means derivative. This factor is added to  $\mu_D$ , to yield  $\mu_D^* = \mu_D + \Delta_n^*$ . Later, McCartney and Smith [1983] derived an improved asymptotic standard deviation of bundle strength, which is

$$\gamma_D^* = \gamma_D \sqrt{1 - 0.320 \left( \frac{\Delta_n^*}{\gamma_D} \right)^2}.$$

In the remainder of this work,  $F(T)$  for fiber strength will follow a Weibull distribution

$$P(X \leq T) = F(T) = 1 - \exp \left\{ - \left( \frac{T}{\sigma_\delta} \right)^\rho \right\},$$

where  $T$  is fiber stress along its axis, and  $\sigma_\delta$  and  $\rho$  are the Weibull scale and shape parameters, respectively. The corresponding  $\mu_D$  and  $\gamma_D$  in Equations (2) and (3) are

$$\mu_D = \sigma_\delta (\rho e)^{-1/\rho}, \quad \gamma_D = \left( \frac{\sigma_\delta}{\sqrt{n}} \right) \rho^{-1/\rho} \sqrt{e^{-1/\rho} (1 - e^{-1/\rho})}, \tag{5}$$

and the correction factor in Equation (4) becomes

$$\Delta_n^* = \frac{0.996 \mu_D}{n^{2/3}} \left( \frac{e^{2/\rho}}{\rho} \right)^{1/3}. \tag{6}$$

The improved  $\mu_D^*$  and  $\gamma_D^*$ , according to [Smith 1982; McCartney and Smith 1983], become

$$\mu_D^* = \mu_D \left\{ 1 + \frac{0.996}{n^{2/3}} \left( \frac{e^{2/\rho}}{\rho} \right)^{1/3} \right\}, \quad \gamma_D^* = \gamma_D \sqrt{1 - 0.317 \left( \frac{\mu_D}{\gamma_D} \right)^2 \left( \frac{e^{2/\rho}}{n^2 \rho} \right)^{2/3}}. \tag{7}$$

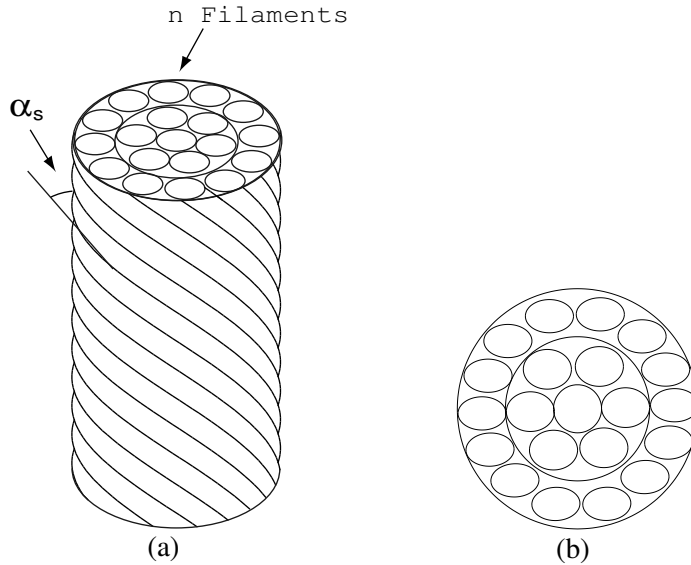


**Figure 1.** (a) Yarn segment and (b) Cross-sectional view of concentric packing.

**4. Strength of twisted fiber bundles**

**4.1. Helical yarn geometry.** The most commonly analyzed geometry of a twisted fiber bundle or yarn is the one in which the fibers lie in concentric cylindrical layers. Within each layer, fibers follow ideal helical paths with the same helix angle, as shown in Figure 1a, but the angle differs from layer to layer. In this idealization, fibers in different layers necessarily must have different lengths to be strain-free yet without slack. This implies that between two yarn cross-sections, fibers (other than the center fiber) will have lengths (when straight) equal to their helical path lengths, and thus, will be longer than the distance between these cross-sections.

Consider an ideal helical structure with  $l$  layers, numbered  $1, \dots, k, \dots, l$ , of fibers with diameter  $d_f$ . The  $l$  layers have respective helix angles  $\alpha_1, \dots, \alpha_k, \dots, \alpha_l$ , and are located at radii  $r_1, \dots, r_k, \dots, r_l$  from the center of the bundle axis. Note that  $r_k$  is the distance from the center of the yarn to the center of the fiber in layer  $k$ . Also the radius of the yarn,  $R$  is taken as  $r_l$ .

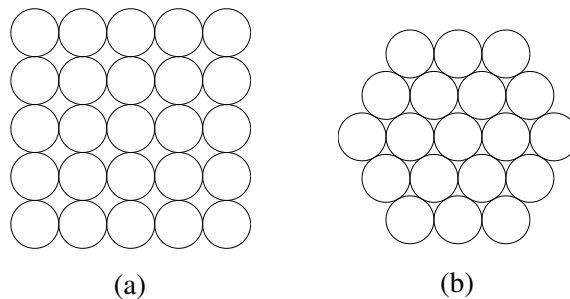


**Figure 2.** Square and hexagonal packing.



Note also that in the cross-sectional view, the fibers are arranged in concentric layers, which we call concentric packing. Concentric packing is different from other commonly used fiber packing models, such as square packing [Figure 2a](#) or hexagonal packing [Figure 2b](#). We also assume that the gap between the layers is negligible compared to the diameter of the fiber. Under these assumptions  $r_k$ , approximately becomes  $r_k \approx (k - 1)d_f$ . If we also assume complete filling of the layers, that is, a fiber will occupy any void in a concentric layer that is large enough to accommodate it, the number of fibers in the  $k^{\text{th}}$  concentric layer,  $n_k$ , is approximately

$$n_k \approx \left\lfloor \frac{2\pi r_k}{d_f} \right\rfloor \approx 2\pi(k - 1), \quad \text{for } k \geq 2, \tag{8}$$

where  $n_1 = 1$  and where  $\lfloor x \rfloor$  means the largest integer less than or equal to  $x$ . As expected,  $n_k$  does not depend on  $d_f$ . The total number of fibers in the bundle  $n$  with  $l$  layers is  $n = n_1 + \dots + n_l$ , but can be approximated as  $n \approx 1 + \pi(l - 1)l$ .

As illustrated in [Figure 1a](#), the helix angle of the outer layer  $\alpha_l$  is especially important and is denoted as  $\alpha_s$ , the surface helix angle. From the yarn twisting process, the helix angle  $\alpha_k$  for concentric layer  $k$  depends on its radius  $r_k$  (being approximately proportional to it) and the surface helix angle,  $\alpha_s$ . From the geometry of the helix illustrated in [Figure 3](#) we have

$$\alpha_k = \tan^{-1} \left( \frac{2\pi r_k}{h} \right), \quad \alpha_s = \tan^{-1} \left( \frac{2\pi R}{h} \right),$$

where the second equation is for the surface layer, located at  $r_l = R$ . Here  $h$  is the height, along the yarn axis, of one turn of twist [Figure 3](#).

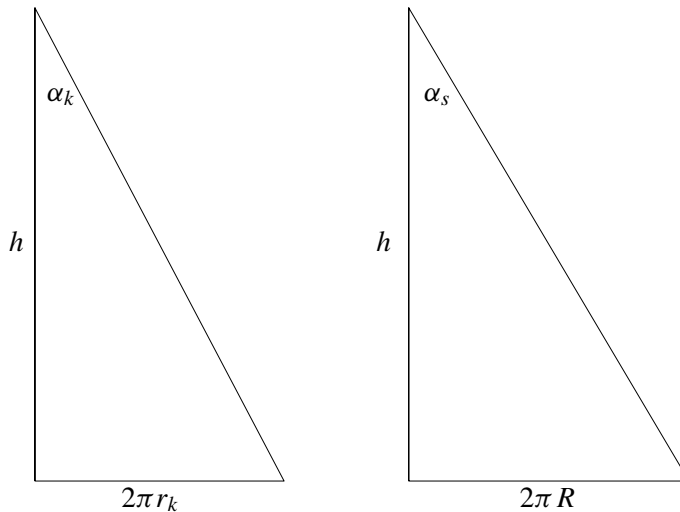


**Figure 3.** The variation of helix angle.

We assume that all layers have the same axial height of one turn of twist,  $h$ , which applies when there is no initial tensile strain or slack in any fiber. Thus,

$$\alpha_k = \tan^{-1} \left( \frac{r_k \tan \alpha_s}{R} \right) \quad (9)$$

in terms of  $\alpha_s$ . In later calculations we will need  $\alpha_{f,i}$ , the helix angle for an individual fiber  $i$ . Let  $\mathfrak{S}_k$  be the set of fibers in layer  $k$ , then  $\alpha_{f,i}$  can be defined as

$$\alpha_{f,i} = \alpha_k, \quad i \in \mathfrak{S}_k \quad \text{and} \quad k = 1, \dots, l.$$

We note that this ideal twisted structure is not common in practice. In a long untwisted yarn all fibers begin with equal lengths, and thus, accomplishing the varying path lengths in different layers during twisting under tension must lead to varying slack or compression in some fibers and uneven strains in others. The yarn attempts to equalize its fiber lengths by the phenomenon called migration. Over a yarn length segment less than or equal to some modest multiple of the yarn diameter, fibers stay within their layer, that is, they do not ‘migrate’. Beyond this length scale, fibers ‘migrate’ to different layers to equalize fiber lengths. If migration is incomplete, there will exist some slack visible as buckling in the fibers due to inefficient migration of fibers, which can lead to inefficiencies in the bundle load-carrying capacity and reductions in strength [Phoenix 1979].

In this paper, we do not model specifically the process of migration. It is assumed that it is complete so that an ideal helical structure is achieved over some bundle length suitable for analysis. Study of the effects of incomplete migration beyond that considered already in [Phoenix 1979] will be left for future work.

**4.2. Transformation of strains.** In this work, we frequently need to transform fiber strains between the individual fiber axis and the bundle axis along which the load is applied. The relationship between the applied bundle strain,  $\epsilon_y$ , and the axial strain,  $\epsilon_f$ , in a fiber of layer  $k$  is taken from basic yarn mechanics [Hearle et al. 1969] and is given by

$$\epsilon_f(\alpha_k) = \epsilon_y(\cos^2 \alpha_k - \nu \sin^2 \alpha_k). \quad (10)$$

In the above,  $\nu$  is the Poisson’s ratio of the yarn. For simplicity we assume  $\nu = 0$ , and thus, neglect any changes in the radial dimension of the yarn under axial loading.

**4.3. Twist-modified equal load-sharing (TM-ELS) rule.** In the case of a parallel fiber bundle, ELS is straightforward and does not violate any of the equilibrium conditions. To modify ELS to apply to a twisted bundle, we simplify the problem greatly by satisfying load equilibrium conditions only in the yarn axis direction. Our general scheme is to model the failure process as progressing in discrete steps  $t = 0, 1, 2, \dots$  in the following way:

- (i) in any particular step,  $t$ , the axial stresses of the surviving fibers are calculated and then compared with the assigned fiber strengths  $X_i$  (as in the case of a parallel fiber bundle);
- (ii) from this comparison, any fiber whose axial stress exceeds its assigned strength is considered breaking in this step. The pre-break stress components in these fibers are resolved along the bundle axis;

- (iii) these resolved components are then redistributed equally to the stress components of the surviving fibers also acting along the yarn axis, and the stresses of these survivors acting along their own respective axes are recalculated;
- (iv) the stresses in these newly broken fibers are then set to zero.

Formulating this approach mathematically, at step  $t$  we denote the stress in fiber  $i$  acting along its own axis (not the yarn axis) as  $T_{f,i}^{(t)}$  as in (i) in the above.  $T_{f,i}^{(t)}$  is considered as composed of two components: The first is the stress carried by the fiber  $T_{f,i}^{\epsilon(t)}$  due to the applied load as if all the fibers are intact and the second component is the sum of the additional stress portions inherited from the broken fibers  $T_{f,i}^{r(t)}$ . Summing these, for fiber  $i$  we have

$$T_{f,i}^{(t)} = \begin{cases} T_{f,i}^{\epsilon(t)} + T_{f,i}^{r(t)}, & \text{for } T_{f,i}^{(t)} < X_i, \\ 0, & \text{otherwise,} \end{cases}$$

where  $X_i$  is its tensile strength. From Equation (10) with  $\nu = 0$ , we have

$$T_{f,i}^{\epsilon(t)} = E_f \epsilon_{f,i} = E_f \epsilon_y^{(t)} \cos^2 \alpha_{f,i}.$$

At each step we recalculate  $T_{f,i}$  according to

$$T_{f,i}^{(t+1)} = \begin{cases} T_{f,i}^{\epsilon(t+1)} + T_{f,i}^{r(t)} + \frac{\sum_{j=1}^{n_b} \cos \alpha_{f,b(j)} X_{b(j)}}{(n - N_b) \cos \alpha_{f,i}}, & \text{for } T_{f,i}^{(t+1)} < X_i, \\ 0, & \text{otherwise,} \end{cases} \tag{11}$$

where  $b(j)$  is the index number of the  $j^{\text{th}}$  failed fiber (that is, the  $j^{\text{th}}$  failed fiber is fiber  $b(j)$  in the yarn),  $n_b$  is the number of new broken fibers when going from step  $t$  to  $t + 1$ , and  $N_b$  is the total number of broken fibers at  $t + 1$ . In this equation, we see a stress enhancement effect in the benefactor fiber (along its axis) that results when it has a larger helix angle compared to the fiber that failed.

The TM-ELS rule is embodied in the RHS of Equation (11), which has three terms: the first term is the stress carried by the fiber as if all the fibers are intact, the sum of the first and second terms is the stress in (i) on page 1432, the numerator of the third term comes from (ii) and (iii), and the denominator in the third term accounts for (iv). We note that  $t$  does not necessarily correspond to an increment in the applied loading; the index  $t$  is increased either

- (a) when we increase the external load level, or
- (b) when at a given external load level, the redistribution of stresses leads to failure of more fibers.

**4.4. Bundle stress.** The cross-sectional area of the bundle (neglecting void space between fibers) is given by

$$\bar{A} = \sum_{k=1}^l \frac{n_k A}{\cos \alpha_k} = \sum_{i=1}^n \frac{A}{\cos \alpha_{f,i}}, \tag{12}$$

where  $A$  is the fiber cross-sectional area perpendicular to the fiber axis. The nominal bundle stress  $\sigma$  is the sum of the fiber force components resolved along the bundle axis divided by the bundle area  $\bar{A}$

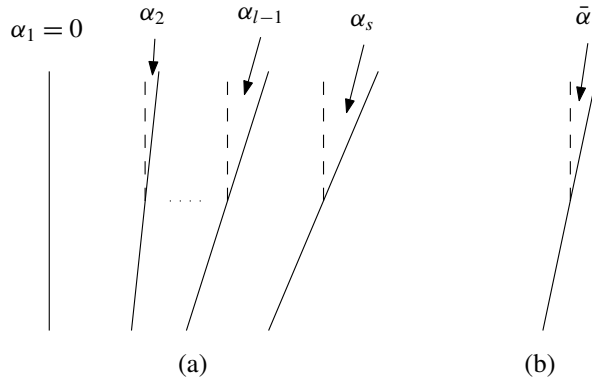


**Figure 4.** Simplified yarn geometry. (a) Layer configuration with multiple angles, (b) simplified geometry where all layers have the same helix angle,  $\bar{\alpha} = \cos^{-1}(\sum_{k=1}^l n_k \cos(\alpha_k)/n)$ , which is the mean helix angle in the general case. The dashed lines indicate the yarn axis direction.

[Phoenix 1979]

$$\sigma = \frac{\sum_{i=1}^n T_{f,i} A \cos \alpha_{f,i}}{\bar{A}} \tag{13}$$

Substituting Equation (12) into Equation (13), we have

$$\sigma = \frac{\sum_{i=1}^n T_{f,i} \cos \alpha_{f,i}}{\sum_{k=1}^l \frac{n_k}{\cos \alpha_k}} = \frac{\sum_{i=1}^n T_{f,i} \cos \alpha_{f,i}}{\sum_{i=1}^n \frac{1}{\cos \alpha_{f,i}}} \tag{14}$$

Note that the stresses in individual surviving fibers will be larger than  $\sigma$  especially when some fibers have failed.

**4.5. Analytical model based on geometrical averaging.** In this section, we develop a probabilistic bundle strength model that averages the fiber helical paths across the bundle to obtain a uniform bundle geometry. In doing so, we define a mean helix angle,  $\bar{\alpha}$ , for the ideal helical structure given as

$$\bar{\alpha} = \cos^{-1} \left( \frac{\sum_{k=1}^l n_k \cos \alpha_k}{n} \right), \tag{15}$$

so that  $\bar{\alpha}$  is weighted by the fraction of all the fibers in each layer  $n_k/n$ , which increases when traveling from center to the surface of the bundle. In essence, this model considers all the fibers to follow the same helical path with  $\bar{\alpha}$  then the TM-ELS rule of Equation (11) reduces to

$$T_{f,i}^{(t+1)} = \begin{cases} T_{f,i}^{\epsilon(t+1)} + T_{f,i}^{r(t)} + \frac{\sum_{j=1}^{n_b} X_{b(j)}}{(n-N_b)}, & \text{for } T_{f,i}^{(t+1)} < X_i, \\ 0, & \text{otherwise,} \end{cases} \tag{16}$$

$$T_{f,i}^{(0)} = T^{(0)} = E_{f\epsilon_y}^{(0)} \cos^2 \bar{\alpha}, \tag{17}$$

where the second line gives the initial stress at  $t = 0$  and where  $\epsilon_y^{(0)}$  is the initially applied bundle strain.

Combining Equations (16) and (17) shows that all intact fibers will sustain the same stress along the fiber axis, that is,

$$T_{f,i}^{(t+1)} = \begin{cases} T & \text{for } T_{f,i}^{(t+1)} < X_i, \\ 0 & \text{otherwise.} \end{cases} \tag{18}$$

In Equation (14), replacing  $\cos \alpha_{f,i}$  by  $\cos \bar{\alpha}$  given in Equation (15), the nominal bundle stress along the bundle axis becomes

$$\sigma = \frac{\sum_{i=1}^n T_{f,i} \cos^2 \bar{\alpha}}{n},$$

and by Equation (18), when there are  $N_b$  failed fibers,  $\sigma$  becomes

$$\sigma = \left(\frac{n - N_b}{n}\right) T \cos^2 \bar{\alpha}. \tag{19}$$

The instantaneous fiber stress component acting along the bundle axis is  $s = T \cos^2 \bar{\alpha}$ , whereby Equation (19) simplifies to

$$s = \left(\frac{n}{n - N_b}\right) \sigma,$$

which is the well-known ELS expression for  $s$  as a function of  $\sigma$ ,  $n$ , and  $N_b$ .

The idea of a mean angle  $\bar{\alpha}$  and an equivalent stress  $T$  for all fibers may well represent the condition of complete migration, which occurs over a short yarn length scale. In this case, a fiber resides in a particular layer only over a very short distance along the yarn axis. Thus, its local tension at a particular cross section is more reflective of the average helix angle than the helix angle of the layer in which it currently resides.

For Weibull fibers under stress  $T$  along its axis, the corresponding fiber failure cumulative probability distribution function (cdf)  $F(T)$  is

$$F(T) = 1 - \exp \left\{ -\left(\frac{T}{\sigma_\delta}\right)^\rho \right\}. \tag{20}$$

As in Daniels' bundle theory, we cast  $F(T)$  in terms of  $s$ , the fiber stress acting along the bundle axis. Substituting  $s = T \cos^2 \bar{\alpha}$  into Equation (20) yields

$$F(s) = 1 - \exp \left\{ -\left(\frac{s}{\cos^2 \bar{\alpha} \sigma_\delta}\right)^\rho \right\}.$$

Following geometric averaging, the strength of a twisted bundle corresponds to that for a parallel bundle of fibers whose strengths follow a Weibull distribution with the same shape parameter  $\rho$  but a 'modified' scale parameter  $\sigma_{\delta,\alpha} = \cos^2 \bar{\alpha} \sigma_\delta$ . Hence, the asymptotic distribution function for bundle strength will be Gaussian with mean  $\mu_G$  and standard deviation  $\gamma_G$  given by

$$\mu_G = \sigma_{\delta,\alpha} (\rho e)^{-1/\rho} = \mu_D \cos^2 \bar{\alpha}, \quad \gamma_G = \left(\frac{\sigma_{\delta,\alpha}}{\sqrt{n}}\right) \rho^{-1/\rho} \sqrt{e^{-1/\rho} (1 - e^{-1/\rho})} = \gamma_D \cos^2 \bar{\alpha},$$

where  $\mu_D$  and  $\gamma_D$  are the mean strength and standard deviation of a Daniels parallel fiber bundle given by Equation (5).

Using the [Smith 1982; McCartney and Smith 1983] corrections we obtain improved estimates,  $\mu_G^*$  and  $\gamma_G^*$ , for the mean and standard deviation:

$$\mu_G^* = \mu_D \cos^2 \bar{\alpha} \left\{ 1 + \frac{0.996}{n^{2/3}} \left( \frac{e^{2/\rho}}{\rho} \right)^{1/3} \right\}, \quad \gamma_G^* = \gamma_D \cos^2 \bar{\alpha} \sqrt{1 - 0.317 \left( \frac{\mu_D}{\gamma_D} \right)^2 \left( \frac{e^{2/\rho}}{n^2 \rho} \right)^{2/3}}.$$

**4.6. Analytical model based on statistical averaging.** In this section, we develop a second probability model for bundle strength, based on statistical averaging, where we average the failure probabilities of the fibers across the layers in an ideal helical structure. In doing so, we find it convenient to change to a continuous description of the bundle geometry. We let  $\bar{r} = r/R$ , that is, the radial distance normalized by yarn radius, so that  $\bar{r} = 0$  is the yarn axis and  $\bar{r} = 1$  corresponds to the yarn radius. The fiber helix angle  $\alpha(\bar{r})$  is taken as a continuous function of  $\bar{r}$ . Accordingly,  $\alpha(\bar{r} = 0) = 0$  and  $\alpha(\bar{r} = 1) = \alpha_s$ . Likewise we let  $n_r(\bar{r})$  be the number of fibers within a cylinder of radius  $\bar{r}$ , taking it to be a continuous function of  $\bar{r}$ . Thus  $n_r(\bar{r} = 0) = 0$  and  $n_r(\bar{r} = 1) = n$ . Therefore  $dn_r(\bar{r})/n$  is the fraction of fibers between  $\bar{r}$  and  $\bar{r} + d\bar{r}$ .

As mentioned earlier, the fiber stresses  $T_{f,i}$  are generally a sum of the stress generated from the applied loading, assuming no fiber breaks,  $T_{f,i}^\epsilon$ , and the stress components transferred from broken fibers,  $T_{f,i}^r$ . The former stresses are distributed nonuniformly depending on the fiber helix angles, whereas the latter additional stresses transferred from fiber breaks will resolve to have same components acting along the yarn axis according to the TM-ELS rule described above. As fiber failures accumulate, these latter contributions,  $T_{f,i}^r$ , typically greatly exceed the nonuniform contributions  $T_{f,i}^\epsilon$ . In this case, the component of  $T_{f,i}$  acting along the yarn axis can be reasonably considered equal for all fibers, and thus, taken as  $s = T_{f,i} \cos^2 \alpha(\bar{r})$ , as defined earlier. Accordingly, the probability of failure  $F(T_{f,i})$  for fiber  $i$ , with helix angle  $\alpha(\bar{r})$ , in terms of  $s$  is

$$F(s) = 1 - \exp \left\{ - \left( \frac{s}{\sigma_\delta \cos^2 \alpha(\bar{r})} \right)^\rho \right\}.$$

The assumption that the component of stress along the yarn axis,  $s$ , is equal for all fibers greatly simplifies the calculation of average failure probability across the yarn cross-section. Denoting this average as  $\bar{F}(s)$ , we have

$$\bar{F}(s) = \int_{\alpha=0}^{\alpha_s} \left[ 1 - \exp \left\{ - \left( \frac{s}{\sigma_\delta \cos^2 \alpha(\bar{r})} \right)^\rho \right\} \right] \frac{dn_r(\bar{r})}{n}. \tag{21}$$

The functions  $n_r(\bar{r})$  and  $\alpha(\bar{r})$  are calculated from the bundle packing density  $\nu(\bar{r})$ . As in [Phoenix 1979], for large bundles we take

$$\nu(\bar{r}) = \frac{\phi^{(\infty)}}{\pi} \cos \alpha(\bar{r}), \quad \phi^{(\infty)} = \frac{1}{2}(1 + \sec \alpha_s), \tag{22}$$

for  $0 \leq \bar{r} \leq 1$ . Equation (22) assumes that the fiber packing density is uniform in the yarn cross-section, that is, the void fraction is constant with respect to radial position. (Actually, the void fraction may be expected to decrease slightly as  $r$  decreases, since the radial pressure in the yarn increases from yarn surface to the yarn center. Nevertheless, such effects are difficult to model, and little is believed to be lost with the uniform packing assumption.) Since  $\nu(\bar{r})$  satisfies

$$\int_0^1 \nu(\bar{r}) 2\pi \bar{r} d\bar{r} = 1,$$

the fraction of all fibers within a cylinder of radius  $\bar{r}$  can be written as

$$\frac{n_r(\bar{r})}{n} = \int_0^{\bar{r}} v(\bar{r}) 2\pi \bar{r} d\bar{r}.$$

Upon differentiating this equation with respect to  $\bar{r}$ , we get

$$\frac{dn_r(\bar{r})}{n} = \frac{\phi^{(\infty)}}{\pi} \cos \alpha(\bar{r}) 2\pi \bar{r} d\bar{r}. \tag{23}$$

Substituting Equation (23) into Equation (21), the ‘average’ probability distribution for fiber failure can be rewritten in terms of  $\alpha(\bar{r})$  only as

$$\bar{F}(s) = \int_{\alpha=0}^{\alpha_s} \left[ 1 - \exp \left\{ - \left( \frac{s \sec^2 \alpha(\bar{r})}{\sigma_\delta} \right)^\rho \right\} \right] \frac{\phi^{(\infty)}}{\pi} \cos \alpha(\bar{r}) 2\pi \bar{r} d\bar{r}. \tag{24}$$

For an ideal yarn geometry we have

$$\tan \alpha(\bar{r}) = \frac{2\pi \bar{r}}{\bar{h}}, \tag{25}$$

where  $\bar{h} = h/R$  and at the surface of the yarn

$$\tan \alpha_s = \frac{2\pi}{\bar{h}}. \tag{26}$$

From Equation (25) we get

$$\sec^2 \alpha d\alpha = \frac{2\pi}{\bar{h}} d\bar{r}. \tag{27}$$

Substituting Equations (24)–(27) into Equation (21) yields

$$\begin{aligned} \bar{F}(s) &= \frac{2\phi^{(\infty)}}{\tan^2 \alpha_s} \int_{\alpha=0}^{\alpha_s} \left[ 1 - \exp \left\{ - \left( \frac{s \sec^2 \alpha}{\sigma_\delta} \right)^\rho \right\} \right] \tan \alpha \sec \alpha d\alpha \\ &= 1 - \frac{2\phi^{(\infty)}}{\tan^2 \alpha_s} \int_{\alpha=0}^{\alpha_s} \exp \left\{ - \left( \frac{s \sec^2 \alpha}{\sigma_\delta} \right)^\rho \right\} \tan \alpha \sec \alpha d\alpha \\ &= 1 - \frac{2\phi^{(\infty)}}{\tan^2 \alpha_s} \int_1^{\sec \alpha_s} \exp \left\{ - \left( \frac{s}{\sigma_\delta} \right)^\rho x^{2\rho} \right\} dx \\ &= 1 - \frac{\phi^{(\infty)}}{\rho \tan^2 \alpha_s} \left( \frac{s}{\sigma_\delta} \right)^{-1/2} \int_{(s/\sigma_\delta)^\rho}^{(s/\sigma_\delta)^\rho \sec^{2\rho} \alpha_s} e^{-y} y^{1/2\rho-1} dy, \end{aligned} \tag{28}$$

where in the third line we made the change of variables  $\sec \alpha = x$ , and again in the fourth line as  $y = (s/\sigma_\delta)^\rho x^{2\rho}$ . The integral in Equation (28) can be written in terms of upper incomplete Gamma functions [Abramowitz and Stegun 1964] as shown below

$$\bar{F}(s) = 1 - \frac{\phi^{(\infty)}}{\rho \tan^2 \alpha_s} \left( \frac{s}{\sigma_\delta} \right)^{-1/2} \left[ \Gamma \left( \frac{1}{2\rho}, \left\{ \frac{s}{\sigma_\delta} \right\}^\rho \right) - \Gamma \left( \frac{1}{2\rho}, \left\{ \frac{s}{\sigma_\delta} \right\}^\rho \sec^2 \alpha_s \right) \right].$$

In statistical averaging, the problem for a twisted bundle reduces to that for a parallel fiber bundle with fiber strength probability distribution given by  $\bar{F}(s)$ . As a result, the bundle strength is asymptotically

normal where the asymptotic bundle mean strength and standard deviation are given by

$$\mu_S = s^*[1 - \bar{F}(s^*)], \quad \gamma_S = \frac{s^*}{\sqrt{n}} \sqrt{\bar{F}(s^*)[1 - \bar{F}(s^*)]},$$

where  $s^*$  is the point where the maximum of  $\mu(s)$  occurs. The final result according to statistical averaging is calculated by applying corrections due to [Smith 1982; McCartney and Smith 1983]. Thus, the improved estimates for the mean and standard deviation,  $\mu_S^*$  and  $\gamma_S^*$  are

$$\mu_S^* = \mu_S + \bar{\Delta}_n^*, \quad \gamma_S^* = \gamma_S \sqrt{1 - 0.320 \left( \frac{\bar{\Delta}_n^*}{\gamma_S} \right)^2},$$

where

$$\bar{\Delta}_n^* = \frac{0.996}{n^{2/3}} \left\{ \frac{\bar{F}'(s^*)^2 s^{*4}}{2\bar{F}'(s^*) + s^* \bar{F}''(s^*)} \right\}^{1/3}.$$

### 5. Simulation algorithms

We now discuss the Monte Carlo simulation algorithm for the failure of a twisted bundle of Weibull fibers having shape parameter  $\rho$ , and scale parameter  $\sigma_\delta$ . These fibers are assumed to have identical diameter, cross-sectional area, and Young’s modulus, and are arranged in  $l$  layers having ideal helical structure. For a given twisted bundle surface helix angle,  $\alpha_s$ , the helix angle of each layer can be determined using Equation (9). The number of fibers in each layer,  $n_k$ , can be determined using Equation (8) and the total number of fibers  $n$  is the sum.

For a given set of values of the above parameters, we first assign a Weibull strength to each of the  $n$  fibers. We assume that these fibers are twisted without tension so the fibers do not have any pre-stress or pre-strain. For a given set of parameter values, the number of replications performed by the Monte Carlo simulation is  $n_s$ .

Starting from zero, we can either apply a monotonically increasing uniform stress or strain. Both algorithms are described briefly below. These two algorithms yield the same empirical probability distribution and mean strength results except that the stress-strain curves obtained by these two algorithms exhibit different characteristics. In a stress-controlled experiment failure is sudden and the external load drops from the maximum to zero. In a strain-controlled experiment, the bundle stress starts from zero, attains a maximum defined as the strength, and then decreases to zero while the bundle strain is monotonically increased indefinitely.

**5.1. Stress-controlled experiment.** In a stress-controlled experiment the stress is increased incrementally in predetermined small steps. Whenever a step encounters a fiber for which its axial stress exceed its strength, the fiber is broken and then its stress is distributed equally among the intact fibers according to TM-ELS. The algorithm then checks to see if the additional loads on the survivors would result in any of their assigned strengths being exceeded, and if so, these fibers are then broken and their updated loads are redistributed. If not, equilibrium has been achieved at that step in which case new incremental steps in external load are applied until some survivors have their strengths exceeded. These fibers are then broken and the stress redistribution process is repeated.



Eventually we reach bundle collapse whereby all remaining fibers fail with no further increase in the applied stress. The threshold external stress beyond which all the fibers fail is recorded as the bundle strength.

**5.2. Strain-controlled experiment.** In a strain-controlled experiment we do not have to explicitly redistribute the load from broken fibers to intact ones. At each increment in applied bundle strain we calculate fiber strains for each layer. If the strain of a fiber in some layer exceeds its failure strain then that fiber becomes broken and the external bundle load and stress for that bundle strain is recalculated. The bundle stress at increment number  $t$  is then given by

$$\sigma^{(t)} = \frac{\sum_{i=1}^n E_t \epsilon_{f,i}^{(t)} \cos \alpha_{f,i}}{\sum_{i=1}^n \frac{1}{\cos \alpha_{f,i}}}, \quad \epsilon_{f,i}^{(t)} = \begin{cases} \epsilon_{f,i} & \text{for } \epsilon_{f,i} < \xi_i, \\ 0 & \text{otherwise,} \end{cases}$$

where  $\xi_i$  is the failure strain of fiber  $i$ . The bundle strength is given by  $\text{strength} = \max_t \{\sigma^{(t)}\}$ .

## 6. Results and discussion

In this section, we discuss and compare the theoretical and Monte Carlo simulation results for the strength of a twisted fiber bundle.

**6.1. Validation of simulation algorithm.** As a form of validation we performed Monte Carlo simulation for the case of a parallel fiber bundle, that is,  $\alpha_s = 0$ . In Figure 5 the simulated bundle mean strength and asymptotic standard deviation normalized by  $\sigma_\delta$  are compared with corrected Daniels' values,  $\mu_D^*$  and  $\gamma_D^*$ , normalized by  $\sigma_\delta$ , given by Equation (7), as  $\rho$  varies from 2 to 10. Note that all estimates for the mean and standard deviation in Figure 5 are normalized by  $\sigma_\delta$ . We achieve good agreement between the parallel bundle theory and simulation for the entire range of  $\rho$  and both bundle sizes considered,  $n = 130$  and  $n = 1185$ . If corrections by [Smith 1982; McCartney and Smith 1983] are not applied, then  $\mu_D$  slightly underestimates and  $\gamma_D$  overestimates the corresponding simulated values. The means for different bundle sizes differ only slightly because of the correction to the Daniels' value. Likewise the standard deviation values will collapse almost onto one curve when scaled by  $\sqrt{n}$  (not shown in the figure).

**6.2. Failure behavior.** From the simulation results we have noticed that both  $\alpha_s$  and  $\rho$  clearly affect the nature of failure. In the case of low  $\alpha_s$  and low  $\rho$  the fiber breaks are spread randomly across the cross-section of the bundle. Also the fraction of failed fibers when the maximum bundle stress is achieved is relatively high, indicative of a ductile-type failure process. In the case of high  $\alpha_s$  and high  $\rho$  there are relatively fewer failed fibers when the peak bundle stress is reached, and these are more likely to concentrate near the center of the bundle, indicative of a brittle-type failure.

The observed transitions in failure mode are a consequence of the interaction of  $\rho$  and the strain distribution among the layers, which depends on  $\alpha_s$ . As the variation in fiber strength increases ( $\rho$  decreases) failure progression becomes dominated by the widely dispersed fiber strengths. It is more dispersed for lower  $\alpha_s$ , as the variation in fiber strains across the bundle is mild. As the variation in fiber strength decreases ( $\rho$  increases) failure progression becomes dominated by the fiber strain distribution. In this case, as we increase  $\alpha_s$  the gradient in strain between the highly strained center and less strained surface layers steepens, promoting failure to be localized towards the center.

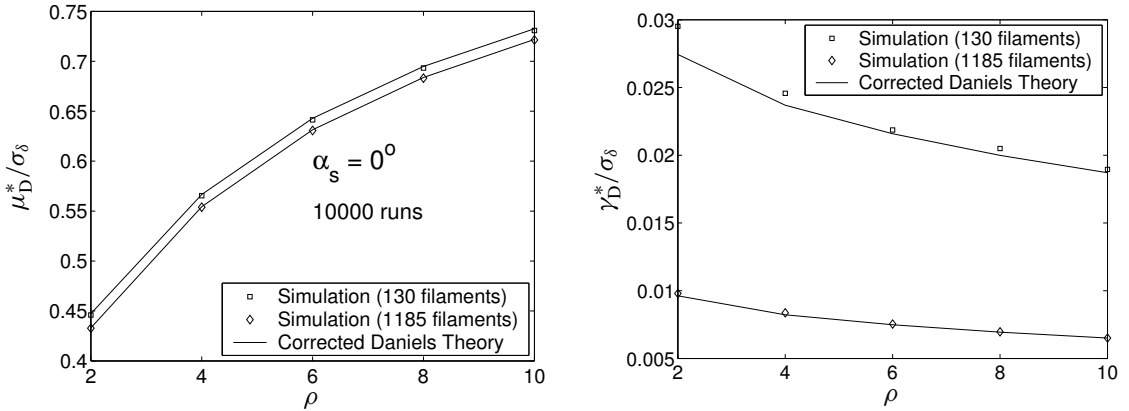


**Figure 5.** Normalized mean and asymptotic standard deviation for bundle strength obtained from Monte Carlo simulation ( $n_s = 10000$ ) as compared with the corresponding corrected Daniels' values given by Equation (7).

**6.3. Stress-strain curves.** Figure 6 shows average stress-strain curves (average of 500 runs) for bundles with 62 and 1185 fibers, respectively, but otherwise the same parameter values  $\alpha_s = 12^\circ$ ,  $\rho = 2$  and 8. Also shown are sample stress-strain curves for three successive realizations. For the smaller bundle with only 62 fibers the sample stress-strain curves show significant deviation from the average behavior reaching 5-10% near the peak stress. This implies that for a long chain of such bundles one might expect the chain to be much weaker than the average bundle strength as the strength would be governed by the weakest bundle. On the other hand, for the 1185 fiber bundle the deviations are much smaller being 1-2%, so a long chain of such bundles would be much closer to the average bundle strength. The fluctuations in the bundle strength grow as the variation in fiber strength increases, such as when  $\rho = 8$  decreases to  $\rho = 2$ .

Figure 6 shows that the initial bundle modulus is independent of  $\rho$ . This high initial modulus occurs because of the initiation of a relatively few randomly dispersed breaks. After further straining, the slope of the stress-strain curve decreases at a rate which depends on  $\rho$ , since this controls the variability and thus, the rate at which weak fibers are encountered as strain increases. Eventually the peak stress is reached when loss of fibers through breakage outweighs the increased stresses occurring in the survivors with increasing strain, these being different from fiber to fiber. (In the stress-controlled experiment this corresponds to the stress (and strain) at which instability is reached and sudden collapse occurs.) Concomitantly the stress drops with further straining at a rate which also depends on  $\rho$ , becoming more abrupt and brittle-like as  $\rho$  increases.

**6.4. Cumulative probability density functions.** Figure 7 shows the simulated cumulative probability distribution function for the strength of a twisted fiber bundle on normal probability paper, namely,  $\text{erf}^{-1}(2G_n - 1)$  vs.  $S/\sigma_\delta$ , where we recall that  $G_n$  is the bundle strength cumulative distribution function. The linearity of the distributions suggests that in all cases the strength distribution is virtually normal. Figure 7a displays its dependence on the surface helix angle  $\alpha_s$ , ( $\alpha_s = 0^\circ, 6^\circ, 12^\circ, 18^\circ, 24^\circ$ )

for the case of  $\rho = 6$  and  $n = 1185$ . Figure 7b shows its dependence on bundle size  $n$ , ( $n = 130, 653, 1185$ ) for  $\rho = 4$  and  $\alpha_s = 12^\circ$ . From Figure 7a we find that the strengths decrease substantially as  $\alpha_s$  increases, while the standard deviation (inversely related to the slope of the curves) stays more or less independent of  $\alpha_s$  and Figure 7b shows that the bundle size  $n$  has its most significant impact on the bundle standard deviation, which is approximately inversely proportional to  $n$ . Also shown in Figure 7 are the corresponding predictions from the model based on statistical averaging. In general, we find that when  $\alpha_s < 18^\circ$  the model achieves very good agreement with the simulation result. For larger values of  $\alpha_s$ , the model provides a conservative estimate.

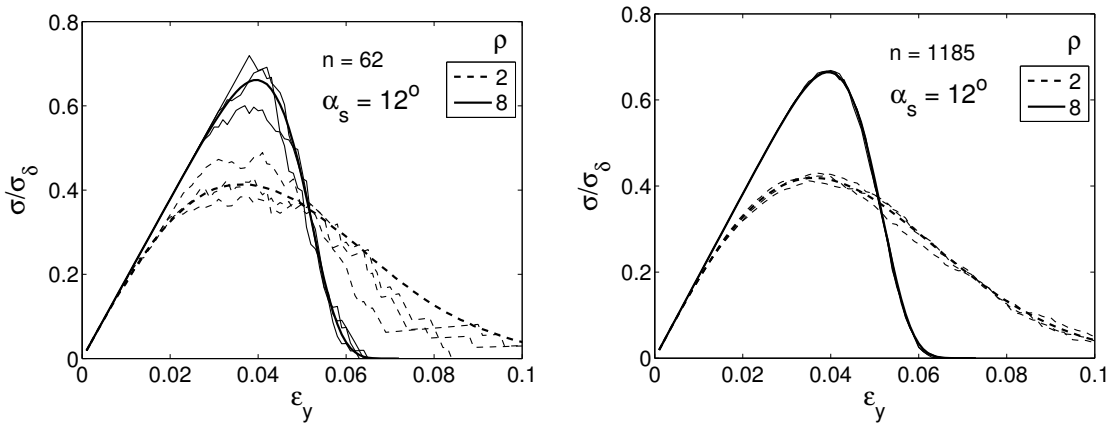


**Figure 6.** Thin lines are sample stress strain curves and thick lines are average (of 500 runs) stress strain curves for given values of  $\rho$ ,  $\alpha_s$ , and  $n$ .

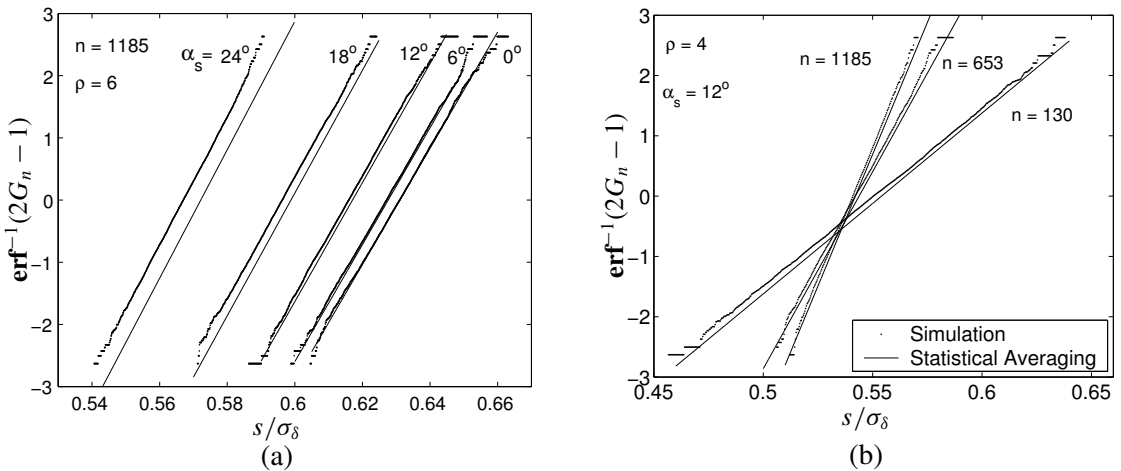


**Figure 7.** Distribution functions on normal probability paper ( $\text{erf}^{-1}(2G_n - 1)$  versus  $S/\sigma_\delta$ ) for 10000 replications. The parameters used for these plots are (a)  $n = 1185$ ,  $\rho = 6$  and  $\alpha_s = 0^\circ, 6^\circ, 12^\circ, 18^\circ, 24^\circ$ ; (b)  $\rho = 4$ ,  $\alpha_s = 12^\circ$  and  $n = 130, 653$ , and  $1185$ . Here  $S$  is the strength of the bundle obtained either from the simulation or size corrected statistical averaging theory.

**6.5. Strength and standard deviation efficiency, and coefficient of variation.** To study the dependence of the mean bundle strength on  $\alpha_s$  and  $\rho$ , we calculate the strength efficiency of the fiber bundle,  $\mathcal{E}_\mu$ , which is the ratio of mean bundle strength to mean fiber strength,

$$\mathcal{E}_\mu = \frac{\mu^*}{E(X)},$$

where  $\mu^*$  is the mean bundle strength for given  $n$  obtained either using one of the theories (corrected for  $n$ ) or a simulation and  $E(X)$  is the mean strength of the fiber. For Weibull fibers,  $E(X) = \sigma_\delta \Gamma(1 + 1/\rho)$ , where  $\Gamma(\cdot)$  is the Gamma function. For instance, in the case of geometrical averaging, the strength efficiency for a very large bundle (not requiring a size correction) is the closed form expression

$$\mathcal{E}_\mu^{(\infty)} = \frac{\cos^2 \bar{\alpha} \sigma_\delta (\rho e)^{-1/\rho}}{\sigma_\delta \Gamma(1 + 1/\rho)} = \frac{\cos^2 \bar{\alpha} (\rho e)^{-1/\rho}}{\Gamma(1 + 1/\rho)},$$

which depends only on the mean helix angle,  $\bar{\alpha}$ , and Weibull shape parameter,  $\rho$ .

Another useful quantity for reflecting variability in the bundle strength is the coefficient of variation, ( $\mathcal{CV}$ ), which is the ratio of the standard deviation to the mean, expressed as

$$\mathcal{CV} = \frac{\gamma^*}{\mu^*}. \tag{29}$$

For a measure of the statistical variation in bundle strength compared to that of a single fiber, we define the transfer efficiency of the variability as the ratio of the bundle standard deviation to the fiber standard deviation, that is

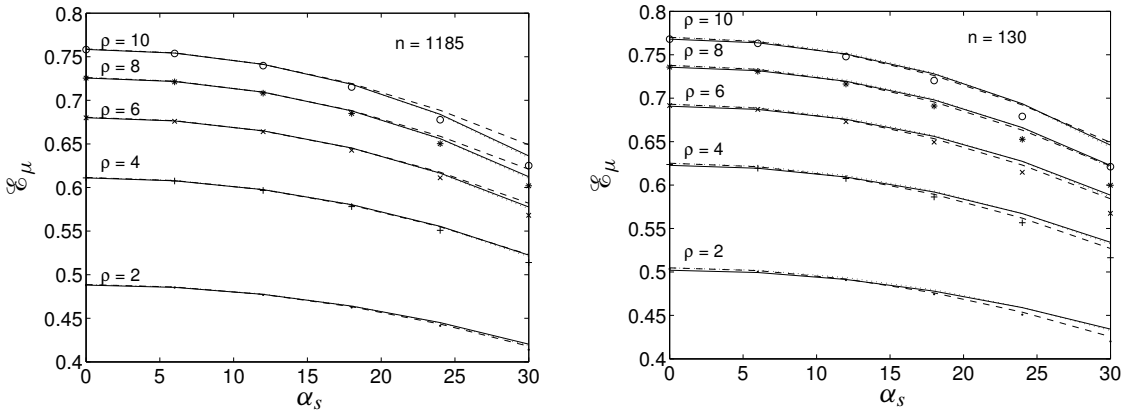
$$\mathcal{E}_\gamma = \frac{\gamma^*}{\sqrt{\text{Var}(X)}}, \tag{30}$$

where  $\text{Var}(X)$  is the variance of fiber strength  $X$ . Again the bundle  $\gamma^*$  and  $\mu^*$  are calculated for a given  $n$  either from one of the three theories (corrected for  $n$ ) or simulation. In the case of geometrical averaging, Equations (29) and (30) for a large bundle (not requiring a size correction) become

$$\mathcal{CV}^{(\infty)} = \sqrt{\frac{1 - e^{-1/\rho}}{n e^{-1/\rho}}}, \quad \mathcal{E}_\gamma^{(\infty)} = \frac{\cos^2 \bar{\alpha} \rho^{-1/\rho} \sqrt{e^{-1/\rho} (1 - e^{-1/\rho})}}{\sqrt{n [\Gamma(1 + 2/\rho) - \Gamma^2(1 + 1/\rho)]}}.$$

In all theories  $\mathcal{CV}$ ,  $\mathcal{E}_\mu$ , and  $\mathcal{E}_\gamma$  are independent of  $\sigma_\delta$ .

Figure 8 compares simulation and theoretical predictions for  $\mathcal{E}_\mu$  vs.  $\alpha_s$  for different values of  $\rho$ . Generally  $\mathcal{E}_\mu$  decreases as  $\rho$  decreases (that is, the variability in the fiber strength increases) and  $\alpha_s$  increases. As  $\alpha_s$  increases, more fibers in the bundle become misaligned with the direction of loading. As  $\rho$  decreases, a higher proportion of weaker fibers exists in the bundle. Figure 8 shows that all theories capture the effects of  $\rho$  and  $\alpha_s$  on the strength efficiency of the twisted fiber bundle very well. For both  $n = 130$  and 1185 and smaller  $\alpha_s$  (up to  $18^\circ$ ) there is almost no difference between theory and simulation. However, for higher values of  $\alpha_s$  there are slight differences, which diminish as  $\rho$  decreases, that is, the variability increases and a rather diffuse-type of failure mode occurs. TM-ELS translates to a diffuse failure pattern when  $\alpha_s$  and  $\rho$  are low, but not when they are both high. Therefore the discrepancy between theory and simulation at high  $\rho$  and high  $\alpha_s$  is attributed to the fact that under these conditions the failure is more or less localized near the center of the yarn, up to the point of collapse.



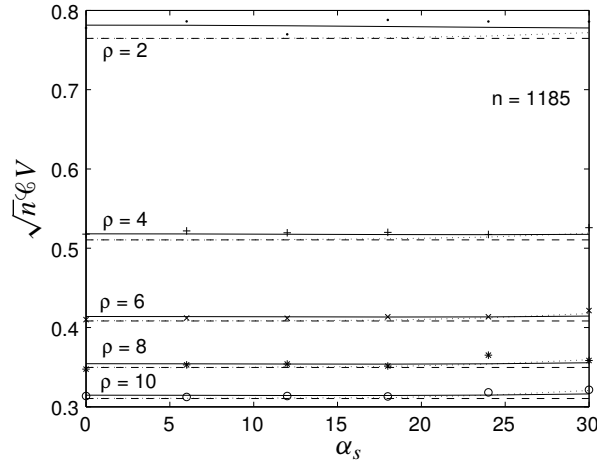
**Figure 8.** Strength efficiency,  $\mathcal{E}_\mu$ , versus surface helix angle,  $\alpha_s$ . Dashed and solid lines correspond to theories based on geometrical averaging and statistical averaging, respectively. Dotted lines are obtained using the theory of [Phoenix 1979]. The marker points are simulation results.

Figure 9 depicts the behavior of the  $\mathcal{C}^V$  for  $n = 1185$ . The simulation results show that it is independent of  $\alpha_s$  with the exception of a slight drop in  $\mathcal{C}^V$  at a high value of  $\alpha_s$  ( $\approx 25^\circ$ ). The latter drop can again be attributed to less variability in the failure patterns from one bundle to another, as  $\alpha_s$  increases. The agreement between the theories and simulation is very good. In cases of smaller  $\rho$ , the statistical averaging model performs better than the other theories discussed earlier. For smaller bundles,  $n = 130$  and lower  $\rho < 4$  the discrepancies between the asymptotic theories and simulation increase as shown in Figure 10. The thick lines in Figure 10 are the  $\mathcal{C}^V$  predictions with corrections applied to both the mean and standard deviation, that is,  $\mathcal{C}^V = \mu^*/\gamma^*$ , as in Figure 9. Again in these cases, the statistical averaging model outperforms the others. The thinner lines in Figure 10 correspond to the  $\mathcal{C}^V$  calculations when correcting the mean only,  $\mathcal{C}^V = \mu^*/\gamma$ , which is shown to provide a conservative estimate.

Figure 11 shows the dependence of  $\mathcal{E}_\gamma$  on  $\rho$  and  $\alpha_s$ . While  $\gamma$  and the  $\mathcal{C}^V$  increase as the variability in fiber strength increases ( $\rho$  decreases), the  $\mathcal{E}_\gamma$  decreases (improves). As shown, the theories provide equally good agreement for  $n = 1185$ , but for  $n = 130$ , the statistical averaging model consistently provides values closer to the simulation results. Also, given in Table 1 are dimensional values of bundle strength mean and standard deviation to show how they compare.

### 7. Effect of friction and chain-of-bundles calculation

Beginning with the model for the failure of a single bundle as introduced earlier in the paper, we outline a basic framework for predicting the strength of a twisted yarn of length  $L$ . For this, we apply the chain-of-bundles (COB) model, where the strength of weakest bundle in the chain is the strength of the chain. The COB model requires defining the length of each bundle or link in the chain, that is, a “characteristic stress transfer length”, which is appropriately defined by the fiber length needed for the fiber to recover the stress away from a break. This length depends on the interfiber friction as well as the contact pressures



**Figure 9.** Coefficient of variation scaled with bundle size,  $\sqrt{n}CV$ , vs surface helix angle,  $\alpha_s$  for  $n = 1185$ , and  $\rho = 2, 4, 6, 8,$  and  $10$ . Dashed and solid lines correspond to theories based on geometrical averaging and statistical averaging, respectively. Dotted lines are obtained using the theory of [Phoenix 1979]. The marker points are simulation results.

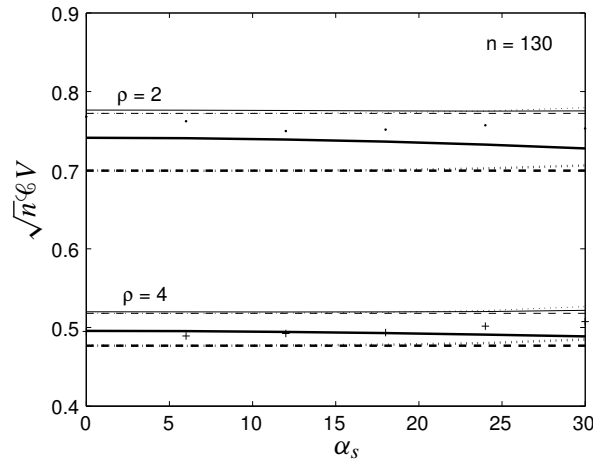


**Figure 10.** Coefficient of variation scaled with bundle size,  $\sqrt{n}CV$ , vs surface helix angle,  $\alpha_s$ . Thick lines correspond to values where correction to both strength mean and standard deviation are applied, and in the case of thin lines, correction is applied to strength mean only. Dashed and solid lines correspond to theories based on geometrical averaging and statistical averaging, respectively. Dotted lines are obtained using the theory of [Phoenix 1979]. The marker points are simulation results.

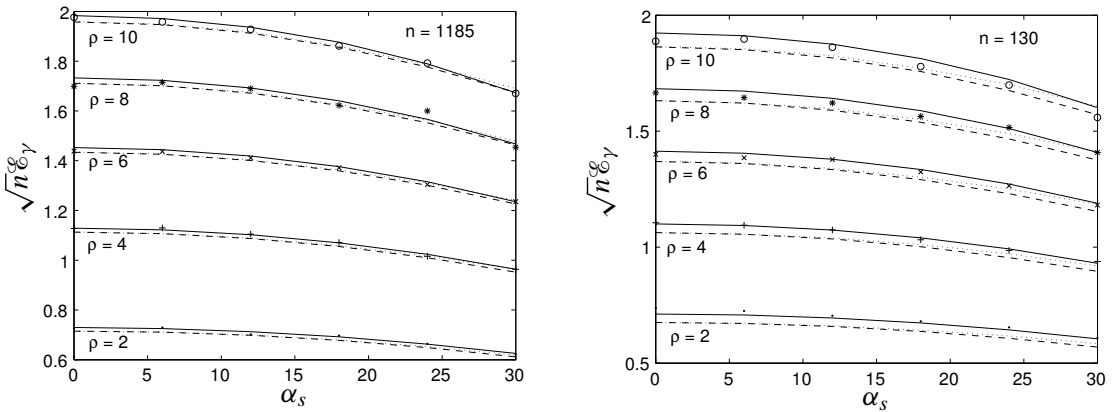


**Figure 11.** Transfer efficiency of the variability  $\sqrt{n\epsilon_\gamma}$  versus surface helix angle  $\alpha_s$ . The left one is for 1185 fibers and the right one is for 130 fibers. Dashed and solid lines correspond to theories based on geometrical averaging and statistical averaging, respectively. Dotted lines are obtained using the theory of [Phoenix 1979]. The marker points are simulation results.

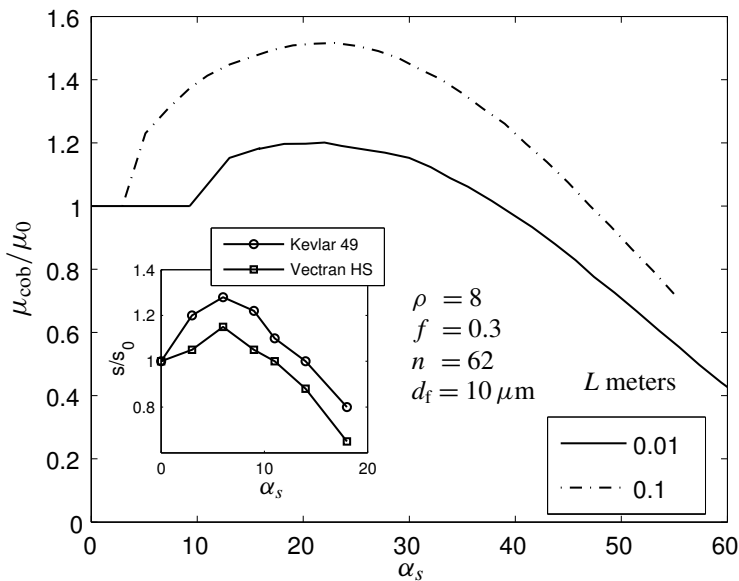


**Figure 12.** Normalized mean yarn strength versus surface helix angle  $\alpha_s$  for yarn length  $L$ . Here  $\mu_0$  is the strength of the yarn when  $\delta_c = L$ . Inset figure (normalized yarn strength  $S/S_0$  versus  $\alpha_s$ ) is plotted using data from [Rao and Farris 2000], where  $S_0$  is the yarn strength when  $\alpha_s = 0$ .

between the fibers caused by twisting. A rigorous analysis of friction effects and their impact on this characteristic link length are beyond the scope of this work and are treated in a sequel.

For a simple demonstration of the COB model, we employ a friction length given by [Alexander 1952]

$$l_f = \frac{\beta_A d_f}{(1 - \phi_A) f \sin^2 \alpha_A},$$

where  $f$  is the friction coefficient,  $\phi_A$  and  $\beta_A$  are two adjustable parameters, taken by Alexander to be  $1/2$ , and  $\alpha_A$  is the corresponding helix angle satisfying  $\tan \alpha_A = \beta_A \tan \alpha_s$ . We define the characteristic length of a bundle in terms of the friction length, with  $\phi_A = \beta_A = 1/2$ , as

$$\delta_c = 2l_f \cos \alpha_A = \frac{2 d_f \cos \alpha_A}{f \sin^2 \alpha_A} = \delta_c(\alpha_s) = \frac{4d_f \sqrt{4 + \tan^2 \alpha_s}}{f \tan^2 \alpha_s}, \quad (31)$$

where we have rewritten it in terms of  $\alpha_s$ . According to Equation (31), the characteristic length decreases as  $\alpha_s$  increases. The number of bundles in the yarn of length  $L$  is  $m(\alpha_s) = L/\delta_c(\alpha_s)$ , and this number increases with  $\alpha_s$ .

Figure 12 clearly shows that the strength rises, as  $\alpha_s$  increases, up to a maximum around  $30^\circ$ . However, the  $\alpha_s$  corresponding to optimal strength is much higher than what is typically observed, though not very different from what [Alexander 1952] obtained for a staple yarn. In an actual yarn with continuous filaments twisting introduces fiber slack in inner fibers that must be relieved by periodic fiber migration along the yarn. Such migration becomes increasingly difficult as the twist angle increases and thus contact forces increase. For this reason the yarn strength peaks prematurely as slack effects cause uneven fiber load distribution, thus reducing the strength beyond the effect of twist discussed earlier in the paper. On the other hand, in a staple yarn that has discontinuous fibers, these slack effects are easily eliminated by fiber sliding and thus strength peaks at a twist angle much closer to our values. Based on the weakest link concept, it is expected that the strength of the longer yarn with  $L = 0.1$  meters would be smaller than that of the shorter yarn with  $L = 0.01$  meters. Results in Figure 12, which plots normalized mean strength versus surface helix angle, show the reverse because of the much smaller normalization strength  $\mu_0$  for the longer yarn with  $L = 0.1$  meters.

## 8. Conclusions

Monte Carlo simulation and analytical models are developed for the statistical strength of twisted fiber bundles having Weibull fibers. We see important effects like the approximate normality of the bundle

	Strength mean (GPa)	Strength standard deviation (GPa)
Fiber	2.78	0.540
Bundle ( $\alpha_s = 0^\circ$ )	1.88	0.023
Bundle ( $\alpha_s = 30^\circ$ )	1.61	0.020

**Table 1.** Typical bundle strength mean and standard deviation values for a fiber with  $\sigma_\delta = 3$  GPa,  $\rho = 6$ , and  $n = 1185$ .



strength distribution, decrease in strength with number of fibers in bundle, transition from a ductile, for small  $\alpha_s$  and  $\rho$ , to brittle failure mode for large  $\alpha_s$  and  $\rho$ . We further use a simple chain-of-bundles model showing the presence of an optimal twist angle that gives maximum strength. However, a more detailed study, which considers pressure development in the bundle and stress build up in fibers from broken ends, is required to fully understand the effects of friction on bundle strength and optimal  $\alpha_s$ .

## References

- [Abramowitz and Stegun 1964] M. Abramowitz and I. A. Stegun, *Handbook of mathematical functions*, Dover Publications, New York, NY, 1964.
- [Alexander 1952] E. Alexander, “Optimal twist in staple yarn”, *Text. Res. J.* **22**:8 (1952), 503–508.
- [Daniels 1945] H. E. Daniels, “The statistical theory of the strength of bundles of threads I”, *P. Roy. Soc. Lond. A Mat.* **183**:995 (1945), 405–435.
- [Hearle et al. 1969] J. W. S. Hearle, P. Grosberg, and S. Vacker, *Structural mechanics of fibers, yarns, and fabrics*, vol. 1, Wiley-Interscience, 1969.
- [McCartney and Smith 1983] L. N. McCartney and R. L. Smith, “Statistical theory of the strength of fiber bundles”, *J. Appl. Mech. (Trans. ASME)* **50**(3) (1983), 601–608.
- [Naik et al. 2001] N. K. Naik, I. Mudzingwa, and M. N. Singh, “Effect of twisting on tensile failure of impregnated yarns with broken filaments”, *J. Compos. Technol. Res.* **23**:3 (2001), 225–234.
- [Pan 1993] N. Pan, “Prediction of statistical strengths of twisted fibre structures”, *J. Mater. Sci.* **28**:22 (1993), 6107–6114.
- [Phoenix 1979] S. L. Phoenix, “Statistical theory of the strength of twisted fiber bundles with applications to yarns and cables”, *Text. Res. J.* **49**:7 (1979), 407–423.
- [Phoenix and Beyerlein 2000] S. L. Phoenix and I. J. Beyerlein, “Statistical strength theory for fibrous composite materials”, pp. 559–639 in *Comprehensive composite materials*, vol. 1, edited by A. Kelly et al., Pergamon (Elsevier Science), 2000. Chapter 1.19.
- [Rao and Farris 2000] Y. Rao and R. J. Farris, “A modeling and experimental study of the influence of twist on the mechanical properties of high-performance fiber yarns”, *J. Appl. Polym. Sci.* **77**:9 (2000), 1938–1949.
- [Smith 1982] R. L. Smith, “The asymptotic distribution of the strength of a series-parallel system with equal load-sharing”, *Ann. Probab.* **10**:1 (1982), 137–171.
- [Vigolo et al. 2000] B. Vigolo, A. Pénicaud, C. Coulon, C. Sauder, R. Pailler, C. Journet, P. Bernier, and P. Poulin, “Macroscopic fibers and ribbons of oriented carbon nanotubes”, *Science* **290**:5495 (2000), 1331–1334.
- [Zhang et al. 2004] M. Zhang, K. R. Atkinson, and R. H. Baughman, “Multifunctional carbon nanotube yarns by downsizing an ancient technology”, *Science* **306**:5700 (2004), 1358–1361.

Received 11 Dec 2005.

PANKAJ K. PORWAL: [pkp2@cornell.edu](mailto:pkp2@cornell.edu)

Theoretical Division, Los Alamos National Laboratory, Los Alamos, NM 87545, United States  
<http://www.tam.cornell.edu/~pkp2>

IRENE J. BEYERLEIN: [irene@lanl.gov](mailto:irene@lanl.gov)

Theoretical Division, Los Alamos National Laboratory, Los Alamos, NM 87545, United States

S. LEIGH PHOENIX: [slp6@cornell.edu](mailto:slp6@cornell.edu)

Department of Theoretical and Applied Mechanics, Cornell University, Ithaca, NY 14853, United States  
<http://www.tam.cornell.edu/Phoenix1.html>

## CONTACT STRESS ON A ROTATING ELASTIC BAND SAW BLADE USING THE THEORY OF A COSSERAT SURFACE

M. B. RUBIN AND E. TUFEKCI

The value of the contact stress between a band saw blade and the driving wheel is modeled using the theory of an elastic Cosserat surface. Specifically, we use nonlinear Cosserat theory to model the bending of an elastic plate into a rotating right circular cylindrical tube with associated end moments. The resulting equations are then linearized, the end moments are relieved and the reference length of the plate is adjusted to cause contact of the blade with the wheel. The results indicate that the nonuniformity in the deformed shape of the saw blade significantly influences the predictions of the value and distribution of the contact stress between the blade and the wheel even though the blade is thin. This is in addition to the influence of a crowned wheel, and the deformed shape due to the tensioning process, which are typically used to help control tracking of the blade on the wheel. Also, we showed that the value of this contact stress predicted by a simple Lamé type solution remains about 50% of that predicted by the Cosserat solution and that the effect of the rotational speed of the wheel is negligible for typical operating conditions of thin wood-cutting saws.

### 1. Introduction

A typical band saw blade is a thin steel strip that has been bent into a cylindrical shell with gullets cut out on one of the edges to create teeth. The blade is positioned over two rotating wheels that are separated by a controlled distance. To prevent catastrophic damage to the teeth and the wheel, the blade is only in partial contact with each wheel so that the teeth can hang freely over the edge of the wheel ([Figure 1](#)). Tension in the blade can be controlled by adjusting the positions of the wheels. Although in practice the force between the band wheels is controlled, the model used here treats the distance between the wheels as displacement controlled instead of load controlled.

A recent review of mechanical problems relating to aluminum-cutting high-speed band saws in [[Gendraud et al. 2003](#)] describes problems which reduce the quality of the surface of the material being cut, reduce the precision of the dimensions of the cut, and shorten the life of the saw blade. In other studies, attention has been focused on saw vibrations [[Mote Jr. 1965](#); [Mote and Naguleswaran 1966](#); [Le-Ngoc and McCallion 1999](#); [Damaren and Le-Ngoc 2000](#); [Gendraud et al. 2003](#); [Kong and Parker 2005](#)] and tracking of the blade on the wheels [[Wong and Schajer 1997](#); [Wong and Schajer 2002](#); [Barcik 2003](#)]. Tracking of the blade can be significantly influenced by the contact stress distribution between the blade and the wheel. In practice, contact stress is modified by using a crowned wheel and by a roll tensioning process which changes the unloaded shape of the blade. Two narrow crowned rollers are used to squeeze the blade, causing plastic deformations and residual stresses. These residual stresses cause the unloaded blade to attain a deformed shape that can be optimized to help control tracking on the wheel. [[Lister and](#)

---

*Keywords:* band saw blade, Cosserat surface, contact stress, elastic.

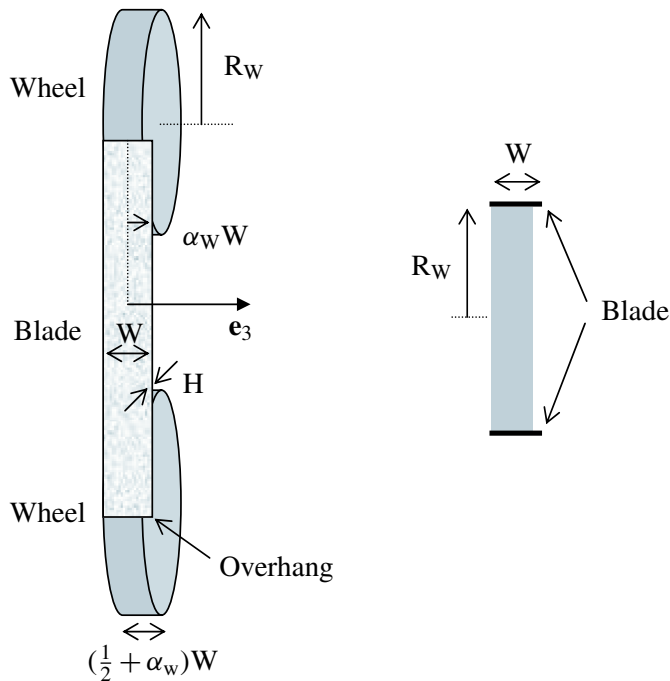


**Figure 1.** Sketch of the geometry of the saw blade and wheel.

Schajer 1993] analyzed this effect using plate theory. Complete elastic-plastic analysis of a saw blade remains a difficult problem because the blade experiences finite rotations and is only in partial contact with the wheels. The objective of this study is to analyze the contact stress and deformations of the rotating band saw blade. Here, a formulation is proposed which can be used to model the effects of a crowned wheel and the tensioning process. Although these effects are significant, we first concentrate on the contact stress distribution caused by nonuniform shape of the blade when a plate is deformed elastically and joined at its edges to form the blade.

In the analysis of contact stress, the straight portions of the blade are ignored and the blade is modeled as a circular cylindrical shell that is stretched and placed in partial axial contact with a circular wheel (Figure 1). The blade is considered to be a plate in its stress-free reference configuration. This plate is then deformed into an axisymmetric shell which is joined perfectly at its seam. The deformation causes circumferential tension near the blade's outer surface and circumferential compression near its inner surface. If the deformed plate (blade) were to remain a right-circular cylinder then the Poisson effect would require nonzero moments to be applied to the axial edges of the blade. However, when these edge moments are relieved and the surfaces and edges of the blade are stress-free, the blade deforms so that its mean radius is not uniform along its axes of symmetry. Consequently, the contact stress between the blade and the wheel is influenced by this prestressed state. These nonuniform deformations are in addition to those that are caused by the tensioning process described earlier. Also, the effect of the angular velocity of the wheel is shown to be negligible for typical operating conditions of wood-cutting saws.

To model the finite deformation of the plate into the axisymmetric shell and the finite rotations of the deformed blade it is necessary to use a nonlinear shell theory. Moreover, it is well known that contact problems of thin structures need to use enhanced theories which model normal extension, that is, changes in thickness, and shear deformation of the structure (for example, [Naghdi and Rubin 1989]). Here, the blade is modeled using the theory of a Cosserat surface of [Naghdi 1972; Rubin 2000]. However, to determine the deformed shape of the blade and the distribution of contact stress the nonlinear equations are linearized about a finitely deformed state.

An outline of this paper is as follows. Section 2 is a brief summary of the nonlinear Cosserat equations, and Section 3 describes a simple finite deformation solution. Section 4 develops approximate equations linearized about the solution in Section 3, and Section 5 describes the procedure used to obtain an analytical solution of these linear equations. Section 6 is a discussion of the results, Appendix A includes further details of the solution and Appendix B shows a Lamé type solution.

Throughout the text, bold-faced symbols are used to denote vector and tensor quantities. Also,  $\mathbf{I}$  denotes the unity tensor;  $\text{tr}(\mathbf{A})$  denotes the trace of the second order tensor  $\mathbf{A}$  and  $\mathbf{A}^T$  denotes the transpose of  $\mathbf{A}$ . The scalar  $\mathbf{a} \cdot \mathbf{b}$  denotes the dot product between two vectors  $\mathbf{a}$ ,  $\mathbf{b}$ ; the scalar  $\mathbf{A} \cdot \mathbf{B} = \text{tr}(\mathbf{A}\mathbf{B}^T)$  denotes the dot product between two second order tensors  $\mathbf{A}$ ,  $\mathbf{B}$ ; the vector  $\mathbf{a} \times \mathbf{b}$  denotes the cross product between  $\mathbf{a}$  and  $\mathbf{b}$ ; and the second order tensor  $\mathbf{a} \otimes \mathbf{b}$  denotes the tensor product between  $\mathbf{a}$  and  $\mathbf{b}$ . The usual summation convention over repeated lower cased indices is implied. The range of Latin indices is (1, 2, 3) and Greek indices is (1, 2). A glossary of notation is included at the end of this paper.

## 2. A brief summary of the nonlinear Cosserat equations

The theory of a Cosserat surface, which is a model for a shell-like body, has been described in detail in [Naghdi 1972]. This theory is sufficiently general to model normal extension and shear deformation. Here, we make use of the formulation and notation presented in [Rubin 2000]. Specifically, the kinematics of the shell's stress-free reference configuration are characterized by

$$\{\mathbf{X}(\theta^\alpha), \mathbf{D}_3(\theta^\alpha)\},$$

where  $\mathbf{X}$  locates a material point relative to a fixed origin, the director vector  $\mathbf{D}_3$  models a material fiber through the shell's thickness, and  $\theta^\alpha$ , ( $\alpha = 1, 2$ ), are convected Lagrangian coordinates. Similarly, the kinematics of the shell's present deformed configuration are characterized by

$$\{\mathbf{x}(\theta^\alpha, t), \mathbf{d}_3(\theta^\alpha, t)\},$$

where  $t$  denotes time. Also, the tangent vectors  $\mathbf{D}_\alpha$ ,  $\mathbf{d}_\alpha$ , and the directors  $\mathbf{D}_3$ ,  $\mathbf{d}_3$  are defined such that

$$\begin{aligned} \mathbf{D}_\alpha &= \mathbf{X}_{,\alpha}, & \mathbf{D}^{1/2} &= \mathbf{D}_1 \times \mathbf{D}_2 \cdot \mathbf{D}_3 > 0, \\ \mathbf{d}_\alpha &= \mathbf{x}_{,\alpha}, & \mathbf{d}^{1/2} &= \mathbf{d}_1 \times \mathbf{d}_2 \cdot \mathbf{d}_3 > 0, \end{aligned}$$

where a comma denotes partial differentiation with respect to  $\theta^\alpha$ . Moreover, it is convenient to introduce the reciprocal vectors  $\mathbf{D}^i$  and  $\mathbf{d}^i$  by the expressions

$$\mathbf{D}^i \cdot \mathbf{D}_j = \delta_j^i, \quad \mathbf{d}^i \cdot \mathbf{d}_j = \delta_j^i,$$

where  $\delta_j^i$  is the Kronecker delta symbol. For elastic shells it is convenient to define the additional kinematic variables

$$\mathbf{F} = \mathbf{d}_i \otimes \mathbf{D}^i, \quad \mathbf{C} = \mathbf{F}^T \mathbf{F}, \quad \mathbf{E} = \frac{1}{2}(\mathbf{C} - \mathbf{I}), \quad \boldsymbol{\beta}_\alpha = \mathbf{F}^{-1} \mathbf{d}_{3,\alpha} - \mathbf{D}_{3,\alpha},$$

where  $\mathbf{F}$  is similar to a deformation gradient,  $\mathbf{E}$  is similar to a Lagrangian strain tensor and  $\boldsymbol{\beta}_\alpha$  are measures of inhomogeneous deformation.

Using the direct approach to the Cosserat theory [Rubin 2000, p. 91], the equations of motion of the shell can be written in the forms

$$m(\dot{\mathbf{v}} + y^3 \dot{\mathbf{w}}_3) = m\mathbf{b} + \mathbf{t}^{\alpha}_{,\alpha}, \tag{2-1a}$$

$$m(y^3 \dot{\mathbf{v}} + y^{33} \dot{\mathbf{w}}_3) = m\mathbf{b}^3 - \mathbf{t}^3 + \mathbf{m}^{\alpha}_{,\alpha}, \tag{2-1b}$$

where a superposed dot denotes material time differentiation holding  $\theta^\alpha$  fixed. Here, (2-1a) represents the balance of linear momentum and (2-1b) represents the balance of director momentum which can be related to a weighted average over the thickness of the shell of the three-dimensional balance of linear momentum. The balance of angular momentum is satisfied by the constitutive equations which require a second order tensor  $\mathbf{T}$  to be symmetric. Also,  $m$  is related to the mass of the shell,  $\{y^3, y^{33}\}$  are constant director inertia coefficients, the velocity  $\mathbf{v}$  and director velocity  $\mathbf{w}_3$  are defined by

$$\mathbf{v} = \dot{\mathbf{x}}, \quad \mathbf{w}_3 = \dot{\mathbf{d}}_3,$$

the quantities  $\{\mathbf{b}, \mathbf{b}^3\}$  are assigned fields due to body force and contact stresses on the shell’s major surfaces, and constitutive equations need to be supplied for the quantities  $\{\mathbf{t}^i, \mathbf{m}^\alpha\}$ .

For the problem under consideration in this paper the stress-free reference configuration of the shell is taken to be a flat plate of uniform thickness  $H$ , with length  $L$  and width  $W$  defined by

$$\begin{aligned} \mathbf{X} &= \theta^1 \mathbf{e}_2 + \theta^2 \mathbf{e}_z, & \mathbf{D}_3 &= \mathbf{D}^3 = \mathbf{e}_1, & \mathbf{e}_z &= \mathbf{e}_3, \\ \theta^2 &= Z, & 0 &\leq \theta^1 \leq L, & -\frac{W}{2} &\leq Z \leq \frac{W}{2}, \\ \mathbf{D}_1 &= \mathbf{D}^1 = \mathbf{e}_2, & \mathbf{D}_2 &= \mathbf{D}^2 = \mathbf{e}_z, & A^{1/2} &= D^{1/2} = 1, \end{aligned}$$

where  $\mathbf{e}_i$  are rectangular Cartesian base vectors and the directions are specified for later convenience in describing the deformed axisymmetric shell.

Now, for a plate made from a uniform homogeneous elastic material the inertia quantities are specified by [Rubin 2000, p. 167], as

$$m = \rho_0^* H, \quad y^3 = 0, \quad y^{33} = \frac{H^2}{\pi^2},$$

where  $\rho_0^*$  is the reference mass density of the material, and the strain energy function, from [Rubin 2000, pp. 168-169] is

$$\begin{aligned} m\Sigma &= \frac{\mu^* H}{1-2\nu^*} (\nu^*(\mathbf{E} \cdot \mathbf{I})^2 + (1-2\nu^*)\mathbf{E} \cdot \mathbf{E}) + \frac{1}{2} H \mathbf{K}^{\alpha\beta} \cdot (\boldsymbol{\beta}_\alpha \otimes \boldsymbol{\beta}_\beta), \\ \mathbf{K}^{11} &= \frac{H^2 \mu^*}{12} \left( \left( \frac{2}{1-\nu^*} \right) \mathbf{e}_2 \otimes \mathbf{e}_2 + \mathbf{e}_z \otimes \mathbf{e}_z \right), \\ \mathbf{K}^{12} &= \frac{H^2 \mu^*}{12} \left( \left( \frac{2\nu^*}{1-\nu^*} \right) \mathbf{e}_2 \otimes \mathbf{e}_z + \mathbf{e}_z \otimes \mathbf{e}_2 \right), \\ \mathbf{K}^{21} &= \frac{H^2 \mu^*}{12} \left( \mathbf{e}_2 \otimes \mathbf{e}_z + \left( \frac{2\nu^*}{1-\nu^*} \right) \mathbf{e}_z \otimes \mathbf{e}_2 \right), \\ \mathbf{K}^{22} &= \frac{H^2 \mu^*}{12} \left( \mathbf{e}_2 \otimes \mathbf{e}_2 + \left( \frac{2}{1-\nu^*} \right) \mathbf{e}_z \otimes \mathbf{e}_z \right), \end{aligned}$$

where the constants  $\{\mu^*, \nu^*\}$  are the shear modulus and the Poisson's ratio of the elastic material in the small deformation limit, respectively. The constitutive equations become

$$\begin{aligned} \mathbf{m}^\alpha &= H \mathbf{K}^{\alpha\beta} \boldsymbol{\beta}_\beta, \\ \mathbf{t}^i &= \frac{\mu^* H}{1-2\nu^*} \mathbf{F} (\nu^*(\mathbf{E} \cdot \mathbf{I}) \mathbf{I} + (1-2\nu^*) \mathbf{E}) \mathbf{D}^i - \mathbf{m}^\alpha (d_{3,\alpha} \cdot \mathbf{d}^i). \end{aligned}$$

For the problem under consideration the body force is neglected, the outer surface of the deformed shell remains traction free, and its inner surface is free to slip over the wheel but is subjected to a normal contact stress  $q$ , which is positive in compression, in regions that make contact with the wheel. Under these conditions the assigned fields  $\{\mathbf{b}, \mathbf{b}^3\}$  are specified by [Rubin 2000, p. 167], now modified to include the function  $f_r(Z)$  associated with a localized moment, to model effects of the tensioning process as

$$\begin{aligned} \mathbf{m}\mathbf{b} &= q \left( \mathbf{x} - \frac{H}{2} \mathbf{d}_3 \right)_{,1} \times \left( \mathbf{x} - \frac{H}{2} \mathbf{d}_3 \right)_{,2}, \\ \mathbf{m}\mathbf{b}^3 &= \frac{qH}{2} \left( \mathbf{x} - \frac{H}{2} \mathbf{d}_3 \right)_{,1} \times \left( \mathbf{x} - \frac{H}{2} \mathbf{d}_3 \right)_{,2} + f_r(Z) \mathbf{e}_r, \end{aligned}$$

Next, the plate is deformed into an axisymmetric shell such that the deformed kinematics are

$$\begin{aligned} \mathbf{x} &= r(Z) \mathbf{e}_r(\theta) + z(Z) \mathbf{e}_z, \quad \theta = \frac{\theta^1}{R} + \omega t, \\ R &= \frac{L}{2\pi}, \\ \mathbf{d}_3 &= \phi_r(Z) \mathbf{e}_r(\theta) + \phi_z(Z) \mathbf{e}_z, \\ \dot{\mathbf{v}} &= -r\omega^2 \mathbf{e}_r, \\ \dot{\mathbf{w}}_3 &= -\phi_r \omega^2 \mathbf{e}_r, \end{aligned} \tag{2-2}$$

where  $\theta$  is the angular coordinate defining the cylindrical polar base vectors

$$\begin{aligned} \mathbf{e}_r(\theta) &= \cos \theta \mathbf{e}_1 + \sin \theta \mathbf{e}_2, \\ \mathbf{e}_\theta(\theta) &= -\sin \theta \mathbf{e}_1 + \cos \theta \mathbf{e}_2, \\ \mathbf{e}_z &= \mathbf{e}_3, \end{aligned}$$

$\omega$  characterizes the angular velocity of the blade, and the functions  $\{r, z, \phi_r, \phi_z\}$  of  $Z$  need to be determined.

Using these expressions it can be shown that

$$\begin{aligned} \mathbf{F} &= \mathbf{d}_i \otimes \mathbf{D}^i = \left(\frac{r}{R} \mathbf{e}_\theta\right) \otimes \mathbf{e}_2 + \left(\frac{dr}{dZ} \mathbf{e}_r + \frac{dz}{dZ} \mathbf{e}_z\right) \otimes \mathbf{e}_z + (\phi_r \mathbf{e}_r + \phi_z \mathbf{e}_z) \otimes \mathbf{e}_1, \\ \mathbf{E} \cdot \mathbf{I} &= \frac{1}{2} \left(\phi_r^2 + \phi_z^2 + \left(\frac{r}{R}\right)^2 + \left(\frac{dr}{dZ}\right)^2 + \left(\frac{dz}{dZ}\right)^2 - 3\right), \\ \boldsymbol{\beta}_1 &= \left(\frac{\phi_r}{r}\right) \mathbf{e}_2, \quad \boldsymbol{\beta}_2 = \frac{\left(\frac{d\phi_r}{dZ} \frac{dz}{dZ} - \frac{d\phi_z}{dZ} \frac{dr}{dZ}\right) \mathbf{e}_1 + \left(-\frac{d\phi_r}{dZ} \phi_z + \frac{d\phi_z}{dZ} \phi_r\right) \mathbf{e}_z}{\left(\frac{dz}{dZ} \phi_r - \frac{dr}{dZ} \phi_z\right)}, \\ \mathbf{m}^1 &= \frac{H^3 \mu^*}{12} \left( \left(\frac{2}{1-v^*}\right) \left(\frac{\phi_r}{r}\right) + \left(\frac{2v^*}{1-v^*}\right) \frac{\left(-\frac{d\phi_r}{dZ} \phi_z + \frac{d\phi_z}{dZ} \phi_r\right)}{\left(\frac{dz}{dZ} \phi_r - \frac{dr}{dZ} \phi_z\right)} \right) \frac{R}{r} \mathbf{e}_\theta, \\ \mathbf{m}^2 &= \frac{H^3 \mu^*}{12} \left( \left(\frac{2v^*}{1-v^*}\right) \left(\frac{\phi_r}{r}\right) + \left(\frac{2}{1-v^*}\right) \frac{\left(-\frac{d\phi_r}{dZ} \phi_z + \frac{d\phi_z}{dZ} \phi_r\right)}{\left(\frac{dz}{dZ} \phi_r - \frac{dr}{dZ} \phi_z\right)} \right) \frac{(-\phi_z \mathbf{e}_r + \phi_r \mathbf{e}_z)}{\left(\frac{dz}{dZ} \phi_r - \frac{dr}{dZ} \phi_z\right)}, \\ \mathbf{t}^1 &= \mu^* H \left( \left(\frac{2v^*}{1-2v^*}\right) (\mathbf{E} \cdot \mathbf{I}) + \left(\frac{r}{R}\right)^2 - 1 \right) \frac{r}{R} \mathbf{e}_\theta - \frac{\phi_r}{r} \mathbf{m}^1, \\ \mathbf{t}^2 &= \mu^* H \left( \left(\frac{2v^*}{1-2v^*}\right) (\mathbf{E} \cdot \mathbf{I}) \right) \left(\frac{dr}{dZ} \mathbf{e}_r + \frac{dz}{dZ} \mathbf{e}_z\right) + \mu^* H \left( \left(\frac{dr}{dZ} \phi_r + \frac{dz}{dZ} \phi_z\right) (\phi_r \mathbf{e}_r + \phi_z \mathbf{e}_z) \right. \\ &\quad \left. + \left( \left(\frac{dr}{dZ}\right)^2 + \left(\frac{dz}{dZ}\right)^2 - 1 \right) \left(\frac{dr}{dZ} \mathbf{e}_r + \frac{dz}{dZ} \mathbf{e}_z\right) \right) - \frac{(-\phi_z \frac{d\phi_r}{dZ} + \phi_r \frac{d\phi_z}{dZ})}{\left(\frac{dz}{dZ} \phi_r - \frac{dr}{dZ} \phi_z\right)} \mathbf{m}^2, \\ \mathbf{t}^3 &= \mu^* H \left( \left(\frac{2v^*}{1-2v^*}\right) (\mathbf{E} \cdot \mathbf{I}) \right) (\phi_r \mathbf{e}_r + \phi_z \mathbf{e}_z) \\ &\quad + \mu^* H \left( (\phi_r^2 + \phi_z^2 - 1) (\phi_r \mathbf{e}_r + \phi_z \mathbf{e}_z) \right. \\ &\quad \left. + \left(\phi_r \frac{dr}{dZ} + \phi_z \frac{dz}{dZ}\right) \left(\frac{dr}{dZ} \mathbf{e}_r + \frac{dz}{dZ} \mathbf{e}_z\right) \right) - \frac{\left(\frac{dz}{dZ} \frac{d\phi_r}{dZ} - \frac{dr}{dZ} \frac{d\phi_z}{dZ}\right)}{\left(\frac{dz}{dZ} \phi_r - \frac{dr}{dZ} \phi_z\right)} \mathbf{m}^2, \\ \mathbf{mb} &= q \left( \frac{r}{R} - \frac{H}{2} \frac{\phi_r}{R} \right) \left( \left(\frac{dz}{dZ} - \frac{H}{2} \frac{d\phi_z}{dZ}\right) \mathbf{e}_r - \left(\frac{dr}{dZ} - \frac{H}{2} \frac{d\phi_r}{dZ}\right) \mathbf{e}_z \right), \\ \mathbf{mb}^3 &= -\frac{qH}{2} \left( \frac{r}{R} - \frac{H}{2} \frac{\phi_r}{R} \right) \left(\frac{dz}{dZ} - \frac{H}{2} \frac{d\phi_z}{dZ}\right) \mathbf{e}_r \\ &\quad + \frac{qH}{2} \left( \frac{r}{R} - \frac{H}{2} \frac{\phi_r}{R} \right) \left(\frac{dr}{dZ} - \frac{H}{2} \frac{d\phi_r}{dZ}\right) \mathbf{e}_z + f_r(Z) \mathbf{e}_r, \end{aligned} \tag{2-3}$$

where  $\mathbf{t}^\alpha$  are forces and  $\mathbf{m}^\alpha$  are couples, both measured per unit of deformed length of the blade's edges.

### 3. A simple finite deformation solution

In this section a simple solution is obtained where the plate is finitely deformed into a right-circular cylindrical shell and the effect of tensioning is neglected, that is,  $[f_r = 0$  in (2-3)]. Specifically, for this solution the functions  $\{r, z, \phi_r, \phi_z\}$  are

$$\begin{aligned} r &= c_1 R, \\ z &= c_2 Z, \\ \phi_r &= c_3, \\ \phi_z &= 0, \end{aligned} \tag{3-1}$$

where  $\{c_1, c_2, c_3\}$  are constants. Now, substituting these functions into the expressions in (2-3), it can be shown that

$$\begin{aligned} \mathbf{m}^1 &= \frac{\mu^* H^3}{6(1-\nu^*)} \left( \frac{c_3}{c_1^2} \right) \frac{1}{R} \mathbf{e}_\theta, \\ \mathbf{m}^2 &= \frac{\mu^* H^3 \nu^*}{6(1-\nu^*)} \left( \frac{c_3}{c_1 c_2} \right) \frac{1}{R} \mathbf{e}_z, \\ \mathbf{t}^1 &= \mu^* H \left( \left( \frac{\nu^*}{1-2\nu^*} \right) (c_1^2 + c_2^2 + c_3^2 - 3) + (c_2^2 - 1) \right) c_1 \mathbf{e}_\theta - \frac{\mu^* H^3}{6(1-\nu^*)} \left( \frac{c_3^2}{c_1^3} \right) \frac{H^2}{R^2} \mathbf{e}_\theta, \\ \mathbf{t}^2 &= \mu^* H \left( \left( \frac{\nu^*}{1-2\nu^*} \right) (c_1^2 + c_2^2 + c_3^2 - 3) + (c_2^2 - 1) \right) c_2 \mathbf{e}_z, \\ \mathbf{t}^3 &= \mu^* H \left( \left( \frac{\nu^*}{1-2\nu^*} \right) (c_1^2 + c_2^2 + c_3^2 - 3) + (c_3^2 - 1) \right) c_3 \mathbf{e}_r. \end{aligned}$$

Moreover, in the absence of contact stress  $q$ , the equations of motion (2-1) reduce to

$$\begin{aligned} \left( \left( \frac{\nu^*}{1-2\nu^*} \right) (c_1^2 + c_2^2 + c_3^2 - 3) + (c_1^2 - 1) \right) - \frac{1}{6(1-\nu^*)} \left( \frac{c_3^2}{c_1^4} \right) \frac{H^2}{R^2} &= \frac{\rho_0^* R^2 \omega^2}{\mu^*}, \\ \left( \left( \frac{\nu^*}{1-2\nu^*} \right) (c_1^2 + c_2^2 + c_3^2 - 3) + (c_3^2 - 1) \right) + \frac{1}{6(1-\nu^*)} \left( \frac{1}{c_1^2} \right) \frac{H^2}{R^2} &= \frac{\rho_0^* H^2 \omega^2}{\mu^* \pi^2}. \end{aligned} \tag{3-2}$$

In addition, for this solution it is assumed that the edges  $Z = \pm W/2$  are free of resultant force ( $\mathbf{t}^2 = 0$ ) so that

$$\left( \frac{\nu^*}{1-2\nu^*} \right) (c_1^2 + c_2^2 + c_3^2 - 3) + (c_2^2 - 1) = 0. \tag{3-3}$$

Next, by introducing the auxiliary constants

$$\begin{aligned} B_1 &= \frac{\nu^*}{1-\nu^*}, \\ B_2 &= \frac{1}{6(1-\nu^*)} \frac{H^2}{R^2}, \end{aligned}$$



the solution of (3-2) and (3-3) is obtained by solving the equation

$$(2B_1 + 1)c_1^8 - \left( (2B_1 + 1) + \frac{\rho_0^* R^2 \omega^2 (B_1 + 1)}{\mu^*} - B_1 \frac{\rho_0^* H^2 \omega^2}{\mu^* \pi^2} \right) c_1^6 - \left( B_2 (2B_1 + 1) + B_2 \frac{\rho_0^* H^2 \omega^2}{\mu^* \pi^2} \right) c_1^2 + B_2^2 = 0,$$

for the positive real root of  $c_1$  near unity, and substituting the solution into the equations

$$c_3^2 - 1 = -\left( \frac{B_1}{B_1 + 1} \right) (c_1^2 - 1) - \left( \frac{B_2}{B_1 + 1} \right) \left( \frac{1}{c_1^2} \right) + \left( \frac{1}{B_1 + 1} \right) \frac{\rho_0^* H^2 \omega^2}{\mu^* \pi^2},$$

$$c_2^2 - 1 = -B_1 (c_1^2 + c_3^2 - 2),$$

for positive real values of  $\{c_3, c_2\}$  near unity. In particular, note that since the value of  $m^2$  is nonzero it is necessary to specify a moment on the edges  $Z = \pm W/2$  to maintain the right circular cylindrical shape of the deformed plate.

#### 4. Linearized equations

To develop simplified equations for determining the contact stress between a deformed saw blade and the wheel, nonlinear equations associated with the kinematic assumption (2-2) are linearized about the finite deformation solution (3-1). Also, the function  $f_r$  associated with tensioning is assumed to be small. For these linearized equations the kinematics of the steady state deformations are specified by

$$r = c_1 R + u_r(Z),$$

$$z = c_2 Z + u_z(Z),$$

$$\phi_r = c_3 + \delta_r(Z),$$

$$\phi_z = \delta_z(Z),$$

and quadratic terms in the displacements and the contact stress  $\{u_r, u_z, \delta_r, \delta_z, q\}$  are neglected.

Straightforward algebraic manipulations yield expressions for the constitutive equations

$$t^1 = t_\theta^1 e_\theta$$

$$= \mu^* H \left( \left( (c_1^2 - c_2^2) c_1 - \frac{c_3^2}{6(1 - \nu^*) c_1^3} \frac{H^2}{R^2} \right) + \left( (c_1^2 - c_2^2) + \frac{2(1 - \nu^*)}{(1 - 2\nu^*)} c_1^2 + \frac{c_3^2}{2(1 - \nu^*) c_1^4} \frac{H^2}{R^2} \right) \frac{u_r}{R} \right. \\ \left. + \left( \frac{2\nu^* c_1 c_3}{(1 - 2\nu^*)} - \frac{c_3}{3(1 - \nu^*) c_1^3} \frac{H^2}{R^2} \right) \delta_r + \left( \frac{2\nu^* c_1 c_2}{1 - 2\nu^*} \right) \frac{du_z}{dZ} - \left( \frac{\nu^* c_3}{6(1 - \nu^*) c_1^2 c_2} \frac{H}{R} \right) H \frac{d\delta_z}{dZ} \right) e_\theta,$$

$$\begin{aligned}
\mathbf{t}^2 &= t_r^2 \mathbf{e}_r + t_z^2 \mathbf{e}_z = \mu^* H \left( c_2 c_3 \delta_z + c_3^2 \frac{du_r}{dZ} \right) \mathbf{e}_r \\
&+ 2\mu^* H \left( \left( \frac{\nu^* c_1 c_2}{1-2\nu^*} \right) \frac{u_r}{R} + \left( \frac{\nu^* c_2 c_3}{1-2\nu^*} \right) \delta_r + \left( \frac{(1-\nu^*)c_2^2}{1-2\nu^*} \right) \frac{du_z}{dZ} - \left( \frac{\nu^* c_3}{12(1-\nu^*)c_1 c_2^2} \frac{H}{R} \right) H \frac{d\delta_z}{dZ} \right) \mathbf{e}_z, \\
\mathbf{t}^3 &= t_r^3 \mathbf{e}_r + t_z^3 \mathbf{e}_z = \mu^* H \left( (c_3^2 - c_2^2) c_3 + \left( \frac{2\nu^* c_1 c_3}{1-2\nu^*} \right) \frac{u_r}{R} + \left( (c_3^2 - c_2^2) + \frac{2(1-\nu^*)c_3^2}{1-2\nu^*} \right) \delta_r \right. \\
&\quad \left. + \left( \frac{2\nu^* c_2 c_3}{1-2\nu^*} \right) \frac{du_z}{dZ} \right) \mathbf{e}_r + \mu^* H \left( (c_3^2) \delta_z + (c_2 c_3) \frac{du_r}{dZ} - \left( \frac{\nu^*}{6(1-\nu^*)c_1 c_2} \frac{H}{R} \right) H \frac{d\delta_r}{dZ} \right) \mathbf{e}_z, \\
\mathbf{m}^1 &= m_\theta^1 \mathbf{e}_\theta = \mu^* H^2 \left( \left( \frac{c_3}{6(1-\nu^*)c_1^2} \frac{H}{R} \right) - \left( \frac{c_3}{3(1-\nu^*)c_1^3} \frac{H}{R} \right) \frac{u_r}{R} \right. \\
&\quad \left. + \left( \frac{1}{6(1-\nu^*)c_1^2} \frac{H}{R} \right) \delta_r + \left( \frac{\nu^*}{6(1-\nu^*)c_1 c_2} \right) H \frac{d\delta_z}{dZ} \right) \mathbf{e}_\theta, \\
\mathbf{m}^2 &= m_r^2 \mathbf{e}_r + m_z^2 \mathbf{e}_z = \mu^* H^2 \left( - \left( \frac{\nu^*}{6(1-\nu^*)c_1 c_2} \frac{H}{R} \right) \delta_z \right) \mathbf{e}_r \\
&\quad + \mu^* H^2 \left( \left( \frac{\nu^* c_3}{6(1-\nu^*)c_1 c_2} \frac{H}{R} \right) - \left( \frac{\nu^* c_3}{6(1-\nu^*)c_1^2 c_2} \frac{H}{R} \right) \frac{u_r}{R} \right. \\
&\quad \left. + \left( \frac{\nu^*}{6(1-\nu^*)c_1 c_2} \frac{H}{R} \right) \delta_r - \left( \frac{\nu^* c_3}{6(1-\nu^*)c_1 c_2^2} \frac{H}{R} \right) \frac{du_z}{dZ} + \left( \frac{1}{6(1-\nu^*)c_2^2} \right) H \frac{d\delta_z}{dZ} \right) \mathbf{e}_z, \\
\mathbf{m}\mathbf{b} &= q \left( c_1 c_2 - \frac{c_2 c_3 H}{2R} \right) \mathbf{e}_r, \\
\mathbf{m}\mathbf{b}^3 &= -q H \left( \frac{c_1 c_2}{2} - \frac{c_2 c_3 H}{4R} \right) \mathbf{e}_r + f_r \mathbf{e}_r. \tag{4-1}
\end{aligned}$$

Then, the linearized equations of motion for the steady state deformations become

$$\begin{aligned}
0 &= q \left( c_1 c_2 - \frac{c_2 c_3 H}{2R} \right) \\
&+ \mu^* \left( \left( -(c_1^2 - c_2^2) \frac{H}{R} - \frac{2(1-\nu^*)c_1^2 H}{1-2\nu^*} \frac{H}{R} - \frac{c_3^2}{2(1-\nu^*)c_1^4} \frac{H^3}{R^3} + \frac{\rho_0^* H R \omega^2}{\mu^*} \right) \frac{u_r}{R} \right. \\
&\quad \left. + \left( - \frac{2\nu^* c_1 c_3}{1-2\nu^*} \frac{H}{R} + \frac{c_3}{3(1-\nu^*)c_1^3} \frac{H^3}{R^3} \right) \delta_r - \left( \frac{2\nu^* c_1 c_2}{1-2\nu^*} \frac{H}{R} \right) \frac{du_z}{dZ} \right. \\
&\quad \left. + \left( c_2 c_3 + \frac{\nu^* c_3}{6(1-\nu^*)c_1^2 c_2} \frac{H^2}{R^2} \right) H \frac{d\delta_z}{dZ} + (c_3^2) H \frac{d^2 u_r}{dZ^2} \right), \tag{4-2a}
\end{aligned}$$

$$0 = \frac{d}{dZ} \left( \left( \frac{\nu^* c_1 c_2}{1 - 2\nu^*} \right) \frac{u_r}{R} + \left( \frac{\nu^* c_2 c_3}{1 - 2\nu^*} \right) \delta_r + \left( \frac{(1 - \nu^*) c_2^2}{1 - 2\nu^*} \right) \frac{du_z}{dZ} - \left( \frac{\nu^* c_3}{12(1 - \nu^*) c_1 c_2^2} \frac{H}{R} \right) H \frac{d\delta_z}{dZ} \right), \quad (4-2b)$$

$$0 = -q \left( \frac{c_1 c_2}{2} - \frac{c_2 c_3}{4} \frac{H}{R} \right) + \mu^* \left( \left( -\frac{2\nu^* c_1 c_3}{1 - 2\nu^*} + \frac{c_3}{3(1 - \nu^*) c_1^3} \frac{H^2}{R^2} \right) \frac{u_r}{R} + \left( - (c_3^2 - c_2^2) - \frac{2(1 - \nu^*) c_3^2}{1 - 2\nu^*} - \frac{1}{6(1 - \nu^*) c_1^2} \frac{H^2}{R^2} + \frac{\rho_0^* H^2 \omega^2}{\mu^* \pi^2} \right) \delta_r - \left( \frac{2\nu^* c_2 c_3}{1 - 2\nu^*} \right) \frac{du_z}{dZ} - \left( \frac{\nu^*}{3(1 - \nu^*) c_1 c_2} \frac{H}{R} \right) H \frac{d\delta_z}{dZ} \right) + f_r, \quad (4-2c)$$

$$0 = - (c_3^2) \delta_z + \left( -c_2 c_3 - \frac{\nu^* c_3}{6(1 - \nu^*) c_1^2 c_2} \frac{H^2}{R^2} \right) \frac{du_r}{dZ} + \left( \frac{\nu^*}{3(1 - \nu^*) c_1 c_2} \frac{H}{R} \right) H \frac{d\delta_r}{dZ} - \left( \frac{\nu^* c_3}{6(1 - \nu^*) c_1 c_2^2} \frac{H}{R} \right) H \frac{d^2 u_z}{dZ^2} + \left( \frac{1}{6(1 - \nu^*) c_2^2} \right) H^2 \frac{d^2 \delta_z}{dZ^2}. \quad (4-2d)$$

Moreover, the radial gap  $\Delta$  of blade's inner surface relative to the radius of the wheel is defined by

$$\Delta = \left( c_1 R - \frac{H}{2} c_3 \right) + \left( u_r - \frac{H}{2} \delta_r \right) - R_W. \quad (4-3)$$

The effects of tensioning on the stiffness and frequencies of vibration of the blade have been studied by [Lister and Schajer 1993] using a model based on deformations of a plate. The linearized equations (4-2a)–(4-2d) and (4-3) can be used to determine the influence of both tensioning and different crowned shapes of the wheel on contact stress  $q$  by specifying forms for the tensioning function  $f_r(Z)$  and the wheel radius  $R_W(Z)$ . For the general case, portions of the blade are in contact with the wheel and other portions are free of contact. For a specified form of the tensioning function  $f_r(Z)$  the equations (4-2) are solved for  $\{u_r, u_z, \delta_r, \delta_z\}$  with  $q = 0$  in the free regions. In contact regions  $\Delta$ , as defined in (4-3) vanishes and the equations (4-2) and (4-3) are solved for  $\{u_r, u_z, \delta_r, \delta_z, q\}$ . Consequently, the tensioning function  $f_r$  influences the functional form of the radial displacement  $u_r$  which in turn controls the shape of the blade in free regions and influences the contact stress  $q$  in contact regions.

Here, the effects of tensioning and the crowned shape of the wheel are omitted by specifying  $f_r = 0$  and a constant value for  $R_W$  and attention is focused on assessing the influence of elastic deformations caused by bending a plate into a circular cylindrical shell. Specifically, the wheel is taken to have a

uniform radius, with the blade and wheel specified by

$$\begin{aligned} E^* &= 200 \text{ GPa}, & \mu^* &= \frac{E^*}{2(1+\nu^*)}, & \nu^* &= 0.3, \\ \rho_0^* &= 7.85 \text{ Mg/m}^3, & H &= 0.0016 \text{ m}, & W &= 0.20 \text{ m}, & R_W &= 0.8 \text{ m}. \end{aligned} \quad (4-4)$$

These values are typical dimensions for wide saw blades used in industrial wood cutting band saws. For other possible values see [Lister and Schajer 1993; Chung and Sung 1998; Damaren and Le-Ngoc 2000]. Using a normalized axial coordinate

$$\alpha = \frac{Z}{W}, \quad (4-5)$$

the wheel's edge is specified by

$$\alpha = \alpha_W = 0.4, \quad (4-6)$$

indicating that 10% of the blade hangs over the wheel's edge (Figure 1). The portion of the blade weakened by the gullets which form the blade's teeth is assumed to provide negligible strength. Also, the reference length of the blade is specified by the normalized misfit of the blade  $\eta$  defined so that

$$R - \frac{H}{2} = R_W + \eta H. \quad (4-7)$$

This formula treats the deformed blade as a right circular cylindrical shell with an inner radius larger than the wheel's radius by the amount of  $\eta H$ .

Details of the solution will be presented in the next section. However, here qualitative aspects are presented in order to discuss the nature of the boundary conditions. Specifically, attention is focused on the following three cases:

Case 1:  $\omega = 0$ ;  $\eta \geq \eta_1$  : 1 free region

Free region:  $-0.5 \leq \alpha \leq 0.5$ ,

Case 2:  $\omega = 0$ ;  $\eta_3 \leq \eta \leq \eta_2$  : 2 free regions and 1 contact region with  $\alpha_2 < \alpha_W$

Free regions:  $-0.5 \leq \alpha \leq \alpha_1$ ,  $\alpha_2 \leq \alpha \leq 0.5$ ,

Contact region:  $\alpha_1 \leq \alpha \leq \alpha_2 < \alpha_W$ ,

Case 3:  $\omega = 0$ ;  $\eta \leq \eta_3$  : 2 free regions and 1 contact region with  $\alpha_2 = \alpha_W$

Free regions:  $-0.5 \leq \alpha \leq \alpha_1$ ,  $\alpha_2 = \alpha_W \leq \alpha \leq 0.5$ ,

Contact region:  $\alpha_1 \leq \alpha \leq \alpha_W$ .

The cases are characterized by three values of  $\eta$

$$\eta_3 < \eta_2 < \eta_1,$$

and two values of  $\alpha$

$$-0.5 < \alpha_1 < \alpha_2 \leq \alpha_W < 0.5.$$

For Case 1 the blade is free and contact first begins at the two points  $\alpha = \alpha_1$  and  $\alpha = \alpha_2 = -\alpha_1$  when  $\eta = \eta_1$ . For  $\eta$  between the values  $\eta_1$  and  $\eta_2$ , the solution is characterized by multiple free and contact regions.

The solutions in this range of  $\eta$  are complicated and are not particularly significant from an engineering point of view since the contact stresses remain quite low. Therefore, they will not be analyzed in this paper. When  $\eta = \eta_2$  these complications disappear and the solution is characterized by Case 2 with two free regions and one contact region  $\alpha_1 \leq \alpha \leq \alpha_2 = -\alpha_1$  and with the blade separating from the wheel before it reaches the wheel's edge ( $\alpha_2 < \alpha_W$ ). Case 3 is also characterized by two free regions and one contact region which now extends to the wheel's edge ( $\alpha_2 = \alpha_W$ ).

In the context of the present theory it is possible to specify three boundary conditions at each edge. It can be seen from (4-1) that the equation of motion (4-2b) requires the axial component of force per unit length to be constant

$$t_z^2 = \text{constant} . \tag{4-8}$$

The boundary conditions at the edges  $\alpha = \pm 0.5$  and the continuity conditions at the boundaries of the free and contact regions are specified by

$$t_r^2 = 0, \tag{4-9a}$$

$$t_z^2 = 0, \tag{4-9b}$$

$$m_z^2 = 0, \quad \text{for } \alpha = -0.5, \tag{4-9c}$$

$$\{u_r, u_z, \delta_r, \delta_z, t_r^2, t_z^2\} \text{ are continuous for } \alpha = \alpha_i \ (i = 1, 2), \tag{4-9d}$$

$$u_z = 0, \quad \text{for } \alpha = \alpha_W, \tag{4-9e}$$

$$t_r^2 = 0, \quad m_z^2 = 0, \quad \text{for } \alpha = 0.5. \tag{4-9f}$$

Here,  $\{t_r^2, t_z^2, m_r^2, m_z^2\}$  correspond, respectively, to the shear force, the axial force, a pinching moment, and a bending moment, each measured per unit length of the blade's edge. The conditions (4-9a), (4-9b), (4-9c), (4-9f) together with the result (4-8) indicate that the edges  $\alpha = \pm 0.5$  are nearly traction free. The theory is not general enough to ensure that the pinching moment  $m_r^2$  vanishes at these edges or that it is continuous at the boundaries  $(\alpha_1, \alpha_2)$ . Also, (4-9d) requires continuity of the normal strain  $\delta_r$  instead of continuity of the bending moment  $m_z^2$ . This means that the geometry of the blade will be continuous at the boundaries  $(\alpha_1, \alpha_2)$  but that the moments  $\{m_r^2, m_z^2\}$  can experience jumps there. Furthermore, the condition (4-9e) removes rigid body translation and requires the same material point on the blade to remain at the wheel's edge.

The locations  $(\alpha_1, \alpha_2)$  of the boundaries of the contact regions are determined by the condition that the contact stress  $q$  in the contact region vanishes at these boundaries and that it is positive in the interior of the contact region. Therefore, this condition requires

$$\text{Case 2: } q = 0, \quad \text{for } \alpha = \alpha_1, \alpha_2, \tag{4-10a}$$

$$\text{Case 3: } q = 0, \quad \text{for } \alpha = \alpha_1. \tag{4-10b}$$

In particular, in Case 3 the contact stress at the wheel's edge ( $\alpha = \alpha_W$ ) can suddenly decrease from a positive value in the contact region to zero in the free region. Also, to discuss the results presented below

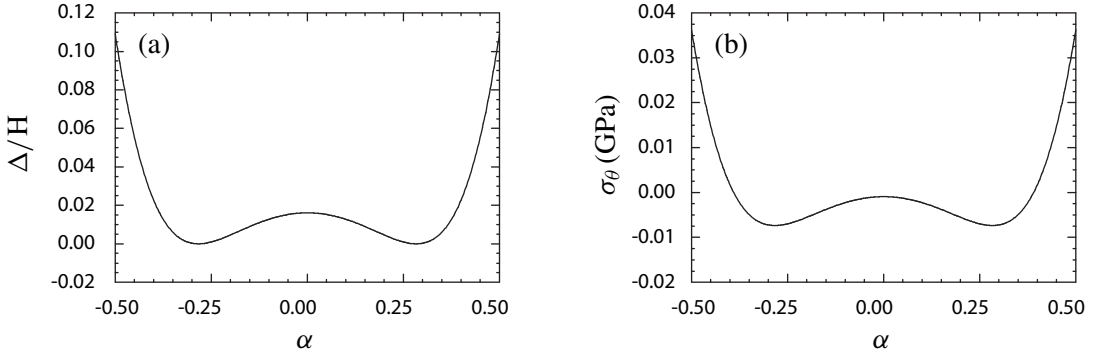


**Figure 2.** Plots of the radial gap  $\Delta$  normalized by the thickness  $H$  and the circumferential stress  $\sigma_\theta$  as functions of the normalized axial coordinate  $\alpha$  for the onset of contact with the normalized misfit of the blade  $\eta = \eta_1$  and no angular velocity  $\omega = 0$ .

it is convenient to approximate the Cauchy circumferential stress  $\sigma_\theta$  in the band saw blade as

$$\sigma_\theta = \frac{t_\theta^1}{c_3 H}, \quad (4-11)$$

where  $t_\theta^1$  is the force per unit present length, and  $c_3 H$  is the present thickness.

Using the solution we present in the following section, we can show that

$$\eta_1 = 1.8171E - 2, \quad \eta_2 = -2.6268E - 04, \quad \eta_3 = -1.4676E - 1 \quad \text{for } \omega = 0. \quad (4-12)$$

Figure 2 shows results for Case 1 with  $\eta = \eta_1$  and  $\omega = 0$  which causes the blade to just make contact with the wheel. Figure 2a shows the deformed inner surface of the blade  $\Delta$  (4-3) and Figure 2b shows the circumferential stress  $\sigma_\theta$ , both as functions of the normalized axial coordinate  $\alpha$ . In Figure 2a note that the edges  $\alpha = \pm 0.5$  experience localized bending due to the relief of the edge moments that must be applied to the simple solution of Section 3. In Figure 2b note that the circumferential stress has a shape similar to the radial gap  $\Delta$  in Figure 2a, with the center region being compressive (negative values) and the edges being tensile (positive values).

## 5. Solution procedure

In view of the conditions (4-8), (4-9b), and (4-9d), the expression for  $t_z^2$  in (4-1) can be solved for  $\delta_r$  in both the free and contact regions to obtain

$$\delta_r = -\left(\frac{c_1}{c_3}\right) \frac{u_r}{R} - \left(\frac{(1-v^*)c_2}{v^*c_3}\right) \frac{du_z}{dZ} + \left(\frac{(1-2v^*)}{12(1-v^*)c_1c_2^3} \frac{H}{R}\right) H \frac{d\delta_z}{dZ}. \quad (5-1)$$

Equation (4–2c) for the contact stress can now be rewritten as

$$\begin{aligned}
 q\left(c_1c_2 - \frac{c_2c_3H}{2R}\right) &= \mu^* \left( \left(4c_1c_3 + \frac{2c_1(c_3^2 - c_2^2)}{c_3} + \frac{(c_1^2 + 2c_3^2)}{3(1 - \nu^*)c_1^3c_3} \frac{H^2}{R^2} - \frac{2\rho_0^*H^2\omega^2c_1}{\mu^*\pi^2c_3}\right) \frac{u_r}{R} \right. \\
 &+ \left( \frac{4c_2c_3}{\nu^*} + \frac{2(1 - \nu^*)(c_3^2 - c_2^2)c_2}{\nu^*c_3} + \frac{c_2}{3\nu^*c_1^2c_3} \frac{H^2}{R^2} - \frac{2\rho_0^*H^2\omega^2(1 - \nu^*)c_2}{\mu^*\pi^2\nu^*c_3} \right) \frac{du_z}{dZ} \\
 &+ \left( -\frac{2\nu^*}{3(1 - \nu^*)c_1c_2} - \frac{(1 - 2\nu^*)(c_3^2 - c_2^2)}{6(1 - \nu^*)c_1c_2^3} - \frac{c_3^2}{3c_1c_2^3} \right. \\
 &\left. - \frac{(1 - 2\nu^*)}{36(1 - \nu^*)^2c_1^3c_2^3} \frac{H^2}{R^2} + \frac{\rho_0^*H^2\omega^2(1 - 2\nu^*)}{6\mu^*\pi^2(1 - \nu^*)c_1c_2^3} \right) \frac{H^2}{R} \frac{d\delta_z}{dZ} \Big). \quad (5-2)
 \end{aligned}$$

Next, using (5–1) and (5–2) the remaining equations of motion (4–2a), (4–2d) become

$$\begin{aligned}
 \left(4c_1c_3 + \frac{2c_1(c_3^2 - c_2^2)}{c_3} - (3c_1^2 - c_2^2) \frac{H}{R} + \frac{(c_1^2 + 2c_3^2)}{3(1 - \nu^*)c_1^3c_3} \frac{H^2}{R^2} \right. \\
 \left. - \frac{(2c_1^2 + 3c_3^2)}{6(1 - \nu^*)c_1^4} \frac{H^3}{R^3} + \frac{\rho_0^*HR\omega^2}{\mu^*} - \frac{2\rho_0^*H^2\omega^2c_1}{\mu^*\pi^2c_3} \right) \frac{u_r}{R} \\
 + \left( \frac{4c_2c_3}{\nu^*} + \frac{2(1 - \nu^*)(c_3^2 - c_2^2)c_2}{\nu^*c_3} + 2c_1c_2 \frac{H}{R} + \frac{c_2}{3\nu^*c_1^2c_3} \frac{H^2}{R^2} \right. \\
 \left. - \frac{c_2}{3\nu^*c_1^3} \frac{H^3}{R^3} - \frac{2\rho_0^*H^2\omega^2(1 - \nu^*)c_2}{\mu^*\pi^2\nu^*c_3} \right) \frac{du_z}{dZ} \\
 + \left( c_2c_3 - \frac{(6\nu^* - 1)c_2^2 + (3 - 4\nu^*)c_3^2}{6(1 - \nu^*)c_1c_2^3} \frac{H}{R} + \frac{\nu^*c_3(c_2^2 - c_1^2)}{6(1 - \nu^*)c_1^2c_2^3} \frac{H^2}{R^2} \right. \\
 \left. - \frac{(1 - 2\nu^*)}{36(1 - \nu^*)^2c_1^3c_2^3} \frac{H^3}{R^3} + \frac{(1 - 2\nu^*)c_3}{36(1 - \nu^*)^2c_1^4c_2^3} \frac{H^4}{R^4} + \frac{\rho_0^*H^2\omega^2(1 - 2\nu^*)}{6\mu^*\pi^2(1 - \nu^*)c_1c_2^3} \frac{H}{R} \right) H \frac{d\delta_z}{dZ} \\
 + \{c_3^2\} H \frac{d^2u_r}{dZ^2} = 0, \quad (5-3a)
 \end{aligned}$$

$$\begin{aligned}
 \{c_3^2\}\delta_z + \left( c_2c_3 + \frac{\nu^*(2c_1^2 + c_3^2)}{6(1 - \nu^*)c_1^2c_2c_3} \frac{H^2}{R^2} \right) \frac{du_r}{dZ} + \left( \frac{\nu^*c_3}{6(1 - \nu^*)c_1c_2^2} + \frac{1}{3c_1c_3} \right) \frac{H^2}{R} \frac{d^2u_z}{dZ^2} \\
 - \left( \frac{1}{6(1 - \nu^*)c_2^2} + \frac{\nu^*(1 - 2\nu^*)}{36(1 - \nu^*)^2c_1^2c_2^4} \frac{H^2}{R^2} \right) H^2 \frac{d^2\delta_z}{dZ^2} = 0. \quad (5-3b)
 \end{aligned}$$

Now, for free regions the contact stress  $q$  vanishes and the equations of motion (5–2) and (5–3) can be rewritten as six first order equations in the matrix form

$$\sum_{j=1}^6 \left( A_{ij}^f \frac{dy_j^f}{dZ} + B_{ij}^f y_j^f \right) = 0, \quad (5-4)$$

in terms of the vector

$$y_i^f = \left( u_r, u_z, \delta_z, \frac{du_r}{dZ}, \frac{du_z}{dZ}, \frac{d\delta_z}{dZ} \right), \quad (5-5)$$

where the components of the  $\{A_{ij}^f, B_{ij}^f\}$  are recorded in [Appendix A](#). The characteristic equation for the eigenvalues  $\lambda$  associated with (5-4) becomes

$$\lambda(a_2^f \lambda^4 + a_1^f \lambda^2 + a_0^f) = 0, \quad (5-6)$$

where  $a_i^f$  are real constants given in (A-1). It then follows that (5-4) represents a fifth order system with eigenvalues that take the forms

$$\lambda = \pm\lambda_1^f, \pm\lambda_3^f, 0; \quad \lambda_1^f = (\lambda_{R1}^f \pm i\lambda_{I1}^f), \quad \lambda_3^f = (\lambda_{R3}^f \pm i\lambda_{I3}^f), \quad (5-7)$$

where  $\{\lambda_{R1}^f, \lambda_{I1}^f, \lambda_{R3}^f, \lambda_{I3}^f\}$  are real positive numbers and  $i = \sqrt{-1}$ . The five independent eigenfunctions  $\phi_j^f$  ( $j = 1, 2, \dots, 5$ ) are, for  $(-W/2 \leq Z \leq \alpha_1 W)$ ,

$$\begin{aligned} \phi_1^f(Z) &= \text{Re}\left(Y_{1j}^f \exp(\lambda_1^f(Z - \beta))\right), \\ \phi_2^f(Z) &= \text{Im}\left(Y_{1j}^f \exp(\lambda_1^f(Z - \beta))\right), \\ \phi_3^f(Z) &= \text{Re}\left(Y_{3j}^f \exp(\lambda_3^f(Z - \beta))\right), \\ \phi_4^f(Z) &= \text{Im}\left(Y_{3j}^f \exp(\lambda_3^f(Z - \beta))\right), \\ \phi_5^f &= (0, 1, 0, 0, 0, 0), \\ \beta &= \frac{1}{2}\left(-\frac{1}{2} + \alpha_1\right)W \quad \text{for } -\frac{W}{2} \leq Z \leq \alpha_1 W, \\ \beta &= \frac{1}{2}\left(\frac{1}{2} + \alpha_2\right)W \quad \text{for } -\alpha_2 W \leq Z \leq \frac{W}{2}, \end{aligned} \quad (5-8)$$

where  $\alpha_1$  and  $\alpha_2$  represent the boundaries of the free region in consideration,  $\beta$  is the average of the these boundaries,  $\text{Re}(x)$  and  $\text{Im}(x)$  represent the real and imaginary parts of the complex quantity  $x$ , and  $\{Y_{1j}^f, Y_{3j}^f\}$  are the eigenvectors which satisfy the equations

$$\sum_{j=1}^6 (A_{ij}^f \lambda_1^f + B_{ij}^f) Y_{1j}^f = 0, \quad \sum_{j=1}^6 (A_{ij}^f \lambda_3^f + B_{ij}^f) Y_{3j}^f = 0. \quad (5-9)$$

Then, the solution in the free region takes the general form

$$y_i^f(Z) = \sum_{j=1}^5 c_j^f \phi_j^f(Z), \quad (5-10)$$

where  $c_j^f$  are real constants to be determined by the boundary conditions. Moreover, for this solution  $\delta_r$  is obtained by (5-1).



In the contact regions the value of  $\delta_r$  in (5-1) is restricted so that  $\Delta$  in (4-3) vanishes, which yields

$$\left(1 + \frac{c_1 H}{2c_3 R}\right) \frac{u_r}{R} + \left(\frac{(1 - \nu^*)c_2}{2\nu^*c_3}\right) \frac{H}{R} \frac{du_z}{dZ} - \left(\frac{(1 - 2\nu^*)}{24(1 - \nu^*)c_1c_2^3}\right) \frac{H^3}{R^2} \frac{d\delta_z}{dZ} = -\left(c_1 - \frac{H}{2R}c_3 - \frac{R_W}{R}\right). \tag{5-11}$$

For the contact regions the contact stress  $q$  in (5-2) is required to remain positive (except at the boundaries of the regions) and the equations of motion (5-11) and (5-3) can be rewritten as six first order equations in the matrix form

$$\sum_{j=1}^6 \left(A_{ij}^c \frac{dy_j^c}{dZ} + B_{ij}^c y_j^c\right) = C_i^c, \tag{5-12}$$

in terms of the vector

$$y_i^c = \left(u_r, u_z, \delta_z, \frac{du_r}{dZ}, \frac{du_z}{dZ}, \frac{d\delta_z}{dZ}\right), \tag{5-13}$$

where the components of  $\{A_{ij}^c, B_{ij}^c, C_i^c\}$  are given in Appendix A. The solution in the contact region is obtained in a manner similar to that in the free regions. Specifically, the characteristic equation for the eigenvalues  $\lambda$  associated with the homogeneous solution of (5-12) becomes

$$\lambda(a_2^c \lambda^4 + a_1^c \lambda^2 + a_0^c) = 0, \tag{5-14}$$

where  $a_i^c$  are real constants given in (A-2). It then follows that (5-14) represents a fifth order system with eigenvalues that take the forms

$$\lambda = \pm \lambda_1^c, \pm \lambda_3^c, 0; \quad \lambda_1^c = (\lambda_{R1}^c \pm i\lambda_{I1}^c), \quad \lambda_3^c = (\lambda_{R3}^c \pm i\lambda_{I3}^c), \tag{5-15}$$

where  $\{\lambda_{R1}^f, \lambda_{I1}^f, \lambda_{R3}^f, \lambda_{I3}^f\}$  are real positive numbers. The five independent eigenfunctions

$$\phi_i^c \quad (i = 1, 2, \dots, 5)$$

are specified in the forms

$$\phi_1^c(Z) = \text{Re}\left(Y_{1i}^c \exp(\lambda_1^c(Z - \beta))\right), \quad \phi_2^c(Z) = \text{Im}\left(Y_{3i}^c \exp(\lambda_1^c(Z - \beta))\right), \tag{5-16}$$

$$\phi_3^c(Z) = \text{Re}\left(Y_{3i}^c \exp(\lambda_3^c(Z - \beta))\right), \quad \phi_4^c(Z) = \text{Im}\left(Y_{3i}^c \exp(\lambda_3^c(Z - \beta))\right), \tag{5-17}$$

$$\phi_5^c = (0, 1, 0, 0, 0, 0), \quad \beta = \frac{1}{2}W(\alpha_1 + \alpha_2), \tag{5-18}$$

where  $\{Y_{1i}^c, Y_{3i}^c\}$  are the eigenvectors which satisfy the equations

$$\sum_{j=1}^6 (A_{ij}^c \lambda_1^c + B_{ij}^c) Y_{1j}^c = 0, \quad \sum_{j=1}^6 (A_{ij}^c \lambda_3^c + B_{ij}^c) Y_{3j}^c = 0. \tag{5-19}$$

In addition, the equations (5-12) require a specific solution of the form

$$y_1^{cP} = \frac{B_{55}^c C_4^c}{B_{41}^c B_{55}^c - B_{45}^c B_{51}^c}, \quad y_2^{cP} = -\left(\frac{B_{51}^c C_4^c}{B_{41}^c B_{55}^c - B_{45}^c B_{51}^c}\right) Z, \tag{5-20}$$

$$y_5^{cP} = -\left(\frac{B_{51}^c C_4^c}{B_{41}^c B_{55}^c - B_{45}^c B_{51}^c}\right), \quad y_3^{cP} = y_4^{cP} = y_6^{cP} = 0. \tag{5-21}$$

Then, the solution in the contact region takes the general form

$$y_i^c(Z) = \sum_{j=1}^5 c_j^c \phi_j^f(Z) + y_i^{cP}(Z), \quad (5-22)$$

where  $c_j^c$  are real constants to be determined by the boundary conditions. Moreover, for this solution  $\delta_r$  is obtained by (5-1) and the contact stress  $q$  is determined by (5-2).

The specification (5-1) for  $\delta_r$  satisfies the condition that  $t_z^2$  vanishes so that boundary conditions on  $t_z^2$  in (4-9) are automatically satisfied. The solutions (5-10) and (5-22) show that there are five constants to be determined in each of the free and contact regions as well as the boundary values of  $\alpha_i$ . For the three cases we present, unknowns and equations are given by:

Case 1:

Unknowns: 5 values of  $c_j^f$ ;

Equations: (4-9a), (4-9c), (4-9e), (4-9f);

Case 2:

Unknowns: 10 values of  $c_j^f$ , 5 values of  $c_j^c$ ,  $\{\alpha_1, \alpha_2\}$ ;

Equations: (4-9a), (4-9c), 10 Equations (4-9d), (4-9e), (4-9f), 2 Equations (4-10a);

Case 3:

Unknowns: 10 values of  $c_j^f$ , 5 values of  $c_j^c$ ,  $\{\alpha_1\}$ ;

Equations: (4-9a), (4-9c), 10 Equations (4-9d), (4-9e), (4-9f), 1 Equation (4-10b).

## 6. Discussion

The equations of the previous section were solved for the problem characterized by (4-4) and (4-6). Figures 3 and 4 plot values of (a) the radial gap  $\Delta$  (4-3), (b) the circumferential stress  $\sigma_\theta$  (4-11), and (c) and (d) the contact stress  $q$  as functions of the normalized axial coordinate  $\alpha$  in (4-5) for  $\omega = 0$  and different values of misfit  $\eta$  (4-7). Specifically, Figure 3 shows the solution for Case 2 associated with the largest value of  $\eta = \eta_2$  (4-12) for which the blade has a single contact region with the wheel and Figure 4 shows the solution for Case 3 associated with the largest value of  $\eta = \eta_3$  (4-12) for which the blade has a single contact region that extends to the edge ( $\alpha = \alpha_W$ ) of the wheel. Figure 5 shows plots of the following values: the radial gap  $\Delta$  (Figure 5a,b); the circumferential stress  $\sigma_\theta$  (Figure 5c); and the contact stress  $q$  (Figure 5d-f) for a high value of tension of  $\eta = -2.5$  and  $\omega = 0$ . Also, these figures include the predictions of the Lamé solution discussed in Appendix B.

Figure 3a, b, Figure 4a, b and Figure 5a,c show that the plots of circumferential stress  $\sigma_\theta$  have the same shapes as those of the radial gap  $\Delta$ . This means that the circumferential tension is dominated by the radial displacement of the saw blade. Figure 5b shows that even for the case of high tension, the end of the blade near  $\alpha = -0.5$  is separated from the wheel. Figures 3c and 4c show two spikes in the contact stress which occur near the regions where the free saw blade has the smallest radius, as shown in Figure 2. For Cases 2 and 3 the shape of the contact stress curve in these regions is symmetrical (Figure 3d and Figure 4d). As Figure 5d-f shows, when the tension is high enough to cause the edge  $\alpha = \alpha_W$  to be in contact with the saw blade, the contact stress is no longer symmetrical with the maximum contact stress occurring near the edge  $\alpha = \alpha_W$  of the wheel. In particular, the maximum contact stress near the

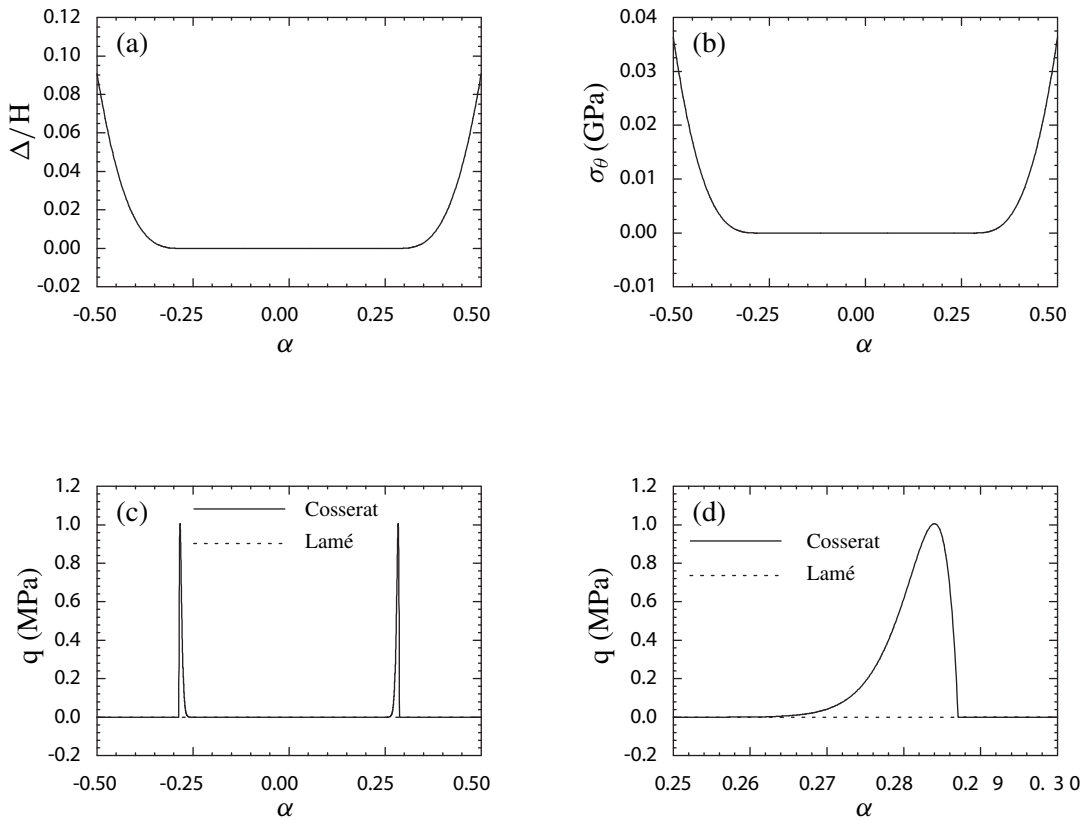


**Figure 3.** Plots of the radial gap  $\Delta$  normalized by the thickness  $H$ , the circumferential stress  $\sigma_\theta$  and the contact stress  $q$  as functions of the normalized axial coordinate  $\alpha$  for the onset of a single contact region with the normalized misfit of the blade  $\eta = \eta_2$  and no angular velocity  $\omega = 0$ .

edge  $\alpha = \alpha_W$  is more than three times that near the edge  $\alpha = \alpha_1$  for  $\eta = -2.5$ . Also, [Figure 5f](#) shows that the contact stress exhibits a small decrease from the value  $q = 0.9$  MPa to zero at the edge  $\alpha = \alpha_W$ .

Moreover, from [Figure 5d–f](#) it can be seen that the Lamé solution predicts a uniform contact stress of about 2 MPa which significantly underpredicts the value of maximum contact stress as well as the value in the nearly uniform region in the center of the wheel. This means that for an accurate prediction of the contact stress it is essential to include an analysis of the nonlinear deformation associated with the formation of the saw blade from a flat plate. In practice, the tensioning process is used to change the deformed shape of the saw blade by applying controlled plastic deformations. Although the analysis of plastic deformations is outside of the scope of the present paper, the results presented here suggest that this process should be carefully analyzed since it could significantly affect the resulting distribution of contact stress.

The speed of a band saw is often measured in terms of its translational velocity. For example, a velocity of 2800 m/min is typical for an industrial wood cutting blade [[Lunstrum 1981](#); [1984](#)]. Also see

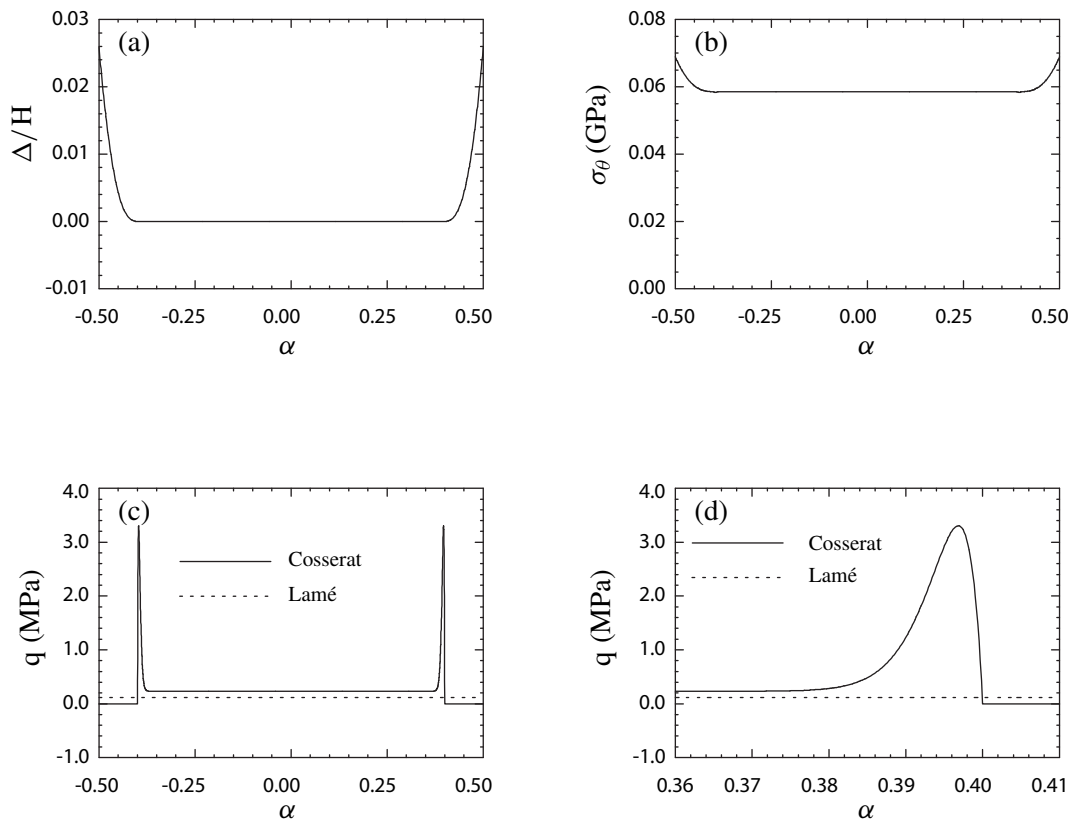


**Figure 4.** Plots of the radial gap  $\Delta$  normalized by the thickness  $H$ , the circumferential stress  $\sigma_\theta$  and the contact stress  $q$  as functions of the normalized axial coordinate  $\alpha$  for the point at which a single contact region reaches the edge of the wheel with the normalized misfit of the blade  $\eta = \eta_3$  and no angular velocity  $\omega = 0$ .

[Eklund 2000; Murata et al. 2002] for velocities associated with other saws. An estimate of the influence of rotation on the contact stress can be obtained by equating this translational velocity with the velocity  $v_W$  of the blade at the surface of the wheel

$$\omega = \frac{v_W}{R_W}. \quad (6-1)$$

Calculations were performed for  $v_W = 2800$  m/min, which corresponds to  $\omega = 58.33$  rad/s for  $\eta = \eta_3$  (Figure 6). The results show that the rotating blade has a higher circumferential stress  $\sigma_\theta$ , a lower contact stress  $q$  and a smaller contact region. The decrease in the contact stress near the blade's center ( $\alpha = 0$ ) is about 0.07 MPa. This is somewhat larger than the magnitude 0.03 MPa predicted by the Lamé solution (B-7). The decrease in the peak value of the contact stress is about 0.5 MPa. However, even for this relatively low tension ( $\sigma_\theta \approx 60$  MPa) in this thin blade the maximum effect of inertia is insignificant. Since the effect of inertia remains relatively constant for a given rotational speed, the effect is even more insignificant for higher tension (that is, for smaller values of  $\eta$ ).

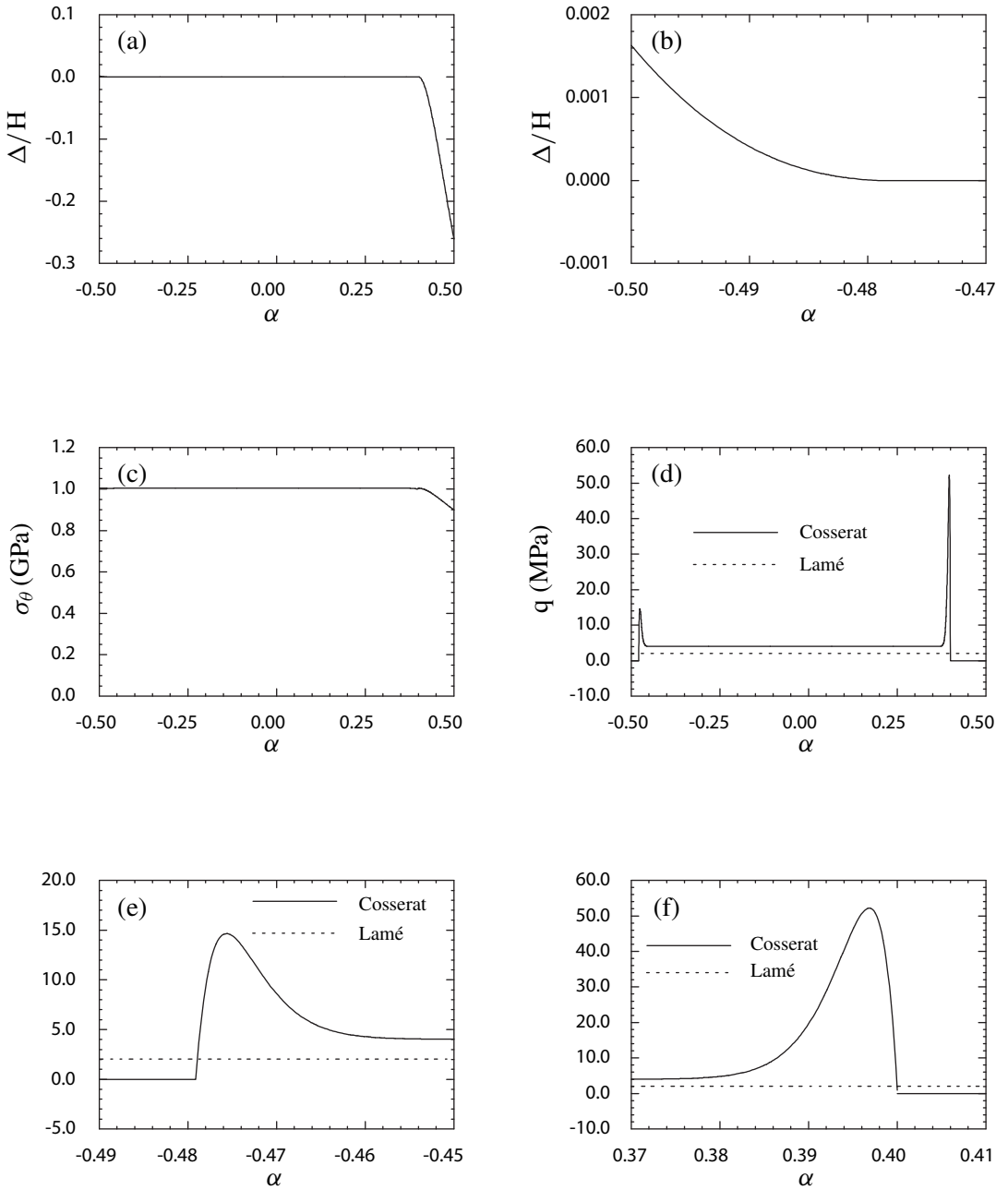


**Figure 5.** Plots of the radial gap  $\Delta$  normalized by the thickness  $H$ , the circumferential stress  $\sigma_\theta$ , and the contact stress  $q$  as functions of the normalized axial coordinate  $\alpha$  for the case of large tension and a single contact region with the normalized misfit of the blade  $\eta = -2.5$  and no angular velocity  $\omega = 0$ .

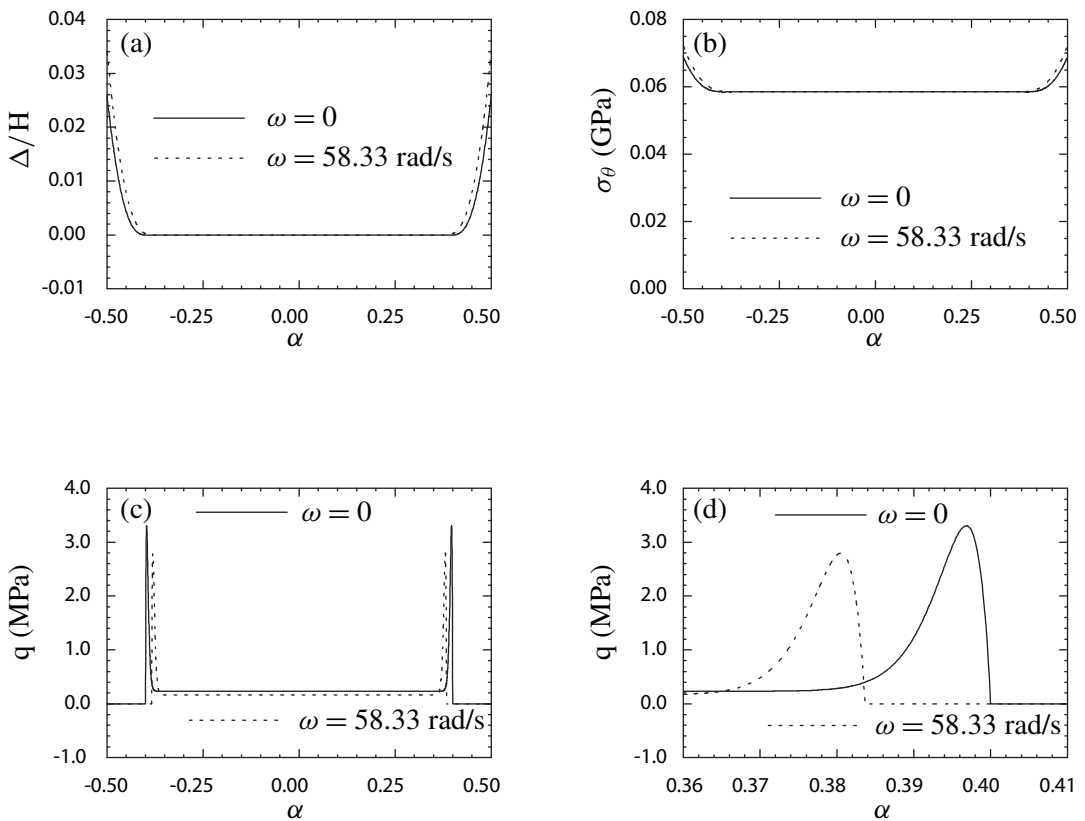


**Figure 6.** Effect of inertia. Plots of the radial gap  $\Delta$  normalized by the thickness  $H$ , the circumferential stress  $\sigma_\theta$ , and the contact stress  $q$  as functions of the normalized axial coordinate  $\alpha$  for the point at which a single contact region reaches the edge of the wheel with the normalized misfit of the blade  $\eta = \eta_3$  and with different angular velocities  $\omega$ .

One of the difficulties in designing band saw blades is ensuring proper tracking of the blade on the wheel. As previously mentioned, the tensioning process and a crowned wheel are used to help control blade tracking [Lister and Schajer 1993; Wong and Schajer 1997; 2002]. The elastic effects of bending a plate into a circular cylindrical shell analyzed here also should influence tracking. It may be possible to exploit the facts that when the blade is free of contact it has a deformed shape (Figure 2a) and that this deformed shape causes stress concentrations when the blade is in contact (Figure 4c and Figure 5d). Specifically, if the wheel were crowned with slight curvature then it may be possible to adjust the curvature so that the blade would tend to hug the wheel (see Figure 7). The equations of Section 4 include a model for the tensioning process through the function  $f_r(Z)$  and allow the wheel to have a crowned shape. Future research could explore the relative importance of these effects combined with the elastic effect that has been analyzed in this paper.

In conclusion, in this paper we model a band saw blade as an elastic plate that has been bent into a circular cylinder. Due to the Poisson effect, axial tension develops on the outer surface of the blade and

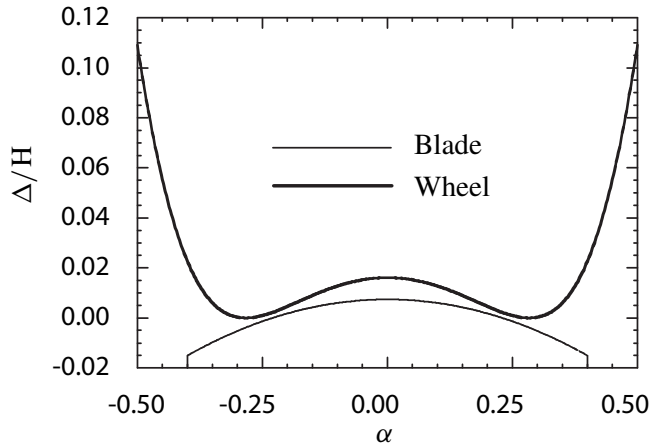


**Figure 7.** Sketch of a blade tracking on a crowned wheel.

axial compression develops on its inner surface. Consequently, end moments are required to maintain a right-circular cylindrical shape. The nonlinear equations of a Cosserat surface used to describe this process have been linearized and the resulting end moments are relieved, causing nonuniform deformation of the blade. It has been shown that this nonuniformity significantly influences the predictions of the value and distribution of the contact stress between the blade and the wheel even though the blade is thin. Also, it has been shown that the value of contact stress predicted by a simple Lamé-type solution is inaccurate and that the effects of the rotational speed of the wheel are negligible for typical operating conditions of thin wood-cutting saw blades.

### Appendix A. Details of the solutions in the free and contact regions

The nonzero coefficients of  $\{A_{ij}^f, B_{ij}^f\}$  associated with the free region are

$$\begin{aligned}
 A_{11}^f &= A_{22}^f = A_{33}^f = 1, \\
 A_{54}^f &= (c_3^2 H), \\
 A_{65}^f &= \left( \frac{\nu^* c_3}{6(1-\nu^*)c_1 c_2^2} + \frac{1}{3c_1 c_3} \right) \frac{H^2}{R}, \\
 A_{66}^f &= - \left( \frac{1}{6(1-\nu^*)c_2^2} + \frac{\nu^*(1-2\nu^*)}{36(1-\nu^*)^2 c_1^2 c_2^4} \frac{H^2}{R^2} \right) H^2,
 \end{aligned}$$

and

$$\begin{aligned}
B_{14}^f &= B_{25}^f = B_{36}^f = -1, \\
B_{41}^f &= \left( 4c_1c_3 + \frac{2c_1(c_3^2 - c_2^2)}{c_3} + \frac{(c_1^2 + 2c_3^2)}{3(1-\nu^*)c_1^3c_3} \frac{H^2}{R^2} - \frac{2\rho_0^*H^2\omega^2c_1}{\mu^*\pi^2c_3} \right) \frac{1}{R}, \\
B_{45}^f &= \left( \frac{4c_2c_3}{\nu^*} + \frac{2(1-\nu^*)(c_3^2 - c_2^2)c_2}{\nu^*c_3} + \frac{c_2}{3\nu^*c_1^2c_3} \frac{H^2}{R^2} - \frac{2\rho_0^*H^2\omega^2(1-\nu^*)c_2}{\mu^*\pi^2\nu^*c_3} \right), \\
B_{46}^f &= \left( -\frac{2\nu^*}{3(1-\nu^*)c_1c_2} - \frac{(1-2\nu^*)(c_3^2 - c_2^2)}{6(1-\nu^*)c_1c_2^3} - \frac{c_3^2}{3c_1c_2^3} \right. \\
&\quad \left. - \frac{(1-2\nu^*)}{36(1-\nu^*)^2c_1^3c_2^3} \frac{H^2}{R^2} + \frac{\rho_0^*H^2\omega^2(1-2\nu^*)}{6\mu^*\pi^2(1-\nu^*)c_1c_2^3} \right) \frac{H^2}{R}, \\
B_{51}^f &= \left( 4c_1c_3 + \frac{2c_1(c_3^2 - c_2^2)}{c_3} - (3c_1^2 - c_2^2) \frac{H}{R} + \frac{(c_1^2 + 2c_3^2)}{3(1-\nu^*)c_1^3c_3} \frac{H^2}{R^2} \right. \\
&\quad \left. - \frac{(2c_1^2 + 3c_3^2)}{6(1-\nu^*)c_1^4} \frac{H^3}{R^3} + \frac{\rho_0^*HR\omega^2}{\mu^*} - \frac{2\rho_0^*H^2\omega^2c_1}{\mu^*\pi^2c_3} \right) \frac{1}{R}, \\
B_{55}^f &= \left( \frac{4c_2c_3}{\nu^*} + \frac{2(1-\nu^*)(c_3^2 - c_2^2)c_2}{\nu^*c_3} + 2c_1c_2 \frac{H}{R} + \frac{c_2}{3\nu^*c_1^2c_3} \frac{H^2}{R^2} \right. \\
&\quad \left. - \frac{c_2}{3\nu^*c_1^3} \frac{H^3}{R^3} - \frac{2\rho_0^*H^2\omega^2(1-\nu^*)c_2}{\mu^*\pi^2\nu^*c_3} \right), \\
B_{56}^f &= \left( c_2c_3 - \frac{(6\nu^* - 1)c_2^2 + (3 - 4\nu^*)c_3^2}{6(1-\nu^*)c_1c_2} \frac{H}{R} + \frac{\nu^*c_3(c_2^2 - c_1^2)}{6(1-\nu^*)c_1^2c_2^3} \frac{H^2}{R^2} \right. \\
&\quad \left. + \frac{(1-2\nu^*)}{36(1-\nu^*)^2c_1^3c_2^3} \frac{H^3}{R^3} + \frac{(1-2\nu^*)c_3}{36(1-\nu^*)^2c_1^4c_2^3} \frac{H^4}{R^4} + \frac{\rho_0^*H^2\omega^2(1-2\nu^*)}{6\mu^*\pi^2(1-\nu^*)c_1c_2^3} \frac{H}{R} \right) H, \\
B_{63}^f &= (c_3^2), \\
B_{64}^f &= \left( c_2c_3 + \frac{\nu^*(2c_1^2 + c_3^2)}{6(1-\nu^*)c_1^2c_2c_3} \frac{H^2}{R^2} \right).
\end{aligned}$$

The coefficients  $a_i^f$  in the characteristic Equation (5–6) are

$$\begin{aligned}
a_0^f &= (B_{41}^f B_{55}^f - B_{45}^f B_{51}^f) B_{63}^f, \\
a_1^f &= A_{65}^f (B_{46}^f B_{51}^f - B_{41}^f B_{56}^f) + A_{66}^f (B_{41}^f B_{55}^f - B_{45}^f B_{51}^f) - A_{54}^f B_{45}^f B_{63}^f + (B_{45}^f B_{56}^f - B_{46}^f B_{55}^f) B_{64}^f, \quad (\text{A-1}) \\
a_2^f &= A_{54}^f (A_{65}^f B_{46}^f - A_{66}^f B_{45}^f).
\end{aligned}$$

The nonzero coefficients of  $(A_{ij}^c, B_{ij}^c, C_i^c)$  associated with the contact region are



$$\begin{aligned}
 A_{ij}^c &= A_{ij}^f, & B_{ij}^c &= B_{ij}^f \quad (\text{except for } i = 4), \\
 B_{41}^c &= \left(1 + \frac{c_1}{2c_3} \frac{H}{R}\right) \frac{1}{R}, & B_{45}^c &= \left(\frac{(1 - \nu^*)c_2}{2\nu^*c_3}\right) \frac{H}{R}, \\
 B_{46}^c &= -\left(\frac{(1 - 2\nu^*)}{24(1 - \nu^*)c_1c_3^2}\right) \frac{H^3}{R^2}, & C_4^c &= -\left(c_1 - \frac{H}{2R}c_3 - \frac{R_W}{R}\right).
 \end{aligned}$$

The coefficients  $a_i^c$  in the characteristic Equation (5–14) are

$$\begin{aligned}
 a_0^c &= (B_{41}^c B_{55}^c - B_{45}^c B_{51}^c) B_{63}^c, \\
 a_1^c &= A_{65}^c (B_{46}^c B_{51}^c - B_{41}^c B_{56}^c) + A_{66}^c (B_{41}^c B_{55}^c - B_{45}^c B_{51}^c) \\
 &\quad - A_{54}^c B_{45}^c B_{63}^c + (B_{45}^c B_{56}^c - B_{46}^c B_{55}^c) B_{64}^c, \\
 a_2^c &= A_{54}^c (A_{65}^c B_{46}^c - A_{66}^c B_{45}^c).
 \end{aligned} \tag{A-2}$$

### Appendix B. Lamé solution

Within the context of small axisymmetric deformations relative to a coordinate system rotating with angular velocity  $\omega$ , the steady state equations of motion can be written as

$$\frac{dT_{RR}^*}{dR^*} + \frac{T_{RR}^* - T_{\theta\theta}^*}{R^*} = -\rho_0^* \omega^2 R^*, \quad \frac{dT_{ZZ}^*}{dZ} = 0. \tag{B-1}$$

For generalized plane stress the displacements are given by

$$u_R^* = u_R^*(R^*), \quad u_\theta^* = 0,$$

and the constitutive equations for the nonzero stresses and the axial strain  $e_{ZZ}$  yield

$$\begin{aligned}
 T_{RR}^* &= \frac{2\mu^*}{(1 - \nu^*)} \left( \frac{du_R^*}{dR^*} + \nu^* \frac{u_R^*}{R^*} \right), \\
 T_{\theta\theta}^* &= \frac{2\mu^*}{(1 - \nu^*)} \left( \nu^* \frac{du_R^*}{dR^*} + \frac{u_R^*}{R^*} \right), & T_{ZZ}^* &= 0, \\
 e_{ZZ} &= -\left( \frac{\nu^*}{1 - \nu^*} \right) \left( \frac{du_R^*}{dR^*} + \frac{u_R^*}{R^*} \right).
 \end{aligned}$$

In these equations a superposed (\*) is used to denote that the quantities are associated with the exact three-dimensional linearized theory.

The boundary conditions for a cylinder of mean radius  $R$  and thickness  $H$  to be in contact with a wheel of radius  $R_W$  with a free outer surface can be expressed as

$$u_R^* = R_W - R_1, \tag{B-2}$$

$$q_L = -T_{RR}^*, \quad \text{for } R^* = R_1 = R \left(1 - \frac{H}{2R}\right), \tag{B-3}$$

$$T_{RR}^* = 0, \quad \text{for } R^* = R_2 = R \left(1 + \frac{H}{2R}\right), \tag{B-4}$$

where  $q_L$  is the contact stress predicted by this Lamé solution and  $R$  is specified by (4–7). It can easily be seen that the equations of motion (B–1) are satisfied provided that

$$\frac{d^2 u_R^*}{dR^{*2}} + \frac{1}{R^*} \frac{du_R^*}{dR^*} - \frac{u_R^*}{R^{*2}} = - \left( \frac{\rho_0^* \omega^2 (1 - \nu^*)}{2\mu^*} \right) R^*, \quad (\text{B-5})$$

which admits the general solution

$$\begin{aligned} u_R^* &= \left( \frac{1 - \nu^*}{1 + \nu^*} \right) A_1 R^* + A_2 \frac{R_1^2}{R^*} - \left( \frac{(1 - \nu^*) \Omega^2}{(3 + \nu^*)} \right) \frac{R^{*3}}{R_1^2}, \\ T_{RR}^* &= 2\mu^* \left( A_1 - A_2 \frac{R_1^2}{R^{*2}} - \Omega^2 \frac{R^{*2}}{R_1^2} \right), \\ T_{\theta\theta}^* &= 2\mu^* \left( A_1 + A_2 \frac{R_1^2}{R^{*2}} - \left( \frac{(1 + 3\nu^*)}{(3 + \nu^*)} \right) \Omega^2 \frac{R^{*2}}{R_1^2} \right), \\ \Omega^2 &= \frac{\rho_0^* \omega^2 (3 + \nu^*) R_1^2}{16\mu^*}, \end{aligned} \quad (\text{B-6})$$

where the constants  $\{A_1, A_2\}$  are determined by the boundary conditions (B–2)

$$\begin{aligned} A_1 &= \left( \frac{(1 + \nu^*)}{(1 - \nu^*) + (1 + \nu^*)(R_2/R_1)^2} \right) \left( \frac{R_W}{R_1} - 1 \right) \\ &\quad + \left( \frac{(1 + \nu^*)}{(3 + \nu^*)} \right) \left( \frac{(1 - \nu^*) + (3 + \nu^*)(R_2/R_1)^4}{(1 - \nu^*) + (1 + \nu^*)(R_2/R_1)^2} \right) \Omega^2, \\ A_2 &= \left( \frac{(1 + \nu^*)(R_2/R_1)^2}{(1 - \nu^*) + (1 + \nu^*)(R_2/R_1)^2} \right) \left( \frac{R_W}{R_1} - 1 \right) \\ &\quad - \left( \frac{(1 - \nu^*)}{(3 + \nu^*)} \right) \left( \frac{-(1 + \nu^*) + (3 + \nu^*)(R_2/R_1)^2}{(1 - \nu^*) + (1 + \nu^*)(R_2/R_1)^2} \right) \Omega^2. \end{aligned}$$

It then follows that the contact stress is

$$q_L = 2\mu \left( \frac{(1 + \nu^*)((R_2/R_1)^2 - 1)}{(1 - \nu^*) + (1 + \nu^*)(R_2/R_1)^2} \right) \left( \left( \frac{R_W}{R_1} - 1 \right) - 2 \left( \frac{(1 - \nu^*) + (3 + \nu^*)(R_2/R_1)^2}{(1 + \nu^*)(3 + \nu^*)} \right) \Omega^2 \right). \quad (\text{B-7})$$

### Nomenclature

$a_0^f, a_1^f, a_2^f$	coefficients of the characteristic equation in the free regions
$a_0^c, a_1^c, a_2^c$	coefficients of the characteristic equation in the contact region
$A^{1/2}$	scalar related to the shell's reference area
$A_{ij}^f$	matrix of the derivatives in the free regions
$A_{ij}^c$	matrix of the derivatives in the contact region
$A_i$	constants in the Lamé solution
$B_1$	auxiliary variable

$B_2$	auxiliary variable associated with the normalized thickness
$B_{ij}^f$	matrix of the linear coefficients in the free regions
$B_{ij}^c$	matrix of the linear coefficients in the contact region
$c_1$	circumferential stretch
$c_2$	axial stretch
$c_3$	radial stretch
$c_j^f$	coefficients of the eigenfunctions in the contact region
$C$	right Cauchy–Green deformation tensor
$C_i^c$	vector in the contact region
$d^{1/2}$	scalar associated with the present configuration
$D^{1/2}$	scalar associated with the reference configuration
$d_\alpha$	tangent vectors to the shell's present surface
$d_3$	director in the present configuration
$d^i$	reciprocal vectors to the present directors $d_i$
$D_\alpha$	tangent vectors to the shell's reference surface
$D_3$	reference director which models a material fiber through the shell's thickness
$D^i$	reciprocal vectors to the reference directors $D_i$
$c_j^f$	coefficients of the eigenfunctions in the free regions
$e_i$	rectangular Cartesian base vectors
$e_r, e_\theta, e_z$	cylindrical polar base vectors
$e_{ZZ}$	axial strain in the Lamé solution
$E^*$	Young's modulus associated with small deformations
$E$	Lagrangian strain tensor
$f_r(Z)$	function associated with the localized moment which models the tensioning process
$F$	deformation gradient
$H$	reference thickness (in the $e_1$ direction) of the rectangular plate
$i$	$\sqrt{-1}$
$I$	unit tensor
$K^{\alpha\beta}$	second order tensors associated with the energy of bending and torsion
$L$	referenced length (in the $e_2$ direction) of the rectangular plate
$m$	mass per unit reference area
$mb$	assigned force due to body force and contact stresses on the shell's major surfaces

$m\mathbf{b}^3$	assigned director couple due to body force and contact stresses on the shell's major surfaces
$m^\alpha$	contact resultant couples on the shell's edges
$m_\theta^1$	circumferential value of $m^1$
$m_r^2$	radial value of $m^2$
$m_z^2$	axial value of $m^2$
$q$	normal contact stress (positive for compression) between the blade and wheel
$q_L$	contact stress in the Lamé solution
$r$	deformed radius of the shell's reference surface
$R$	auxiliary variable associated with the deformed radius of the cylindrical shell
$R^*$	radial coordinate in the Lamé solution
$R_1, R_2$	radii in the Lamé solution
$R_W$	radius of the wheel
$t$	time
$\mathbf{t}^\alpha$	contact resultant forces on the shell's edges
$\mathbf{t}^3$	intrinsic director couple
$t_\theta^1$	circumferential value of $\mathbf{t}^1$
$t_r^2$	radial value of $\mathbf{t}^2$
$t_z^2$	axial value of $\mathbf{t}^2$
$T_{RR}^*, T_{\theta\theta}^*, T_{ZZ}^*$	stress components associated with the Lamé solution
$u_r$	radial displacement
$u_z$	axial displacement
$u_R^*$	radial displacement in the Lamé solution
$u_\theta^*$	circumferential displacement in the Lamé solution
$\mathbf{v}$	velocity vector
$v_W$	blade's translational velocity
$\mathbf{w}_3$	director velocity
$W$	reference width (in the $\mathbf{e}_z$ direction) of the rectangular plate
$\mathbf{x}$	location of a material point in the present configuration
$\mathbf{X}$	location of a material point in the reference configuration
$y_i^f$	variables in the free regions
$y_i^c$	variables in the contact region

$y_i^{cP}$	vector associated with the particular solution in the contact region
$y^3$	director inertia coefficient
$y^{33}$	director inertia coefficient
$Y_{1j}^f, Y_{3j}^f$	eigenvectors in the free regions
$Y_{1j}^c, Y_{3j}^c$	eigenvectors in the contact region
$z$	deformed axial position of the shell's reference surface
$Z$	reference axial coordinate
$\alpha$	normalized axial coordinate
$\alpha_1$	value of $\alpha (< 0)$ where the blade loses contact with the wheel
$\alpha_2$	value of $\alpha (> 0)$ where the blade loses contact with the wheel
$\alpha_W$	normalized axial location of the wheel's edge
$\beta$	auxiliary variable
$\beta_\alpha$	inhomogeneous deformation vectors
$\delta_r$	radial director displacement
$\delta_z$	axial director displacement
$\delta_j^i$	Kronecker delta symbol
$\Delta$	radial gap of the blade's inner surface relative to the wheel
$\eta$	normalized misfit of the inner radius of the cylindrical shell relative to that of the wheel
$\eta_1$	value of $\eta$ for which the blade first contacts the wheel
$\eta_2$	largest value of $\eta$ for which the blade first experiences two free regions and one contact region
$\eta_3$	smallest value of $\eta$ for which the blade first experiences two free regions and one contact region with the edge of the contact region being the edge of the wheel $\alpha_2 = \alpha_W$
$\theta$	angular coordinate
$\theta^\alpha$	convected Lagrangian coordinates
$\lambda$	eigenvalue
$\lambda_1^f, \lambda_3^f$	eigenvalues in the free regions
$\lambda_{R1}^f, \lambda_{R3}^f$	real parts of the eigenvalues in the free regions
$\lambda_{I1}^f, \lambda_{I3}^f$	imaginary parts of the eigenvalues in the free regions
$\lambda_1^c, \lambda_3^c$	eigenvalues in the contact region
$\lambda_{R1}^c, \lambda_{R3}^c$	real parts of the eigenvalues in the contact region
$\lambda_{I1}^c, \lambda_{I3}^c$	imaginary parts of the eigenvalues in the contact region

$\mu^*$	shear modulus associated with small deformation
$\nu^*$	Poisson's ratio associated with small deformations
$\rho_0^*$	reference mass density (mass per unit volume)
$\sigma_\theta$	approximate value of the circumferential stress
$\Sigma$	strain energy of the shell per unit reference area
$\phi_r$	radial component of the deformed director $\mathbf{d}_3$
$\phi_z$	axial component of the deformed director $\mathbf{d}_3$
$\phi_j^f$	eigenfunctions in the free regions
$\phi_i^c$	eigenfunctions in the contact region
$\omega$	angular velocity of the saw blade
$\Omega$	normalized angular velocity of the saw blade

### Acknowledgments

This research was partially supported by M. B. Rubin's Gerard Swope Chair in Mechanics and by the fund for the promotion of research at the Technion. M.B. Rubin would also like to acknowledge helpful discussions with G. Schajer related to the simplified model of the problem as a shell in contact with a wheel.

### References

- [Barcik 2003] S. Barcik, "Experimental cutting on the table band-sawing machine", *Holz Roh Werkst.* **61**:4 (2003), 313–320.
- [Chung and Sung 1998] Y. Y. Chung and C. K. Sung, "Dynamic behavior of the band/wheel mechanical system of industrial band saws", *J. Vib. Acoust. (Trans. ASME)* **120** (1998), 842–847.
- [Damaren and Le-Ngoc 2000] C. J. Damaren and L. Le-Ngoc, "Robust active vibration control of a bandsaw blade", *J. Vib. Acoust. (Trans. ASME)* **122**:1 (2000), 69–76.
- [Eklund 2000] U. Eklund, "Influencing factors on sawing accuracy in a bandsawmill", *Holz Roh Werkst.* **58**:1-2 (2000), 102–106.
- [Gendraud et al. 2003] P. Gendraud, J. C. Roux, and J. M. Bergheau, "Vibrations and stresses in band saws: a review of literature for application to the case of aluminium-cutting high-speed band saws", *J. Mater. Process. Technol.* **135**:1 (2003), 109–116.
- [Kong and Parker 2005] L. Kong and R. G. Parker, "Vibration of an axially moving beam wrapping on fixed pulleys", *J. Sound Vib.* **280**:3-5 (2005), 1066–1074.
- [Le-Ngoc and McCallion 1999] L. Le-Ngoc and H. McCallion, "Self-induced vibration of bandsaw blades during cutting", *Proc. Inst. Mech. Eng. C J. Mech. Eng. Sci.* **213**:4 (1999), 371–380.
- [Lister and Schajer 1993] P. F. Lister and G. S. Schajer, "The effectiveness of the light-gap method for indicating changes in bandsaw frequency and stiffness", *Holz Roh Werkst.* **51** (1993), 260–266.
- [Lunstrum 1981] S. J. Lunstrum, "Circular sawmills and their efficient operation", Technical report, U.S. Department of Agriculture, Forest Service, State and Private Forestry, Madison, WI, 1981, Available at <http://www.fpl.fs.fed.us/documnts/misc/circsaw.pdf>.
- [Lunstrum 1984] S. J. Lunstrum, "Balanced saw performance", pp. 16–37 in *Sawing technology: the key to improved profits*, Forest Products Research Society, Madison, WI, 1984. Also published as Technical report no. 12, U.S. Department of Agriculture, Forest Service, Forest Products Utilization, Madison, WI, 1985.

- [Mote and Naguleswaran 1966] C. D. Mote and S. Naguleswaran, “Theoretical and experimental bandsaw vibrations”, *J. Eng. Ind. (Trans. ASME)* **88** (1966), 151–156.
- [Mote Jr. 1965] C. D. Mote Jr., “A study of band saw vibrations”, *J. Franklin I.* **279**:6 (1965), 430–444.
- [Murata et al. 2002] K. Murata, Y. Ikami, and K. Fujiwara, “Change in revolution speeds of band saw wheels and power consumption during sawing”, *Bulletin of FFPRI (Forestry and Forest Products Research Institute)* **1**:2 (2002), 141–149.
- [Naghdi 1972] P. M. Naghdi, “The theory of plates and shells”, pp. 425–640 in *S. Flugge’s Handbuch der Physik*, vol. VIa/2, edited by C. Truesdell, Springer, Berlin, 1972.
- [Naghdi and Rubin 1989] P. M. Naghdi and M. B. Rubin, “On the significance of normal cross-sectional extension in beam theory with application to contact problems”, *Int. J. Solids Struct.* **25**:3 (1989), 249–265.
- [Rubin 2000] M. B. Rubin, *Cosserat theories: shells, rods and points*, Solid Mechanics and its Applications **79**, Kluwer, Dordrecht, 2000.
- [Wong and Schajer 1997] D. C. Wong and G. S. Schajer, “Effect of wheel profile on bandsaw tracking stability”, pp. 41–52 in *Proceedings of the 13th International Wood Machining Seminar* (Vancouver), 1997.
- [Wong and Schajer 2002] D. C. Wong and G. S. Schajer, “Factors controlling bandsaw tracking”, *Holz Roh Werkst.* **60**:2 (2002), 141–145.

Received 20 Dec 2005.

M. B. RUBIN: [mbrubin@tx.technion.ac.il](mailto:mbrubin@tx.technion.ac.il)

Faculty of Mechanical Engineering, Technion - Israel Institute of Technology, 32000 Haifa, Israel

E. TUFEKCI: [tufekcie@itu.edu.tr](mailto:tufekcie@itu.edu.tr)

Faculty of Mechanical Engineering, Istanbul Technical University, Gumussuyu TR-34437, Istanbul, Turkey

# A DIRECT ONE-DIMENSIONAL BEAM MODEL FOR THE FLEXURAL-TORSIONAL BUCKLING OF THIN-WALLED BEAMS

GIUSEPPE RUTA, MARCELLO PIGNATARO AND NICOLA RIZZI

In this paper, the direct one-dimensional beam model introduced by one of the authors is refined to take into account nonsymmetrical beam cross-sections. Two different beam axes are considered, and the strain is described with respect to both. Two inner constraints are assumed: a vanishing shearing strain between the cross-section and one of the two axes, and a linear relationship between the warping and twisting of the cross-section. Considering a grade one mechanical theory and nonlinear hyperelastic constitutive relations, the balance of power, and standard localization and static perturbation procedures lead to field equations suitable to describe the flexural-torsional buckling. Some examples are given to determine the critical load for initially compressed beams and to evaluate their post-buckling behavior.

## 1. Introduction

The flexural-torsional buckling of so-called thin-walled beams is an interesting problem in the field of the elastic stability of structural elements. This phenomenon was first investigated in [Wagner 1929] and [Kappus 1937], and since the publication of these pioneering works, many further studies have appeared on the subject, including [Vlasov 1961; Epstein 1979; Reissner 1983; Simo and Vu-Quoc 1991]. More recently, [Di Egidio et al. 2003] investigated modelization aspects, and [Anderson and Trahair 1972; Casciaro et al. 1991; Lanzo and Garcea 1996] presented a search of numerical results for standard elements. It is remarkable that most of the beam models presented in the literature are derived by projection of the results of three-dimensional continuum models on shell models (as in Vlasov 1961) or beam models (as in Simo and Vu-Quoc 1991).

In recent years, the authors have considered the direct one-dimensional beam model, originally introduced in [Tatone and Rizzi 1991; Rizzi and Tatone 1996]. This model describes the kinematics of the beam through the placement of the points of the beam axis, the rotation of the beam cross-sections (which are assumed to be plane in the reference configuration), and a coarse description of the warping of the beam cross-sections. Using a mechanical theory of grade one (see, for example Germain 1973a and 1973b, and Di Carlo 1996), the interaction of the beam with the surrounding environment is defined as a linear function of the velocities and of their first-order spatial approximations. In this way, the mechanical actions naturally appear as dual to the kinematic fields. In particular, actions which spend power on the warping velocity and on its spatial derivative are interpreted as bi-shear and bi-moment, respectively. As is customary in the literature, two inner constraints are assumed to hold: the shearing

---

*Keywords:* thin-walled beams, direct one-dimensional models, flexural-torsional buckling.

Giuseppe C. Ruta gratefully acknowledges the financial support of the *Progetto giovani ricercatori* (2002) of the Università La Sapienza of Rome.



strain between the axis and the cross-section is assumed to vanish, and the coarse warping measure is directly proportional to the measure of twist.

In previous papers [Rizzi and Tatone 1996; Pignataro and Ruta 2003; Pignataro et al. 2004], field equations in terms of the components of the displacement were obtained, and some flexural-torsional buckling cases were investigated. For this purpose, nonlinear hyperelastic constitutive relations were adopted. However, since no clear distinction was made between the position of the centroid and of the shear center in the plane of the cross-section, it turns out that the results obtained in the above mentioned papers are precise only for beams with symmetric cross-sections.

The aim of this paper is to overcome this drawback by presenting a refined beam model suitable for describing the flexural-torsional buckling of beams with generic, nonsymmetric cross-sections. We will describe the strain measures with respect to two beam axes (one passing through the centroids, and the other through the shear centers of the cross-sections). Then, we suitably decompose the power expended by inner actions, to distinguish clearly between actions applied at each of the two places. Introducing the same inner constraints as in the papers cited above generates reactive terms that must be added to the determined part of the contact actions, and those terms account for the geometry of nonsymmetric cross-sections. In this way, we are able to obtain field equations which are more general than those found by authors of previous studies. To test the validity of the proposed model, we present some simple examples of flexural-torsional buckling and post-buckling phenomena. The results coincide with those in the literature, for example [Timoshenko and Gere 1961; Grimaldi and Pignataro 1979].

## 2. A direct one-dimensional beam model

Let  $\mathcal{E}$  be the standard three-dimensional Euclidean ambient space. The vector space of the translations of  $\mathcal{E}$ , here denoted  $\mathcal{U}$ , is assumed to be equipped with the standard Euclidean norm and scalar (dot) product. Let us consider in  $\mathcal{E}$  a smooth curve  $\mathcal{C}_o$  and a prototype region  $\mathcal{R}$  belonging to a plane  $\mathcal{P}$ . We then attach a copy of  $\mathcal{R}$  to each point of  $\mathcal{C}_o$ , always in correspondence to the same place  $o \in \mathcal{P}$ . The region of  $\mathcal{E}$  occupied by this construction represents the beam. The curve  $\mathcal{C}_o$  corresponds to the axis of the beam, and the copies of  $\mathcal{R}$  are the beam cross sections. With no loss of generality, and only from the point of view of introducing constitutive relations, we can imagine that the place  $o \in \mathcal{P}$  is actually the centroid of the cross-section. Hence, the axis  $\mathcal{C}_o$  is a centroidal axis. Of course, the beam can be equally described using an analogous construction starting from a different curve  $\mathcal{C}_c$  in  $\mathcal{E}$ . Again, with no loss of generality, one can imagine that the place  $c \in \mathcal{P}$  is actually the shear center of the cross-sections. For the time being, we ignore the question of whether this is the shear center according to Timoshenko or Trefftz. Indeed, for open thin-walled beams the question is immaterial since either definition provides the same place (see, for example, [Andreus and Ruta 1998; Ruta 1998]). In this way, we can call the curve  $\mathcal{C}_c$  the shear axis, or the axis of the shear centers.

A change of placement is described by the placement of the axes, the rotation of each cross-section with respect to the attitude in the first placement, and a warping superposed to these two. The transformations of the axes and the rotations of the cross-sections can be described exactly, but we will limit ourselves with a coarse description of the warping by using a single scalar parameter. We can suitably define this parameter as a (possibly weighted) average of the warping over the cross-section, or as the value of the warping at a particular place of (plane of) the cross-section. A motion is naturally defined as a

one-parameter family of changes of placements,  $t \in [0, +\infty]$  being the evolution scalar real parameter (the time, for instance).

Let us consider a motion and let  $\mathcal{S}_0$  be the shape of the beam at  $t = 0$ . This may be assumed, with no loss of generality, to be the reference configuration. It is always possible to assume that  $\mathcal{S}_0$  is such that the copies of the prototype plane region  $\mathcal{R}$  remain plane, that is, the cross-sections undergo no warping. Once a place in  $\mathcal{E}$  is chosen as origin, the axes of the beam in  $\mathcal{S}_0$  are described by the regular enough position vector fields

$$\mathbf{q}_o : \rho \in [0, l] \rightarrow \mathbf{q}_o(\rho) \in \mathcal{U}, \quad \mathbf{q}_c : \rho \in [0, l] \rightarrow \mathbf{q}_c(\rho) \in \mathcal{U},$$

where  $\rho$  is a curvilinear abscissa along one of the axes compatible with the Euclidean metric of the ambient space  $\mathcal{E}$ . The unit vector fields tangent to the axes of the beam are

$$\mathbf{q}'_o(\rho), \quad \mathbf{q}'_c(\rho),$$

where the prime denotes derivation with respect to  $\rho$ . With no loss of generality, one can assume that in  $\mathcal{S}_0$  the relative position of the places  $o$  and  $c$  in the planes containing the cross-sections does not depend on  $\rho$ , so that

$$\mathbf{q}'_o(\rho) = \mathbf{q}'_c(\rho), \quad \text{for all } \rho \in [0, l]. \quad (1)$$

Let  $\mathcal{S}_t$  be the configuration assumed by the beam in the motion we are considering at the present value  $t$  of the evolution parameter. Such a configuration is described by:

- a vector field  $\mathbf{p}_o(\rho, t)$  (or, equivalently,  $\mathbf{p}_c(\rho, t)$ ), providing the position of the substantial point identified by  $\mathbf{q}_o(\rho)$  (or, equivalently,  $\mathbf{q}_c(\rho)$ ) in  $\mathcal{S}_0$ ;
- a proper orthogonal tensor field  $\mathbf{R}(\rho, t)$ , providing the rotation of the cross-sections when passing from  $\mathcal{S}_0$  to  $\mathcal{S}_t$ ;
- a scalar field  $\alpha(\rho, t)$ , providing a coarse description of the cross-sections' warping superposed to displacements induced by the rotation  $\mathbf{R}(\rho, t)$ .

The tensors  $\mathbf{R}(\rho, t)$  are required to be proper orthogonal to prevent reflections of the cross-sections. Henceforth, the fields  $\mathbf{p}_o$ ,  $\mathbf{p}_c$ ,  $\mathbf{R}$ ,  $\alpha$  will be assumed to be regular enough for the analytical developments we adopt. Also, for the sake of simplicity of notation, and when no confusion may arise, in the following the dependent variables of the indicated fields will be understood and hence omitted, as well as the measures of integration in the integrals.

The tangent vector fields to the axes of the beam in the present configuration are given by

$$\mathbf{p}'_o(\rho, t), \quad \mathbf{p}'_c(\rho, t).$$

The derivative of a field with respect to  $t$  is denoted by a superimposed dot, and  $\text{skw}(\mathcal{U} \otimes \mathcal{U})$  denotes the space of skew tensors on  $\mathcal{U}$ .

The velocity fields for the beam are

$$\begin{aligned} \mathbf{w}_o &= \dot{\mathbf{p}}_o \in \mathcal{U}, & \mathbf{w}_c &= \dot{\mathbf{p}}_c \in \mathcal{U}, \\ \mathbf{W} &= \dot{\mathbf{R}}\mathbf{R}^\top \in \text{skw}(\mathcal{U} \otimes \mathcal{U}), & \omega &= \dot{\alpha} \in \mathbb{R}. \end{aligned} \quad (2)$$

A rigid, or neutral, change of placement is one such that the rotation of the cross-sections is uniform with respect to  $\rho$ , any vector out of the plane of the cross-sections (for example, either  $\mathbf{p}'_o$  or  $\mathbf{p}'_c$ ) is rotated according to this uniform rotation, and the warping remains identical to zero.

Hence, in a rigid change of placement

$$\begin{aligned} \mathbf{R} &= \mathbf{R}_0, & \mathbf{p}'_o &= \mathbf{R}_0 \mathbf{q}'_o, \\ \mathbf{p}'_c &= \mathbf{R}_0 \mathbf{q}'_c = \mathbf{R}_0 \mathbf{q}'_o, & \alpha &= 0. \end{aligned} \quad (3)$$

Deformation is the difference between the considered change of placement and a rigid one, and must vanish if evaluated for a neutral change of placement. Suitable strain measures, pulled back to  $\mathcal{S}_0$ , are

$$\begin{aligned} \mathbf{E} &= \mathbf{R}^\top \mathbf{R}', & \alpha, & \eta = \alpha', \\ \mathbf{e}_o &= \mathbf{R}^\top \mathbf{p}'_o - \mathbf{q}'_o, & \mathbf{e}_c &= \mathbf{R}^\top \mathbf{p}'_c - \mathbf{q}'_c = \mathbf{e}_o + \mathbf{E} \mathbf{c}, \end{aligned} \quad (4)$$

where the skew tensor field  $\mathbf{E}$  provides the change of curvature of one of the beam axes when passing from  $\mathcal{S}_0$  to  $\mathcal{S}_t$ . The vector fields  $\mathbf{e}_o$  and  $\mathbf{e}_c$  represent the differences between the tangent to the axes in  $\mathcal{S}_t$ , pulled back to  $\mathcal{S}_0$ , and the tangent to the axes in  $\mathcal{S}_0$ . The vector  $\mathbf{c}$  defines the position of the place  $c$  with respect to  $o$  in the plane of the cross-sections in  $\mathcal{S}_0$ , and  $\mathbf{c}$  is uniform with respect to  $\rho$  because of (1). When the change of placement is neutral, the relations given in (3) imply that the quantities defined by (4) vanish. The strain measures given by (4) are invariant under a change of observer.

With no loss of generality, let  $\mathcal{S}_0$  be a set of parallel cross-sections orthogonal to the beam axes, each of which is assumed to be a rectilinear segment of length  $l$ . Let us fix a system of orthogonal Cartesian coordinates with the  $x_1$  axis parallel to the beam axes in  $\mathcal{S}_0$  ( $\rho \equiv x_1$ ). Furthermore, let us consider an orthonormal right-handed vector basis ( $\mathbf{i}_1, \mathbf{i}_2, \mathbf{i}_3$ ) for  $\mathcal{U}$  adapted to the introduced coordinate system such that

$$\mathbf{i}_1 = \mathbf{q}'_o = \mathbf{q}'_c.$$

With respect to the introduced basis, consider the decompositions

$$\begin{aligned} \mathbf{E} &= \chi_1 \mathbf{i}_2 \wedge \mathbf{i}_3 + \chi_2 \mathbf{i}_3 \wedge \mathbf{i}_1 + \chi_3 \mathbf{i}_1 \wedge \mathbf{i}_2, \\ \mathbf{e}_o &= \varepsilon_1 \mathbf{i}_1 + \varepsilon_2 \mathbf{i}_2 + \varepsilon_3 \mathbf{i}_3, \\ \mathbf{e}_c &= \varepsilon_{1c} \mathbf{i}_1 + \varepsilon_{2c} \mathbf{i}_2 + \varepsilon_{3c} \mathbf{i}_3 = (\varepsilon_1 + \chi_2 c_3 - \chi_3 c_2) \mathbf{i}_1 + (\varepsilon_2 - \chi_1 c_3) \mathbf{i}_2 + (\varepsilon_3 + \chi_1 c_2) \mathbf{i}_3, \end{aligned} \quad (5)$$

where  $\chi_1$  is the torsion curvature (or twist),  $\chi_2$  and  $\chi_3$  are the bending curvatures,  $\wedge$  is the exterior product between vectors of  $\mathcal{U}$  which provide skew tensors on  $\mathcal{U}$ ,  $\varepsilon_1$  is the elongation of the axis of the centroids,  $\varepsilon_2$  and  $\varepsilon_3$  are the shearing strains between the axis of the centroids and the cross-sections, and  $c_2$  and  $c_3$  are the components of  $\mathbf{c}$ . Equation (5)<sub>3</sub> provides, with respect to the shear axis, quantities similar to those provided by (5)<sub>2</sub>. In addition, it expresses these last in terms of the components of  $\mathbf{E}$  and  $\mathbf{e}_o$  (see (4)<sub>5</sub>).

It is useful to write the strain measures in terms of the displacement field  $\mathbf{u}$  of the axis of the centroids starting from  $\mathcal{S}_0$  as

$$\mathbf{u} = \mathbf{p}_o - \mathbf{q}_o = u_1 \mathbf{i}_1 + u_2 \mathbf{i}_2 + u_3 \mathbf{i}_3,$$

and to decompose the rotation  $\mathbf{R}$  as

$$\mathbf{R} = \mathbf{R}_3 \mathbf{R}_2 \mathbf{R}_1, \quad (6)$$

where  $\mathbf{R}_1$  is a rotation of amplitude  $\varphi_1$  about  $\mathbf{i}_1$ ,  $\mathbf{R}_2$  is a rotation of amplitude  $\varphi_2$  about  $\mathbf{R}_1\mathbf{i}_2$  (that is, the  $\varphi_1$ -transformed of  $\mathbf{i}_2$ ), and  $\mathbf{R}_3$  is a rotation of amplitude  $\varphi_3$  about  $\mathbf{R}_2\mathbf{R}_1\mathbf{i}_3$  (that is, the  $\varphi_2 \circ \varphi_1$ -transformed of  $\mathbf{i}_3$ ). It can be proved (see [Di Carlo and Tatone 1980]) that the matrix representation  $(\mathbf{R})_0$  of  $\mathbf{R}$  with respect to the basis  $(\mathbf{i}_1, \mathbf{i}_2, \mathbf{i}_3)$  is

$$(\mathbf{R})_0 = (\mathbf{R}_1)_0(\mathbf{R}_2)_1(\mathbf{R}_3)_2, \tag{7}$$

where  $(\mathbf{R}_1)_0$  is the matrix representation of  $\mathbf{R}_1$  with respect to the reference basis  $(\mathbf{i}_1, \mathbf{i}_2, \mathbf{i}_3)$ ,  $(\mathbf{R}_2)_1$  is the matrix representation of  $\mathbf{R}_2$  with respect to the  $\varphi_1$ -transformed of the reference basis, and  $(\mathbf{R}_3)_2$  is the matrix representation of  $\mathbf{R}_3$  with respect to the  $\varphi_2 \circ \varphi_1$ -transformed of the reference basis.

Equations (4)–(7) yield expressions of the components of the strain measures in terms of the components of the displacement of the axis of the centroids starting from the reference configuration  $\mathcal{S}_0$  as

$$\begin{aligned} \varepsilon_1 &= (1 + u'_1) \cos \varphi_2 \cos \varphi_3 + u'_2(\cos \varphi_1 \sin \varphi_3 + \sin \varphi_1 \sin \varphi_2 \cos \varphi_3) \\ &\quad + u'_3(\sin \varphi_1 \sin \varphi_3 - \cos \varphi_1 \sin \varphi_2 \cos \varphi_3) - 1, \\ \varepsilon_2 &= -(1 + u'_1) \cos \varphi_2 \sin \varphi_3 + u'_2(\cos \varphi_1 \cos \varphi_3 - \sin \varphi_1 \sin \varphi_2 \sin \varphi_3) \\ &\quad + u'_3(\sin \varphi_1 \cos \varphi_3 + \cos \varphi_1 \sin \varphi_2 \sin \varphi_3), \\ \varepsilon_3 &= (1 + u'_1) \sin \varphi_2 - u'_2 \sin \varphi_1 \cos \varphi_2 + u'_3 \cos \varphi_1 \cos \varphi, \\ \chi_1 &= \varphi'_1 \cos \varphi_2 \cos \varphi_3 + \varphi'_2 \sin \varphi_3, \\ \chi_2 &= -\varphi'_1 \cos \varphi_2 \sin \varphi_3 + \varphi'_2 \cos \varphi_3, \\ \chi_3 &= \varphi'_1 \sin \varphi_2 + \varphi'_3. \end{aligned}$$

### 3. Balance of power and balance equations

Let us assume that the interaction of the beam with the environment in its present configuration  $\mathcal{S}_t$  is quantified, for each test velocity field attainable by the beam, using a linear functional of the velocity fields, which we will call the external power  $P^e$ . Standard representation theorems of linear forms in finite-dimensional vector spaces equipped with a scalar product then let us express external power as

$$P^e = \int_0^l (\mathbf{b} \cdot \mathbf{w}_c + \mathbf{B} \cdot \mathbf{W} + \beta\omega) + \left| \mathbf{t} \cdot \mathbf{w}_c + \mathbf{T} \cdot \mathbf{W} + \theta\omega \right|_{0^-} + \left| \mathbf{t} \cdot \mathbf{w}_c + \mathbf{T} \cdot \mathbf{W} + \theta\omega \right|_{l^+}, \tag{8}$$

where the integral term quantifies the power expended by bulk actions, and the boundary terms quantify the power expended by contact actions. The vector fields  $\mathbf{b}$  and  $\mathbf{t}$  represent external force density (bulk and contact, respectively), the skew tensor fields  $\mathbf{B}$  and  $\mathbf{T}$  represent external couple density (bulk and contact, respectively), and the scalar fields  $\beta$  and  $\theta$  represent the bulk and contact actions density, respectively, which exert power on the warping. It is essential and will be fundamental henceforth that in the representation of  $P^e$  the velocity used is that of the points of the shear axis.

If we move in the frame of a mechanical theory of grade one (see, for example [Di Carlo 1996]), let us assume that the behavior of any substantial point on the (axis of the) beam is influenced by the substantial points contained in one of its neighborhoods. The interaction among different parts of the beam is then quantified for each test velocity field attainable by the beam, using a linear functional of the velocity fields and of their first derivatives with respect to  $x_1$ . This functional, denoted  $P^i$ , is also called

the internal power. The theorems we used to represent external power  $P^e$  enable us to express  $P^i$  as

$$P^i = \int_0^l (\mathbf{c}_0 \cdot \mathbf{w}_c + \mathbf{C}_0 \cdot \mathbf{W} + \gamma_0 \omega + \mathbf{c}_1 \cdot \mathbf{w}'_c + \mathbf{C}_1 \cdot \mathbf{W}' + \gamma_1 \omega'), \tag{9}$$

where the vector fields  $\mathbf{c}_0$  and  $\mathbf{c}_1$  represent self-force and internal force densities, respectively, the skew tensor fields  $\mathbf{C}_0$  and  $\mathbf{C}_1$  represent the self-couple and internal couple densities, respectively, and the scalar fields  $\gamma_0$  and  $\gamma_1$  represent the self-action and the internal action densities which spend power on the warping and on its spatial rate, respectively.

It is natural to assert that  $P^i \equiv 0$  for any change of placement leaving the beam mechanical state unaltered, and that is the situation for a the change of placement induced by a neutral velocity field. Substituting (3) into (2) and then into (9), the generality of the kinematic fields present in the integrand leads to the following reduced expression for the internal power

$$P^i = \int_0^l (\mathbf{c}_1 \cdot \mathbf{w}'_c - (\mathbf{p}'_c \wedge \mathbf{c}_1) \cdot \mathbf{W} + \mathbf{C}_1 \cdot \mathbf{W}' + \gamma_0 \omega + \gamma_1 \omega'). \tag{10}$$

Hence, in this beam model the self-force density necessarily vanishes, while the self-couple density is actually the moment of the internal force density with respect to the shear center, as expressed by the term containing the wedge product in the integrand of Equation (10).

Let us postulate that for any test velocity field attainable by the beam the interactions of the beam with the environment and of the parts of the beam with each other are such that at any value of the evolution parameter  $t$  the total power vanishes (see [Germain 1973a; 1973b; Di Carlo 1996]), or equivalently,

$$P^e = P^i. \tag{11}$$

From (11), standard localization procedures under suitable regularity hypotheses yield the law of action and reaction

$$\left| \mathbf{t} \cdot \mathbf{w}_c + \mathbf{T} \cdot \mathbf{W} + \theta \omega \right|_{x_1^-} = - \left| \mathbf{t} \cdot \mathbf{w}_c + \mathbf{T} \cdot \mathbf{W} + \theta \omega \right|_{x_1^+}, \quad \text{for all } x_1 \in [0, l]. \tag{12}$$

As a consequence of (12), the boundary terms for the expression of external power (8), can be compacted with respect to the actions on the positive side of the cross-sections. Applying the fundamental theorem of integral calculus, the balance of power (11) becomes

$$\int_0^l [(\mathbf{t}' + \mathbf{b}) \cdot \mathbf{w}_c + (\mathbf{T}' + \mathbf{p}'_c \wedge \mathbf{c}_1 + \mathbf{B}) \cdot \mathbf{W} + (\beta + \theta' - \gamma_0) \omega + (\mathbf{t} - \mathbf{c}_1) \cdot \mathbf{w}'_c + (\mathbf{T} - \mathbf{C}_1) \cdot \mathbf{W}' + (\theta - \gamma_1) \omega'] = 0. \tag{13}$$

For generality of the velocity fields and their first spatial derivatives contained in the integrand, (13) yields

$$\begin{aligned} \mathbf{c}_1 &= \mathbf{t}, & \mathbf{C}_1 &= \mathbf{T}, \\ \mathbf{t}' + \mathbf{b} &= \mathbf{0}, & \mathbf{T}' + \mathbf{p}'_c \wedge \mathbf{t} + \mathbf{B} &= \mathbf{0}, \\ \gamma_0 &= \tau = \beta + \theta', & \gamma_1 &= \mu = \theta. \end{aligned} \tag{14}$$

Equations (14)<sub>1,2</sub> represent two identification equations and tell us that in this beam model the internal action densities  $\mathbf{c}_1$  and  $\mathbf{C}_1$  actually coincide with contact force and couple densities, respectively. Equations (14)<sub>3,4</sub> express the local balance of force and torque. By torque we mean an action which spends power on an angular velocity, and is hence expressed both by a couple and the moment of a force. Equation (14)<sub>5</sub> is an auxiliary equation for  $\gamma_0$ , henceforth denoted  $\tau$  and interpreted as bishear [Vlasov 1961]. Equation (14)<sub>6</sub> is an auxiliary equation for  $\gamma_1$ , henceforth denoted  $\mu$  and interpreted as a bimoment [Vlasov 1961].

The equations in (14) were obtained by the balance of power in the present configuration. In any case, neither the identities in (14)<sub>1,2</sub> nor the scalar auxiliary (14)<sub>5,6</sub> depend on the configuration. It seems advisable, however, to pull back the local balance equations (14)<sub>3,4</sub> to the reference configuration. Let us then propose

$$\mathbf{s} = \mathbf{R}^\top \mathbf{t}, \quad \mathbf{S} = \mathbf{R}^\top \mathbf{TR}, \quad \mathbf{a} = \mathbf{R}^\top \mathbf{b}, \quad \mathbf{A} = \mathbf{R}^\top \mathbf{BR},$$

where  $\mathbf{s}$ ,  $\mathbf{S}$ ,  $\mathbf{a}$ , and  $\mathbf{A}$  are the contact and bulk action densities pulled back to  $\mathcal{S}_0$ . Taking into account the definitions of  $\mathbf{e}_c$ ,  $\mathbf{E}$ , and Equation (4), the local balance equations (14)<sub>3,4</sub>, become

$$\begin{aligned} \mathbf{s}' + \mathbf{E}\mathbf{s} + \mathbf{a} &= \mathbf{0}, \\ \mathbf{S}' + \mathbf{E}\mathbf{S} - \mathbf{S}\mathbf{E} + (\mathbf{q}'_c + \mathbf{e}_c) \wedge \mathbf{s} + \mathbf{A} &= \mathbf{0}, \end{aligned} \tag{15}$$

while the reduced expression of the internal power (10), and the balance of power (11), become

$$P^i = \int_0^l (\mathbf{s} \cdot \dot{\mathbf{e}}_c + \mathbf{S} \cdot \dot{\mathbf{E}} + \tau\omega + \mu\omega') = P^e. \tag{16}$$

We decompose the contact action densities in  $\mathcal{S}_0$  as

$$\mathbf{s} = Q_1 \mathbf{i}_1 + Q_2 \mathbf{i}_2 + Q_3 \mathbf{i}_3, \quad \mathbf{S} = M_1 \mathbf{i}_2 \wedge \mathbf{i}_3 + M_2 \mathbf{i}_3 \wedge \mathbf{i}_1 + M_3 \mathbf{i}_1 \wedge \mathbf{i}_2. \tag{17}$$

We now express the strain with respect to the shear axis  $\mathbf{e}_c$  in terms of the strain with respect to the centroidal axis  $\mathbf{e}$ , according to (4)<sub>3</sub>. Then, we can write the full expression of the internal power (16), taking into account the decompositions in (17), as

$$\int_0^l (Q_1 \dot{\epsilon}_1 + Q_2 \dot{\epsilon}_{2c} + Q_3 \dot{\epsilon}_{3c} + M_1 \dot{\chi}_1 + (M_2 + c_3 Q_1) \dot{\chi}_2 + (M_3 - c_2 Q_1) \dot{\chi}_3 + \tau\omega + \mu\omega'). \tag{18}$$

Equation (18) shows that  $Q_1$ , interpreted as normal force, spends power on the speed of elongation of the centroidal axis, while  $Q_2$  and  $Q_3$ , interpreted as shearing forces, spend power on the speed of shearing between the cross-sections and the shear axis. That is, we imagine the normal force to be applied at the centroid of the cross-section, while the shearing forces are applied at the shear center of the cross-section. The twisting couple  $M_1$  spends power on the speed of twisting, while the bending torques  $M_2 + c_3 Q_1$  and  $M_3 - c_2 Q_1$ , which are composition of a couple and of the moment of a force, respectively, spend power on the speed of bending. Also, note that the bending torques introduced are thus evaluated with respect to the centroid of the cross-section.

Substituting (5)<sub>3</sub> and (17) into (15), and assuming the bulk actions to vanish as is customary, we obtain the components of the local balance equations for contact force and torque, with all the kinematic

quantities written with respect to the centroid of the cross-sections, as

$$\begin{aligned}
 Q'_1 + \chi_2 Q_3 - \chi_3 Q_2 &= 0, \\
 Q'_2 + \chi_3 Q_1 - \chi_1 Q_3 &= 0, \\
 Q'_3 + \chi_1 Q_2 - \chi_2 Q_1 &= 0, \\
 M'_1 + \chi_2 M_3 + \chi_3 M_2 + (\varepsilon_2 - \chi_1 c_3) Q_3 - (\varepsilon_3 + \chi_1 c_2) Q_2 &= 0, \\
 M'_2 + \chi_3 M_1 + \chi_1 M_3 + (\varepsilon_3 + \chi_1 c_2) Q_1 - (1 + \varepsilon_1 + \chi_2 c_3 - \chi_3 c_2) Q_3 &= 0, \\
 M'_3 + \chi_1 M_2 + \chi_2 M_1 + (1 + \varepsilon_1 + \chi_2 c_3 - \chi_3 c_2) Q_2 - (\varepsilon_2 - \chi_1 c_3) Q_1 &= 0.
 \end{aligned}$$

**4. Inner constraints and constitutive relations**

If the beam is made of homogeneous and elastic material, standard axioms of the constitutive theory [Truesdell and Noll 1965] state that the most general material response function assumes the reduced expression

$$S = \hat{S}(\mathbf{e}, \mathbf{E}, \alpha, \eta), \tag{19}$$

where  $S$  represents each of the components of  $\mathbf{s}$  and  $\mathbf{S}$ , and  $\tau$  and  $\mu$ .

Let us now introduce some inner constraints. The first takes into account a standard assumption in the literature, that is, that warping actually depends on the other strain measures, and vanishes when no strain is present, as

$$\alpha = \hat{\alpha}(\mathbf{e}, \mathbf{E}), \quad \hat{\alpha}(\mathbf{0}, \mathbf{0}) = 0, \tag{20}$$

where  $\hat{\alpha}$  is a scalar function independent of the frame of reference, since both  $\mathbf{e}$  and  $\mathbf{E}$  are likewise independent. On the basis of the literature, it seems natural to postulate the particular expression for Equation (20)

$$\alpha = \xi \chi_1, \quad \xi \in \mathbb{R}, \quad \eta = \xi \chi'_1, \tag{21}$$

where  $\xi$  is a numerical constant [Vlasov 1961; Reissner 1983; Simo and Vu-Quoc 1991; Tatone and Rizzi 1991; Rizzi and Tatone 1996]. In particular, with reference to [Simo and Vu-Quoc 1991], a possible kinematic interpretation for  $\alpha$  is that of a suitably weighted average of out-of-plane displacement of the points initially lying on the same plane cross section.

Furthermore, let us assume that the shearing strains between the cross-sections and the axis of the centroids vanishes. This implies that in a neighborhood of the centroid, the cross section remains orthogonal to the axis of the centroids, as

$$\mathbf{e} = \varepsilon_1 \mathbf{q}'_o = \varepsilon_1 \mathbf{e}_1 \Rightarrow \varepsilon_2 = \varepsilon_3 = 0. \tag{22}$$

Note that this assumption does not imply that the whole of the cross-section remains orthogonal to the beam axes. Indeed,  $\varepsilon_{2c}$  and  $\varepsilon_{3c}$  do not vanish, as is easily obtained from (4)<sub>3</sub>.

According to the principle of determinism for constrained materials [Truesdell and Noll 1965], introducing constraints implies that the contact actions consist of the sum of two contributions. One of these is determined by the motion according to a constitutive relation (19), but the other is not. For this reason, the former is called active and the latter reactive. The reactive part of the contact actions is here denoted by the subscript  $r$  and is characterized, for so-called smooth constraints [Truesdell and Noll 1965], by spending no power on any velocity field compatible with the introduced constraints. In

our case, the introduced constraints are those between warping and twist (21), and of vanishing shearing strain between the cross-sections and the centroidal axis (22). Characterization of smooth constraints yields

$$0 = \int_0^l (\mathbf{s}_r \cdot \dot{\mathbf{e}}_c + \mathbf{S}_r \cdot \dot{\mathbf{E}} + \tau_r \dot{\alpha} + \mu_r \dot{\eta}) = \int_0^l (Q_{1r} \dot{\epsilon}_1 + (M_{1r} - c_3 Q_{2r} + c_2 Q_{3r} + \xi \tau_r) \dot{\chi}_1 + (M_{2r} + c_3 Q_{1r}) \dot{\chi}_2 + (M_{3r} - c_2 Q_{1r}) \dot{\chi}_3 + \mu_r \xi \dot{\chi}'_1), \quad (23)$$

where we used the reduced expression for the internal power (16) and the decompositions of the strain measure (4)<sub>3</sub> and of the contact actions (17). For generality of the velocity fields and of the domain of integration in (23), we obtain

$$\begin{aligned} Q_{1r} &= 0, & Q_{2r}, Q_{3r} &\in \mathbb{R}, \\ M_{1r} &= c_3 Q_{2r} - c_2 Q_{3r} - \xi \tau_r, & M_{2r} &= M_{3r} = 0, \\ \tau_r &\in \mathbb{R}, & \mu_r &= 0. \end{aligned} \quad (24)$$

Thus, the normal force, the bending couples and the bi-moment are entirely determined by the motion (that is, their reactive part vanishes). On the other hand, the shearing forces and the bi-shear have a reactive part entirely undetermined by the motion. If, as is standard in the literature, the shearing force is assumed to depend only on the shearing strain, the inner constraint on the shearing strain makes the shearing force purely a constraint reaction which is altogether undetermined by the motion. Analogous reasoning can be produced for the bi-shear, to yield

$$Q_2 = Q_{2r}, \quad Q_3 = Q_{3r}, \quad \tau = \tau_r. \quad (25)$$

Thus, some actions are purely active, others purely reactive. The exception is the twisting couple, which has an active part and a reactive one. The reactive part takes into account reactive bi-shear and shearing forces, which are considered to be applied at the shear center. The presence of bi-shear as a reactive component of the twisting couple is well known in the literature, and was first reported by [Vlasov 1961], where it arises from the inner constraint of vanishing shearing strain of the cross-section middle line in its own plane.

To study possible cases of bifurcations of elastic equilibrium, we use a static perturbation technique [Budiansky 1974]. Let us suppose that the contact actions derive from an elastic potential, thus remaining within the limits of the standard theory established in [Koiter 1945]. Let us further assume that the material of the beam is hyperelastic. Then, we adopt nonlinear constitutive relations for the active part of the contact actions, that is, those determined by the motion. These are denoted by the subscript *a* and



are

$$\begin{aligned}
 Q_{1a} &= Q_1 = a\varepsilon_1 + \frac{1}{2}d\chi_1^2, \\
 M_{1a} &= (c + d\varepsilon_1 + f_2\chi_2 + f_3\chi_3 + g\eta)\chi_1, \\
 M_{2a} &= M_2 = b_2\chi_2 + \frac{1}{2}f_2\chi_1^2, \\
 M_{3a} &= M_3 = b_3\chi_3 + \frac{1}{2}f_3\chi_1^2, \\
 \mu_a &= \mu = h\eta + \frac{1}{2}g\chi_1^2,
 \end{aligned}
 \tag{26}$$

where the coefficients  $a, b_j$  ( $j=2, 3$ ),  $c, h$  represent the rigidities in extension, bending, torsion, warping, respectively, and  $d, f_j$  ( $j=2, 3$ ), and  $g$  take into account the couplings between extension and torsion, bending and torsion, warping and torsion, respectively [Truesdell and Noll 1965; Møllmann 1986]. In (26), only those contact actions which are not entirely reactive have been characterized. Furthermore, the consequences of (24) have been considered, and the coincidence of some of the contact actions with their active part has been put into evidence.

If the bulk action  $\beta$  vanishes, which is a standard assumption in continuum mechanics, the Equations (14)<sub>5,6</sub>, (21), (24)<sub>3,5,6</sub>, (25), and (26) yield

$$\begin{aligned}
 \mu &= h\xi\chi_1' + \frac{1}{2}g\chi_1^2 \Rightarrow \tau = \mu' = h\xi\chi_1'' + g\chi_1\chi_1', \\
 M_1 &= M_{1a} + M_{1r} = (c + d\varepsilon_1 + f_2\chi_2 + f_3\chi_3)\chi_1 - h\xi^2\chi_1'' + c_3Q_2 - c_2Q_3.
 \end{aligned}$$

Comparing Equation (V.1.10)<sub>3</sub> in [Vlasov 1961] and our Equation (21)<sub>3</sub> we can make the following correspondences:

$$\begin{aligned}
 a &= EA, & b_j &= EI_j \quad (j = 2, 3), & c &= GI_c, \\
 d &= EI_d, & f_j &= EI_{f_j} \quad (j = 2, 3), & h\xi^2 &= EI_\omega,
 \end{aligned}$$

where  $E$  and  $G$  are the elasticity moduli in extension and shear, respectively,  $A$  is the area of the cross-section,  $I_j$  ( $j = 1, 2$ ) are the centroidal, principal moments of inertia of the cross-section,  $I_c$  is the torsion inertia factor for thin-walled cross-sections,  $I_d$  is the polar moment of inertia of the cross-section with respect to the shear center,  $I_\omega$  is the warping inertia (the second moment of the sectorial area with respect to the area of the cross-section), and  $I_{f_j} = \int_{\mathcal{A}} x_j r^2$  ( $j = 2, 3$ ), where  $x_j$  is the coordinate of a point of the cross-section with respect to the centroid and  $r$  the distance of the same point from the shear center.

### 5. Buckling of compressed beams

Let us consider a beam compressed by a dead load (that is, a force constant in magnitude, direction and sign) of magnitude  $\lambda$ . It is very easy to see by means of elementary considerations that one solution of the elastic static problem, called the fundamental equilibrium path, is described by the following fields,

denoted by the superscript f:

$$\begin{aligned} \mathbf{u}^f &= -\frac{\lambda}{a}x_1\mathbf{i}_1, & \mathbf{R}^f &= \mathbf{I}, & \alpha^f &= 0, \\ \mathbf{e}^f &= -\frac{\lambda}{a}\mathbf{i}_1, & \mathbf{E}^f &= \mathbf{0}, & \eta^f &= 0, \\ \mathbf{s}^f &= -\lambda\mathbf{i}_1, & \mathbf{S}^f &= \mathbf{0}, & \tau^f &= 0, & \mu^f &= 0. \end{aligned}$$

A possible different solution of the same problem, called the bifurcated path, is denoted by the superscript b, and is then described by the fields

$$\begin{aligned} \mathbf{u}^b &= \mathbf{u} - \frac{\lambda}{a}x_1\mathbf{i}_1, & \mathbf{R}^b &= \mathbf{R} + \mathbf{I}, & \alpha^b &= \alpha, \\ \mathbf{e}^b &= \mathbf{e} - \frac{\lambda}{a}\mathbf{i}_1, & \mathbf{E}^b &= \mathbf{E}, & \eta^b &= \eta, \\ \mathbf{s}^b &= \mathbf{s} - \lambda\mathbf{i}_1, & \mathbf{S}^b &= \mathbf{S}, & \tau^b &= \tau, & \mu^b &= \mu. \end{aligned} \tag{27}$$

From Equation (27) on, symbols of fields without superscripts denote the differences between quantities as evaluated in the bifurcated and in the fundamental paths, that is,

$$(\cdot) := (\cdot)^b - (\cdot)^f.$$

In other words, the strain measures, local balance and auxiliary equations and constitutive relations henceforth will be written in terms of differences. Differences will also be assumed to depend, with regularity sufficient to our scope, on a scalar parameter  $\sigma$ , as

$$(\cdot) = (\cdot)(\sigma), \quad \sigma \in [0, 1], \quad (\cdot)|_{\sigma=0} = 0,$$

that is, the differences are assumed to vanish in the fundamental path, where  $\sigma = 0$ .

Since we are using a static perturbation procedure, let us perform a formal  $\sigma$ -power series expansion of the fields of interest and of the load multiplier  $\lambda$  in a neighborhood of  $\sigma = 0$ . The field equations at the first order of such a formal expansion are

$$\begin{aligned} a\bar{u}_1 &= 0 \\ b_3\bar{u}_2'''' + \lambda\left(\frac{a-\lambda}{a}\right)\bar{u}_2'' - \lambda c_3\bar{\varphi}_1'' &= 0 \\ b_2\bar{u}_3'''' + \lambda\left(\frac{a-\lambda}{a}\right)\bar{u}_3'' + \lambda c_2\bar{\varphi}_1'' &= 0 \\ h\xi^2\bar{\varphi}_1'''' + \left(\frac{d\lambda-ac}{a}\right)\bar{\varphi}_1'' + \lambda(c_2\bar{u}_3'' - c_3\bar{u}_2'') &= 0 \end{aligned} \equiv D_{ij}\bar{v}_j = 0, \tag{28}$$

where a superimposed bar indicates the first-order increment of the indicated quantities with respect to the perturbation parameter  $\sigma$ . Equation (28) has been written both in extended and in compact form, with  $\bar{v}_j = (\bar{u}_1, \bar{u}_2, \bar{u}_3, \bar{\varphi}_1)$  and  $D_{ij}$  a symbolic linear differential operator.

Equation (28)<sub>1</sub> is independent of Equations (28)<sub>2-4</sub>, while these last constitute a coupled system of ordinary differential equations with constant coefficients. The equations in (28), along with suitable boundary conditions, form an eigenvalue problem which provides the critical values  $\lambda_{ci}$ , for  $i = 1, 2, 3$

of the load multiplier and the mode shapes of the linearized displacement components  $\bar{u}_2, \bar{u}_3, \bar{\varphi}_1$ . In the following sections, we consider two benchmark examples, one for a simply supported beam, and one for a clamped beam.

**5.1. Simply supported beam.** In this case the linearized boundary conditions we considered are

$$\begin{aligned} x_1 = 0 : \quad & \bar{u}_i = \bar{M}_i = 0, \quad i = 1, 2, 3; \quad \bar{\mu} = 0, \\ x_1 = l : \quad & \bar{u}_2 = \bar{u}_3 = \bar{\varphi}_1 = \bar{Q}_1 = \bar{M}_2 = \bar{M}_3 = \bar{\mu} = 0. \end{aligned} \tag{29}$$

Note that the hinge at  $x_1 = 0$  does not inhibit warping, while the support at  $x_1 = l$  permits axial displacement and warping and inhibits transverse displacement and torsion rotation of the cross-section.

The solution of (28)<sub>1</sub> is not interesting from the point of view of finding a linearized bifurcated path. With the relevant boundary conditions in (29) it is immediately evident that  $\bar{u}_1 = 0$ . On the other hand, nontrivial solutions of equations (28)<sub>2-4</sub>, with the relevant boundary conditions of (29), of the form

$$\begin{aligned} \bar{u}_2 &= V \sin\left(\frac{\pi x_1}{l}\right), \\ \bar{u}_3 &= W \sin\left(\frac{\pi x_1}{l}\right), \\ \bar{\varphi}_1 &= \Phi \sin\left(\frac{\pi x_1}{l}\right), \end{aligned} \tag{30}$$

where  $V, W,$  and  $\Phi$  are arbitrary integration constants, exist under the condition

$$\det \begin{pmatrix} b_3 \left(\frac{\pi}{l}\right)^2 - \lambda + \frac{\lambda^2}{a} & 0 & \lambda c_3 \\ 0 & b_2 \left(\frac{\pi}{l}\right)^2 - \lambda + \frac{\lambda^2}{a} & -\lambda c_2 \\ \lambda c_3 & -\lambda c_2 & h\xi^2 \left(\frac{\pi}{l}\right)^2 - \frac{d\lambda}{a} + c \end{pmatrix} = 0. \tag{31}$$

Equation (31) expresses an eigenvalue problem which provides the searched critical load multipliers. It coincides, modulo the necessary identifications of the constitutive coefficients, with the result provided in [Grimaldi and Pignataro 1979], which was obtained starting from a shell model inspired by [Vlasov 1961]. By writing (31) explicitly, we obtain the characteristic equation of the bifurcation problem, which turns out to be a third-order polynomial in terms of the load multiplier  $\lambda$ . The real solutions of such an equation provide the critical values of the load multiplier, and the relevant eigenmodes are the buckling modes. It is apparent from (31) that the critical loads and the buckling modes depend on the material properties of the beam, but are also strongly influenced by the shape of the cross-sections. In particular, symmetries of the cross sections are of particular importance.

When the cross-section of the beam exhibits two axes of symmetry, the centroid coincides with the shear center, that is,  $c_2 = c_3 = 0$ . Then, it is apparent that the left hand side of (31) reduces to the product of three distinct factors. Hence there are three real and distinct eigenvalues of the characteristic equation

$$\begin{aligned} \lambda_{c1} &= \frac{ac}{d} \left( 1 + \frac{h\xi^2\pi^2}{cl^2} \right), \\ \lambda_{c2} &= \frac{a}{2} \left( 1 - \sqrt{1 - \frac{4b_3\pi^2}{al^2}} \right), \\ \lambda_{c3} &= \frac{a}{2} \left( 1 - \sqrt{1 - \frac{4b_2\pi^2}{al^2}} \right). \end{aligned} \tag{32}$$

The three pertaining buckling modes (two purely flexional, one purely torsional) occur separately. These results coincide with those in [Grimaldi and Pignataro 1979] and also those in [Timoshenko and Gere 1961; Pignataro and Ruta 2003]. When  $a \rightarrow \infty$ , the two flexional critical loads in (32) reduce to the standard Euler flexional buckling loads, and no torsional buckling appears. This result can be inferred from [Timoshenko and Gere 1961] as well. Indeed, in a nonextensible beam with the centroid coincident with the shear center, a compressive dead load cannot produce, even in a buckled shape, a torsion couple inducing twist. Only flexional buckling modes are possible.

When the cross-section of the beam exhibits one axis of symmetry, for instance,  $x_3$ , it necessarily follows that  $c_2 = 0$ . Then, the left hand side of (31) is the product of two factors. One provides the same flexional buckling load  $\lambda_{c3}$  as in (32)<sub>3</sub>. However, the only real root of the other factor has a really complicated expression which is not reported here for the sake of simplicity. Instead we present a simplified expression, obtained from this complicated one by considering a nonextensible beam, that is, letting  $a \rightarrow \infty$ , yielding

$$\lambda_{c1} = \lambda_{c2} = \frac{1}{2c_3^2} \left( \sqrt{c + h\xi^2\frac{\pi^2}{l^2}} \sqrt{c + h\xi^2\frac{\pi^2}{l^2} + 4b_3c_3^2\frac{\pi^2}{l^2}} - \left( c + h\xi^2\frac{\pi^2}{l^2} \right) \right). \tag{33}$$

Hence we deduce two very interesting results for beams with cross-sections exhibiting one axis of symmetry. First, there are two only possible buckling modes. One is purely flexional and Euler-like, in the plane described by the axis of the beam and the axis of symmetry of the cross-section (in this case,  $\bar{u}_3$ ). The other is a coupled flexural-torsional mode (in this case, a combination of  $\bar{u}_2$  and  $\bar{\varphi}_1$ ). Second, since the centroid does not coincide with the shear center, even for nonextensible beams, a torsional (or more exactly, a flexural-torsional) buckling mode is present. This result clearly coincides with the original one provided in [Grimaldi and Pignataro 1979].

When the cross-section exhibits no symmetries, the presence of both coordinates of the shear center in the characteristic equation (31), yields a single real-valued critical load, providing flexural-torsional buckling, and the three modes  $\bar{u}_2, \bar{u}_3, \bar{\varphi}_1$  are coupled and occur together. That is, under the critical load the beam bends in both transverse directions and twists. The expression of the critical load, even in the case of nonextensible beams, is cumbersome and is not reported here for the sake of simplicity. This result also clearly coincides with that in [Grimaldi and Pignataro 1979].

**5.2. Clamped beam.** In this case the considered linearized boundary conditions are

$$\begin{aligned} x_1 = 0: & \quad \bar{u}_i = \bar{\varphi}_i = 0, \quad i = 1, 2, 3; \quad \varphi'_1 = 0, \\ x_1 = l: & \quad \bar{Q}_i = \bar{M}_i = 0, \quad i = 1, 2, 3; \quad \bar{\mu} = 0. \end{aligned} \tag{34}$$

That is, all the displacements vanish and warping is prevented at the clamped end, while all the contact actions, as well as the bi-moment, are assumed to vanish at the free end. As in the case of the simply supported beam, here as well the solution of (28)<sub>1</sub> is of no interest for determining a linearized buckling path, and easily can be proved to be identically equal to zero.

On the other hand, nontrivial solutions of equations (28)<sub>2-4</sub>, with the relevant boundary conditions in equations (34), of the form

$$\begin{aligned}\bar{u}_2 &= V \left[ 1 - \cos \left( \frac{\pi x_1}{2l} \right) \right], \\ \bar{u}_3 &= W \left[ 1 - \cos \left( \frac{\pi x_1}{2l} \right) \right], \\ \bar{\varphi}_1 &= \Phi \left[ 1 - \cos \left( \frac{\pi x_1}{2l} \right) \right],\end{aligned}\tag{35}$$

where  $V$ ,  $W$ , and  $\Phi$  are arbitrary integration constants, exist under the condition

$$\det \begin{pmatrix} b_3 \left( \frac{\pi}{2l} \right)^2 - \lambda + \frac{\lambda^2}{a} & 0 & \lambda c_3 \\ 0 & b_2 \left( \frac{\pi}{2l} \right)^2 - \lambda + \frac{\lambda^2}{a} & -\lambda c_2 \\ \lambda c_3 & -\lambda c_2 & h\xi^2 \left( \frac{\pi}{2l} \right)^2 - \frac{d\lambda}{a} + c \end{pmatrix} = 0.\tag{36}$$

It is apparent that (36) provides a characteristic equation which has the same form as that provided by (31) for the simply supported beam. The only difference between the two characteristic equations is in the coefficient  $(2l)^2$  instead of  $l^2$  in the terms multiplying  $b_2$ ,  $b_3$  and  $h\xi^2$ . Hence, apart from this numerical difference, it is obvious that all the results obtained for the simply supported beam are the same of those for the clamped beam. It follows that our analysis and remarks for the simply supported beam can be equally reproduced for the clamped beam. The obtained results are then qualitatively the same as those in [Grimaldi and Pignataro 1979] and for symmetric cross-sections, coincide with those in [Timoshenko and Gere 1961; Pignataro and Ruta 2003].

## 6. Post-buckling paths

A fundamental aspect of the study of bifurcation paths is the analysis of the post-buckling behavior of the structural element under consideration. That is, it is essential to understand whether the considered element has a stable or unstable post-buckling behavior. This also can tell us if the element is sensitive to imperfection. Another interesting aspect is related to the possibility of interaction between buckling modes, which occurs when the geometrical and mechanical characteristics are such that two or more buckling modes occur under the same critical load.

To study all these aspects, we must analyze the field equations at the second order of the formal power series expansion in terms of  $\sigma$  in a neighborhood of the bifurcation point. These turn out to be

$$\begin{aligned}
 D_{11}\bar{\bar{u}}_1 &= -2\left(a(\bar{u}'_2\bar{u}''_2 + \bar{u}'_3\bar{u}''_3) + d\bar{\varphi}'_1\bar{\varphi}''_1 + \frac{a}{a-\lambda_c}(\bar{u}''_2(\lambda_c c_3\bar{\varphi}'_1 - b_3\bar{u}''_2) - \bar{u}''_3(\lambda_c c_2\bar{\varphi}'_1 + b_2\bar{u}''_3))\right), \\
 D_{22}\bar{\bar{u}}_2 + D_{24}\bar{\bar{\varphi}}_1 &= 2b_2(\bar{u}''_2\bar{\varphi}'_1)'' + 2f_2(\varphi'_1\varphi''_1)' + 2\lambda_c c_2(\bar{u}'_2\bar{u}''_3)' + 2\lambda_c c_3(\bar{\varphi}'_1)^2 \\
 &\quad + 2\lambda_c\left(1 - \frac{\lambda_c}{a}\right)\bar{u}''_2\bar{\varphi}_1 + 2\left(c - \frac{d\lambda_c}{a} - b_3\right)(\bar{u}''_2\bar{\varphi}'_1)' \\
 &\quad - 2b_3\bar{u}''_2\bar{\varphi}'_1 - 2h\xi^2(\bar{u}''_2\bar{\varphi}''_1)' + \frac{2ac_3}{a-\lambda}(\lambda_c(c_3(\bar{u}''_2\bar{\varphi}'_1)' - c_2(\bar{u}''_3\bar{\varphi}'_1)') - b_2(\bar{u}''_3\bar{u}''_3)' - b_3(\bar{u}''_2\bar{u}''_2)') \\
 &\quad - 2\bar{\lambda}\left(\left(1 - \frac{\lambda_c}{a}\right)\bar{u}''_3 + \frac{1}{a-\lambda_c}(ac_2\bar{\varphi}''_1 + b_2\bar{u}''_3)\right), \\
 D_{32}\bar{\bar{u}}_3 + D_{34}\bar{\bar{\varphi}}_1 &= -2b_3(\bar{u}''_3\bar{\varphi}'_1)'' + 2f_3(\varphi'_1\varphi''_1)' - 2\lambda_c c_3(\bar{u}'_2\bar{u}''_3)' \\
 &\quad + 2\lambda_c c_2(\bar{\varphi}'_1)^2 + 2b_3\bar{u}''_2\bar{\varphi}'_1 + 2h\xi^2(\bar{u}''_3\bar{\varphi}''_1)' \\
 &\quad - 2\lambda_c\left(1 - \frac{\lambda_c}{a}\right)\bar{u}''_3\bar{\varphi}_1 - 2\left(c - \frac{d\lambda_c}{a} - b_2\right)(\bar{u}''_3\bar{\varphi}'_1)' \\
 &\quad + \frac{2ac_2}{a-\lambda}(\lambda_c(c_3(\bar{u}''_2\bar{\varphi}'_1)' - c_2(\bar{u}''_3\bar{\varphi}'_1)') - b_2(\bar{u}''_3\bar{u}''_3)' - b_3(\bar{u}''_2\bar{u}''_2)') \\
 &\quad - 2\bar{\lambda}\left(\left(1 - \frac{\lambda_c}{a}\right)\bar{u}''_2 - \frac{1}{a-\lambda_c}(ac_3\bar{\varphi}''_1 + b_3\bar{u}''_2)\right), \\
 D_{42}\bar{\bar{u}}_2 + D_{43}\bar{\bar{u}}_3 + D_{44}\bar{\bar{\varphi}}_1 &= 2h\xi^2(\bar{u}'_2\bar{u}''_3)''' + 2(b_2 - b_3)\bar{u}''_2\bar{u}'_3 \\
 &\quad + 2\left(\frac{d\lambda_c}{a} - c\right)(\bar{u}'_2\bar{u}''_3)' + 2\lambda_c(c_3\bar{u}_3\bar{\varphi}_1 + c_2\bar{u}''_2\bar{\varphi}_1) \\
 &\quad + 2\left(\bar{\varphi}'_1(f_3\bar{u}''_2 - f_2\bar{u}''_3)\right)' + 2\bar{\lambda}\left(c_3\bar{u}''_2 - c_2\bar{u}''_3 - \frac{d}{a}\bar{\varphi}''_1\right), \quad (37)
 \end{aligned}$$

where  $\lambda_c$  is one of the critical values of the load multiplier and the  $D_{ij}$  are the components of the symbolic linear differential operator introduced in (28). That is, the field equations at the second order of the formal power series expansion in terms of  $\sigma$  have the same formal structure of the equations at the first order. The difference is that first order equations are homogeneous while second order equations are not (see also [Budiansky 1974; Pignataro et al. 1991]). Hence, since  $\lambda_c$  is an eigenvalue, that is, the symbolic operator  $D_{ij}$  is singular, a condition of solvability of the system described by equations (37) must be introduced. This turns out to be given by the requirement that the right-hand side of (37) be orthogonal to any of the eigensolutions of the first order equations provided by (28). In this case, the dot product yielding an orthogonality condition is given by the integral over the length of the beam of the sum of the products between each right hand side of (37) and the corresponding eigenmode. Such a condition, supplemented by a normalization condition on the buckling modes, will provide the expressions for determining  $\bar{\lambda}$ , that is, the slope of the post-buckling path. Roughly speaking, when  $\bar{\lambda} = 0$ , the considered buckling mode is symmetric, otherwise it is imperfection-sensitive (see also [Budiansky 1974; Pignataro et al. 1991]).

In the following sections, we investigate the case of the simply supported beam considered before. Indeed, since the eigenmodes (35) are qualitatively the same as the eigenmodes (32), the qualitative behaviour of the clamped beam is the same as this of the simply supported one. Since the equation

for the axial component of the displacement is immaterial for the study of buckling and hence also of post-buckling, we will leave it aside, and focus attention on eqs. (37)<sub>2,3,4</sub>.

We will limit ourselves to examine the case when the cross section exhibits two axes of symmetry, the eigenmodes are provided by equations (30) and the critical load multipliers are given by the equations of (32). Furthermore, in that case we have  $c_2 = c_3 = 0$  and  $f_2 = f_3 = 0$ . As a consequence, the right-hand side of (37) assumes a much simpler form (which is not reported here for the sake of brevity).

For post-buckling behavior in bending, with no loss of generality, let us suppose that the buckling mode which has taken place is  $\bar{u}_2 = V \sin\left(\frac{\pi x_1}{l}\right)$  (see (30)). Once we denote the right-hand side of (37)<sub>2</sub> by  $r_2(x_1)$ , when  $\bar{u}_1 = \bar{u}_3 = \bar{\varphi}_1 = 0$ , the solvability condition yields

$$\int_0^l r_2(x_1)\bar{u}_2(x_1) dx_1 = 0 \Rightarrow \bar{\lambda} = 0.$$

That is, the post-buckling path is symmetric, a well known result of Euler-like buckling for symmetric beams.

For post-buckling behavior in torsion, the eigenmode is  $\bar{\varphi}_1 = \Phi \sin\left(\frac{\pi x_1}{l}\right)$  (see (30)). Once we denote the right hand side of (37)<sub>4</sub> by  $r_4(x_1)$ , when  $\bar{u}_1 = \bar{u}_2 = \bar{u}_3 = 0$ , the solvability condition yields

$$\int_0^l r_4(x_1)\bar{\varphi}_1(x_1) dx_1 = 0 \Rightarrow \bar{\lambda} = 0.$$

Therefore, the post-buckling path in torsion is also symmetric, which is also a well known feature of symmetric beams.

## 7. Conclusions

In this paper we presented a direct, one-dimensional beam model suitable for describing the flexural-torsional buckling of thin-walled beams. The kinematic description makes use of two different beam axes: the centroids, and the shear centers (we left aside the definition of the latter). Using this, we can imagine the contact forces applied at different places of the planes of the (unwarped) cross sections and the contact torques evaluated with respect to different places of the planes of the (unwarped) cross sections. The constitutive relations are nonlinear and hyperelastic. Two inner constraints are assumed to hold, that is, the (unwarped) cross sections remain orthogonal to the centroidal axis, and the descriptor of the warping is proportional to the twist. This makes it possible to use a static perturbation technique to look for bifurcations. Moreover, it is possible to provide a rough description of the quality of the post-buckling behavior and of the interaction of multiple buckling modes. The qualitative description of the phenomena coincides with that obtained with other beam models, yet with all the advantages of a direct model. Further developments of this study will be related to the qualitative analysis of frames.

## References

- [Anderson and Trahair 1972] J. M. Anderson and N. S. Trahair, "Stability of monosymmetric beams and cantilevers", *J. Struct. Div. ASCE* **98** (1972), 269–286.
- [Andreas and Ruta 1998] U. A. Andreas and G. Ruta, "A review of the problem of the shear centre(s)", *Continuum Mech. Therm.* **10**:6 (1998), 369–380.

- [Budiansky 1974] B. Budiansky, “Theory of buckling and postbuckling behavior of elastic structures”, pp. 1–65 in *Advances in applied mechanics*, vol. 14, edited by C. S. Yih, Academic Press, New York, 1974.
- [Casciaro et al. 1991] R. Casciaro, G. Salerno, and A. D. Lanzo, “Finite element asymptotic analysis of slender elastic structures: a simple approach”, *Int. J. Numer. Methods Eng.* **35**:7 (1991), 1397–1426.
- [Di Carlo 1996] A. Di Carlo, “A non-standard format for continuum mechanics”, pp. 263–268 in *Contemporary research in the mechanics and mathematics of materials*, edited by R. C. Batra and M. F. Beatty, CIMNE, Barcelona, 1996.
- [Di Carlo and Tatone 1980] A. Di Carlo and A. Tatone, *Analisi numerica della biforcazione dell’equilibrio di travi elastiche in 3D*, vol. 35, Istituto di Scienza delle Costruzioni, Università di L’Aquila, 1980.
- [Di Egidio et al. 2003] A. Di Egidio, A. Luongo, and F. Vestroni, “A non-linear model for the dynamics of open cross-section thin-walled beams, I: Formulation”, *Int. J. Solids Struct.* **38** (2003), 1067–1081.
- [Epstein 1979] M. Epstein, “Thin-walled beams as directed curves”, *Acta Mech.* **33**:3 (1979), 229–242.
- [Germain 1973a] P. Germain, “La méthode des puissance virtuelles en mécanique des milieux continus, 1ère partie: la théorie du second gradient”, *J. Mécanique* **12** (1973), 235–274.
- [Germain 1973b] P. Germain, “The method of virtual power in continuum mechanics, II: Microstructure”, *SIAM J. Appl. Math.* **25**:3 (1973), 556–575.
- [Grimaldi and Pignataro 1979] A. Grimaldi and M. Pignataro, “Postbuckling behavior of thin-walled open cross-section compression members”, *J. Struct. Mech.* **7**:2 (1979), 143–159.
- [Kappus 1937] R. Kappus, “Drillknicken zentrich gedrückter Stäbe mit offenem profil im elastischen Bereich”, *Luftfahrtforschung* **851** (1937), 444–57. Translated in NACA TM 851 (1938).
- [Koiter 1945] W. T. Koiter, *Over de stabiliteit van het elastisch evenwicht*, Thesis, Delft, 1945. translated in NASA TT F-10 vol. 833 (1967) and AFFDL Report TR 70-25 (1970).
- [Lanzo and Garcea 1996] A. D. Lanzo and G. Garcea, “Koiter’s analysis of thin-walled structures by a finite element approach”, *Int. J. Numer. Methods Eng.* **39**:17 (1996), 3007–3031.
- [Møllmann 1986] H. Møllmann, “Theory of thin-walled beams with finite displacements”, pp. 195–209 in *EUROMECH Colloquium 197*, edited by W. e. Pietraszkiewicz, Springer-Verlag, New York, 1986.
- [Pignataro and Ruta 2003] M. Pignataro and G. C. Ruta, “Coupled instabilities in thin-walled beams: a qualitative approach”, *Eur. J. Mech. A Solids* **22**:1 (2003), 139–149.
- [Pignataro et al. 1991] M. Pignataro, N. L. Rizzi, and A. Luongo, *Stability, bifurcation and postcritical behaviour of elastic structures*, Elsevier, Amsterdam, 1991.
- [Pignataro et al. 2004] M. Pignataro, N. L. Rizzi, and G. C. Ruta, “Buckling and post-buckling in a two-bar frame: a qualitative approach”, pp. 337–346 in *4th International Conference on Coupled Instabilities in Metal Structures—CIMS 2004*, edited by V. Gioncu et al., ESA, Rome, 2004.
- [Reissner 1983] E. Reissner, “On a simple variational analysis of small finite deformations of prismatical beams”, *Z. Angew. Math. Phys.* **34**:5 (1983), 642–648.
- [Rizzi and Tatone 1996] N. Rizzi and A. Tatone, “Nonstandard models for thin-walled beams with a view to applications”, *J. Appl. Mech. (Trans. ASME)* **63** (1996), 399–403.
- [Ruta 1998] G. Ruta, “On the flexure of a Saint-Venant cylinder”, *J. Elasticity* **52**:2 (1998), 99–110.
- [Simo and Vu-Quoc 1991] J. C. Simo and L. Vu-Quoc, “A geometrically exact rod model incorporating shear and torsion-warping deformation”, *Int. J. Solids Struct.* **27**:3 (1991), 371–393.
- [Tatone and Rizzi 1991] A. Tatone and N. Rizzi, “A one-dimensional model for thin-walled beams”, pp. 312–320 in *Trends in applications of mathematics to mechanics*, edited by W. ed. Schneider et al., Longman, Avon, 1991.
- [Timoshenko and Gere 1961] S. P. Timoshenko and J. M. Gere, *Theory of elastic stability*, McGraw-Hill, New York, 1961.
- [Truesdell and Noll 1965] C. Truesdell and W. Noll, *The non-linear field theories of mechanics*, vol. 3, Handbuch der Physik, Springer-Verlag, New York, 1965.
- [Vlasov 1961] V. Z. Vlasov, *Thin-walled elastic beams*, Monson, Jerusalem, 1961.



[Wagner 1929] H. Wagner, “Verdrehung und knickung von offenen profilen (Torsion and buckling of open sections)”, in *25th Anniversary Publication*, Technische Hochschule, Danzig, 1929. Translated in NACA TM 807 (1936).

Received 13 Jan 2006.

GIUSEPPE RUTA: [giuseppe.ruta@uniroma1.it](mailto:giuseppe.ruta@uniroma1.it)

*Dipartimento di Ingegneria Strutturale e Geotecnica, Università “La Sapienza”, via Eudossiana 18, 00184 Rome, Italy*

<http://w3.disg.uniroma1.it/GiuseppeRuta>

MARCELLO PIGNATARO: [marcello.pignataro@uniroma1.it](mailto:marcello.pignataro@uniroma1.it)

*Dipartimento di Ingegneria Strutturale e Geotecnica, Università “La Sapienza”, via Eudossiana 18, 00184 Rome, Italy*

NICOLA RIZZI: [nlr@uniroma3.it](mailto:nlr@uniroma3.it)

*Dipartimento di Strutture, Università Roma Tre, via Vito Volterra 62, 00146 Rome, Italy*

*Journal of*  
***Mechanics of***  
***Materials and Structures***

**DISCUSSION OF “STUDY OF VISCOELASTIC AND FRICTION  
DAMPER CONFIGURATIONS IN THE SEISMIC MITIGATION OF  
MEDIUM-RISE STRUCTURES”**

Julius Marko, David Thambiratnam and Nimal Perera

***Volume 1, N° 8***

***October 2006***



mathematical sciences publishers

## DISCUSSION OF “STUDY OF VISCOELASTIC AND FRICTION DAMPER CONFIGURATIONS IN THE SEISMIC MITIGATION OF MEDIUM-RISE STRUCTURES”

JULIUS MARKO, DAVID THAMBIRATNAM AND NIMAL PERERA

Volume 1:6 (2006), 1001–1039

### Izuru Takewaki writes:

The discussor is very interested in the paper presented by Julius Marko, David Thambiratnam and Nimal Perera. This paper includes various interesting aspects, for example, comparison of the effectiveness of various damper systems (viscoelastic, friction and hybrid), optimal damper configuration and location, and the influence of different types of earthquake ground motions on the response reduction by dampers.

The authors draw several references for readers. In the discussor’s opinion, more versatile investigations on optimal damper configuration and location have been made in the scientific community of earthquake engineering, and computing algorithms based on certain theoretical backgrounds have been proposed [Austin and Pister 1985; Takewaki 1997; Takewaki and Yoshitomi 1998; Takewaki 1999; Takewaki et al. 1999; Takewaki 2000a; Takewaki 2000b; Takewaki 2000c; Garcia 2001; Singh and Moreschi 2001; Singh and Moreschi 2002; Garcia and Soong 2002; Liu et al. 2003; Silvestri et al. 2003; Kiu et al. 2004; Park et al. 2004; Trombetti and Silvestri 2004; Xu et al. 2004; Liu et al. 2005; Tan et al. 2005; Trombetti and Silvestri 2006; Wongprasert and Symans 2004; Lavan and Levy 2005; Lavan and Levy 2006; Aydina et al. 2007]. For example, the optimal quantity and location of dampers can be obtained automatically with the help of these algorithms; the *gradient-based algorithm* is a representative one [Takewaki 1997; Takewaki and Yoshitomi 1998; Takewaki 1999; Takewaki 2000a; Takewaki 2000b; Takewaki 2000c; Takewaki et al. 1999]. It is obvious that dampers have various kinds of nonlinearities, and a time-history response analysis is often required to simulate the behaviors of structures with such dampers. However, many useful equivalent linearization techniques have been proposed [Roberts and Spanos 1990], and these techniques certainly make it possible to treat those behaviors almost theoretically. Although the equivalent linearization techniques have some limitations on the range of applicability, most of building structures are designed within this range of applicability.

The authors point out another interesting aspect, that is, the influence of different types of earthquake ground motions on the response reduction by dampers. The broad-range parametric simulation using recorded ground motions may be attractive and lead to many useful conclusions. However, it is also true that theoretical approaches enable one to capture more essential features of permanent interest even if the range of applicability is limited. For example, the concept of critical excitation or worst-case analysis

---

*Keywords:* dampers, multistory buildings, seismic mitigation, finite element techniques.

seems to provide a powerful means for overcoming the difficulties caused by uncertainties of earthquake ground motions [Drenick 1970; Shinozuka 1970; Takewaki 2000b; Takewaki 2001; Takewaki 2002a; Takewaki 2002b; Takewaki 2002c; Takewaki 2004; Takewaki 2007]. The tough and robust design may be possible using this concept [Takewaki 2000b; Takewaki 2002b; Takewaki 2007].

In closing, the discussor would like to call the attention of interested readers to the work reported in [Takewaki 1997; Takewaki and Yoshitomi 1998; Takewaki 1999; Takewaki et al. 1999; Takewaki 2000a; Takewaki 2000b; Takewaki 2000c; Garcia 2001; Singh and Moreschi 2001; Liu et al. 2003; Park et al. 2004; Silvestri et al. 2003; Trombetti and Silvestri 2004; Lavan and Levy 2005; Liu et al. 2005; Lavan and Levy 2006; Takewaki 2007] to provide a broader context for the results reported by Julius Marko, David Thambiratnam and Nimal Perera.

IZURU TAKEWAKI: [takewaki@archi.kyoto-u.ac.jp](mailto:takewaki@archi.kyoto-u.ac.jp)

*Dept. of Urban and Environmental Engineering, Graduate School of Engineering, Kyoto University  
Kyotodaigaku-Katsura, Nishikyo-ku Kyoto 615-8540, Japan*

### **The authors respond:**

The authors would like to thank the discussor for the encouraging remarks and the valuable comments. We reviewed the work by Austin, Pister, Takewaki, Yoshitomi, Singh, Moreschi, Garcia, Soong et al. referred to by the discussor as part of this study and found that work to be very useful and informative. This specific research project is part of a comprehensive study by industry collaborators actively involved in the structural design of high-rise buildings with the intent of gaining an understanding of the relationship between nature of ground excitation, ground structure interaction, structural system response and the effective influence of damping systems to mitigate adverse effects. The ultimate aim of this research is to explore the potential for total interactive design that includes ground support, structural framing and the various forms and configurations of damping as an integral part of high-rise building design. In doing so, we believe that it is possible to design not only the dampers but the entire building and its foundations as an integral part of the response reduction mechanism. Hence our focus on the nature of ground excitation and its interactive response with dampers.

This was only possible via a study which involved the numerous parameters that we investigated, such as earthquake type (frequency band and magnitude), damper type, location and configuration, etc. We acknowledge the discussor's comments that "theoretical approaches enable one to capture more essential features of permanent interest", and we plan to continue our work incorporating such an approach combined with synthetic ground excitations to overcome the unpredictability of ground motions.

### **References**

- [Austin and Pister 1985] M. A. Austin and K. S. Pister, "Design of seismic-resistant friction-braced frames", *J. Structural Engineering* **111**:12 (1985), 2751–2769.
- [Aydina et al. 2007] E. Aydina, M. H. Boduroglu, and D. Guney, "Optimal damper distribution for seismic rehabilitation of planar building structures", *Engineering Structures* **29** (2007), 176–185.
- [Drenick 1970] R. F. Drenick, "Model-free design of aseismic structures", *J. Engineering Mechanics Div., ASCE* **96**:EM4 (1970), 483–493.

- [Garcia 2001] D. L. Garcia, "A simple method for the design of optimal damper configurations in MDOF structures", *Earthquake Spectra* **17**:3 (2001), 387–398.
- [Garcia and Soong 2002] D. L. Garcia and T. T. Soong, "Efficiency of a simple approach to damper allocation in MDOF structures", *J. Structural Control* **9**:1 (2002), 19–30.
- [Kiu et al. 2004] W. Kiu, M. Tong, Y. Wu, and G. Lee, "Optimized damping device configuration design of a steel frame structure based on building performance indices", *Earthquake Spectra* **20**:1 (2004), 67–89.
- [Lavan and Levy 2005] O. Lavan and R. Levy, "Optimal design of supplemental viscous dampers for irregular shear-frames in the presence of yielding", *Earthquake Engineering and Structural Dynamics* **34**:8 (2005), 889–907.
- [Lavan and Levy 2006] O. Lavan and R. Levy, "Optimal design of supplemental viscous dampers for linear framed structures", *Earthquake Engineering and Structural Dynamics* **35**:3 (2006), 337–356.
- [Liu et al. 2003] W. Liu, M. Tong, X. Wu, and G. C. Lee, "Object-oriented modeling of structural analysis and design with application to damping device configuration", *J. Computing in Civil Engineering, ASCE* **17**:2 (2003), 113–122.
- [Liu et al. 2005] W. Liu, M. Tong, and G. C. Lee, "Optimization methodology for damper configuration based on building performance indices", *J. Structural Engineering, ASCE* **131**:11 (2005), 1746–1756.
- [Park et al. 2004] J.-H. Park, J. Kim, and K.-W. Min, "Optimal design of added viscoelastic dampers and supporting braces", *Earthquake Engineering and Structural Dynamics* **33**:4 (2004), 465–484.
- [Roberts and Spanos 1990] J. B. Roberts and P. Spanos, *Random vibration and statistical linearization*, John Wiley & Sons, 1990.
- [Shinozuka 1970] M. Shinozuka, "Maximum structural response to seismic excitations", *J. Engineering Mechanics Div., ASCE* **96**:EM5 (1970), 729–738.
- [Silvestri et al. 2003] S. Silvestri, T. Trombetti, and C. Ceccoli, "Inserting the mass proportional damping (MPD) system in a concrete shear-type structure", *Int. J. Structural Engineering and Mechanics* **16**:2 (2003), 177–193.
- [Singh and Moreschi 2001] M. P. Singh and L. M. Moreschi, "Optimal seismic response control with dampers", *Earthquake Engineering and Structural Dynamics* **30**:4 (2001), 553–572.
- [Singh and Moreschi 2002] M. P. Singh and L. M. Moreschi, "Optimal placement of dampers for passive response control", *Earthquake Engineering and Structural Dynamics* **31**:4 (2002), 955–976.
- [Takewaki 1997] I. Takewaki, "Optimal damper placement for minimum transfer functions", *Earthquake Engineering and Structural Dynamics* **26**:11 (1997), 1113–1124.
- [Takewaki 1999] I. Takewaki, "Displacement-acceleration control via stiffness-damping collaboration", *Earthquake Engineering and Structural Dynamics* **28**:12 (1999), 1567–1585.
- [Takewaki 2000a] I. Takewaki, *Dynamic structural design: inverse problem approach*, WIT Press, UK, 2000. 268 pages.
- [Takewaki 2000b] I. Takewaki, "Optimal damper placement for critical excitation", *Probabilistic Engineering Mechanics* **15**:4 (2000), 317–325.
- [Takewaki 2000c] I. Takewaki, "Optimal damper placement for planar building frames using transfer functions", *Structural and Multidisciplinary Optimization* **20**:4 (2000), 280–287.
- [Takewaki 2001] I. Takewaki, "Probabilistic critical excitation for MDOF elastic-plastic structures on compliant ground", *Earthquake Engineering and Structural Dynamics* **30**:9 (2001), 1345–1360.
- [Takewaki 2002a] I. Takewaki, "Critical excitation for elastic-plastic structures via statistical equivalent linearization", *Probabilistic Engineering Mechanics* **17**:1 (2002), 73–84.
- [Takewaki 2002b] I. Takewaki, "Robust building stiffness design for variable critical excitations", *J. Structural Engineering, ASCE* **128**:12 (2002), 1565–1574.
- [Takewaki 2002c] I. Takewaki, "Seismic critical excitation method for robust design: a review", *J. Structural Engineering, ASCE* **128**:5 (2002), 665–672.
- [Takewaki 2004] I. Takewaki, "Bound of earthquake input energy", *J. Structural Engineering, ASCE* **130**:9 (2004), 1289–1297.
- [Takewaki 2007] I. Takewaki, *Critical excitation methods in earthquake engineering*, Elsevier, January 2007.

- [Takewaki and Yoshitomi 1998] I. Takewaki and S. Yoshitomi, “Effects of support stiffnesses on optimal damper placement for a planar building frame”, *J. of The Structural Design of Tall Buildings* **7**:4 (1998), 323–336.
- [Takewaki et al. 1999] I. Takewaki, S. Yoshitomi, K. Uetani, and M. Tsuji, “Non-monotonic optimal damper placement via steepest direction search”, *Earthquake Engineering and Structural Dynamics* **28**:6 (1999), 655–670.
- [Tan et al. 2005] P. Tan, S. J. Dyke, A. Richardson, and M. Abdullah, “Integrated device placement and control design in civil structures using genetic algorithms”, *J. Structural Engineering, ASCE* **131**:10 (2005), 1489–1496.
- [Trombetti and Silvestri 2004] T. Trombetti and S. Silvestri, “Added viscous dampers in shear-type structures: The effectiveness of mass proportional damping”, *J. Earthquake Engineering* **8**:2 (2004), 275–313.
- [Trombetti and Silvestri 2006] T. Trombetti and S. Silvestri, “On the modal damping ratios of shear-type structures equipped with Rayleigh damping systems”, *J. Sound and Vibration* **292**:1-2 (2006), 21–58.
- [Wongprasert and Symans 2004] N. Wongprasert and M. D. Symans, “Application of a genetic algorithm for optimal damper distribution within the nonlinear seismic benchmark building”, *J. Engineering Mechanics, ASCE* **130**:4 (2004), 401–406.
- [Xu et al. 2004] Z. D. Xu, H. T. Zhao, and A. Q. Li, “Optimal analysis and experimental study on structures with viscoelastic dampers”, *J. Sound and Vibration* **273**:3 (2004), 607–618.

Received 1 Dec 2006.

JULIUS MARKO: [j2.marko@student.qut.edu.au](mailto:j2.marko@student.qut.edu.au)

School of Urban Development, Queensland University of Technology, GPO Box 2434, Brisbane 4001, Australia

DAVID THAMBIRATNAM: [d.thambiratnam@qut.edu.au](mailto:d.thambiratnam@qut.edu.au)

School of Urban Development, Queensland University of Technology, GPO Box 2434, Brisbane 4001, Australia

NIMAL PERERA: [n2nperera@hotmail.com](mailto:n2nperera@hotmail.com)

Robert Bird & Partners, Warwick House, 25 Buckingham Palace Road, London SW1W 0PP, United Kingdom

# SUBMISSION GUIDELINES

## ORIGINALITY

Authors may submit manuscripts in PDF format on-line. Submission of a manuscript acknowledges that the manuscript is *original and has neither previously, nor simultaneously, in whole or in part, been submitted elsewhere*. Information regarding the preparation of manuscripts is provided below. Correspondence by email is requested for convenience and speed. For further information, write to:

[Marie-Louise Steele](#)  
Division of Mechanics and Computation  
Durand Building, Room 262  
Stanford University  
Stanford CA 94305

## LANGUAGE

Manuscripts must be in English. A brief abstract of about 150 words or less must be included. The abstract should be self-contained and not make any reference to the bibliography. Also required are keywords and subject classification for the article, and, for each author, postal address, affiliation (if appropriate), and email address if available. A home-page URL is optional.

## FORMAT

Authors are encouraged to use L<sup>A</sup>T<sub>E</sub>X and the standard article class, but submissions in other varieties of T<sub>E</sub>X, and, exceptionally in other formats, are acceptable. Electronic submissions are strongly encouraged in PDF format only; after the refereeing process we will ask you to submit all source material.

## REFERENCES

Bibliographical references should be listed alphabetically at the end of the paper and include the title of the article. All references in the bibliography should be cited in the text. The use of B<sub>I</sub>B<sub>T</sub>E<sub>X</sub> is preferred but not required. Tags will be converted to the house format (see a current issue for examples), however, in the manuscript, the citation should be by first author's last name and year of publication, e.g. "as shown by Kramer, et al. (1994)". Links will be provided to all literature with known web locations and authors are encouraged to provide their own links on top of the ones provided by the editorial process.

## FIGURES

Figures prepared electronically should be submitted in Encapsulated PostScript (EPS) or in a form that can be converted to EPS, such as GnuPlot, Maple, or Mathematica. Many drawing tools such as Adobe Illustrator and Aldus FreeHand can produce EPS output. Figures containing bitmaps should be generated at the highest possible resolution. If there is doubt whether a particular figure is in an acceptable format, the authors should check with production by sending an email to:

[production@mathscipub.org](mailto:production@mathscipub.org)

Each figure should be captioned and numbered so that it can float. Small figures occupying no more than three lines of vertical space can be kept in the text ("the curve looks like this:"). It is acceptable to submit a manuscript with all figures at the end, if their placement is specified in the text by means of comments such as "Place Figure 1 here". The same considerations apply to tables.

## WHITE SPACE

Forced line breaks or page breaks should not be inserted in the document. There is no point in your trying to optimize line and page breaks in the original manuscript. The manuscript will be reformatted to use the journal's preferred fonts and layout.

## PROOFS

Page proofs will be made available to authors (or to the designated corresponding author) at a web site in PDF format. Failure to acknowledge the receipt of proofs or to return corrections within the requested deadline may cause publication to be postponed.

# JOURNAL OF MECHANICS OF MATERIALS AND STRUCTURES

Volume 1    No. 8    October 2006

---

Effect of tip profile on cutting processability of a trapezoidal cutting blade indented to an aluminum sheet	205
SEKSAN CHAJIT, SHIGERU NAGASAWA, YASUSHI FUKUZAWA, MITSUHIRO MURAYAMA AND ISAMU KATAYAMA	
A one-dimensional variational formulation for quasibrittle fracture	227
CLAUDIA COMI, STEFANO MARIANI, MATTEO NEGRI AND UMBERTO PEREGO	
Dynamic buckling of impulsively loaded prismatic cores	249
ENRICO FERRI, EMILIO ANTINUCCI, MING Y. HE, JOHN W. HUTCHINSON, FRANK W. ZOK AND ANTHONY G. EVANS	
Axially symmetric contact problem of finite elasticity and its application to estimating residual stresses by cone indentation	271
HAO TIAN-HU	
Crack initiation prediction for V-notches under mixed-mode loading in brittle materials	289
JIA LI AND XIAO-BING ZHANG	
A closed-form solution for a crack approaching an interface	309
BORIS NULLER, MICHAEL RYVKIN AND ALEXANDER CHUDNOVSKY	
Statistical strength of a twisted fiber bundle: an extension of daniels equal-load-sharing parallel bundle theory	329
PANKAJ K. PORWAL, IRENE J. BEYERLEIN AND S. LEIGH PHOENIX	
Contact stress on a rotating elastic band saw blade using the theory of a Cosserat surface	353
M. B. RUBIN AND E. TUFEKCI	
A direct one-dimensional beam model for the flexural-torsional buckling of thin-walled beams	383
GIUSEPPE RUTA, MARCELLO PIGNATARO AND NICOLA RIZZI	
Discussion of "Study of viscoelastic and friction damper configurations in the seismic mitigation of medium-rise structures"	401
JULIUS MARKO, DAVID THAMBIRATNAM AND NIMAL PERERA	